CRANFIELD UNIVERSITY

NASYITAH GHAZALLI

PASSIVE BISTATIC RADAR BASED ON STARING RADAR ILLUMINATORS OF OPPORTUNITY

SCHOOL OF CRANFIELD DEFENCE AND SECURITY
Centre for Electronic Warfare, Information and Cyber (EWIC)

PhD
Academic Year: 2015–2018

Supervisor: Dr Alessio Balleri
November 2018

CRANFIELD UNIVERSITY

SCHOOL OF CRANFIELD DEFENCE AND SECURITY
Centre for Electronic Warfare, Information and Cyber
(EWIC)

PhD

Academic Year: 2015–2018

NASYITAH GHAZALLI

PASSIVE BISTATIC RADAR BASED ON STARING RADAR ILLUMINATORS OF OPPORTUNITY

Supervisor: Dr Alessio Balleri
November 2018

Abstract

Passive Bistatic Radar (PBR) systems use non-cooperative illuminators of opportunity to detect, localise and track targets. They have attracted considerable research interest in recent years because they can be operated and deployed at a relatively low cost, they are difficult to detect and hence allow covert operations in hostile environments, and they do not require the allocation of an increasingly more congested frequency spectrum. Various analogue and digital communication systems have been studied and exploited as illuminators of opportunity for PBR in recent years.

Despite the extensive work carried out on PBR that exploit random communication signals, there has been limited research investigating the use of existing non-cooperative radar systems as illuminators of opportunity. The exploitation of radar signals to achieve passive bistatic detection is attracting as it may offer significant advantages. Because common radar waveforms are deterministic, a reference channel is essentially not required to detect a target. The knowledge of the deterministic waveform allows the passive receiver to be matched with the illuminator of opportunity and thus generate a Doppler map. Radar signals are also designed for detection and provide a large bandwidth, a good compression ratio and hence enhanced range resolution.

The work presented in this thesis investigates PBR solutions that exploit non-random signals transmitted by non-cooperative staring radar systems. Staring radar offer a constant illumination of the volume under surveillance and, unlike radar systems that deploy a rotating antenna, offer a continuous signal of opportunity. They are very attractive illuminators in particular for short range applications to detect low-RCS and slow-moving targets, such as drones.

In this research, a passive radar prototype, capable of operating with and without a reference channel, was developed and detection performance investigated on data collected in a set of experimental trials with the Thales-Aveillant Gamekeeper staring radar. Results show that moving targets, including drones, could be successfully detected with a PBR exploiting radar signals and operating with and without the reference channel.

Contents

List of Figures

List of Tables

List of Abbreviations

PBR	Passive Bistatic Radar
GEO	Geostationary Orbit
LEO	Low Earth Orbit
CSK	COSMO-SkyMed
TSX	TerraSAR-X
PRF	Pulse Repetition Frequency
PRI	Pulse Repetition Interval
FFT	Fast Fourier Transform
IFFT	Inverse Fast Fourier Transform
OFDM	Orthogonal Frequency Division Multiplexing
USRP	Universal Software Defined Radio Peripheral
SDR	Software Defined Radio
UMTS	Universal Mobile Telecommunication System
LTE	Long Term Evolution
WiFi	Wireless Fidelity
LFM	Linear Frequency Modulation
CFO	Carrier Frequency Offset
LO	Local Oscillator
AF	Ambiguity Function

DTV	Digital Television
DVB-T	Digital Video Broadcasting – Terrestrial
SAR	Synthetic Aperture Radar
SNR	Signal to Noise Ratio
RCS	Radar Cross Section

Acknowledgements

Firstly, I thank my Mother for her continuous support, patience and encouragement. Your prayers always followed me in this life.

The support of my lovely husband, Alex, is a strength throughout this journey. Thank you for your patience and always having faith in me.

I would like to express my deep gratitude to my PhD supervisor Dr Alessio Balleri for his excellent guidance and constant support. Your guidance helped me a lot throughout my Phd journey and writing this thesis. Besides my supervisor, I would like to thank Dr Fabiola Colone, Dr Mohammed Jahangir and Prof. Chris Baker for sharing their knowledge, idea and insightful comments.

I would also like to take the opportunity to thank my fellow students, friends and family for their discussions and advices over the course of my studies. Thank you for all the good times and being there during the hard times. You have all contributed to this research more than you know.

Finally, I would like to thank Majlis Amanah Rakyat (MARA), Malaysia for funding this Phd scholarship and Martin-Baker Aircraft Co. Ltd. for providing this computer.

In loving memory of

Haji Ghazalli Abd Kadir

&

Noor Adibah Ghazalli

Chapter 1

Introduction

Passive Bistatic Radar (PBR) detect, localise and track targets passively by processing signals of opportunity transmitted by non-cooperative sources of illumination. They are also often referred to as Passive Coherent Location (PCL) radar, Passive Covert Radar (PCR), non-cooperative radar and opportunistic radar [1].

In recent years, PBR have attracted significant interest among the radar community due to some attractive characteristics that offer key operational advantages. Because PBR are completely passive, a dedicated transmitter is not required and, as a result, they are smaller and relative lower cost than monostatic radar, they only require a limited amount of power and they are easy to operate and install. Because they operate silently, PBR are covert and difficult to detect and localise in hostile environments [1]. In addition to all these, PBR exploit signals already available in the environment and do not require the allocation of a dedicated portion of a frequency spectrum which is becoming increasingly more and more congested [2].

The general shifting of illuminators of opportunity from analogue to digital, to-

gether with larger available processing power at the receiver, have brought greater bandwidth, better range resolution and significant performance improvement. Typical sources of non-cooperative illumination include signals from broadcast systems (including TV and radio signal), cellular base stations and local area networks (LAN). The choice of different types of illuminators is driven by their strengths and weaknesses for each specific application. These include the signal parameters, the experimental configuration, and power budget calculations [3].

Although PBR has matured rapidly in the past few years, they are continuing to attract significant research interest. Ongoing research efforts are, for example looking at improving passive receiver systems and processing techniques, and at identifying optimal deployment and configuration solutions that exploit a wider range of transmitters of opportunity with better waveform properties [4]. Despite all these efforts, to date, there has still been very little work to develop PBR that exploit existing non-cooperative radar systems of opportunity. The work presented in this thesis represents a significant research step in this direction.

The exploitation of radar signals to achieve passive bistatic detection is attracting as it may offer significant advantages that are worth investigating. Because common radar waveforms are deterministic, the bistatic configuration does not essentially require a reference channel to detect a target. The knowledge of the deterministic waveform allows the passive receiver to be matched with the illuminator of opportunity and thus generate a Doppler map. Radar signals are often characterised by a large bandwidth and a good compression ratio and hence they provide enhanced range resolution. Despite these advantages, using radar platforms as illuminators of opportunity also introduces some technical challenges, especially when the transmitter is non-stationary. Airborne illuminators, for example, are continuously moving

and can provide coverage only for a limited amount of time. PBR need to rely on some prior knowledge on the presence of the signal and, because the platform is moving, there are Doppler effects induced by the platform dynamics that have to be taken into account.

To date, research attempting to use radar signals for PBR has been mostly based on the exploitation of SAR systems with the use of a reference channel. In the literature, there have been few studies of PBR that do not use a reference channel but the vast majority of these exploit random signals of opportunity, such as DVB-T [5] and DTV [6] signals.

The Thales-Aveillant Gamekeeper radar is a staring array Air Traffic Control (ATC) radar with a wide beam transmitter antenna which offers a constant illumination of the entire volume under surveillance. Unlike classic Air Traffic Control (ATC) radar systems that deploy a rotating antenna, the Thales-Aveillant Gamekeeper provides continuous target illumination and offers a constant signal of opportunity. This makes it a very attractive illuminator, in particular for short range applications detecting low-RCS and slow-moving targets, such as drones.

Drones are small targets that have increasingly become a significant danger to manned air traffic and pose a security [7] and privacy threat. Passive solutions to detect and track drones represent a very attractive option, especially in the vicinity of airports, where the risk of interfering with other existing radar and communication systems is high. A passive receiver network sited in the vicinity of the Thales-Aveillant Gamekeeper radar benefits from continuously available signals of opportunity and can use long integration times to provide fine Doppler resolution for detection, tracking and classification of small targets.

The aim of this work is to investigate and demonstrate feasibility of PBR target detection exploiting non-random radar signals of opportunity transmitted by non-cooperative existing staring radar illuminators. A passive radar prototype is developed and performance is investigated on data collected in a set of experimental trials, in a controlled environment at the Defence Academy of the UK and in an uncontrolled environment with the Thales-Aveillant Gamekeeper radar. A passive prototype was successfully developed that can operate without the use of a reference channel to demonstrate detection performance of single-channel PBR exploiting radar signals. Although the illuminator of opportunity is not cooperative, the work presented in this thesis is based on the assumption that the waveform transmitted by the illuminator is known a-priori. Signals transmitted by existing radars are deterministic and often show little variability. They can therefore be estimated on the fly or in advance with Electronic Support Measure systems (ESM) and made available in the form of prior intelligence. Results have shown moving targets, including drones, could be successfully detected.

1.1 Aim and Objectives

The research work carried out was organised into a set of specific technical objectives as follows;

- Design and develop a passive receiver prototype using SDR based on National Instrument (NI) USRP-2943R and LabVIEW
- Carry out a set of initial experimental trials to inform the design of the final prototype and evaluate the performance with respect to detection performance

during the prototyping phase

- Investigate target detection without the use of a reference channel
- Carry out a set of experimental trials exploiting transmissions by the Thales-Aveillant Gamekeeper staring radar
- Investigate target detection performance of moving targets including a human, a car and a drone with the Thales-Aveillant Gamekeeper staring radar at an airfield
- Evaluate and compare the prototype performance with and without the use of the reference channel

1.2 Thesis Layout

This thesis was built on a series of experiments to show target detection in PBR without the use of a reference channel. Throughout the experiments, the study on the features and characteristics of the transmitter of opportunity as well as signal processing was presented. The organization and arrangement of this thesis is as follows.

Chapter 1, *Introduction*, gives an overview and the outlook of the study. It also includes an overview of the thesis, a list of novel contributions and a list of published works

Chapter 2 contains a literature review on PBR. The review presents an overview of the relevant research to date on both analogue and digital transmissions. This includes ground-based, airborne and space-based illuminators.

Chapter 3, *Background Theory*, describes the relevant background theory of PBR. This includes a description of the bistatic geometry, the bistatic radar range equation and bistatic radar resolution. The ambiguity function of pulsed radars based on rectangular pulses is also presented. Windowing methods and their application to the ambiguity function are introduced.

Chapter 4, *PBR Feasibility Study* contains the feasibility study of bistatic radar without the use of a reference channel. The concept is experimentally implemented and analysed. The performance of the experimental work is assessed from the Doppler frequency obtained and by a comparison with the theoretical results.

Chapter 5, *Prototype Design and Development* presents the prototype and hardware implementation of the SDR using an NI USRP-2943R. This solution provides for a low-cost, flexible and fast prototyping. This prototype is used through out the field experiments described in subsequent chapters.

Chapter 6, *Exploitation of Staring Radar for PBR* demonstrates PBR target detection exploiting the Thales-Aveillant Gamekeeper staring radar as an illuminator of opportunity. This experimental trial aimed to detect a person running, a moving car and a flying drone. This chapter presents results obtained with the use of a reference channel.

Chapter 7, *PBR Without Reference Channel* presents the results for PBR target detection without the use of a reference channel. DC conversion is implemented to obtain the correct Doppler frequency. The comparisons of target detection performance with and without a reference channel is also presented.

Chapter 8, *Conclusions and Future Works* contains a discussion on the ex-

periments carried out as part of the work presented in this thesis. This chapter includes an indication of the challenge faced during this study. Finally, this chapter summarises the main findings and provides suggestions for future work.

1.3 Publications

As part of this work, the following papers have arisen:

Journal

- N. Ghazalli, A. Balleri, M. Jahangir, F. Colone and C. J. Baker, "Passive Detection of Drones Using a Staring Radar Illuminator of Opportunity," in submission to *IET Radar, Sonar and Navigation*

Conference Paper

- N. Ghazalli, A. Balleri and F. Colone, "Exploitation of Deterministic Signals for Passive Single-Channel Detection," *Sensor Signal Processing for Defence Conference 2017 (SSPD)*, pp. 1-5, 6-7 Dec, London, 2017, .

Presentation Without Papers

- N. Ghazalli, A. Balleri, F. Colone "Exploitation of Deterministic Signals for Passive Single Channel Detection," Poster presentation in *Electromagnetic System Interest Group (EMSIG Away Day)*, Birmingham, June 2018

- N. Ghazalli, A. Balleri "Exploitation of Deterministic Signals for Passive Single-Channel Detection on Moving Platforms," *Radar Away Day*, Birmingham, June 2017

- N. Ghazalli, A. Balleri, F. Colone "Exploitation of Deterministic Signals for Passive Single-Channel Detection on Moving Platforms," *PCL Focus Day*, Fraunhofer FHR, Germany, May 2017

- N. Ghazalli, "Passive Bistatic Radar Detection Using Non-Stationary Transmitters of Opportunity," Three Minute Thesis (3MT) in *2016 Defence and Security Doctoral Symposium*, Shrivenham, November 2016

- N. Ghazalli, A. Balleri "Passive Bistatic Radar By Satellite-borne Illuminator," Poster presentation in *2015 Defence and Security Doctoral Symposium*, Shrivenham, November 2015

Chapter 2

Literature Review

This literature review will focus on previous work related to this study in order to highlight gaps in literature and explain how the work carried out in this project contributes to creation of new knowledge. An overview of Passive Bistatic Radar (PBR) is outlined at the beginning of this chapter followed by a more specific review of the literature with respect to different illuminators of opportunity exploited in the past, starting from the early study that used analog transmissions to those exploiting digital transmissions. Published research on passive radars exploiting deterministic signals that are relevant to the research also been reviewed.

2.1 Overview of Passive Bistatic Radar

Passive Bistatic Radar (PBR) is a system that exploits existing transmitters of opportunity as non-cooperative source of illumination. A PBR system consists of one or more passive receivers that exploit non collocated transmitters of opportunity to detect, track and identify targets. Various illuminators of opportunity from analogue signal sources to digital ones, exploiting a wide range of ground-based, airborne and space-based systems have been studied and exploited in recent years. These include commercial TV and radio broadcast systems, cellular base stations and WiFi local area networks.

Griffiths and Baker explained the fundamentals of bistatic radar in [8]. This paper presented bistatic radar range equation and the direct path signals. The direct signal is a common issue in PBR radar. It is contributed by the fraction of reflected signal and the direct signal. This paper also presented an exploitation of FM radio transmitter to estimate detection range. The bistatic self ambiguity function (AF) from the signal was presented which is the output of the matched filter response of the direct signal. This paper also showed the effect of geometry can be studied by normalising the waveform contribution.

In [1] the book edited by Willis and Griffiths explained and discussed about the advancement of bistatic radar starting from mid 1990s. The authors presented ongoing research in bistatic radar including air surveillance. Furthermore, the performance of geometry dependent in bistatic radar was discussed through the AF. It was found that the AF for bistatic radar can be divide into two parts which is a waveform part and a geometrical part. A waveform part is efficiently analysed by applying monostatic ambiguity function while the geometrical part by applying

bistatic ambiguity function [9].

It was also presented in [1] a model to estimate the target location errors of PBR operated in multistatic mode with two or more FM transmitters with the errors for bistatic range and Doppler measurements was developed. This model could be considered as an alternative to the existing range, Doppler and angular resolution presented in [10].

PBR has attracted significant interest over the years because it is operated and deployed at a relatively low cost. It only needs a bistatic receiver which is operated passively. PBR does not need a dedicated transmitter, and because it is completely passive, it is inherently covert difficult and hence difficult to be detected and localised by hostile players. This also makes it insusceptible to electronic countermeasures. Moreover, PBR does not require a dedicated allocation of an increasingly congested Electro-Magnetic(EM) spectrum [2]. The proliferation of digital illuminator of opportunity also makes PBR gained significant interest among radar community [1]. In military application, PBR improved the detection and tracking of the piloted and unpiloted stealth system [11].

Despite these advantages, PBR also has some limitations. One of them is that when the target moves on the baseline, (that is the direct line between the transmitter and receiver) the target range rate of change is zero and therefore Doppler detection is not possible. However, few studies have been carried out to show the capability of PBR under this geometry. These type of PBR are commonly referred to as forward scatter radar (FSR). GPS signals have been used to detect an airplane on forward scatter geometry in [12]. A detailed study on FSR was presented in [13] where it was shown that the study of forward scatter in PBR managed to improve

Doppler resolution, cross section in forward direction and utilisation of leakage signal. In addition, the use of GSM as an illuminator of opportunity in a FSR geometry was shown in [14] and another recent study investigated the use of WiFi in passive FSR [15].

PBR by definition operates in a bistatic geometry and this introduce more complexity compared to monostatic system. To achieve a bistatic range measurement, there is a need for some synchronisation between the transmitter and the receiver such as a time reference of the initial transmission and the phase of the signal for coherent processing. A method of synchronising multiple receivers was presented in [16]. PBR operation is dependent on third party (non-cooperative) transmitters, typically communication or broadcast (TV/radio) systems. These transmitters are not under the control of the radar system, which can result in limited PBR performance. In the next section, an analysis of an analogue illuminator of opportunity will be presented.

2.2 PBR Exploiting Analogue Signal

PBR system using analogue terrestrial TV as an illuminator of opportunity were investigated by Griffiths and Long [17] in 1986. The signal used was a Phase Alternating Line (PAL) TV signal which is the colour encoding system for analogue TV signals. The experiment used 625-line PAL TV signals. This signal was characterised by a filtered Amplitude Modulation (AM) and consisted of an asymetric sideband waveform. The vision carrier fell at ± 1.25 MHz to transmit AM signals whereas the sound carrier it fell at 6 MHz above the vision carrriera and was trans-

mitted as Frequency Modulated (FM) signals. The authors showed that there are high ranges of sidelobes due to broad peaks from autocorrelation at 64µs intervals corresponding to the line sync pulse. This results in the strong ambiguities and limitations of dynamic range [17]. The same results were agreed by Ringer et al. [18] who showed that the echo received from a single target was composed of a number of multiple returns which were separated by a 64 µs interval. It was agreed in this report that using television signal as an illuminator of opportunity introduced high clutter. However, it was also shown that clutter contribution could be controlled by making sure the processing gain given by BT_{int} is large.

The work on PBR with TV signal was continued by Howland in [19] to demonstrate that such systems could provide target detection and tracking. An aircraft ascending, descending and taking-off was used in the experiment. There is no bistatic range information due to no timing measurements being made. The method presented in this work does not need synchronisation between the TV signal. The target tracks were estimated from the Doppler shift at the target echoes and the measurements of angle. In order to identify target echo, the Doppler bearing tracking techniques was implemented and fed into a cell averaging constant false alarm rate detector (CA-CFAR). This detection scheme allowed the noise rejection and unwanted carrier harmonics. The Lavenberg-Marquardt algorithm was used to track the target. Then, to maintain the target track, an extended Kalman Filter was used to associate Doppler and direction of arrival (DOA) information from the same target. This study successfully showed that aircraft detection and tracking could be achieved using TV transmitters of opportunity at the ranges up to 260 km, despite a limitation in term of target accuracy.

In 1997, Sahr and Lind [20] investigated commercial FM broadcasts to measure

ionospheric turbulence. FM signals have an advantage due to the broad coverage within a frequency range of 88-108 MHz and relatively high transmit power. In this study, FM signals with constant amplitude were extracted from music and speech signals. The study found that wideband frequency modulation from the FM signal resulted in better resolution and Doppler shift. They obtained a range resolution of about 1 km from a single station and suggested that this could be potentially further improved by using multiple stations.

The ambiguity function of FM radio signals was investigated in [21] [22]. It was found that the performance of range and Doppler resolution was based on the type of content the FM signal transmitted. It was shown in [21] that signals that present a high spectral content, such as rock music, can achieve better performance with lower sidelobe levels and a narrower peak of the ambiguity function. Similarly, it was shown that speech modulation gives poorest performance, especially within pauses between words.

A further analysis of performance predictions in FM radio signals was presented in [22] by combining two transmitters. The transmit power for the transmitters were 250 kW and 4 kW, respectively. For the single transmitter with a transmit power at 250 kW, the detection range at 25 km was achieved while maintaining Signal-to-Noise-Ratio (SNR) of 15 dB or higher. Moreover, with the transmitter at 4 kW, the detection range achieved was less than around 10 km with the SNR at 15 dB. The detection range was improved when these two transmitters exploited together and, as a result, target detection was extended to over 30 km. With high transmit power and wide coverage area, it was shown that FM radio signal can be exploited to detect a target at long-range.

In PBR application, one of the problem that contribute from this system is the direct signal interference (DSI). The radar receiver need to detect low power target echoes in the presence of a continuous signal from the illuminator of opportunity. Because most of broadcast signal is continuous, PBR does not have privilege of a pulsed transmission thus no period of transmitter silence to listen for echoes. A DSI based on FM signals was studied in [23]. The approach used in the study is by applying Adaptive Fractional Delay Estimation (AFDE). At the beginning, LMS based algorithm was used to reduce the effect of DSI is LMS based time delay estimation for initialisatio. Then, the LMS was applied again to minimise the error iteratively to achieve unbiased parameter estimation in time domain AFDE. This method showed that 40 dB peak suppression was achieved when applying in the real experimental data.

The effects of direct path of Line Of Sight (LOS) interference at the receiver were investigated in [24] where it was shown that this limited the performance of FM radio signals. An adaptive filtering method to the echo signal was implemented to remove this interference. The cross-correlation of the reference and echo signal then produced a range-Doppler surface which then fed into a CFAR algorithm to detect the target. To track the target, the Kalman filter was applied to the system. This system performed immense realization of ground-based FM PBR to detect and track an aircraft at ranges over 150 km in real time operation.

The Doppler resolution of PBRs can be improved with longer integration times. This is because Doppler resolution is inversely proportional to the integration time. Therefore, by having longer integration time, targets will have a narrower Doppler response that results in finer Doppler resolution. However, it needs to be taken into consideration when deciding to increase integration time because having it too

long will results in range migration [25]. Despite that, this is not the case with the range resolution which cannot be improved without changing the bandwidth or the waveform.

Range resolution performance of PBR was analysed in [26] by exploiting multiple FM channels from the same collocated transmitter. It was shown theoretically that the range resolution could be improved from 6-7 km to 1 km. The multi frequency approach for PBR was also investigated by Bongioanni et al. by exploiting high frequency diversity of FM radio signal [27]. This approach resulted in better target detection performance with respect to single frequency systems. After frequency compensation and scaling, the range Doppler surface in each channel was summed incoherently. This also resulted in a large target detection improvement of over 160 km with the robustness against bandwidth fluctuations.

In 2011, it was proposed an alternative method to improve range resolution by exploiting multiple adjoin channels coming from a single transmitter [28]. The study focused on the matched filter improvement for better range resolution via correlation. This included the difference of the Doppler shift in targets for each channel and the synchronisation between channels. The combination of analogue and digital illuminators of opportunity was studied in [29]. A prototype was developed to show that ground and aerial target could successfully detected and tracked by combining FM, DAB and DVB-T.

In [30], a hybrid passive radar sensor was presented in air guidance and surveillance three dimensional (ARGUS 3D) project. This project aim was to improve air traffic control radar (ATC) for civillian applications. This project showed that FM radio, DVB-T and DAB signals offered high performance in terms of target

position and range estimates. Result showed that FM radio signals with bandwidth of 200 kHz provides range resolution up to several kilometres and 1 Hz of Doppler resolution with 1 s integration time. In addittion, the high bandwidth of DAB and DVB-T signals (1.5 and 7.6 MHz) provided high range resolution, but the coherent integration was reduced below 0.5 s with 2 Hz of Doppler resolution.

A recent study in FM radio signals by [31] showed that rather than receiving the direct signal from the antenna, it can be estimated using the beamforming method. The beamforming method was also used to perform target angle estimation. In addition, the range-Doppler was estimated by applying a matched-filter and a least squares method. In the next section, PBRs exploiting digital signals will be presented. This is to show the advance of PBR along with the current digital signals technology.

2.3 PBR Exploiting Digital Signal

PBR exploiting digital transmissions of oppotunity has been widely exploited in recent years due to the increased bandwidth offered by digital signals and hence better range resolution and ambiguity function characteristics. Global System for Mobile Communication (GSM) is one of the digital signals of opportunity that have been used in PBR. The performance of mobile phone base stations was shown in [22] for a transmitter operating at 1800 MHz with a bandwidth of 55 kHz. Results showed that, for a 0.1 s integration time and a $1m^2$ RCS target, a SNR of 15 dB could be achieved with corresponding detection range around 1.2 km. The authors provided suggestions to improve the SNR and the detection range by solutions offereing with

better suppression of noise and direct signal. An additional demonstration of GSM performance in PBR was presented in [32]. A prototype was developed to show that ground moving target could be successfully detected. This paper also proposed the use of adaptive digital beamforming algorithms and a compact array antenna to reduce direct path signal interference. Results showed that the range resolution obtained was quite poor (1.845 km) concluding that GSM-based passive radar is more suitable for Doppler detection and tracking.

In [33], the works exploiting GSM signal was carried out to present a method to estimate the reference signal from the direction of arrival using two-element antenna array. The optimum beamforming was employed to separate the reference signal and to attenuate direct signal interference. Results showed that a high speed train with velocity of 150 km/h was successfully detected. However, with slow moving targets that reside close with main beam clutter in range-Doppler map is difficult to detect. The Internal Clutter Motion (ICM) worsen this problem by spreading the clutter power in Doppler frequency. The clutter echoes with non-zero Doppler components was mitigated with two methods which are an extension of a CLEAN-like algorithm and extended adaptive matched filters to noise-like signals. In [34], the GSM-Railway (GSM-R) radio communication infrastructure was exploited to monitor trains and estimate their positions and velocities. A fast moving train and a slow moving train were successfully detected.

Another mobile network that has been exploited in PBR is the Long Term Evolution (LTE) network which provides high speed wireless communication and data for mobile devices [35]. An experiemntal study on PBR with LTE was carried out in [36] to detect a moving car. Results showed that a car was successfully detected with a minimum range resolution of 15 m and a minimum velocity resolution of

0.284 m/s. The paper concluded that LTE can be used for velocity and range target detection and estimation. A further study within LTE in [37] showed the capability of LTE-based passive radar to detect ground moving targets including cars, a motorbike and humans. To detect the target against interference and background noise, an adaptive Constant False Alarm Rate (CFAR) algorithm was used by comparing the signal to a threshold. The threshold was determined after estimating the noise power from the adjacent cells.

LTE-based passive radar was also investigated for air traffic surveillance. A feasibility study to exploit such system was presented in [38] with the results of simulations of aircraft target detection. There is also a study attempted to exploit future mobile radio networks, namely 5G. A very recent study in [39] showed the possibility of 5G to be used in PBR applications and mainly in vehicular technology.

In 2006, BAE Systems developed a wideband PBR to demonstrate the use of DAB and DVB-T signals [40]. An antenna with a frequency band covering from 200 MHz to 2GHz was designed to provide sufficient bandwidth and continuous data. However, the sensitivity of the system was limited by the dynamic range of the receiver. To optimise the performance of this system, a response from the receiver channel was needed and matched by implementing channel equalisation filters. A further study with a more advanced testbed and analogue cancellation was implemented [41]. The captured data was enhanced so that the RF switching capability could be exploited. The target (civil passenger aircraft) was detected at a bistatic range of over 80 km using cross ambiguity processing.

Palmer et al. studied DVB-T to detect automotive and airborne targets at various range [42]. The developed passive system consisted of a direct path antenna

and a surveillance antenna. The direct path and echo signal was cross-correlated so that the Doppler shift for target detection can be found. Five targets from automotive traffic were detected with velocities ranging from 30 to 60 km/hr at ranges of 200 m to 1050 m.

In 2014, the use of DVB-T was further explored for maritime surveillance capabilities by Langellotti et al. [43]. This study investigated the detection and localisation of vessels beyond the territorial waters. The high sidelobes and unnecessary peak resulting from the DVB-T signals were removed by cascading the pilot signal equalization. The zero Doppler was removed by applying a Residual Peaks Removal (RPR). Targets with a range of 20-100 km were successfully detected beyond the standard radar horizon.

DVB-T as an illuminator of opportunity provides a reduction of ambiguity peaks present in the cross ambiguity function. This reduction is due to undesired peaks from guard intervals and pilot subcarriers present in DVB-T. With this limitation, there are some restrictions to detect targets. Most of the techniques used to enhance the ambiguity function of DVB-T are based on modifying the reference signal before it is cross correlated with the echo signal. Undesired peaks resduction was investigated in [44] and [45]. The methods were proposed to reduce the ambiguity peaks by symbol insertion in the location of the pilot carriers and transport parameter signalling. In 2012, Colone et al. [46] proposed a technique to further overcome the limitation by cascading the linear filters responsible for power equalizers and the pilot carriers.

Wireless networking transmissions were used to explore the potential and possibility of using WiFi signals with PBR systems. The most common standards are

the IEEE 802.11a, IEEE 802.11b and IEEE 802.11g. These standards operate in the 2.4 GHz and in the 5 GHz spectrum bands respectively. The detection of two moving human target was studied by Guo et al. [47] using IEEE 802.11 beacon transmission. The two targets with 12 m and 35 m separation were moving towards the receiver with the distance between reference antenna-transmitter-receiver set to 50 m. Results showed that the two targets cannot be separated due to the sidelobe despite sufficient distance between them. However, only one target was detected because it was moving closer towards the receiver. This study is applicable in quiet situation with no clutter and interference.

It was shown in [48] through the wall sensing application exploiting WiFi signals in PBR. The feasibility study was carried out to shown the detection capability of through the wall detection. Results showed that a moving person was detected through a wall with multilayer structure. A new DSI suppression techniques based on CLEAN algorithm was introduced to remove stationary clutter and the DSI component. It was shown in the results that this new technique successfully reduced DSI and stationary clutter components at approximately 19 dB which improved overall detection sensitivity.

PBR based on WiFi was further investigated by Falcone et al. in [49] to detect targets in outdoor environments. Moving targets, such as humans and vehicles, were considered. A moving vehicle was detected at the range of 95 m and for the human target; it was detected at a range of 85 m. In addition, the application of WiFi based PBR was also suggested in monitoring people in the building and security measures in airport. It was shown in [50] the use of WiFi signals in observing signs of life from breathing. The phase extraction method was used for the detection due to small Doppler shift and lower amplitude induced by the movement. Results showed the

detection of stationary human in two scenarios which are in room and through the wall.

With the development of space exploration, the use of satellite in PBR gives a new dimension. Satellite borne illuminators that send digital transmissions use noise like signal. These satellites mainly reside on Geostationary Orbits (GEO), Medium Earth Orbit (MEO) and Low Earth Orbit (LEO). In 1992 Griffiths et al. investigated direct broadcast by Satellite Television which orbiting Geostationary Orbit (GEO) as illuminator of opportunity [51]. They explored the capability of the ground receiver to receive the transmitted signals from the satellite and to achieve target detection and ranging. This study is important as pioneered the usage of satellite systems for PBR. The advantage of satellites that resides in GEO orbit is they have fixed geographical coverage with time.

In 1993, Tsui and Shaw investigated a method to determine the distance of a target utilizing four Global Positioning System (GPS) satellites [52]. The GPS satellites reside in MEO at an altitude of about 20,000 km and they are mainly used for navigational aids. They first measured the angle of arrival of echoes from the target so that the distance between the target and the receiver could be calculated. This study involved the implementation of a radar range equation without a detail study of the signal properties or a Doppler analysis.

In 1995, Kosch and Westphal further studied the application of Global Navigation Satellite Systems (GNSS) in PBR for detection of airborne targets [53]. The US NAVSTAR-GPS and the Russian GLONASS were used to form a passive multistatic space-borne radar that exploited 48 satellites transmitting at L-band (1-2 GHz). They successfully detected military and civil aircraft by utilizing these satellites.

However, the study did not provide a power budget analysis taking into account dynamic range effects. In addition, because these satellites are not designed for remote sensing application, there was a drawback in terms of resolution capability [54]. This was also investigated by Glennon et al. [55] where it was shown the use of GPS signals was limited by the limited transmitted power level of this system (about 25 to 30 Watt).

The study on communication satellites for PBR was expanded with the launched of the Iridium satellite, a satellite system which resides on a LEO orbit. The constellation of this system consists of 66 cross linked operational. Iridium satellites were considered as a meshed network [56] to detect an air target at a distance of 30 km from a passive receiver on the ground [57]. It was observed that a challenge of exploiting satellite on LEO orbits is the relative motion of the satellite with respect to the ground.

In general, the use of digital signals in PBR involved more complex and advanced signal processing to estimate the signals from the transmitter of opportunity. Exploiting digital signals as illuminator of opportunity in PBR mainly associated to the absence of illumination control because it use broadcast signals where the estimation of transmitted signal is essential. The direct signal interference is also one of general issue in PBR. It is important to ensure that the direct signal does not interfere and swamp the target from the surveillance signal. This will be the case for PBR target detection unless measures were taken to suppress this direct signal. In addition, more studies and experiments to investigate the capability of PBR to track and detect moving targets with low target profile and speed could be done in future.

Based on the literature review presented in this and previous sections, communication signals transmitting random signals have been mainly used as illuminators of opportunity in PBR. In addition, there are still ongoing efforts and a lot of interest in using these type of signals in PBR. In the next section, previous attempts to use deterministic signals, such as radar transmissions, will be reviewed.

2.4 PBR Exploiting Radar Signal

This section presents previous works on PBR aiming at exploiting deterministic radar signals. The use of radar signals offers some advantages especially in terms of target detection and tracking, and presents some limitations such as could be interrupted with other signals, could be expensive to use and easily affected by wind farms .

To date, the existing studies of exploiting radar systems as illuminators of opportunity are been limited to space-borne SAR transmitter and over the horizon radar [58]. Satellite based earth observation has had a significant growth over the decades. This increasing trend has helped the development of PBR systems.

SAR satellite mainly transmits chirp signals with a wide bandwidth and hence offer very good range resolution. There are some drawbacks in using SAR satellite in LEO. First of all, the transmitter needs to be tracked so that the passive receiver is always pointing towards the transmitter to collect the reference signal. Furthermore, this satellites do not have a fixed geographical coverage, and move with a high velocity. This motion results in the displacements or shifts in target detection [59].

A study on commercial based SAR by Griffiths et al. in 2002 investigated SAR illuminators using a satellite in LEO orbit [58]. The Envisat satellite was selected carrying an Advanced Synthetic Aperture Radar (ASAR) operating at C-band with a carrier frequency of 5.331 GHz. SAR transmissions were exploited to detect air targets. This study only involved theoretical analysis introducing the concept of implementation but no experiments were carried out.

In 2003, the works was continued for moving target detection by Whitewood et al. [60]. A stationary ground based receiver was employed to receive the echo from the flying target. The electronic Displaced Phase Centre Antenna (DPCA) pulse canceller was implemented where this technique was used to improve the detection performance of platform motions that are subject to clutter. However, DPCA canceller caused SNR to decrease especially for slow moving target. Hence, the large number of coherent pulse is needed so that sufficient integration gain is achievable. The later study by Whitewood et al. [61] on Envisat focusing on bistatic imaging experiments. However, the technique presented could be used in target detection such as aircrafts. The study with Envisat ended further to its end of mission following the unexpected loss of contact on 2012 [62].

Another study on PBR using non-cooperative radar signals of opportunity was carried out in [63]. In this study, the pulse radar signal transmitted by the mechanically scanning transmitter of an Air Traffic Control (ATC) radar was exploited to detect an aircraft. Results showed that the aircraft could be successfully detected with a passive receiver prototype using a reference channel, demonstrating the capability of ATC radars as potential illuminators of opportunity.

In [64], the exploitation of Airport Surveillance Radar (ASR) radar was further

investigated. The reference signal was received from the direct signal of ASR radar. It was assumed in this paper the parameters of transmit signals is unknown and need to be estimated. A replica of pulse signal was extracted from the reference signal and this was used in pulse compression. Then, the PRI was estimated using the time difference between adjacent pairs of TOA. After that, the PRI filtering was implemented to separate the TOA train for every PRI. The window function for every estimated PRI was multiplied by the received signals which then generates the PRI components. Finally, the range-Doppler map was formed where the target was extracted.

The exploitation of digital high frequency (HF) broadcast band (3-30 MHz) in PBR application was discussed in [65]. The study exploit Digital Radio Mondiale (DRM) HF transmission. HF signals have high Effective Radiated Powers (ERP) compared to other illuminators of opportunity [22]. Exploiting HF signals in PBR provides very long range detection because this signals can propagate beyond the radio horizon. HF Surface-Wave Radars (HFSWR) is the example of beyond the horizon radar that propagate by utilising the surface-wave propagation mode that diffracts along the earth surface. In monostatic case, this radar has potential to detect targets beyond 300 km [1]. It was found that HF radar gives large range resolution given that the it has low bandwidths due to either ionospheric and interference constraints. The use of HF radar also required a phased array for sufficient coverage in long range propagation in PBR application [65].

The issue from exploiting HF PBR based on DRM as illuminator of opportunity was studied by Xianrong et al. [66]. They addressed a several problems arises from HF passive radar which are variety of vice-peaks from DRM signal AF, direct path rejection, clutter from multipath in surveillance channel and extraction of reference

signal. A suppression method was applied to reduce the peaks by reducing pilot symbol amplitudes, setting guard intervals and setting the corresponding useful parts to zeros. The technique used for multipath clutter rejection were temporal filter and spatial filter. The simulated target was seen after multipath clutter rejection was applied. Further study by Zhao et al. presented the experimental study on HF PBR exploiting DRM signal based on hybrid sky-surface wave [67]. The preliminary results showed that DRM based HF can be exploited in PBR application for sea state remote sensing. However, future studies and improvements are needed before this system can be applied.

2.5 UAVs and Drones Detection in PBR

Drones are small targets that have increasingly become a significant danger to manned air traffic and pose a security [7] and privacy threat. It is available to general public with a low price and not difficult to operate. This platform was used for personal leisure, in search and rescue mission during disaster mission and agriculture monitoring [68]. However, such platform started to pose danger such as violation of privacy, crimes and terror act [7]. This results in serious threats towards public safety and air surveillance.

Using traditional radar for drone detection, tracking and classification is a challenging task due to this platform having small radar cross section (RCS), slow speed compared to conventional aircraft and fly at low altitude. Thus, passive solutions to detect and track drones represent a very attractive option, especially in the vicinity of airports, where the risk of interfering with other existing radar and communication

systems is high.

The first experimental study to exploit GSM signals to detect a small UAV (namely drone) was presented in [69]. However, the GSM signal used was locally generated, rather than using actual GSM network signals. Results from the experiment showed that the drone was successfully detected from the Doppler shift obtained in the time-Doppler map.

A WiFi-based passive radar was also exploited for detection of ultralight aircrafts and drones [70]. The aim of this study is to improve security of small airfields and outdoor areas. Results showed the capability of this system to detect and localise ultra-light aircraft and drones in 3D in short range PBR by exploiting WiFi signals.

A study on PBR exploiting UMTS 3G signals was presented by Chadwick in [71] for micro-drone detections. Results showed the potential of UMTS transmitters as illuminators of opportunity for drone detection. The resulting micro-Doppler signatures and characteristics were presented as a mean to provide a basis to differentiate drones from non-drone targets.

It was shown in [72] the feasibility of using digital television system for drone detection. The drone was detected within the coverage of the array beam. In this paper, the author suggested that, for drone detection, longer integration time is needed based on the nature of drones flying at a low altitude, with small RCS and slow speed. In a very recent study by G. Fang et al., the feasibility of multistatic single-antenna based on digital television based passive radar was presented [6]. The multistatic configuration consisted of one transmitter and three receivers. The reference signal was reconstructed from the surveillance signal. A drone was successfully detected and tracked with the suggestion to perform such experiment in different

environment.

From the literature presented, it was shown that PBR offered alternative solution for drone and UAV detection, tracking and localisation. There is no dedicated transmitter needed which provides low-cost solution and covert operation especially for military and anti-terrorism application. Thus, it is essential to provide a countermeasure solution for drone and UAVs detection and tracking and interception system.

PBR with single-channel detection

As mentioned before, radar waveforms are deterministic. Thus, this feature allows the development of single-channel PBR systems that do not require a reference channel to detect a target. This can be implemented with some prior or acquired knowledge of the transmitted signal, which allows the passive receiver to be matched with the illuminator of opportunity [73].

In the literature, there are few studies of PBR without the use of a reference channel, and most of them exploit random signals of opportunity. Single receiver processing was studied in [74] by exploiting digital television (DTV) signals. The reference channel was recovered by remodulation and demodulation of the surveillance channel. Target was detected at the range between 1.4 km and 3.4 km. However, no investigation into the effect of clutter cancellation from the remodulated reference signal.

The reconstruction of the reference signal may result in poor cancellation performance as it was shown in [5]. This study exploited DVB-T signals. Zhang et

al. [75] used an antenna arrays as a surveillance antenna as compared to previous studies that use omni-directional surveillance antenna to study single channel detection. The reference signal was recovered from the covariance matrix and it was shown that cancellation performance was improved with the maximisation cancellation ratio. The authors claimed that their method is not restricted to DTV or DVB-T signals.

In the literature presented, it was found that the use of communication and broadcast signals as an illuminator of opportunity are widely exploited. In addition, there are few studies using radar signals as an illuminator of opportunity. Thus, there are a few gaps that were found from the literature presented which include:

1. The exploitation of radar signals in PBR still draws a significant interest in the research community. This is because the advantage that radar signals offered are worth investigating

2. There are few studies on detecting UAV especially drones using PBR which exploit radar signals

3. It is evident for PBR that exploiting radar signals without the use of reference channel still an open area to be explored.

Based on the gap found in the literature, the foundation of this thesis will work on exploiting radar signals that transmit deterministic signals for target detection. The staring radar will be used as a non-cooperative illuminator of opportunity to detect drone, car and human. Because staring radar transmit deterministic signals where the signals is known, it was possible to remove the reference channel where targets still can be detected.

2.6 Summary

In this chapter, the literature on PBR target detection and the literature on illuminatos of opportunity have been reviewed. The illuminators of opportunity from analogue signals to digital signal was presented and noted in order to understand the works and methodologies of target detections. With the vast majority of the emitters were telecommunications signals, there were few studies that exploit active radar signal as illuminator of opportunity. However, these were all with reference channel. Based on the literatures, there is an area that still open to be explored which is PBR target detection that does not essentially require a reference channel. This can be done with the use of deterministic signals where the priori knowledge of the signal is known.

Chapter 3

Background Theory

This chapter presents the background theory and concepts of PBR that relate to this research. Based on the literature review presented in the previous chapter, the mathematical tools used in the thesis together with the functional blocks that make up the developed passive radar prototype system and the waveforms used will be discussed. The principle on radar operation is introduced followed by radar signal processing. Then, the monostatic radar system is presented which this include radar equation, radar resolution and range ambiguity. The bistatic radar system is introduced where the algorithm involved in bistatic radar processing will be presented. The background theory is a key foundation needed to understand the experiments discussed in the next chapters.

3.1 Radar Principles

Radar is an electronic system consisting of a sensor that uses electromagnetic waves (EM waves) to detect the presence of a target. This sensor transmits pulses of energy. When a target is hit by these pulses, energy is reflected in all directions and a measurable amount of this energy is scattered back in the direction of the receiver. This reflected energy is called the echo signal and it is what reveals the presence of targets. The fundamental modules that form a typical radar system are;

1. Transmitter: The transmitter generates, up-converts and amplifies the signal which will be transmitted to detect the presence and position of the target

2. Antenna: An antenna is used to convert the voltage signal to EM waves and also to receive the echo signal reflected from the target. Depending on the application, the antenna may be shared between the transmitter and the receiver or there can be one antenna for the transmitter and another one for the receiver.

3. Receiver: The receiver is the signal conditioner which amplifies, filters and down converts the received echo signals from the target

4. Signal Processor and display: The output signal from the receiver is processed so that the position, velocity and the characteristics of the target are determined

3.1.1 Pulse Compression

The purpose of pulse compression in radar processing is to enable the radar to transmit a modulated long pulse to increase the energy on the target and achieve a good range resolution. The range resolution is dependent on the bandwidth of the signal from the equation [76]

$$\Delta R = \frac{c}{2B} \tag{3.1}$$

where c is the speed of light (3×10^8) m/s and B is the bandwidth of the signal. For an unmodulated pulsed radar system, the bandwidth is $1/\tau$ where τ is the pulse width given as

$$B = \frac{1}{\tau} \tag{3.2}$$

It can be seen in Equations 3.2 the bandwidth is inversely proportional to the pulse width. Hence, having short pulses are better for range resolution. However, the power of received signal is proportional to the pulse duration, hence, long pulse width enable target detection in long range. Thus, to solve this issue, the transmitter will transmits a long modulated pulse and compress it into a narrow pulse in the receiver. In a pulse compression where the transmit signal is modulated in phase or frequency $B >> 1/\tau$ and the width of the pulse at the output of the matched filter is equal to $1/B$.

3.1.1.1 Matched Filter

Matched filter is well known signal processing for pulse compression. It is also known as correlation processor. Matched filter is a linear filter to detect a known signal in white noise, thus, maximize the SNR at the receiver output [77]. The

matched filter impulse response $h(t)$ is the function of the waveform $s(t)$ or $S(f)$ with predetermined delay t_0 given as [78]

$$\begin{aligned} h(t) &= Ks^*(t_0 - t) \\ H(f) &= KS^*(f)e^{-j2\pi f t_0} \end{aligned} \tag{3.3}$$

where K is the arbitrary constant that scaled the impulse response. The frequency response is the complex conjugate of the transmit signal spectrum.

The output of the matched filter $y(t)$ is the convolution between the input signal and the impulse response of the filter. It is shaped as the auto-correlation function written as

$$y(t) = s(t) * h(t) = \int_{-\infty}^{\infty} s(\tau_d)s^*(\tau_d - t)d\tau_d \tag{3.4}$$

where $s(\tau_d)$ is the signal with the delay at τ_d. The result of the matched-filter is a complex number, the magnitude indicating the likelihood of a target being present. The zero output is then the energy of the input signal and is the maximum output value given as

$$y(0) = \int_{-\infty}^{\infty} |s(\tau_d)|^2 d\tau_d = E_{s(\tau_d)} \tag{3.5}$$

3.1.2 Radar Waveform

There are two types of radar waveform that are typically used in radar applications; continuous wave radar (for radar which simultaneously transmits and receives signals) and pulsed radar (for radar which interleaves the transmit and receive periods). Unless otherwise stated, this study will use pulsed radar illuminators. The standard for radar frequency bands established by the IEEE is shown in Table 3.1.

This standard is used worldwide and will be used through out the thesis.

Table 3.1: IEEE Std 521-2002 Standard Letter Designations for Frequency Range in Radar [79]

Designation	Frequency Range
HF	0.003-0.03 GHz
VHF	0.03-0.3 GHz
UHF	0.3-1 GHz
L	1-2 GHz
S	2-4 GHz
C	4-8 GHz
X	8-12 GHz
Ku	12-18 GHz
K	18-12 GHz
Ka	27-40 GHz
V	40-75 GHz
W	75-110 GHz
mm	110-300 GHz

3.1.2.1 Continuous Wave Radar

For frequency modulated waveforms, a real narrow bandpass signal can be described as [78]

$$s(t) = a(t)cos[2\pi f_c t + \vartheta(t)] \tag{3.6}$$

where $a(t)$ is natural envelope and $\vartheta(t)$ is the instantaneous phase. The real complex envelope of the the signal $s(t)$ can be written as

$$\begin{aligned} s(t) &= \Re\left\{a(t)e^{j(2\pi f_c t+\vartheta(t))}\right\} \\ &= \Re\left\{a(t)e^{j\vartheta(t)}e^{j2\pi f_c t}\right\} \\ &= \Re\left\{u(t)e^{j2\pi f_c t}\right\} \end{aligned} \tag{3.7}$$

where $u(t)$ is the complex envelope of the signal. The signal is frequency only modulated signal if $a(t)$ is constant whereas the signal is amplitude only modulated if $\vartheta(t)$ is constant.

In continuous wave radar, the transmitter continuously transmits a waveform and the receiver continuously receives target echoes. The motion sensing of this type of radar is by the Doppler shifts seen in the echoes which means the velocity of the target can be measured. However, continuous wave radar does not have ranging capability and thus cannot provide range resolution. This then can be solved by using frequency modulated continuous wave (FMCW) radar. In comparison with the CW radar, FMCW signals during transmission are modulated in frequency or in phase. An FMCW radar is the ideal form of pulse compression where the compressed signals gives better sidelobes, Doppler tolerance and there is no blind range [80]. Therefore, this give advantage of FMCW to be applied in the processing of long modulated pulse. In CW, the range cannot be determined because there is no necessary timing mark to allow the system to accurately time the transmit and receive cycle.

The transmit signal level is dependent on the achievable isolation of the direct signal between the transmitter and the receiver. This restricts the amount of power that can be transmitted and hence causes limitations in detection range. The transmitter and receiver isolation issue can be solved by increasing the physical separation between antennas, the use of different polarisations in transmission and on receive, improved antenna beam patterns and use of Radar Absorbing Material (RAM) between the two antennas.

Figure 3.1 shows the block diagram for a monostatic CW radar with dual an-

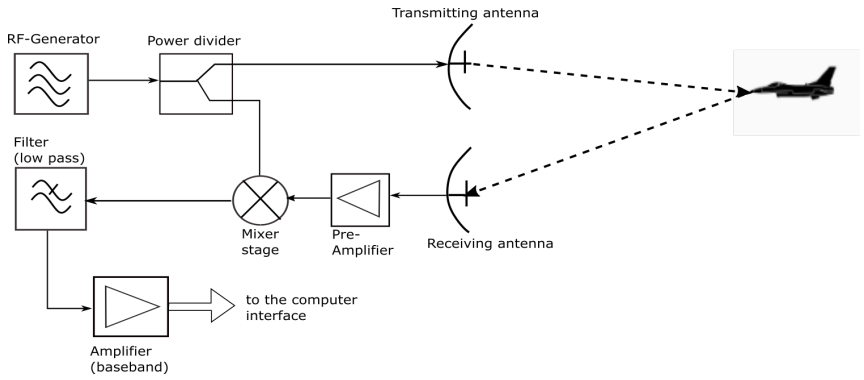

Figure 3.1: Block diagram for CW radar with dual antennas. Adapted from [81]

tennas. The continuous waveform is generated in the RF-Generator. The output from the RF-Generator is fed into the power divider. Then, half of the power from the signal is sent to the transmit antenna and the other half to drive the LO port of the mixer. The transmit carrier frequency is the same as the frequency generated in the RF-Generator. At the receiver, the received signal is amplified and the amplified signal output is fed into mixer and multiplied with the output from the power divider. The output of the mixer (in baseband) is filtered with a low-pass filter to block the high frequency components of the signal and amplified by the audio amplifier. The signal is sent to the computer interface for future processing. The echo signal is an attenuated and delayed version of the transmit signal which is written as

$$S_R(t) = A_R cos(2\pi f_c(t - t_0) + \vartheta) \tag{3.8}$$

where A_R is a constant amplitude of the echo signal, f_c is the carrier frequency, t_0 is the delay given by the two-way path divided by the speed of propagation and ϑ is the constant phase of the echo signal.

3.1.2.2 Pulsed Radar

The pulsed radar intermittently transmits the signal in short pulses and listens for the echoes in the time intervals between transmissions. Unlike CW radar, pulse radar can give correct range measurements if the separation between pulses is sufficient for the pulse to reach the target and return before the next transmission. This is done by measuring the elapsed time between the transmitted pulse and its received echo. Targets further away lead to ambiguities as their reflections arrive after the next pulse has been transmitted.

Rectangular Pulsed Radar

A rectangular pulse with pulse width τ and amplitude A can be defined mathematically as follows

$$g(t) = A\,\mathrm{Rect}\left(\frac{t}{\tau}\right) \tag{3.9}$$

The Fourier transform of $g(t)$ is

$$\begin{aligned} G(f) &= \int_0^{\tau} Ae^{-j2\pi ft}dt \\ &= A\tau\left(\frac{sin(\pi f\tau)}{\pi f\tau}\right) \end{aligned} \tag{3.10}$$

Equation 3.10 can be simplified by applying the sinc function which by definition is

$$sinc(\lambda) = \frac{sin(\pi\lambda)}{\pi\lambda} \tag{3.11}$$

where λ is the independent variable which in this case is $\lambda = f\tau$. Therefore, by re-arranging the equation, the spectrum of rectangular pulse is written as

$$G(f) = A\tau sinc(f\tau) \tag{3.12}$$

Based on the equation above, the Fourier transform pair can be written as

$$A\,\mathrm{Rect}\left(\frac{t}{\tau}\right) \rightleftharpoons A\tau sinc(f\tau) \tag{3.13}$$

Figure 3.2a shows a simulation of a rectangular pulse with pulse width $\tau = 2\mu$s and bandwidth 500 kHz. The normalized amplitude spectrum $|G(f)|$ is presented in Figure 3.2b and show the first zero crossing of the spectrum occurs at $f = \pm 1/\tau$. The bandwidth of a rectangular pulse can be reduced by increasing the pulse width τ to move the first zero crossing towards the origin and obtain a narrower and more constrained spectrum. In other words, if the pulse is narrowed in time, the frequency spectrum is widen.

LFM Pulsed Radar

Another waveform commonly used in pulsed radar is a linear frequency modulated (LFM) signal, also referred to as a chirp signal. In this waveform, the instantaneous frequency varies linearly over time. It is a constant amplitude waveform and so the energy it contains is spread widely in the frequency domain.

The instantaneous frequency of a LFM signal having linear changing instanta-

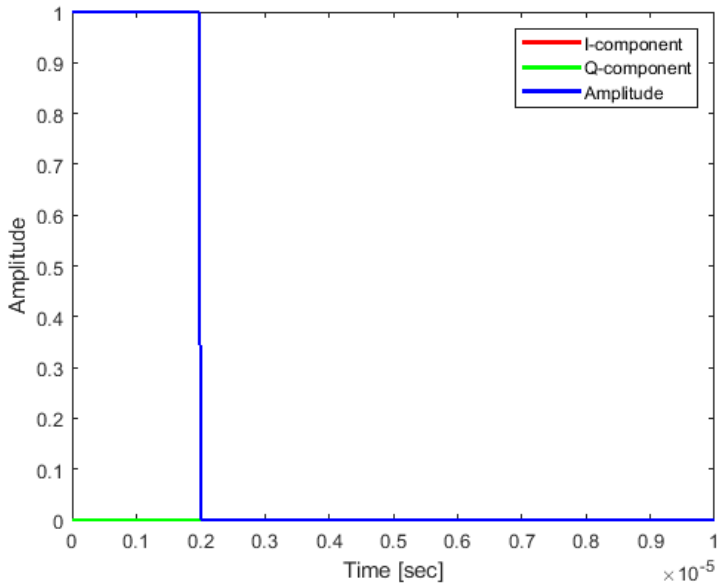

(a) Rectangular pulse with pulse width = 2 μs. (This figure was zoomed to magnify the pulse width)

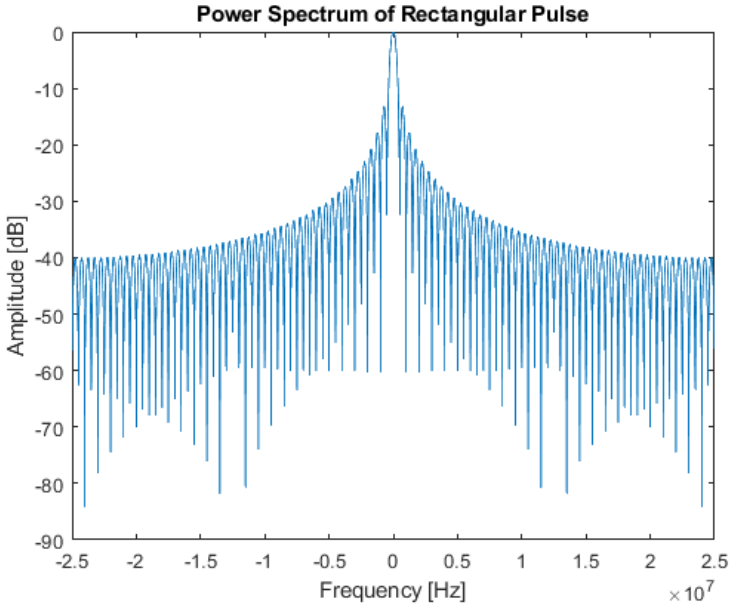

(b) Normalized spectrum of rectangular pulse with bandwidth at $1/\tau$

Figure 3.2: A rectangular pulse in the time domain and its power spectrum. The pulse width τ is 2 μs

neous frequency over an interval [-T/2,T/2] is defined as

$$f_{IF} = \gamma t \tag{3.14}$$

where γ is the frequency sweep rate given as

$$\gamma = \frac{f_{IF}(T/2) - f_{IF}(-T/2)}{T} \tag{3.15}$$

The complex chirp in time domain has a constant magnitude over the interval [-T/2,T/2] and zero outside. It can be written as

$$\begin{aligned} S_T(t) &= \text{Rect}\left(\frac{t-T/2}{T}\right) cos(2\pi f_c t + \gamma t^2) \\ &= \Re\left\{\text{Rect}\left(\frac{t-T/2}{T}\right) e^{j\pi\gamma t^2} e^{j2\pi f_c t}\right\} \end{aligned} \tag{3.16}$$

where f_c is the carrier frequency, γ is a chirp rate from B/τ with τ being the pulse width and $B = f_{IF}(T/2) - f_{IF}(-T/2)$ is the bandwidth. The signal will give a rectangular pulse signal when $\gamma = 0$.

For LFM signal $x(t)$ in time domain, with a bandwidth B and duration of T, it can be written as

$$s(t) = \text{Rect}\left(\frac{t}{T}\right) e^{j\pi\gamma t^2} \tag{3.17}$$

where γ is the chirp rate. Thus, the Fourier transform of of a linear chirp $X(f)$ can

be written as [82]

$$\begin{aligned} X(f) &= \int_{-\infty}^{\infty} s(t)e^{-j2\pi ft}dt \\ &= \int_{-\infty}^{\infty} \text{Rect}\left(\frac{t}{T}\right))e^{-j2\pi(ft-\frac{\gamma t^2}{2})}dt \\ &= \int_{-T/2}^{T/2} s(t)e^{-j2\pi(ft-\frac{\gamma t^2}{2})}dt \end{aligned} \tag{3.18}$$

However, Equation 3.18 is not in closed form analytical solution. Thus, the simple representation is derived using stationary phase approximation for time-bandwidth ($BT >> 1$) written as [83]

$$S_T(f) = \sqrt{\frac{1}{\gamma}} \cdot e^{-j\pi\frac{1}{\gamma}f^2} e^{j\frac{\pi}{4}} Rect\left(\frac{f}{B}\right) \tag{3.19}$$

where it has a constant magnitude, a constant phase residual $\pi/4$ and a square law phase modulation.

Figure 3.3a shows a simulation of a LFM pulse with pulse width $\tau = 20\mu$s, and the bandwidth is 5 MHz. The spectrum plot in Figure 3.3b shows the bandwidth of the signal is 5 MHz where this can be seen from the top flat of the signal. It can be seen in the figure the bandwidth of the transmit signal is still 5 MHz when longer pulse is transmitted which this would not possible for the rectangular pulse.

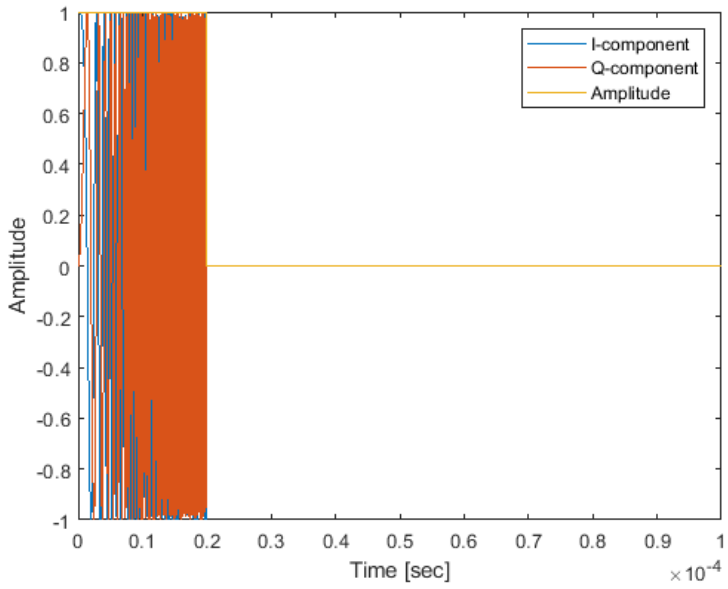

(a) LFM pulse with pulse width = 20 μs. (This figure was zoomed to magnify the pulse width)

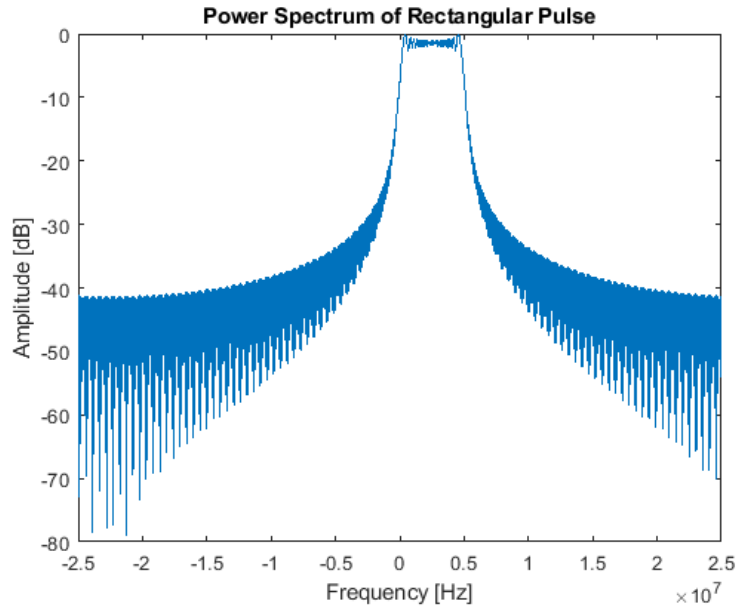

(b) Normalized spectrum of LFM pulse with bandwidth at 5 MHz

Figure 3.3: A LFM pulse in the time domain and its power spectrum. The pulse width $\tau = 20\mu$s and the signal bandwidth is 5 MHz

Pulsed Train

In the clutter environment, a coherent pulsed train is useful to be used for target detection. This is due to the detected Doppler frequency was measured from the phase changes in pulse to pulse basis. Any changes in the phase shifts from the target echo are detectable in the receiver. In this section, two types of train of pulse signals are studied; rectangular and LFM pulsed train signals.

Figure 3.4 shows a train of rectangular pulses. The top plot is the transmitted pulses and the bottom plot is the received pulses. Note the time delay between the two figures. In the figure, the Pulse Repetition Interval (PRI) is the time from beginning of one pulse to the start of the next pulse. The delay of the signal caused by the time taken for the signal to reach and return from target is denoted as Δt. The pulse width is denoted as τ. The Pulse Repetition Frequency (PRF) is the rate at which the pulses are transmitted, defined as the inverse of PRI hence $\text{PRF} = 1/\text{PRI}$.

The train of pulse repeated every PRI can be written as

$$s(t) = \sum_{m=-\infty}^{\infty} x(t - m\text{PRI}) \tag{3.20}$$

where $x(t)$ is the signal used in the transmission. The Fourier transform of this signal can be written as

$$S(f) = \sum_{m=-\infty}^{\infty} X(f) e^{-j2\pi f m\text{PRI}} \tag{3.21}$$

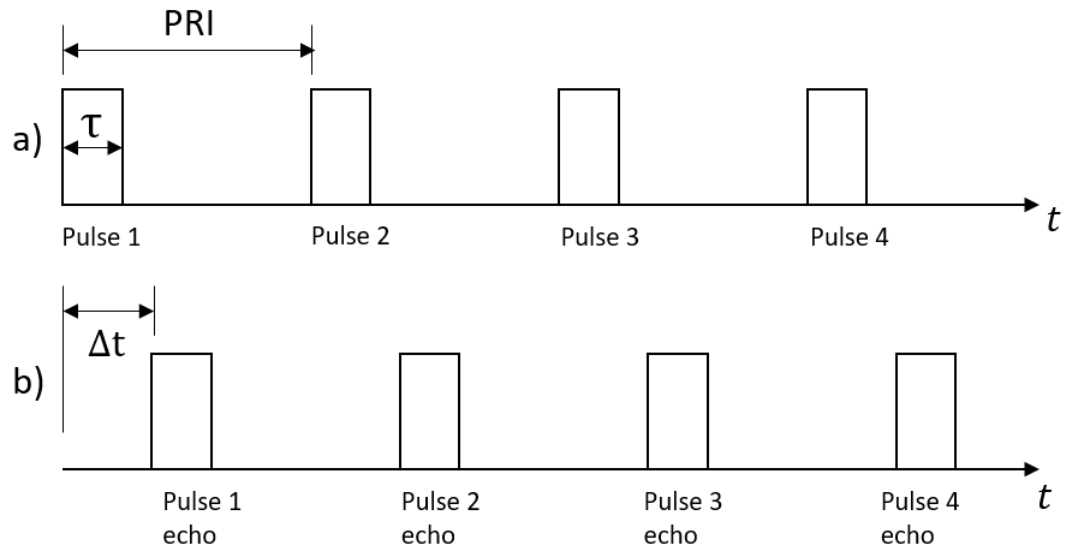

Figure 3.4: Train of rectangular pulses (a) transmitted signal (b) received signal

Equation 3.21 can be simplified to

$$S(f) = X(f)\frac{1}{PRI}\sum_{m=-\infty}^{\infty}\delta\left(f - \frac{m}{PRI}\right) \tag{3.22}$$

To obtain the Fourier transform of rectangular pulse, the signal was convolved with sinc function in time domain which the final result is

$$S(f) = \frac{AT_{int}}{PRI}\sum_{m=-\infty}^{\infty}\tau\, sinc\left(\frac{m\tau}{PRI}\right) sinc\left[T_{int}\left(f - \frac{m}{PRI}\right)\right] \tag{3.23}$$

where T_{int} is the integration time.

The train of rectangular pulses can be described by an extended form of Equation 3.9, given as

$$g(t) = A\sum_{m=-\infty}^{\infty}\text{Rect}\left(\frac{t - m\text{PRI}}{\tau}\right)e^{-j2\pi f_c t} \tag{3.24}$$

where m is the pulse index and f_c is the carrier frequency of the signal.

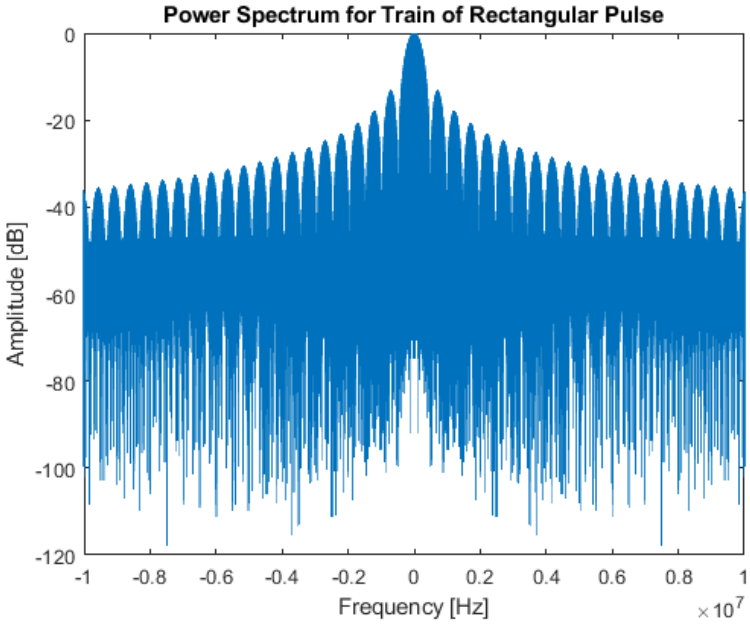

(a) Power spectrum of rectangular pulse train

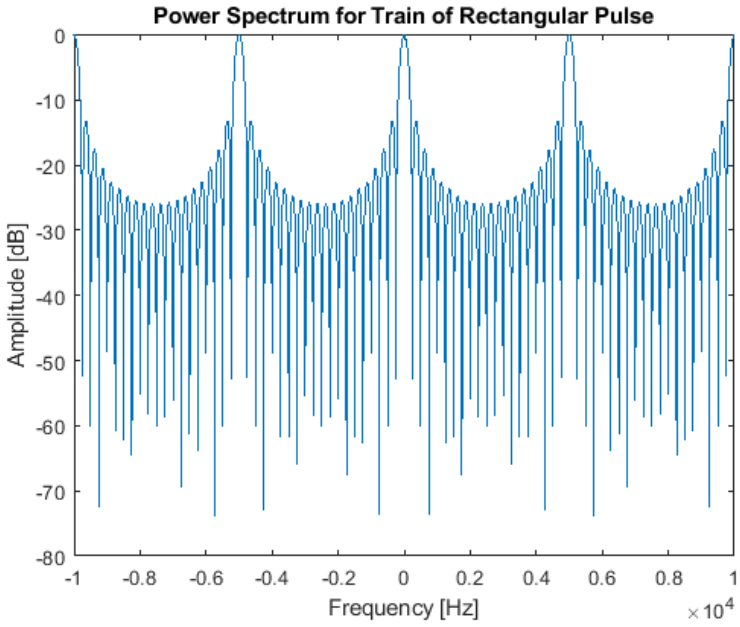

(b) Power spectrum of rectangular pulse train (zoomed)

Figure 3.5: Power spectrum of rectangular pulse train. The pulse width is 2 μs, the bandwidth is 5 MHz and the PRF is 5 kHz

Figure 3.5 shows a spectrum of rectangular pulse train. 50 pulses were integrated. The pulse width is 2 μs and the bandwidth of 5 MHz. It can be seen in Figure 3.5b the zoom in plot of the signal spectrum. The spectrum consist of multiple lines where the distance between each peek is PRF. In this simulation, the PRF is 5 kHz equal to PRI of 200 μs. The Doppler resolution obtained from the simulation is 50 Hz. It can be seen from the spectrum of rectangular pulse train the plot is decaying train of sinc functions with the spectrum of lines separated at PRF.

Similarly, the equation of a train of LFM pulses, can be extended from Equation 3.16

$$g(t) = A \sum_{m=-\infty}^{\infty} e^{j\gamma\pi(t-m\mathrm{PRI})^2} \mathrm{Rect}\left(\frac{t-m\mathrm{PRI}}{T}\right) e^{-j2\pi f_c t} \tag{3.25}$$

where m is the pulse index, γ is the LFM rate and f_c is the carrier frequency of the signal.

The power spectrum of the LFM pulse train is shown in Figure 3.6. It can be seen in Figure 3.6b, the spectrum of the pulse train for LFM signal consists of multiple lines separated at PRF. The Doppler resolution obtained from the simulation is 80 Hz.

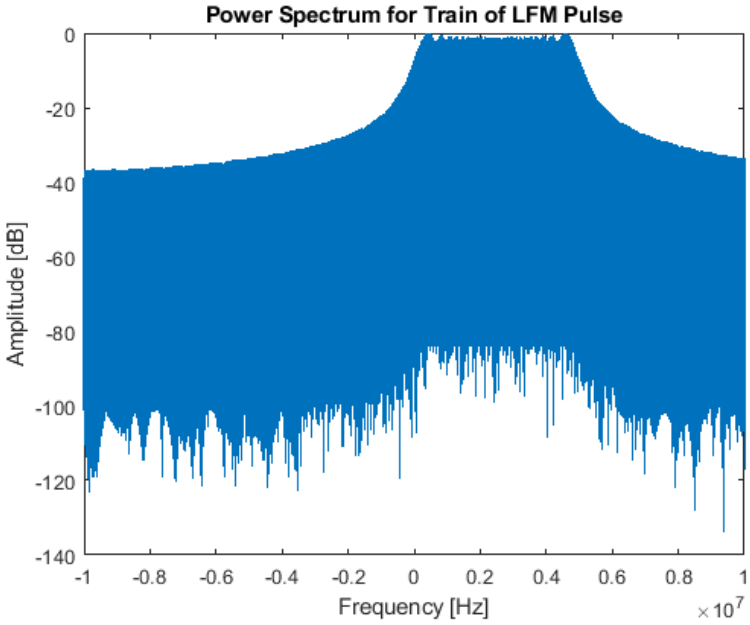

(a) Power spectrum of LFM pulse train

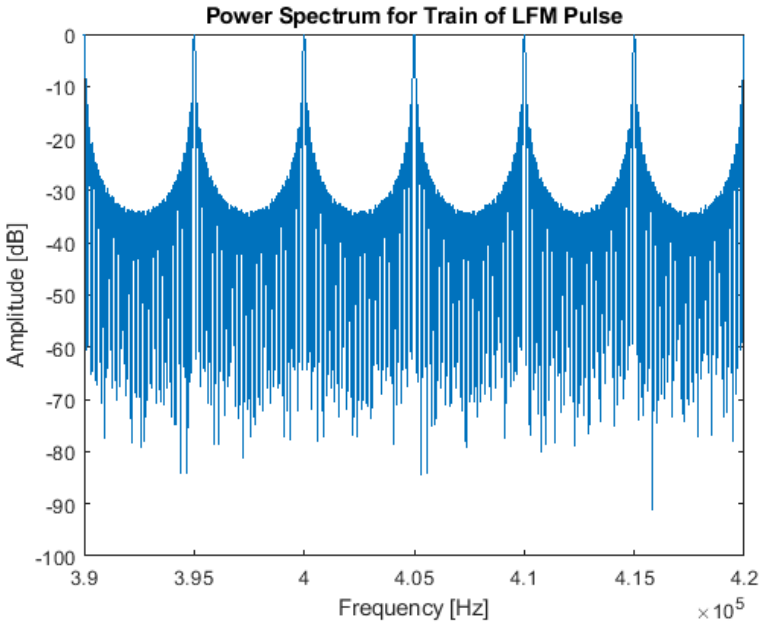

(b) Power spectrum of LFM pulse train (zoomed)

Figure 3.6: Power spectrum of LFM pulse train. The pulse width is 20 μs, the bandwidth is 5 MHz and the PRF is 5 kHz

3.2 Monostatic Radar

A monostatic radar is defined as a radar system with collocated transmit and receive antennas. The monostatic radar system is shown in Figure 3.7

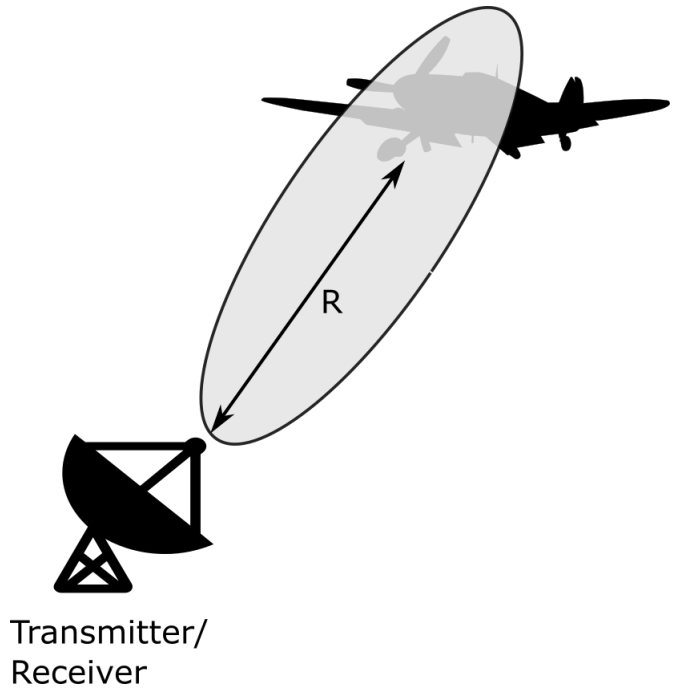

Figure 3.7: Monostatic Radar System. Target is detected in the beamwidth of the radar with the distance from the Transmitter/ Receiver is referred as R

3.2.1 Radar Equation

The received power for monostatic radar observed from a target is given by [84]

$$P_r = \frac{P_t G A_e \sigma}{(4\pi)^2 R^4} \tag{3.26}$$

where P_r is the received power at the receiver(in Watt), P_t is the transmitted power radiated by the antenna, G is the gain of the antenna, A_e is the effective area of the

received antenna and σ is the radar cross section of the target. The effective area of the antenna is found from the physical area of the antenna multiplied with the antenna aperture efficiency.

3.2.2 Radar Range Equation

The maximum range $R_{\max}$ is the distance over which the target cannot be detected. This occurs when $S_{\min}$ which is minimum detectable signal just equals to the received signal power P_r. Rearranging Equation 3.26 and substitute P_r with $S_{\min}$ gives [84]

$$R_{\max} = \left[\frac{P_t G A_e \sigma}{(4\pi)^2 S_{\min}}\right]^{1/4} \tag{3.27}$$

In Equation 3.27 above P_t is defined as the peak power.

3.2.3 Radar Resolution

Range resolution describes the capability of the radar to detect and discriminate between targets that are in close proximity. In the monostatic case, for two targets positioned at range R_1 and R_2, they must be separated by at least ΔR so that they can be resolved. The difference between these two ranges (ΔR) is

$$\Delta R_M = R_2 - R_1 = \frac{c}{2}(t_2 - t_1) = \frac{c}{2}\Delta t \tag{3.28}$$

where Δt is the time delay between two targets. The range resolution depends on the width of of the pulse τ, the size and type of the target and the efficiency of the receiver.

In the monostatic case, the range resolution is defined as

$$\Delta R_M = \frac{c\tau}{2} = \frac{c}{2B} \tag{3.29}$$

where c is the speed of light (3×10^8) and τ is the pulse width of the radar [10][85].

3.2.4 Range Ambiguity

In order for radar to correctly detect the target's range, the target's echo needs to be received before the next pulse is transmitted. Range ambiguity occurs when the target is detected, but the transit time exceeds the PRI. The target can still be detected, but it will be at a false location because the echo is received after the next pulse is transmitted which yields a shorter indicated target range. In Figure 3.8 the

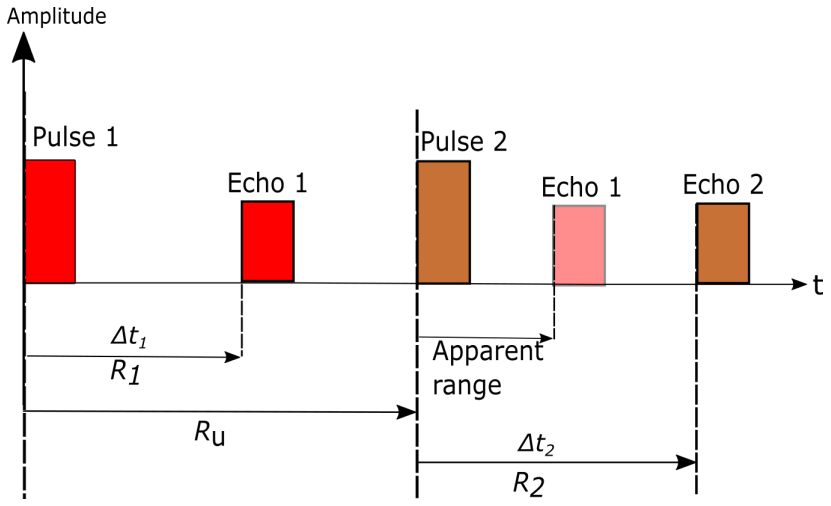

Figure 3.8: Range Ambiguity. Echo 1 is the return from a target at R_1 and echo 2 is the return from the pulse 2 at R_2 . The range ambiguity occurred when the transmitter fires again before echo 2 from the pulse 2 is received.

R_u corresponds to the maximum ambiguous range. The two way trip transit time

for this range is the inter-pulse period:

$$R_u = \frac{cPRI}{2} \tag{3.30}$$

where R_u is the maximum unambiguous range and c is the speed of ligh. R_u is limited by the PRI where the shorter the PRI, the shorter the distance travelled before the next pulse. Therefore, the greater the repetition frequency (which allows more pulses per second) the shorter is the time between the pulses, and the shorter is R_u. Using a low PRI can increase R_u.

3.3 Bistatic Radar

This section presents the concept of bistatic radar and algorithm related to the processing. In bistatic radar, the system operates in a bistatic geometry as the transmitter and receiver are not collocated. Therefore, a monostatic radar can be upgraded with a bistatic receiver system or with two monostatic radar operates in bistatic geometry. Passive bistatic radar (PBR) is the bistatic radar system that exploits non-cooperative illuminators of opportunity to detect, localise and track targets.

There are two different modes in which a PBR scheme can be processed. This is based on the information about the transmit signal that is available at the receiver as shown in Figure 3.9. Figure 3.9a illustrates the scenario where there is information available at the receiver about the transmit signal. This scenario requires the direct path signal (also known as the reference channel) which is used as a reference in the processing. As this is the direct signal with no reflections or other distortions, this

is ideally just a time-delay version of the transmitted signal. Figure 3.9b represents the scenario when there is no reference channel available. The radar operation still can potentially be done provided the parameters of transmit signal are estimated. This requires transmit signal to be deterministic and it is the research challenge examined in this thesis.

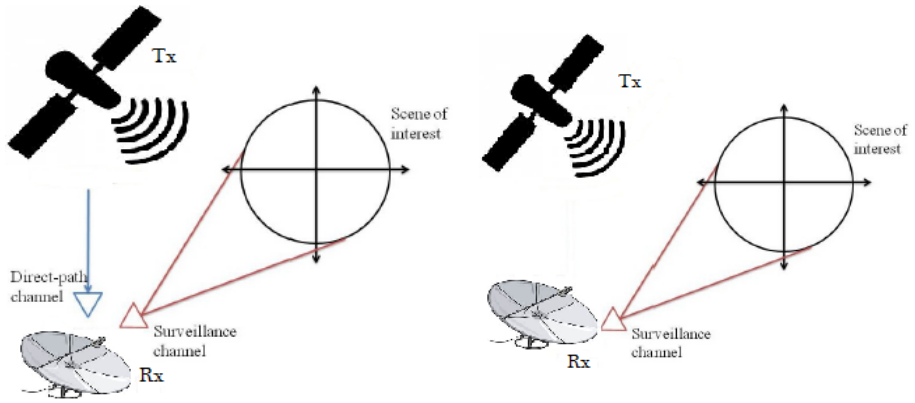

(a) PBR scenario assuming a reference signal is available at the receiver

(b) PBR scenario assuming a reference signal is not available at the receiver

Figure 3.9: PBR scenarios based on the knowledge of the transmit signal at the receiver

Considering the bistatic triangle shown in Figure 3.10, the direct path runs from the transmitter (Tx) of choice (also called illuminator of opportunity) to the receiver (Rx) . At the Rx site, a reference antenna is used to measure the direct signal from Tx. This signal is referred to as the reference signal. The range from Tx to the target is denoted as R_T. During operation, the signal from the Tx travels to the target and is reflected towards the receiver. This signal is referred to as the target echo. The target range is R_R. At the Rx site, the echo signal is analysed to calculate the range of the target and the bistatic distance which also includes the direct signal from the Tx. The direct path which is also called the baseline is the distance between the

transmitter and receiver.

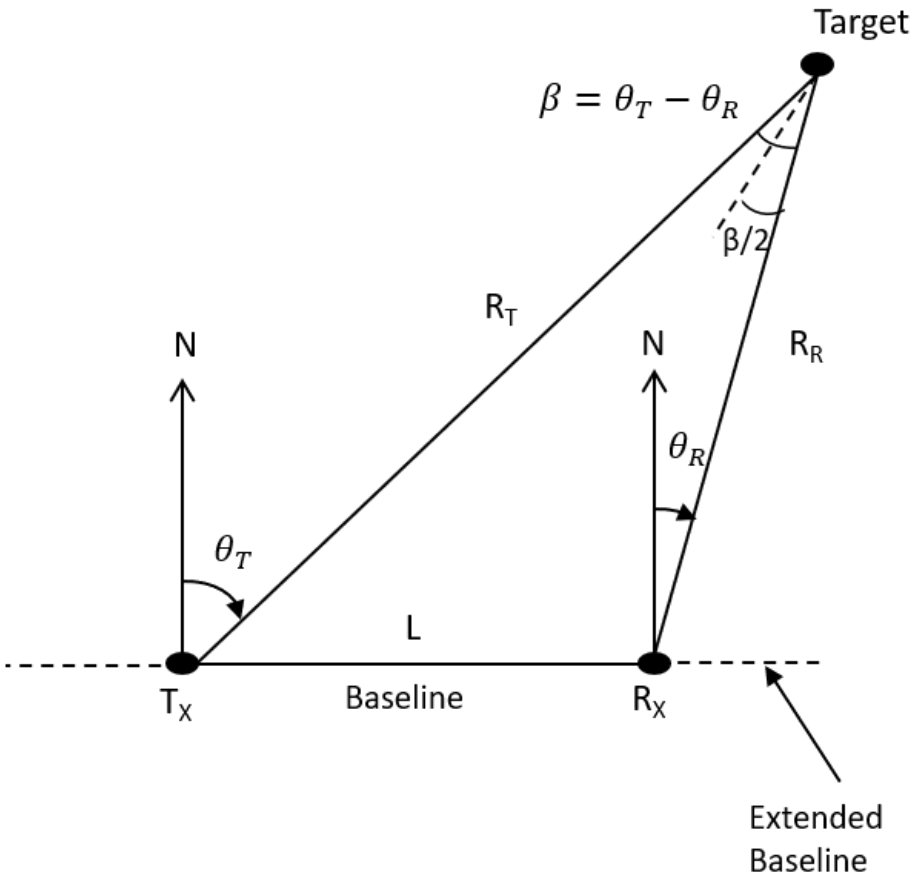

Figure 3.10: Bistatic Radar Geometry adapted from [10]

The coordinate system and parameters are positioned in the bistatic plane. The bistatic angle (β) is the angle between the transmitter and receiver with the vertex at the target. The angle β is constructed from θ_T and θ_R which are the look angles of the transmitter and the receiver respectively (also called angles of arrivals (AOA)). From Figure 3.10 and fundamental geometry this can be shown to be:

$$\beta = \theta_T - \theta_R \tag{3.31}$$

where θ_T is defined as the angle between the north direction and the line of sight from Tx to the target and θ_R is defined as the angle between the north direction and the line of sight from Rx to the target. Given knowledge of β, the more commonly used parameter is the bisector of the bistatic angle that can be calculated using $\beta/2$ as seen in Figure 3.10. The values of θ_T, θ_R and β are used to calculate transmitter and receiver related parameters [10]. In a bistatic range-Doppler plot, the relative bistatic range is the range sum minus the baseline distance written as

$$RR = R_T + R_R - L \tag{3.32}$$

where RR is the relative bistatic range. The delay for calculated range is expressed in terms of range as below

$$\Delta t = \frac{R_T + R_R}{c} \tag{3.33}$$

The target location is calculated by measuring the range sum $(R_T + R_R)$. With the known position of the transmitter and the receiver and the azimuth angle θ_T and θ_R [10] given as

$$R_T = \frac{(R_T + R_R)^2 - L}{2(R_T + R_R + Lsin\theta_T)} \tag{3.34}$$

and

$$R_R = \frac{(R_T + R_R)^2 - L}{2(R_T + R_R + Lsin\theta_R)} \tag{3.35}$$

3.3.1 Bistatic Radar Equation

The radar equation for a bistatic radar is derived in a similar way as that for monostatic radar. In the case of a bistatic radar, instead of one range parameter, the

range is separated into two different parameters [9]

$$\frac{P_r}{P_n} = \frac{P_t G_t}{4\pi R_T^2} \sigma_b \frac{1}{4\pi R_R^2} \frac{G_r \lambda^2}{4\pi} \frac{1}{kT_0 BF} L \tag{3.36}$$

where

P_r = received signal power $[W]$

P_n = receiver noise power $[W]$

P_t = transmit signal power $[W]$

G_t = transmitting antenna gain

R_T = range from transmitter to target $[m]$

σ_b = radar cross-section of target $[m^2]$

R_R = range from target to receiver $[m]$

G_r = receiving antenna gain

λ = wavelength $[m]$

k = Boltzmann's constant $[1.38 \times 10^{-23} W/(HzK)]$

T_0 = noise reference temperature, 290 K

B = receiver bandwidth

F = receiver noise figure

$L(\leq 1)$ = system losses

From equation 3.36, the noise power P_n can be determined by

$$P_n = kT_0 B \tag{3.37}$$

This equation can be applied to any type of waveform for example CW, Frequency Modulated (FM), Amplitude Modulated (AM) or pulsed signals [10].

Since the value of P_r and P_n, the SNR value can be calculated. To calculate the SNR output at the receiver, the processing gain is considered as shown below:

$$SNR_{out} = \frac{P_r}{P_n} * processing\,gain \tag{3.38}$$

For a chirp signal, the $processing\,gain = B * \tau$ where τ is the pulse width and B is the bandwidth of the signal.

It is important to comprehend the value for each parameter in this radar equation because it directly predicts the performance of a bistatic radar system. For a PBR which use communication and broadcast signals as illuminators of opportunity, having significantly high transmit power P_t is essential due to inefficient antennas and no line-of-sight to the transmitter. To overcome the inefficiencies and losses, the transmit power used must be high.

3.3.2 Range Resolution

The range resolution of a bistatic radar is not only influenced by the bandwidth of the transmitted signal and the beamwidths of the transmit and receive antennas, but also by the bistatic geometry. Determining the range therefore requires information on the location of the transmitter and the receiver, the trajectory of the target and also the bandwidth of the transmitted signal.

The bistatic radar range resolution is influenced by the geometry as shown in Figure 3.11 with Ovals of Cassini. The Ovals of Cassini are contours of constant SNR and the product of the range $R_T R_R$ shown in Figure 3.11. This figure shows two dotted lines where the blue dot is the transmitter and the red dot is the receiver.

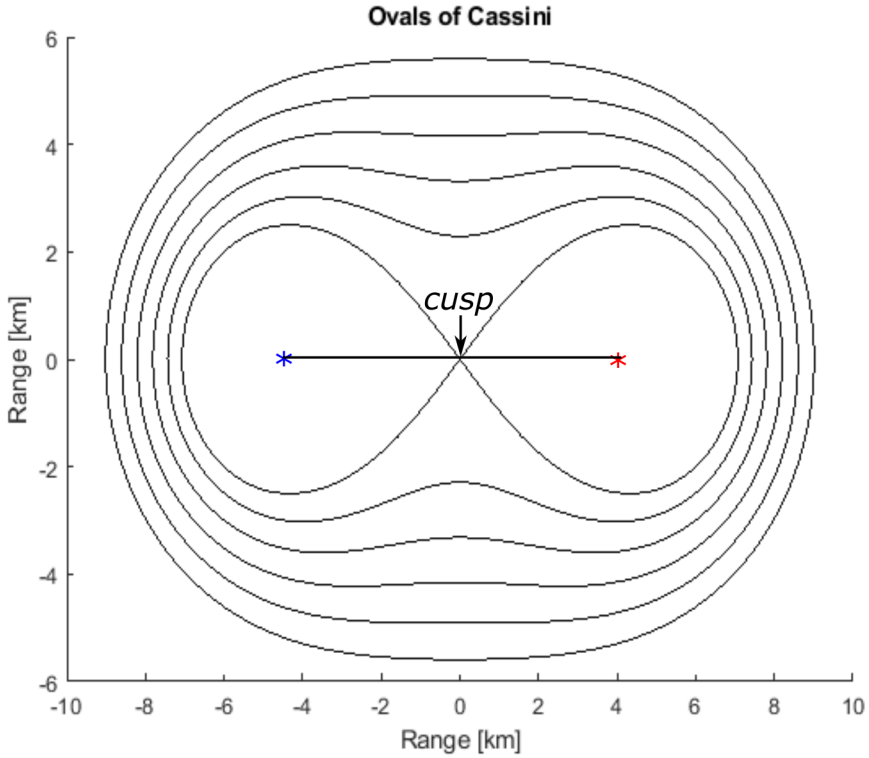

Figure 3.11: Ovals of Cassini. Dotted blue colour indicate Transmitter and dotted red colour indicate Receiver adapted from [10]

In Ovals of Cassini, the SNR is highest around the transmitter and receiver sites and decrease as one gets further and further away. At one point, the ovals will break into two non-connected ovals where one is around the transmitter and the other around the receiver on the middle of the baseline. The baseline point is called *cusp* where the ovals breaks into two parts. The ovals is called *lemniscate* (of two parts) at this SNR where it looks like an infinity sign ∞ as shown in Figure 3.11. If the baseline is increased, the ovals will be getting smaller towards a lemniscate and finally collapsed in a circle, one around the transmitter and the other around the receiver [10]. As the distance of the target increases and gets further away from the transmitter and the receiver, the Ovals of Cassini will approach circles and come close with monostatic case. The Ovals of Cassini often overlaid with

isorange contours which is the constant range ellipses for a bistatic radar system. For example, two equal targets at different range profiles can give same SNR or two equal targets with same isorange contour can give different SNR.

3.3.3 Doppler Shift

The Doppler effect is a frequency shift of the echo by a frequency proportional to the radial motion between the radar and the target illuminated. For stationary target, the time delay t_d is constant and with the target in motion, the distance to the radar changes and the time delay t_d also changes. A target's echo has a positive frequency shift when there is relative motion towards the radar and a negative frequency shift when the target is moving away from the radar. The bistatic Doppler shift is also influenced by the bistatic geometry.

In the bistatic configuration, for the stationary transmitter and receiver ($V_{Tx} = V_{Rx} = 0$) observing a moving target ($V_{Tgt} \neq 0$) the bistatic Doppler can be found based on the geometry in Figure 3.10. The direction of the velocity vector for the target to the transmitter-target can be expressed as $\mathrm{d}R_{Tx}/\mathrm{d}t$ as shown below

$$\frac{d_{Tx}}{dt} = V cos(\delta - \beta/2) \tag{3.39}$$

where δ is the relative velocity angle of the target.

Likewise, the direction of the velocity vector for the target to the receiver-target can be shown as:

$$\frac{d_{Rx}}{dt} = V cos(\delta + \beta/2) \tag{3.40}$$

Then, these two equations can be combined, yielding the below equation which gives

the Doppler frequency of the target

$$\begin{aligned} f_D = f_{Tgt} &= (V_{Tgt}/\lambda)[cos(\delta - \beta/2) + cos(\delta + \beta/2)] \\ &= \frac{2V}{\lambda}(cos\delta cos(\beta/2)) \end{aligned} \tag{3.41}$$

Considering the carrier frequency of the signal, this equation can be rewritten as follows

$$f_D = \frac{2V_{Tgt}f_c}{c} cos\delta cos(\beta/2) \tag{3.42}$$

3.3.4 Doppler Resolution

In order to discriminate between two targets, the Doppler resolution is defined so that these targets are within minimum required Doppler separation. The monostatic and bistatic Doppler resolution is expressed as the inverse of the receiver's coherent processing interval which is

$$\Delta F_d = \frac{1}{T_d} \tag{3.43}$$

where ΔF_d is the Doppler resolution of the radar in Hz and T_d is the dwell time or the look time in s. From the equation, it can be seen that the radar system that has long dwell time gives better Doppler resolution. Figure 3.12 shows two collocated targets that share common bisectors $\beta/2$. The minimum velocity difference needed to resolve the two separately is:

$$\Delta V = (V_1 cos(\delta_1) - V_2 cos(\delta_2)) = \frac{\lambda}{2T_d cos(\beta/2)} \tag{3.44}$$

However, this collocation restriction can be flexible as long as

- The separation cannot allow resolution in another dimension such as range or

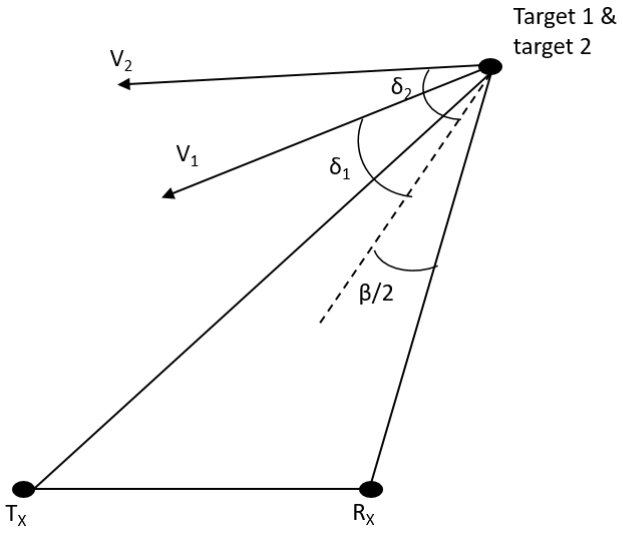

Figure 3.12: The geometry for bistatic Doppler resolution

angle

- The angle between the targets bistatic bisectors is small

3.4 Ambiguity Function

Within the context of radar, the ambiguity function (AF) is an important tool to analyse radar signals so as to evaluate their range, Doppler characteristics and optimize the radar receiver [86]. The autocorrelation and ambiguity functions define the fundamental measurement capability of the waveform that represents the output of the matched filter.

The ambiguity function is described as a matched filter output can be written as [78]

$$|\chi(\tau_d, f_D)| = \left| \int_{-\infty}^{\infty} S_T(t) S_T^*(t+\tau) e^{j2\pi f_D t} dt \right| \tag{3.45}$$

where $\chi(\tau_d, f_D)$ is the ambiguity response at the delay τ and Doppler frequency f_D and $S_T(t)$ is the complex envelope of the signal. Using Equation 3.45, the relationship of the range and Doppler resolution in AF can be seen.

To give an example of AF, a series of periodic rectangular pulses with time duration as shown in equation 3.24 was used. Taking Figure 3.4 as a reference, the matched filter which is the correlation of the transmit pulse and receive pulse in the presence of Doppler shift is given by the periodic AF. The signal that consists of pulse burst waveform can be defined as

$$s(t) = \sum_{m=0}^{M-1} x_p(t - m\text{PRI}) \tag{3.46}$$

where $x_p(t)$ is the single pulse of the signal, M is the number of coherent pulses and PRI is the PRI of the pulse. Using Equation 3.45, the AF of $s(t)$ as a function of $x_p(t)$ can be written as [87]

$$\chi(\tau, f_D) = \sum_{m=0}^{M-1} \sum_{n=0}^{M-1} \int_{-\infty}^{\infty} x_p(t - m\text{PRI}) x_p^*(t - \tau - n\text{PRI}) e^{-j2\pi f_D t} dt \tag{3.47}$$

substituting $t' = t - m\text{PRI}$ gives

$$\chi(\tau, f_D) = \sum_{m=0}^{M-1} e^{j2\pi f_D m\text{PRI}} \sum_{n=0}^{M-1} \int_{-\infty}^{\infty} x_p(t') x_p^*(t' - \tau - n\text{PRI} + m\text{PRI}) e^{-j2\pi f_D t'} dt' \tag{3.48}$$

for the AF of a single pulse, $x_p(t)$ was expressed as $\chi_p(\tau, f_D)$, the integral of the burst of pulses is $\chi_p(\tau + (n-m)\text{PRI}, f_D)$ which gives

$$\chi(\tau, f_D) = \sum_{m=0}^{M-1} e^{-j2\pi f_D m\text{PRI}} \sum_{n=0}^{M-1} \chi_p(\tau - (m-n)\text{PRI}, f_D) \tag{3.49}$$

the double sum of the equation was simplified by enumerating the combination of

double summation and after that, the decomposition was applied to Equation 3.49 which then yields to the final equation of a pulse train AF is

$$\chi(\tau, f_D) = \sum_{m=-(M-1)}^{M-1} \chi_p(\tau - m\text{PRI}, f_D) e^{-j2\pi f_D(M-1+m)\text{PRI}} \frac{sin(\pi f_D(M-|m|)\text{PRI})}{sin(\pi f_D \text{PRI})} \tag{3.50}$$

The replication of 3.50 will not overlap for the case where $\text{PRI} > 2\tau'$ where τ' is the pulse width. The magnitude of the sum will be equal to the sum of the magnitude of the individual terms. The AF of the pulse burst can then be written as

$$\chi(\tau, f_D) = \sum_{m=-(M-1)}^{M-1} |\chi_p(\tau - m\text{PRI}, f_D)| \left| \frac{sin(\pi f_D(M-|m|)\text{PRI})}{sin(\pi f_D \text{PRI})} \right| \; for \; \text{PRI} > 2\tau' \tag{3.51}$$

The AF of the simulated signal was found and plotted in Figure 3.13.

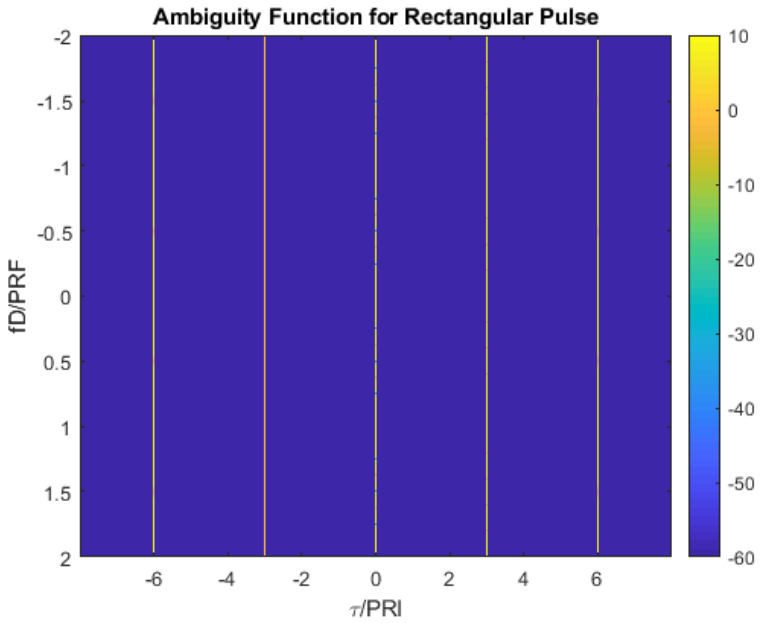

Figure 3.13: The ambiguity function to all delays with number of pulses N = 8

The range-cut and Doppler-cut plots can be conveniently obtained from the AF.

The range cut was obtained by setting $f_D = 0$ will give

$$\chi(\tau,0) = \begin{cases} \sum_{m=-(m-1)}^{M-1} (M-|m|)\left(1-\frac{|t-m\text{PRI}|}{\tau'}\right), & |t-m\text{PRI}| \leq \tau' \\ 0 & elsewhere \end{cases}$$

This function was plotted and is shown in Figure 3.14. The shape of the output is similar with the single-pulse matched filter. A Doppler cut taken at $|\chi(\tau,0)|$ represents the output of the matched filter when there is no Doppler mismatch as was plotted in Figure 3.15.

Meanwhile, the zero-Delay cut or Doppler cut was found by setting $\tau = 0$ which gives

$$\chi(0,f_D) = \left|\frac{sin(\pi f_D \tau')}{\pi f_D \tau'}\right| \left|\frac{sin(\pi f_D M\text{PRI})}{sin(\pi f_D \text{PRI})}\right| \tag{3.52}$$

The result of this equation is the sinc function with the first zero crossing occurring at $f_D = 1/M\text{PRI}$ and repeated every 1/PRI as shown in Figure 3.15.

The AF for bistatic radar can be broken into two parts according to [9] and [1], one of which is a waveform part and the other is geometrical part. However, this study focuses on the waveform part which is efficiently analysed using the presented ambiguity function as in Equation 3.51.

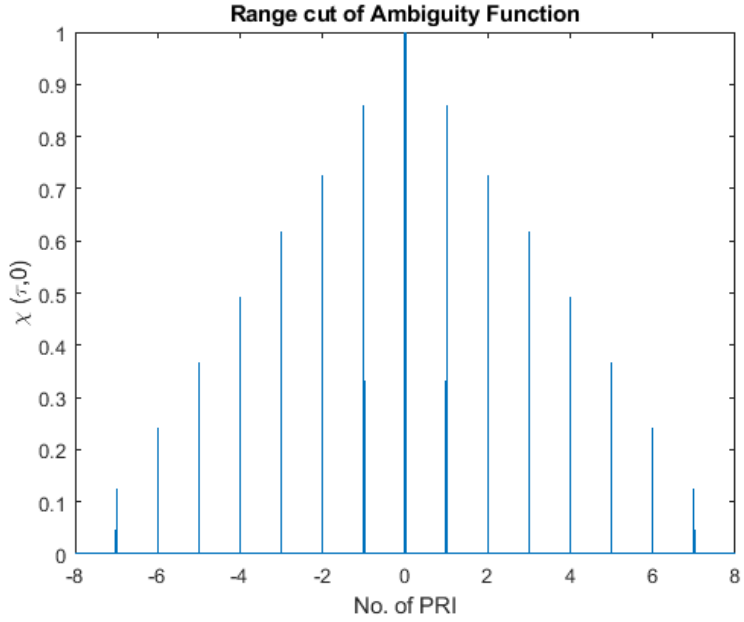

Figure 3.14: Range cut of the ambiguity function

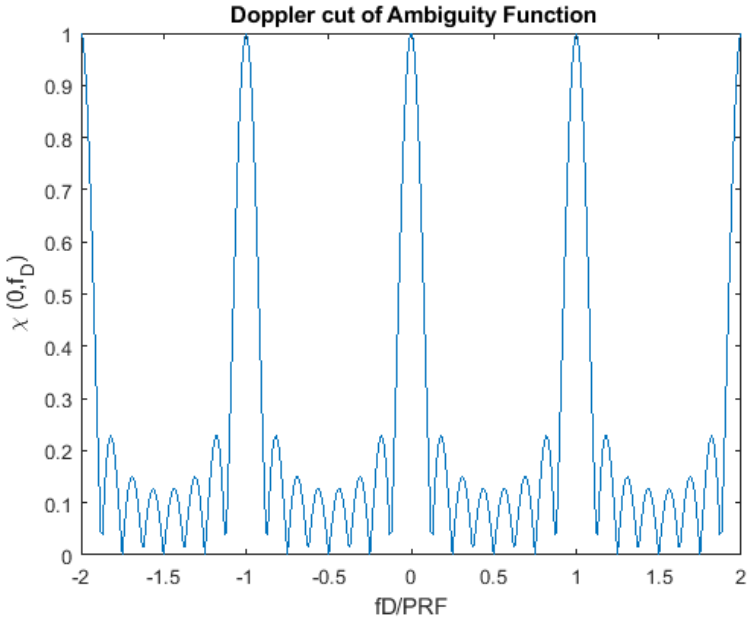

Figure 3.15: Doppler cut of the ambiguity function

3.5 Windowing Method

In a range-Doppler map, the power that is associated with a dedicated cell is smeared into another range cell due to the sidelobes on the spectrum used to produce the range profile. The effect of this phenomena will cause interference with velocity components associated with other range cells. This effect can be minimized by using a technique called windowing or tapering.

The most commonly used windowing methods are Blackman, rectangular window, flat top, Hamming and Hanning. These windows are called generalized cosine window [88]. These windows are combinations of sinusoidal sequences with frequencies that are multiplies of $2\pi/(N-1)$ where N is the window length. The symmetric periodic versions of these generalized cosine windows can be written as

$$w(n) = \sum_{k=0}^{K} (-1)^k a_k cos\left(\frac{2\pi kn}{N-1}\right), \quad 0 \leq n \leq N-1 \tag{3.53}$$

and for even-values of N they are written as

$$w(n) = \sum_{k=0}^{K} (-1)^k a_k cos\left(\frac{2\pi kn}{N}\right), \quad 0 \leq n \leq N-1 \tag{3.54}$$

for the case of $K = 1$, the customary cosine-sum windows can be written as

$$w(n) = a_0 - (1-a_0) \cdot os\left(\frac{2\pi n}{N-1}\right), \quad 0 \leq n \leq N-1 \tag{3.55}$$

by setting $a_0 = 0.5$, the equation gives the Hanning window. The zero phase version of equation 3.55 is given as

$$w(n) = a_0 + a_1 \cdot cos\left(\frac{2\pi n}{N}\right) \quad -\frac{N+1}{2} < n < \frac{N+1}{2} \tag{3.56}$$

where the perfect cancellation of the first sidelobe occurs at $a_0 = 0.54$. This window is called the Hamming window when the value of $a_1 = 0.46$. Both Hanning and Hamming windows give wide peak but low sidelobes. Unlike the Hanning window, the Hamming window does not reach zero at both ends and has a slight discontinuity in the signal. Due to this, the Hamming window is better at cancelling the nearest sidelobe.

A Hamming window and the spectrum of the train of rectangular pulses is shown in Figure 3.17. A train of rectangular pulses consisting of 8 pulses is used in the simulation. Figure 3.17a shows the spectrum of the Hamming window used in the simulation whereas Figure 3.17b shows the FFT of the rectangular pulse train. These two functions are multiplied together which the result is shown in Figure 3.17c. The resulting signal was used to produce AF. The windowing was applied in range dimensions to mitigates range sidelobes.

The result of windowing the AF is shown in the plot of range and Doppler cut shown in Figure 3.18. From the results, it can be seen that windowing did not change the power of the signal as it only reduce the sidelobes. Windowing can be applied in both transmitter and receiver to maintain the matched-filter. However, for transmission in fixed amplitude, the windowing can be focused in the receiver with the downside of SNR loss and difference in delay Doppler response [78].

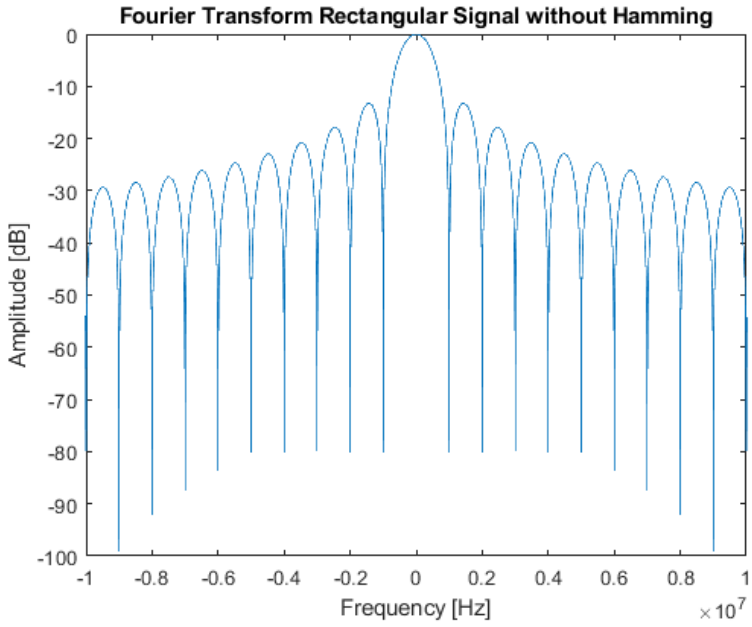

(a) Result of Fourier transform for rectangular pulse without Hamming window

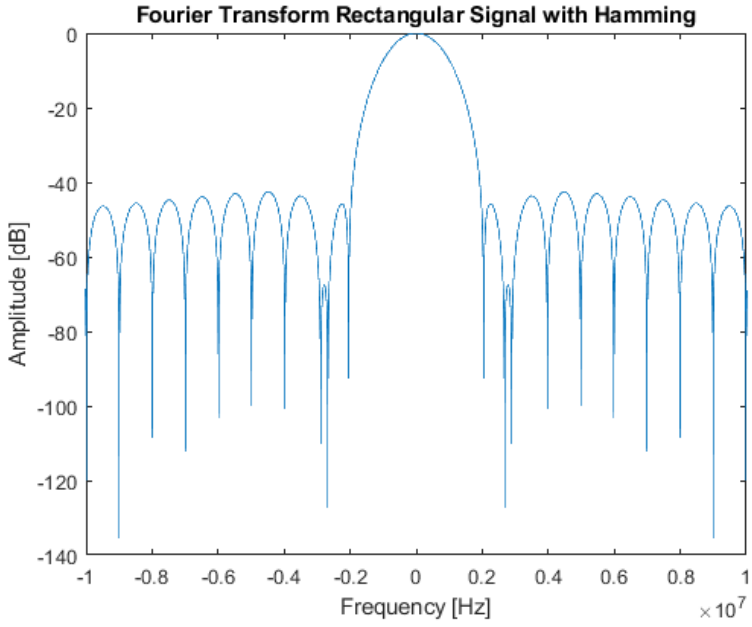

(b) Result of Fourier transform for rectangular pulse with Hamming window

Figure 3.16: Results of Fourier transform for rectangular pulse when applying Hamming window. Relative to the main lobe, the sidelobe level was reduced by -45 dB and the peak also become wider

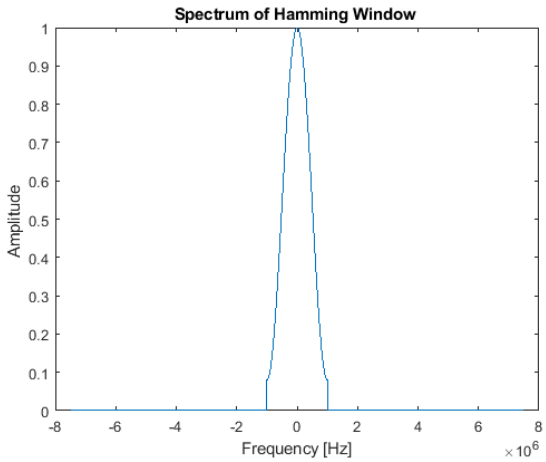

(a) Spectrum of Hamming Window

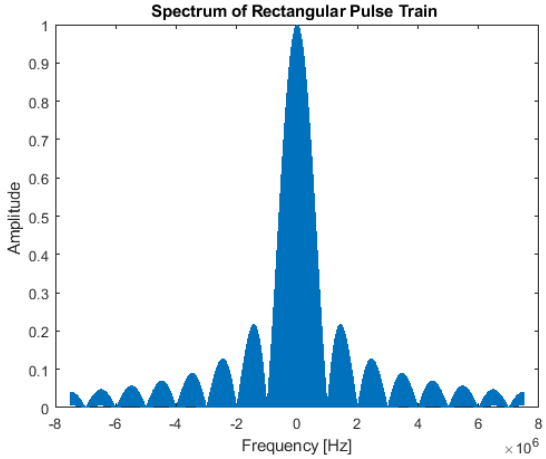

(b) Fourier transform of rectangular pulse train

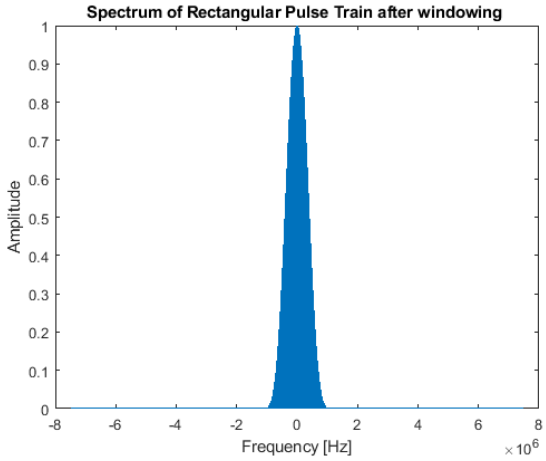

(c) Fourier transform of rectangular pulse train after windowing applied

Figure 3.17: Top: Spectrum of Hamming window. Middle: Fourier transform of rectangular pulse train. Bottom: Fourier transform of rectangular pulse train after windowing applied

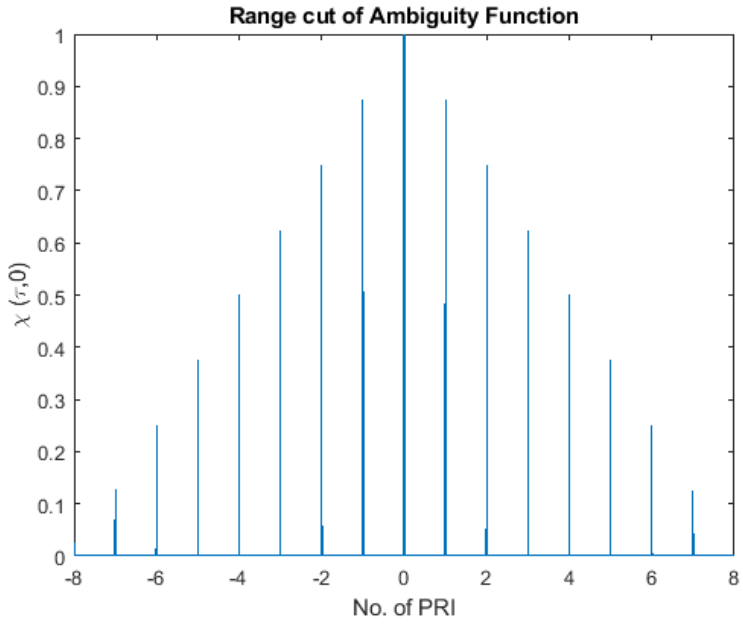

(a) Range cut of the AF after windowing

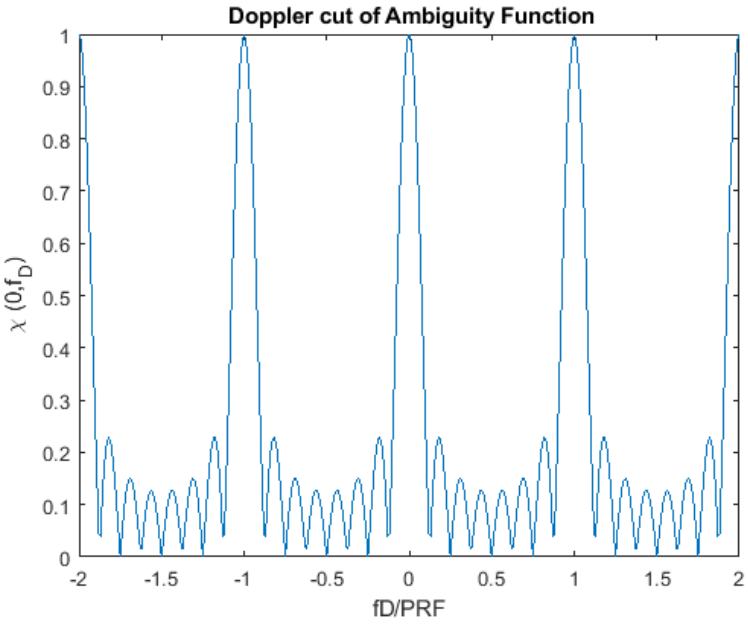

(b) Doppler cut of the AF after windowing

Figure 3.18: Top: Range cut of the AF after windowing. Bottom: Doppler cut of the AF window after windowing

3.6 Summary

In this chapter, the background theory of radar and signal processing which will be used through out this thesis was presented. This also allows the reader to understand the results obtained from the simulations and experimental work. The basic principles of radar which includes range resolution, range ambiguity and Doppler effect were defined and explained. The bistatic geometry of PBR was introduced along with the definition of bistatic angle and baseline which differs from active radar systems. These concepts are important in this research where the experiments and the results analysis will use the algorithms presented.

Furthermore, the radar equation was shown as well as an SNR calculation for the performance of target detection. The radar waveforms that are typically used in active radar were presented and analysed. The algorithm for ambiguity function for the radar system was used to analyse the performance of the target detection and the capability of target resolution. Finally, the windowing method was presented and applied to the ambiguity function.

Chapter 4

PBR Feasibility Study

In this chapter, the radar theory concept and signal processing related to bistatic radar discussed in previous chapter is applied. This will be done with a preliminary experiment in bistatic geometry without the use of a reference channel. This experiment aimed to detect a moving car using Doppler frequency shifts obtained from echoes induced by a transmitter of opportunity emitting a deterministic pulsed signal of the type of pulsed Doppler radar. The experimental setup including the hardware and software for data collection and signal processing is described. Finally, theoretical results based on the experimental geometry are compared with the experimental results.

4.1 Experimental Setup

At the beginning of this study, the implementation of bistatic radar target detection was done in order to learn the features and characteristics of bistatic radar. This

is important for the prototype that is under development. It will benefit in giving better understanding on how the final prototype should have looked like.

In this experiment, the transmitter acts as an illuminator of opportunity that transmits a deterministic pulse signal. The transmitter is non-cooperative and the signal was generated in the lab and assumed known prior knowledge for the experiments. There is no synchronisation between the transmitter and the receiver as they work independently. The main purpose of this feasibility study is to help familiarise with the concepts and operation of bistatic radar without the use of a reference channel.

The aim of the experiment is to detect a moving car in the vicinity of the transmitter and the receiver using a series of continuous deterministic pulse signals. The experiment was conducted in a car park at the Defence Academy of United Kingdom. Measurements were taken on a weekend when the car park was mostly empty in order to reduce reflections from other targets. The weather during the experiment was clear and calm.

The experimental geometry is shown in Figure 4.1. Note the positions of the transmitter, the receiver and the target. The distance between the transmitter and the receiver is called the baseline distance. In most real world applications, this distance is large enough to create non-zero bistatic angles. For example, baseline distance could be from a few miles to several hundred miles for airborne targets and hundreds to thousands of miles for satellite targets [84].

In this experiment, the baseline distance remained constant at 112.8 m throughout the experiment. The receiver was triggered manually when the car was located on the target point. At this point, the car was travelling at its maximum velocity

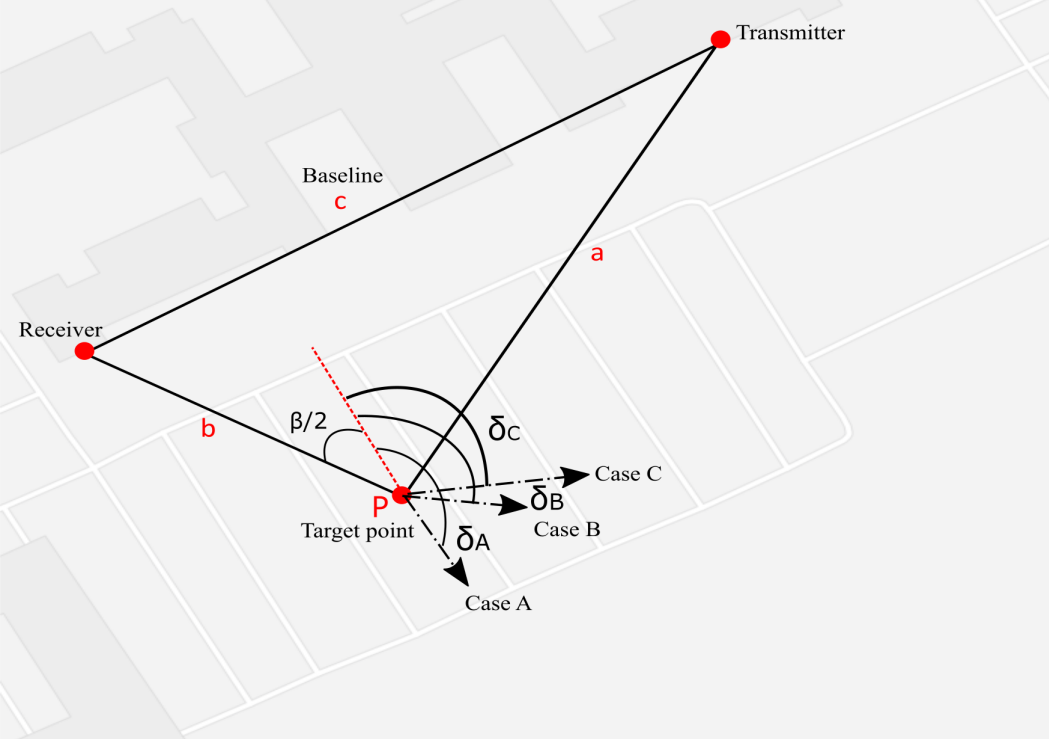

Figure 4.1: Plan view of experiment

around 12 m/s (27 mph). The transmitter and the receiver were located on the first floor of the building at a height of 4.49 m.

Data was gathered when the car moved in three different directions with respect to the baseline as shown in Figure 4.1. In case A, the target moved from the baseline towards the target point. In case B, the target moved away from the baseline along the line of sight between the receiver and the target. Finally, in case C, the target moved along the car park to the target point. The transmitter was set up to transmit a pulsed signal continuously to replicate a typical radar system illuminator of opportunity.

4.2 Hardware Setup

For this experiment, the transmitter system consisted of a pulsed signal generator (Anritsu MG3700A) and a horn antenna. The receiver consisted of a signal analyser (Anritsu MS2691A), a horn antenna and a PC for signal processing. In order to generate the pulsed signal, a baseband digital pulse with 1 MHz bandwidth was modulated with a carrier frequency at 6 GHz and produced by the signal generator. The transmitter system is shown in Figure 4.2.

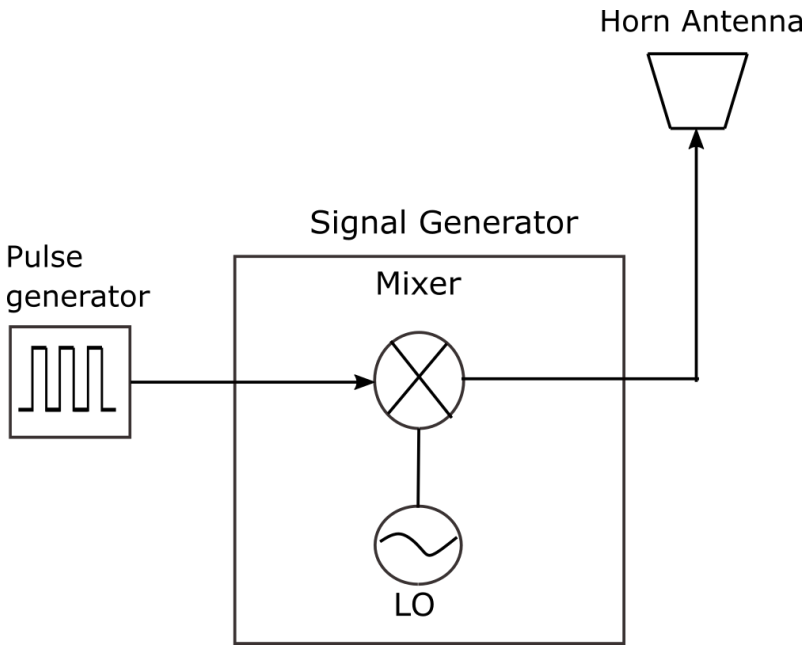

Figure 4.2: Block diagram for the transmitter system

The PRF for the pulsed signal was 4 kHz, corresponding to a PRI of 0.25 ms. The signal was then fed to the horn antenna for transmission. The frequency range for this horn antenna was 5.4 - 8.2 GHz. When operating at 6 GHz, the beamwidth in azimuth for the horn antenna is 22.9° and was calculated as

$$sin\Theta = \frac{\lambda}{L} \tag{4.1}$$

where L is the dimension of the horn antenna (118.62 mm) and $\lambda = c/f_c$ where c is the speed of light (3×10^8 m/s) and f_c is the carrier frequency (6 GHz). The horn antenna was pointed towards the target point. The transmit signal $S_T(t)$ is a series of pulses with a constant amplitude modulated with the sine wave

$$S_T(t) = A \sum_{m=0}^{\infty} \text{Rect}\left(\frac{t - m(\text{PRI})}{\tau}\right) e^{-j2\pi f_c t} \tag{4.2}$$

where τ is the duration of each pulse, A is the amplitude and f_c is the carrier frequency. The transmitted signal had a 20% duty cycle. Using the value of the duty cycle, the pulse width, τ, is calculated using equation $\tau = \text{PRI} \times \textit{duty cycle}$ which equal to 50 μs. The characteristics of the transmitted signal are summarised in Table 4.1.

Table 4.1: Characteristics of the transmitted signal

Duty Cycle	20%
PRF	4 kHz
PRI	0.25 ms
Pulse width τ	50 μs

The block diagram of the receiver system is shown in Figure 4.3. This system consisted of a horn antenna and the signal analyser. The horn antenna was pointed at the target path to detect the reflected signal from the target. The horn antenna used in the receiver system had the same characteristics as the antenna in the transmitter system. The receiver captured the signal for a dwell time $T_D = 0.2$ s resulting in $1/T_D = 5$ Hz frequency resolution (i.e. equivalent to $T_D \times \text{PRF} = 800$ integrated pulses).

The signal analyser received the reflected transmit signal from the antenna.

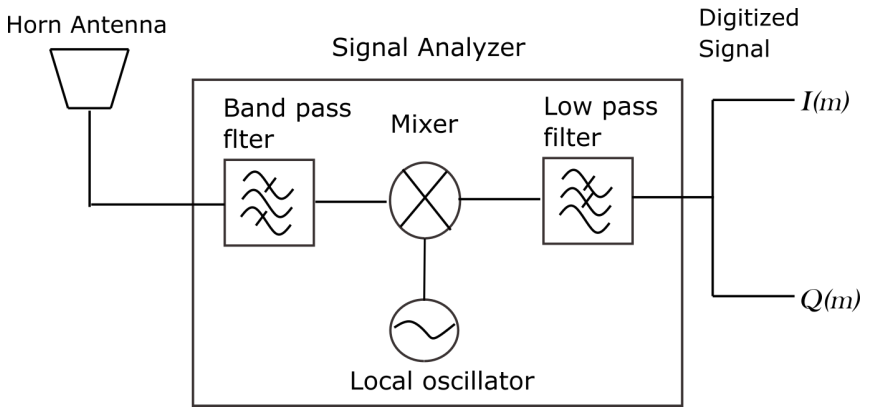

Figure 4.3: Block diagram for pulse radar detection

In the signal analyser, a superheterodyne receiver (a mixer and the local oscillator (LO)) was used to down-convert the received signal spectrum. After down-conversion to an intermediate frequency, the signal is filtered by the low-pass filter in order to prevent aliasing and filter out unwanted negative frequencies.

The down-converted signal was digitised to provide complex (I/Q) sampling with a rate of 2 MHz. The digitised signal was analysed with MATLAB where an FFT was applied to examine the spectrum and hence the Doppler shift of the received signal.

The signal analyser was connected to the PC via a General Purpose Interface Bus (GPIB) using a USB/GPIB converter. This cable provided a direct connection from the PC to the signal analyser. The USB/GPIB is a plug and play interface, easy to use and high speed, enabling large transfers. In addition, the PC could also control the signal analyser using the USB/GPIB interface and the Virtual Instrument Standard Architecture (VISA) in MATLAB.

4.3 Theoretical Results

The theoretical value of Doppler shift was calculated in order to check that the experimental setup was working as expected. Firstly, the bistatic angle was calculated from the bistatic configuration shown in Figure 4.1. The reference position of the moving target (P in Figure 4.1) was used as the reference point between the theoretical and experimental results. The bistatic angle is the angle between the transmitter and the receiver with the vertex at the target point. The triangle that was formed by the bistatic configuration is $c^2 = a^2 + b^2 - 2ab\cos\beta$ using the law of cosines. Because of the transmitter and the receiver were located on the first floor of a building (at 4.49 m), the 3D bistatic angle is calculated.

The 3D triangle was formed where the bistatic angle β was calculated as

$$\beta = cos^{-1}\left(\frac{a^2 + b^2 - c^2}{2ab}\right) \tag{4.3}$$

where a is the distance between the transmitter and the target (90.6 m), b is the distance between target point-receiver (60.0 m) and c is the baseline distance which was 112.8 m. Substituting these values into Equation 4.3 gives the bistatic angle as 101.73°.

With the bistatic angle value obtained, the value of the angle of the projected velocity vector δ can be estimated based on the directions of the target velocity on the ground shown in Figure 4.1. The value of δ was different depending on the direction of the target motion. It can be estimated from the car's trajectory. For case A, the value of δ is 180°, for case B, δ is 140° and for case C, δ is 105°. For the stationary transmitter and receiver where ($V_{Tx} = V_{Rx} = 0$) and with the moving

target $V_{Tgt} \neq 0$ the bistatic Doppler frequency can be calculated based on Equation 3.42.

With the values of δ and β known, the Doppler frequency obtained for case A is -303.0 Hz, for case B is -232.2 Hz and for case C is -68.2 Hz. The calculated value for all Doppler shifts were negative. In the next section, the experimental results from the measurements will be presented and compared with the theoretical results.

4.4 Experimental Results

This section presents the experimental results in all three cases. Targets were detected by their Doppler frequency obtained from the frequency shift at the receiver. Results showed there was also phase jitter in the equipment which appeared in the results as a frequency shift in the received signal. This jitter may resulted from non-harmonics spurs which occurred in a periodic manner randomly. A non-harmonics spurs creates deviations in edge timing that drift about the ideal timing point in a sinusoidal manner. This jitter also may originated from the output signal of an oscillator which contains unwanted noises and signals associated with a noisy oscillator or generated by the non-linearity of any component in the oscillator circuitry. In every test that was run, the value was different and needed to be considered when analysing the results.

In this experiment, there is no direct link and synchronisation between the transmitter and the receiver. There is no range measurement due to no pulse compression applied in processing the result. The processing was done by assuming the transmit signal known prior knowledge, thus the Doppler frequency was found by applying

direct Fast Fourier Transform (FFT). In addition, the LOs between the transmitter and the receiver was unsynchronised and independent which cause frequency shift or jitter.

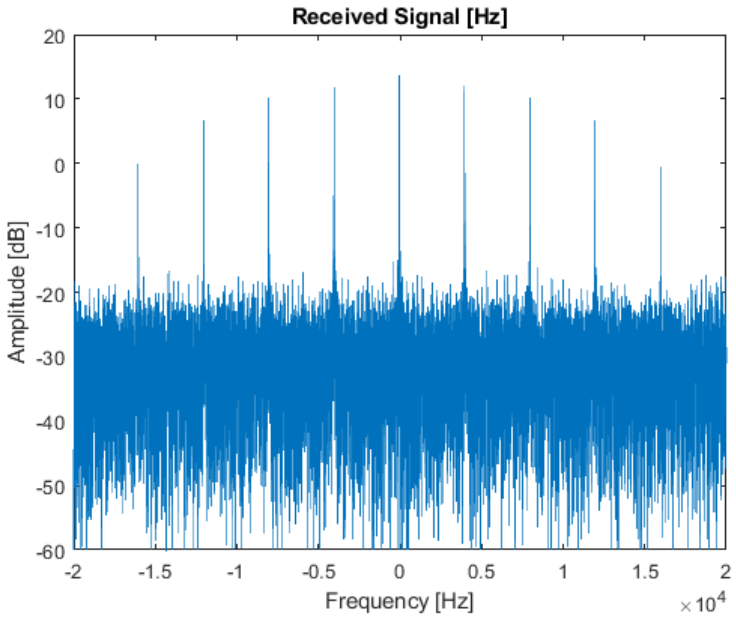

Figure 4.4: Periodic received signal

In this experiment, the phase jitter was characterised by using the return from a static target present within the scene. At the beginning of the experiment, the transmitter was pointed towards the car park without a moving target to measure the stationary scene and obtain a jitter value. The result of this measurement is shown in Figure 4.4. A series of periodic peaks in the first measurement without the moving target can be seen at non-zero Doppler shift where the separation between the peaks was, as expected, at PRF.

A zoom of Figure 4.4 around zero Doppler is shown in Figure 4.5. The peak at 0 Hz as in Figure 4.5a is a result from the non-variable unwanted system noise which can be suppressed by removing the mean value from the spectrum. In Figure 4.5b

the mean value is removed and the value of the jitter is -42.44 Hz. This system noise only occurred at the zero frequency and is not repetitive. The plot at PRF is shown in Figure 4.6 before and after zero mean suppression. Result in Figure 4.6a shows that there is no other peak other than at PRF (4 kHz). Figure 4.6b also shows that there is no peak other than at PRF. These results showed that this unwanted system noise only occurred at 0 Hz.

The result for case A, the car moving from the baseline towards the target point is shown in Figure 4.7. As mentioned earlier, the moving target is represented by the periodical peaks around the Doppler frequency as shown in Figure 4.7a To find the Doppler shift for case A, the figure was zoomed as shown in Figure 4.7b. From the result shown, the jitter is -45.78 Hz. So, the Doppler frequency shift of the car for case A is $-347.10\,Hz - (-45.78\,Hz) = -301.32\,Hz$, corresponding to a bistatic velocity of 15.1 m/s (33.8 mph).

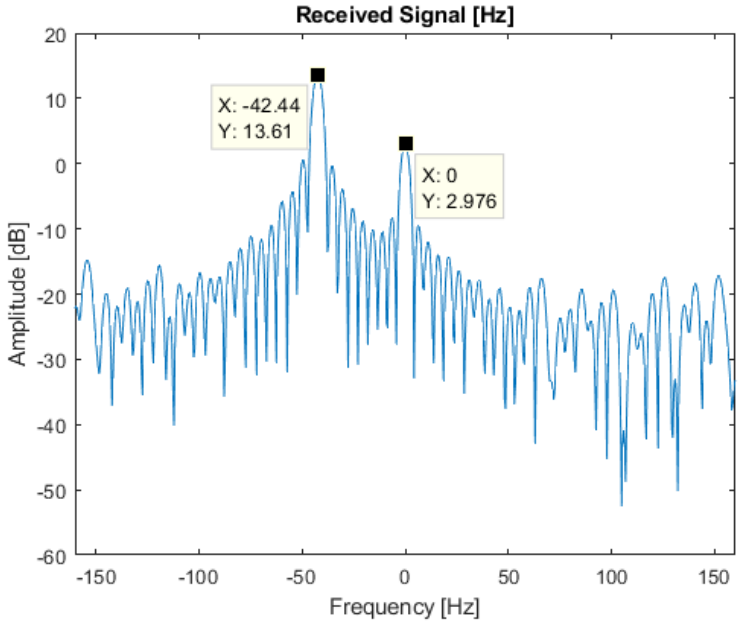

(a) Received signal without moving target

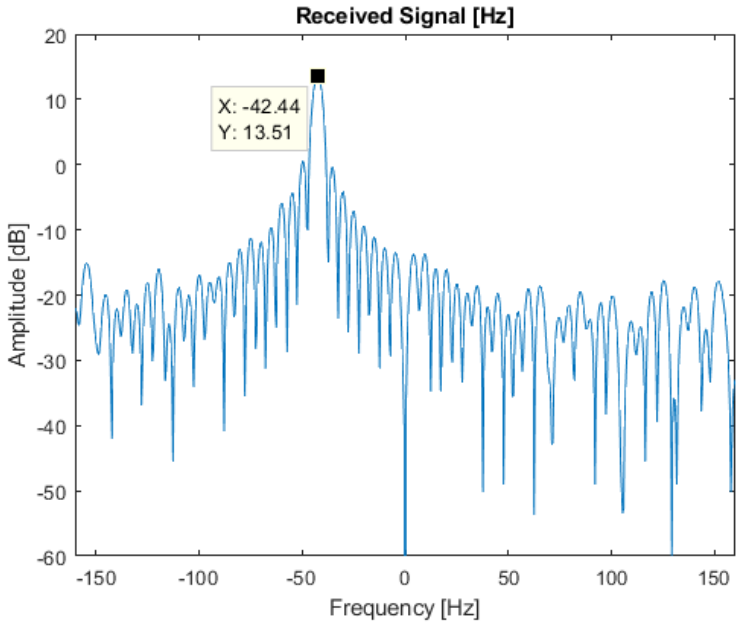

(b) Received signal without moving target after mean value removal. Note response at 0 Hz has been suppressed

Figure 4.5: Received signal without moving target

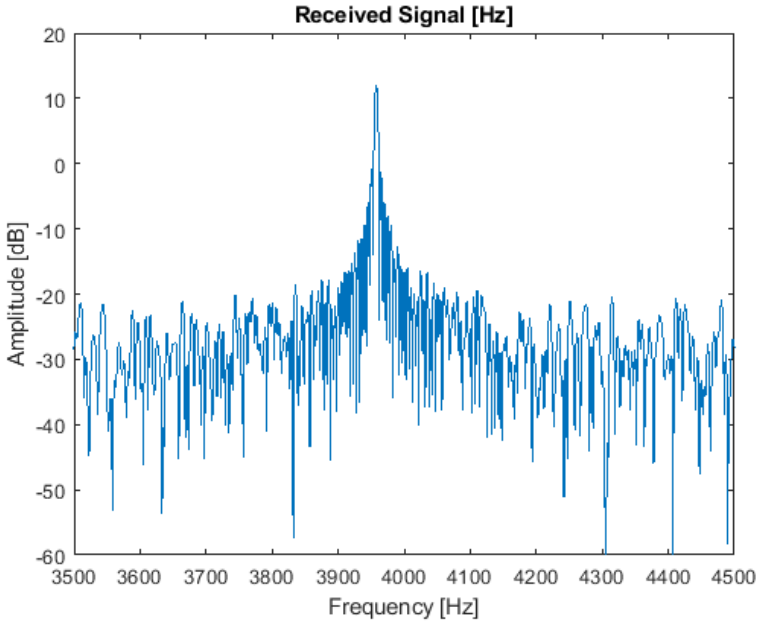

(a) Received signal without moving target at PRF before mean value removal

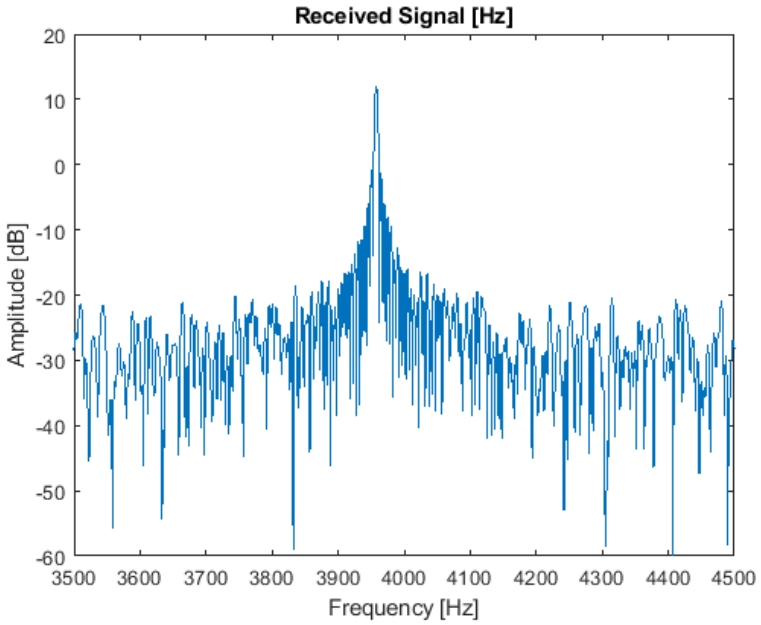

(b) Received Signal without moving target after mean value removal at PRF

Figure 4.6: Received signal without moving target at PRF. Note that there is no peak detected around PRF in both figures

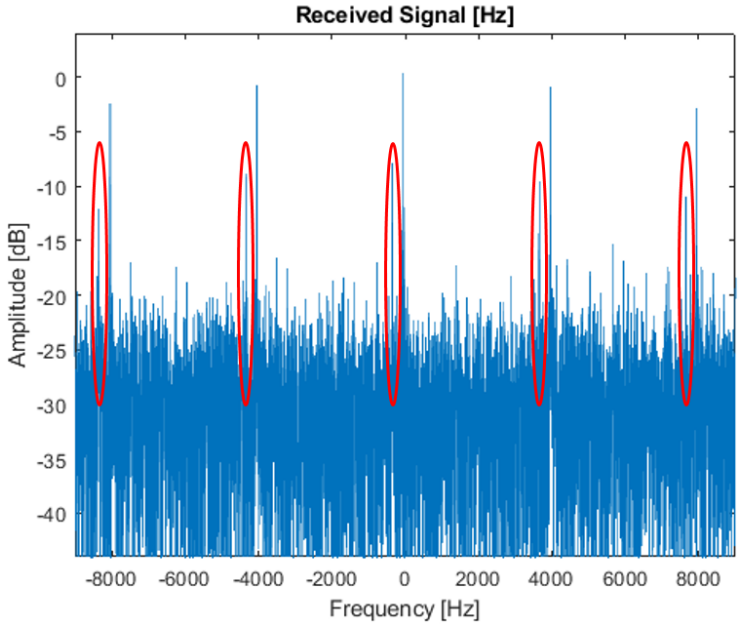

(a) Case A: Direction of the target from the baseline towards the target point. Note red circles in the figure shows the Doppler shift response

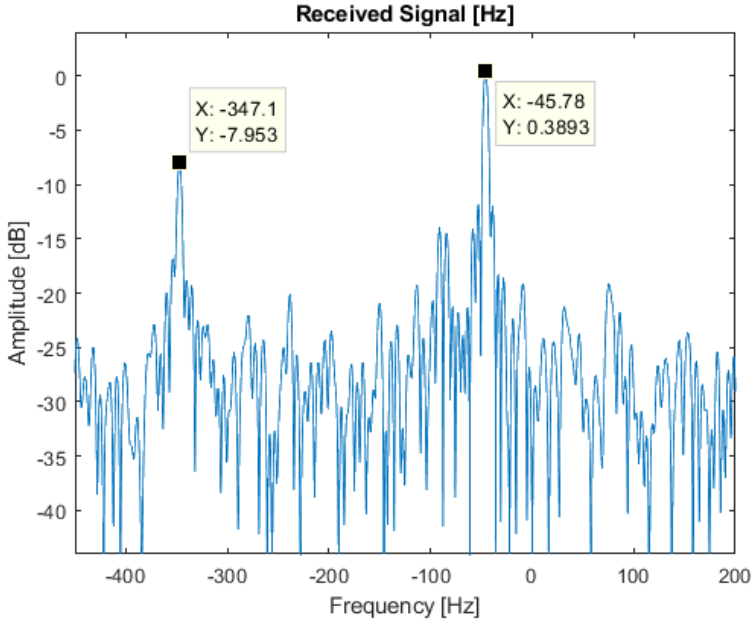

(b) Case A: Direction of the target from the baseline towards the target point (zoom in)

Figure 4.7: Case A: Received signal with moving target in case A

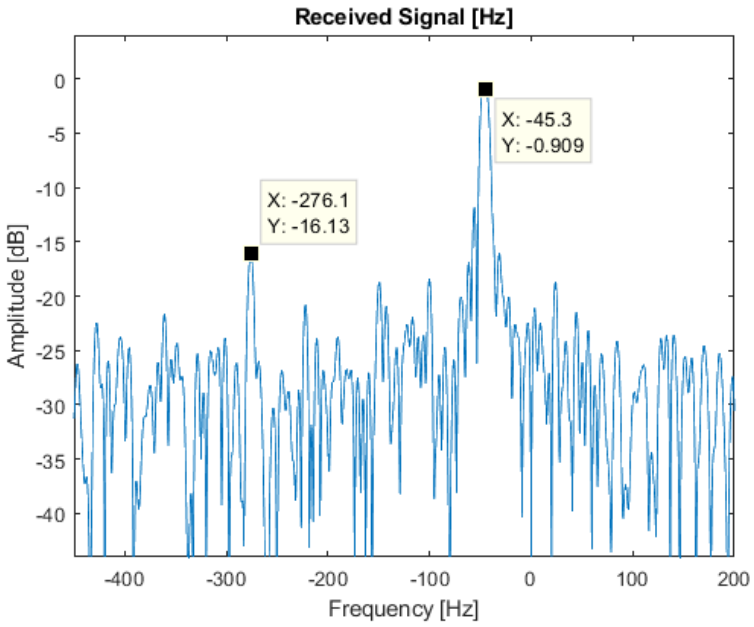

Figure 4.8: Case B: Direction of the target inline with the receiver towards the target point (zoom in)

The result for case B, that is for the target moving inline with the receiver and target point, is shown in Figure 4.8. From the result shown, the jitter is -45.30 Hz. So, the Doppler frequency shift of the car for Projection B is $-276.10\,Hz - (-45.30\,Hz) = -230.80\,Hz$ corresponding to a bistatic velocity of 11.54 m/s (25.1 mph). The response where the target was detected is repetitive in every PRF.

Finally, in case C, the car moved along the car park, towards the transmitter. From the result in Figure 4.9., the jitter is -43.39 Hz. So, the Doppler frequency shift of the car for case C is $-43.39\,Hz - (4.768\,Hz) = -48.16\,Hz$ corresponding to a bistatic velocity of 2.41 m/s (5.4 mph).

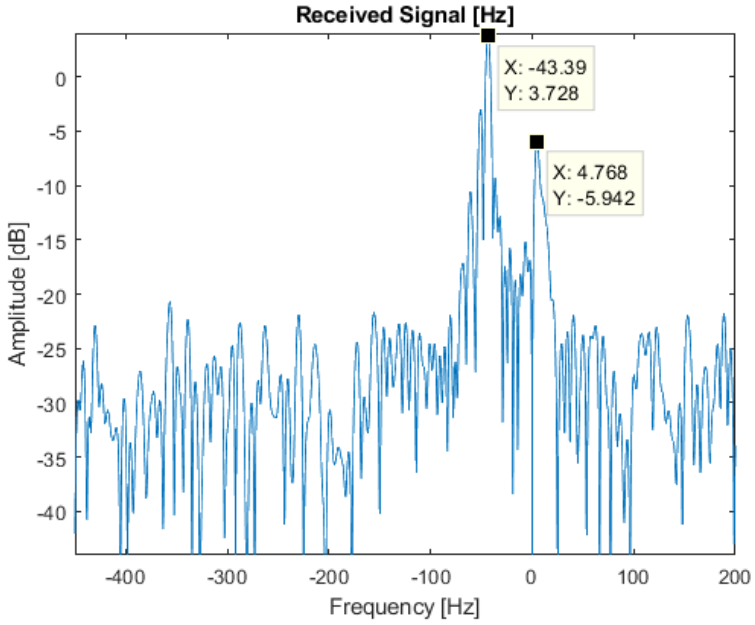

Figure 4.9: Case C: Direction of the target along the car park towards the target point (zoom in)

4.5 Analysis of Results

From these experimental results, it was found that there are slight differences between the calculated and experimentally values found in Doppler. Despite a good agreement, it was found that the experimental value were slightly different from the theoretical values as shown in Table 4.2.

Table 4.2: Theoretical and experimental results

	Theoretical (T)	Experimental (E)	Difference (|E-T|)	% Error
Case A	-303.0 Hz	-301.3 Hz	1.7 Hz	0.7%
Case B	-232.2 Hz	-230.8 Hz	1.4 Hz	0.6%
Case C	-68.2 Hz	-48.2 Hz	20.0 Hz	41.5%

There are several factors that could cause these differences. The measurement was manually triggered and therefore there may be some delay between the car

passing the target point at maximum speed and the measurement being taken. Also, the speedometer of the car may over estimate the true speed by as much as 10% [89]. In addition, the speed of the car was manually controlled by the driver which gives another source of error. There is also no GPS measurement to be used as a ground truth. Finally, geometric errors can cause Doppler errors. An error of 5° in the car's direction gives the following of $\delta = 175°$, 135° and 98°. These gives theoretical Doppler values of -301.9 Hz for case A, -214.3 Hz for case B and -42.2 Hz for case C. As can be seen, the largest effect of geometric errors are for case C as per the experimental results. Based on the results in Table 4.2, all the three cases indicate that the Doppler shift is negative.

From this initial experiment, the detection of the target by implementing the concept of passive bistatic radar based on deterministic illuminators was successfully performed. The target was detected in three different directions with negative Doppler shifts. It was also shown that the Doppler shift was obtained without the reference channel due to the known transmitted signal. The echo signal reflected from the moving target resulted in Doppler shift in the received signal. Moreover, the feasibility of bistatic radar target detection without a reference channel was shown.

4.6 Summary

In this chapter, an initial experiment of passive bistatic radar target detection has been carried out. The purpose of this experiment is to help understanding the concept of bistatic radar by exploiting deterministic signals. The transmitter is

non-cooperative and the signal was generated in the lab and assumed known prior knowledge for the experiments. The knowledge of this feasibility study is important because it will be used in the next experiment exploiting non-cooperative radar signals. Moreover, it was found that the initial prototype presented in this chapter require improvement in terms of equipment (from the jitter introduced in the results) and more signal processing for better results.

The bistatic geometry was implemented to detect a moving car using an early prototype version consisting of a signal generator, a signal analyser and horn antennas. To the best of my knowledge, this experiment was the first analysis to study the feasibility of passsive bistatic target detection without the use of a reference channel with radar signal. The target was successfully detected, despite a jitter was present and system noise needed to be removed by mean value subtraction.

The measured Doppler frequencies from three different target directions were compared with theoretical predictions. The results were in reasonable agreement. Possible error sources include the speed and direction of the manually controlled target and timing errors in the manually triggered measurements. Moreover, the processing for the data is simply a direct Fourier transform where sometimes the target is not clearly seen due to the high background noise. In the next chapter, the lesson learnt with this experimental campaign are applied towards the development of a more complex prototype will be introduced and more experimental results will be presented.

Chapter 5

Prototype Design and Development

This chapter details the implementation of a prototype passive radar system using a software defined radio (SDR) on a Universal Software Radio Peripheral (USRP). This prototype will be used during all the following experimental work in this thesis. This system is smaller and more configurable than the setup used in Chapter 4. These features make it more suitable for off-site experiments, such as those exploiting illuminators of opportunity. The prototype was deployed in PBR target detection without the use of a reference channel. The experimental study was started with a monostatic configuration to test the developed prototype and followed by real bistatic configuration.

5.1 Universal Software Radio Peripheral (USRP)

USRP hardware directly connected to a host computer was used in this research in order to implement the signal processing and the radio applications. Software Defined Radio (SDR) has the ability to be reconfigured through the application of software and redefinable logic which is achieved by implementing digital signal processing (DSP) on field programmable gate arrays (FPGA). However, in this research, the focus is more on the application of DSP software to build the radar prototype, hence the default FPGA configuration was used with custom signal processing implemented in software.

Figure 5.1: USRP-2943R from National Instrument (NI) [90]

Figure 5.1 shows the USRP-2943R used in this work. This provides 2x2 multiple input multiple output (MIMO) channels with tunable center frequencies ranging from 1.2 GHz to 6 GHz with a bandwidth of up to 120 MHz. To transmit and receive the signal, antennas are connected to the transmitter and receiver ports - no external RF amplifiers are required because the USRP contains built-in amplifiers.

This makes the USRP very convenient to use.

SDR minimises analogue components in the digital domain and also enables additional functions that are not possible in the analogue domain such as digital filters. These digital filters are implemented in the software that can adapt to various applications. The functions provided by a USRP also include input signal digitization, frequency selection within the IF band and decimation [91]. This provides a cheap, flexible and high speed radio prototyping test bed.

5.1.1 USRP Configuration

This section describes the system configuration for SDR. SDR configuration can be simplified to transmitter and receiver block. The USRP used in the prototype is of the same general architecture for SDR.

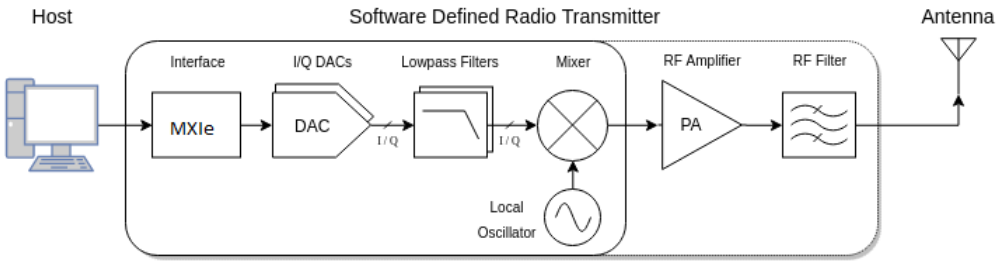

Figure 5.2: Simplified direct conversion transmitter adapted from [92]

In the transmit path shown in Figure 5.2, the host computer synthesizes baseband I/Q signals and transmits the signals to the USRP over an interface cable. The digital signals are converted from the digital to analogue domains in the digital-to-analogue (DAC) converter. The unwanted high frequency noise components of the signal are reduced by the low-pass filters. In the mixer, the analogue signal is up-

converted to the required transmit frequency using the Local Oscillator (LO) which can be locked to an external reference signal. The voltage signal is then amplified by an RF amplifier and filtered by the RF filter to remove spurious frequencies generated by the mixer.

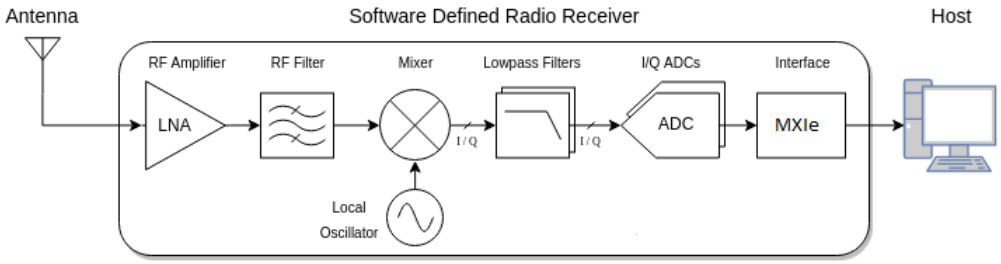

Figure 5.3: Simplified direct conversion receiver adapted from [92]

For the receive path shown in Figure 5.3, an antenna converts the RF signal (electromagnetic waves) into a voltage signal. This signal is then amplified, and filtered before being passed to the mixer. The mixer down-converts the signal to the baseband with I/Q components using an internal LO. The signal is then filtered to remove unwanted frequencies. The analogue-to-digital converter then digitise the I/Q data with streaming to the host computer for further signal processing.

5.2 Signal Processing

This section will describe the signal processing methodology including Doppler signal processing and cross-correlation that will be used to analyse the results. For both monostatic and bistatic experiments, a continuous pulse chirp signal was transmit-

ted. The linear deterministic chirp pulse is defined as

$$S_T(t) = \Re\left\{e^{j2\pi f_c t} e^{j\gamma\pi t^2}\right\} \text{Rect}\left(\frac{t}{\tau}\right) \tag{5.1}$$

where $\gamma = B/\tau$ is the chirp rate, B is the bandwidth, τ is the pulse width and f_c is the carrier frequency. Rearranging this equation to obtain a train of pulses, the continuous form of the signal is written as

$$S_T(t) = \sum_{m=0}^{\infty} e^{j\gamma\pi(t-mPRI)^2} e^{j2\pi f_c t} \text{Rect}\left(\frac{t-mPRI}{\tau}\right) \tag{5.2}$$

Once the echo is received, the Doppler domain can be used to separate the returns from different targets. This was done with range-Doppler maps by implementing a cross-correlation and an FFT as shown in Figure 5.4. The received signals were stored in a matrix as shown in the top of Figure 5.4 (labelled as (1)). Each fast-time row holds the return from one pulse and successive echoes are stored in the slow-time dimensions.

Based on Figure 5.4, the first step for the signal processing is the correlation process or also called matched filtering (labelled as (1)). In the correlation process, the the signal from the reference and surveillance channel were cross-correlated together. However, in the case when there was no reference channel, the correlation process will still involve the surveillance channel and a software copy of the deterministic transmitted signal. A software copy of the signal was constructed so that it is accurate and most importantly it is cleaner from any unwanted noise.

The use of reference channel to collect direct signal may experience noise from the transmitter and returns from the clutter. In addition, the direct signal may also

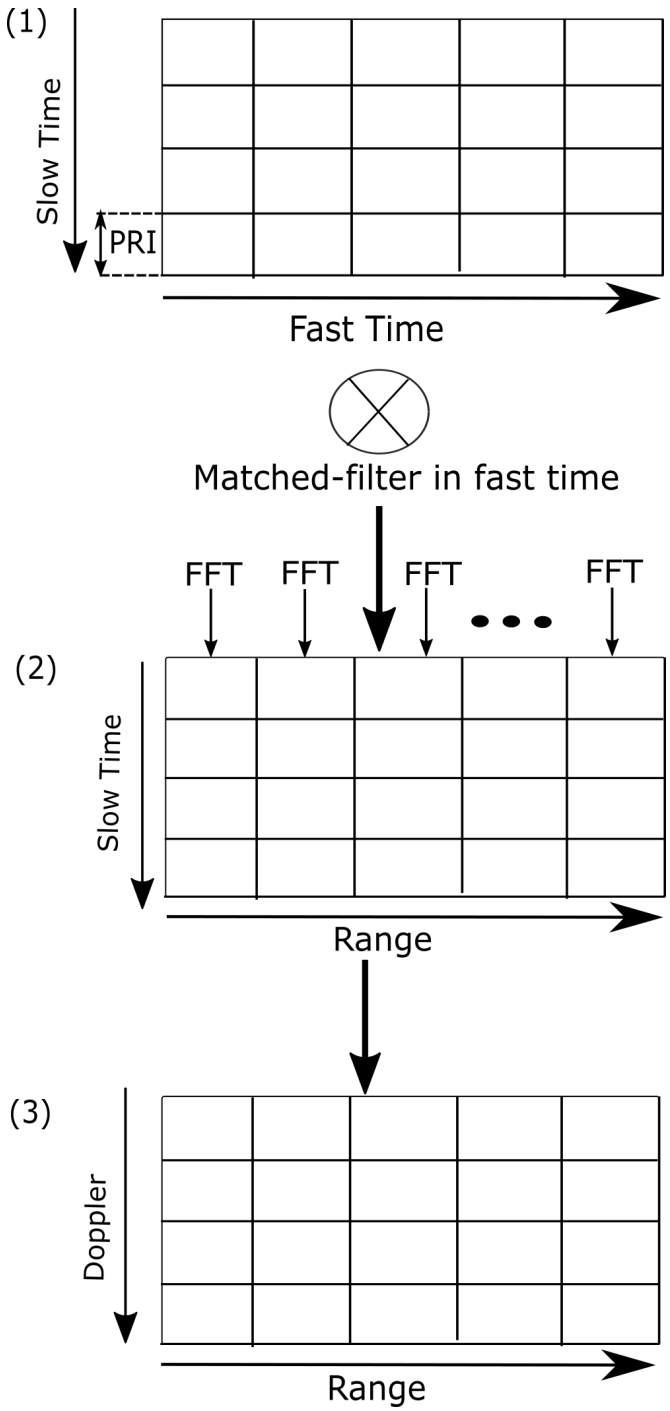

Figure 5.4: Steps for range-Doppler map construction. (1) is the data matrix in slow-time and fast-time, (2) is the matrix after cross-correlation in fast-time and (3) is the range-Doppler map which result from FFT in slow-time

suffer from multipath if the transmitter is located in dense environment. Thus, with the use of a software copy of the signal, the pristine copy of transmitted signal is obtained.

After cross-correlation to form a range-map, an FFT was applied to each range bin (labelled as (2)). Finally, the result from the FFT in the slow-time dimension produced the range-Doppler map as shown in Figure 5.4 (labelled as (3)).

For the number of pulses used to obtain the range-Doppler map, the target can be said to be located at the same range bin if the dwell time is short enough with respect to the speed of the target. When no range migration occurs, the slow-time data corresponding to the target range bin contains information on the Doppler shift induced by the target which can be used to estimate the target radial velocity. The slow-time was sampled at PRF, thus, the FFT of the slow time data for a range bin results in an unambiguous Doppler spectrum from (-PRF/2, PRF/2).

5.3 Experimental Setup

In this section, the experimental campaign was conducted with a monostatic and a passive bistatic configuration in order to test the capability of the USRP-2943R prototype for PBR target detection. For the monostatic experiment, one USRP was used and for the bistatic experiment, two USRPs were used. The aim of this experiment was to detect a moving target by exploiting deterministic signals of opportunity without the use of a reference channel. As described in Chapter 4, the experiments were repeated in a car park at the Defence Academy of the United Kingdom when the car park was mostly empty so that the clutter was minimized.

The monostatic configuration was only used to test the receiver before running the main bistatic trials.

5.3.1 Monostatic Configuration

The monostatic experiment is important because it was used to test the developed receiver prototype in a simple configuration. In the monostatic configuration, one USRP was used with Channel 1 (referred to as RF0) acting as the transmitter and Channel 2 (referred to as RF1) configured as the receiver. RF0 is configured so that it transmits continuous waveforms and is connected directly to a horn antenna. RF1 was also directly connected with an antenna and received the continuous echo signal. The antennas used for transmitting and receiving signals were the same horn antenna, a standard gain horn with a frequency range of 3.4 to 5.9 GHz (Model 643 produced by Narda). The beamwidth in azimuth for the antennas was 29.7°, obtained from

$$sin\theta = \frac{\lambda}{L} \tag{5.3}$$

where $L = 12$ cm is the width of the antenna and $\lambda = 0.06$ cm is the wavelength at 5 GHz. Both of the antennas were arranged in cross-polarisation to reduce direct signal interference. The parameters of the transmitted waveform and experiments are presented in Table 5.1

The experimental setup is shown in Figure 5.5. In the monostatic configuration, the transmitter and the receiver were collocated. The target was a car moving at a maximum velocity of 10 m/s (22 mph). Data was gathered when the car reached its maximum velocity. Two separate runs were conducted, one with the target moving away from the radar and another with the target moving towards the radar.

Table 5.1: Signal Parameters

Parameter	Value
Sampling frequency	45 MHz
Number of samples	400000
Bandwidth	20 MHz
Pulse width (τ)	2 μs
PRF	5 kHz
Dwell time	8.9 ms
Range resolution	7.5 m

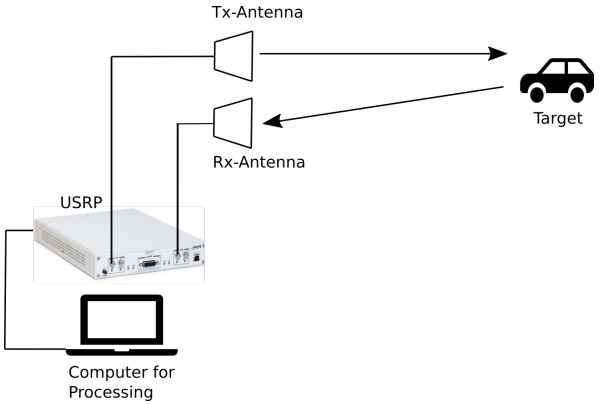

Figure 5.5: Monostatic configuration where the transmit and receive antenna was located side by side

Figures 5.6a and 5.6b shows the range-Doppler map for the target moving away and towards the radar. The direct signal interference can be seen in both figures which is the the response (in yellow) at zero-Doppler. The straight line along the zero-Doppler is the system noise from the USRP. In these figures target cannot be seen because the response from the direct signal is strong. It can also be seen in both figures that the direct signal is not at zero-range. This is because there is no range information gathered during the experiment, having transmitter and the receiver independent.

The direct signal interference may come from the configuration between the

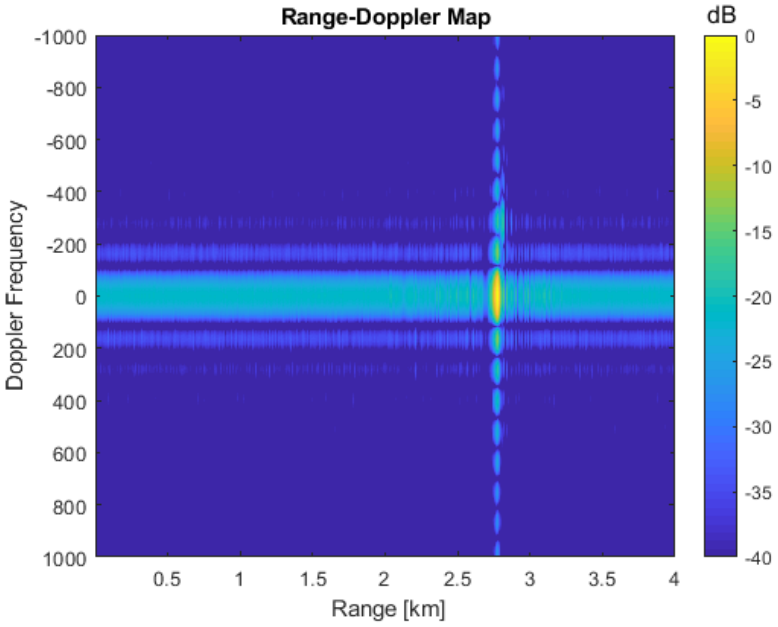

(a) Range-Doppler map for the target moving away from the radar

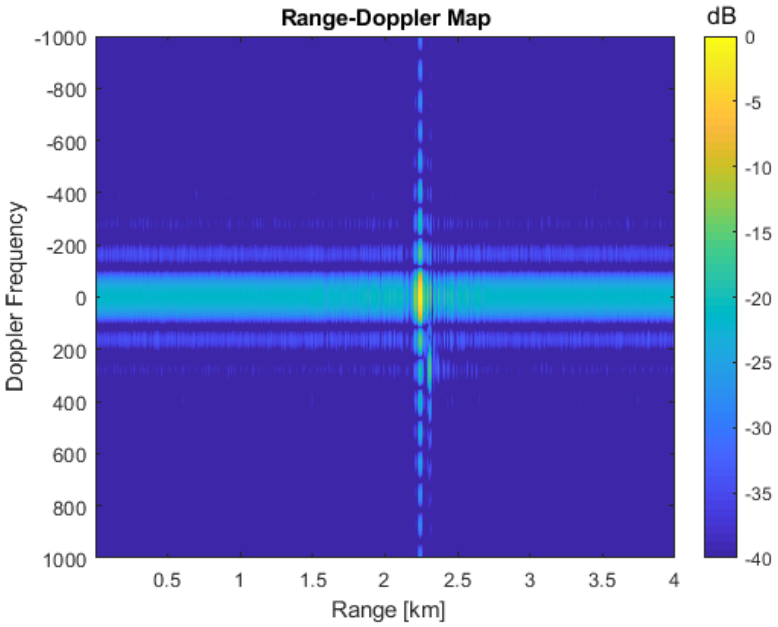

(b) Range-Doppler map for the target moving towards the radar

Figure 5.6: Results for the monostatic configuration. Top: Range-Doppler map for the target moving away from the radar. Bottom: Range-Doppler map for the target moving towards the radar

transmitter and receiver antenna. The direct signal (and its effect) can be reduced by physically steering the antennas so that the transmitter falls in a null or low sidelobe of the receive antenna. In this experiment, the direct signal was removed by applying mean value removal. Mean value removal was applied to remove zero Doppler before the FFT used to form the range-Doppler map.

Figure 5.7 shows a range-Doppler map for the target moving away and towards the radar after mean value removal. Figure 5.7a shows the target moving away from the radar with the Doppler shift -273.4 Hz. For the target moving towards the radar in Figure 5.7b, it was shown that target was detected at the positive Doppler of 268.6 Hz. This compares well with the theoretical value of 333.3 Hz. As per Chapter 4, errors could be from car speed with the car speedometer and the sample trigger.

Note that the direct signal was removed after mean value removal. It can be seen in the figure that zero-Doppler removal successfully extracts the target from the range-Doppler map. After mean value removal, the straight line induced by the direct signal along the Doppler frequency next to the detected target can still be seen. The distance between the detected Doppler frequency and the straight line can be used to approximately determine target distance. This can be shown in the range-cut plot of the target. But, before that, the straight line need to be filtered out by applying windowing approach. This was done by applying a Hamming window in the Doppler domain by windowing each of the slow-time columns and range bin.

Figure 5.8 shows the results after windowing was applied. It can be seen that after windowing, the contributions from the sidelobes and the hardware imprecisions was reduced. The SNR for the target moving away from the radar is found at 35.4

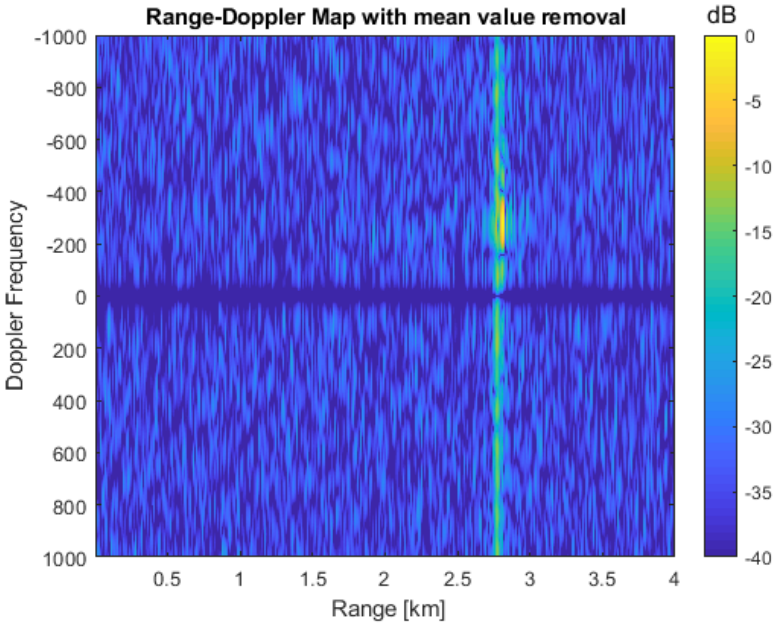

(a) Range-Doppler map for the target moving away from the radar after mean value removal

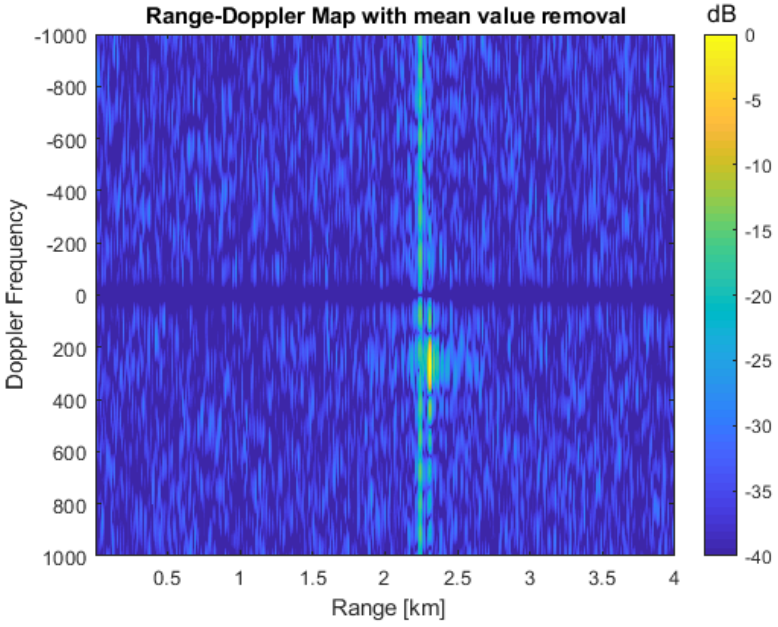

(b) Range-Doppler map for the target moving towards the radar after mean value removal

Figure 5.7: Results for monostatic configuration after mean value removal

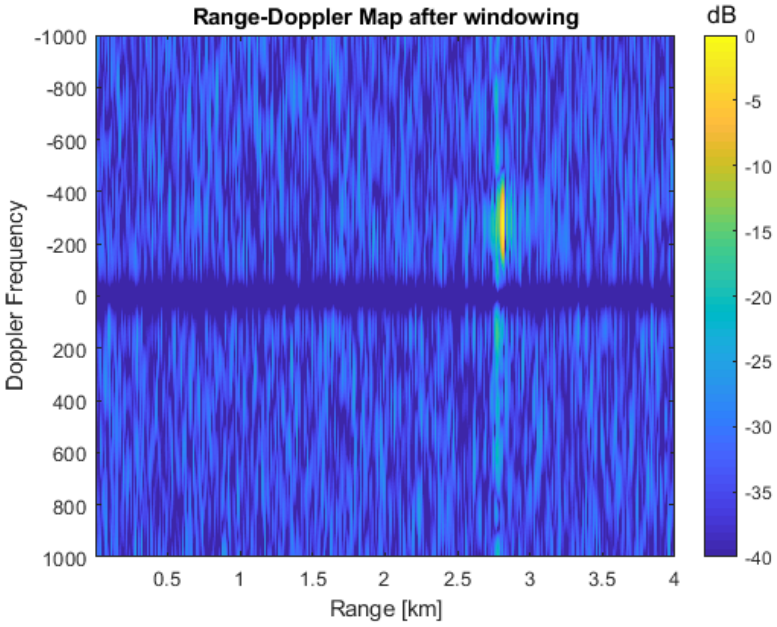

(a) Range-Doppler map for the target moving away from the radar after windowing

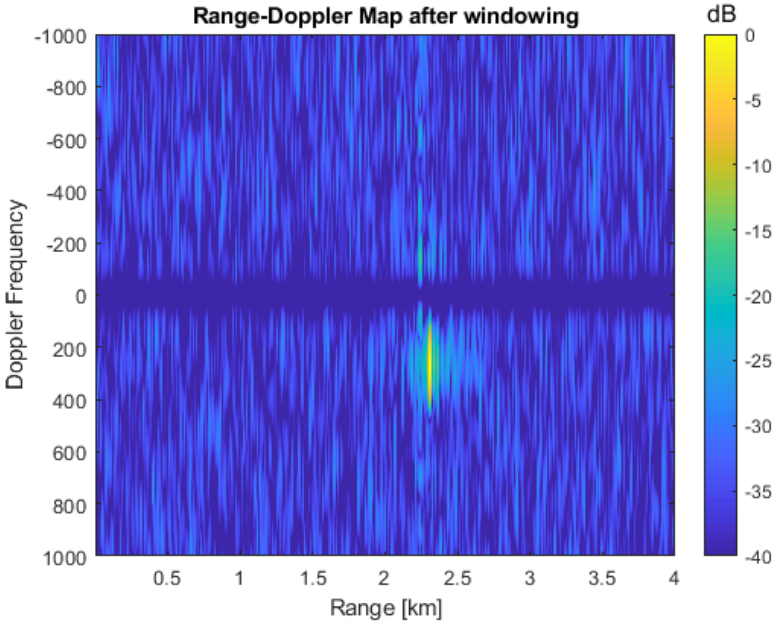

(b) Range-Doppler map for the target moving towards the radar after windowing

Figure 5.8: Results for monostatic configuration after windowing

dB whereas the SNR for the target moving towards the radar is at 37.6 dB. The Doppler frequency induced by the target was also shown in Doppler-cut plot in Figure 5.9.

From the range-cuts shown in Figure 5.10, both figures shows that there were two peak responses at different distance. In Figure 5.10a, the distance between the two peaks is 27 m whereas in Figure 5.10b, the distance between the two peaks is 60 m. These values agree with the distance between the target and radar during the measurement. There is a difference in distance for target moving towards and away from the radar. This is due to the difference when the target was recorded in the radar which was triggered manually. The focus of this experiment was to test the receiver prototype before running out the important bistatic trials.

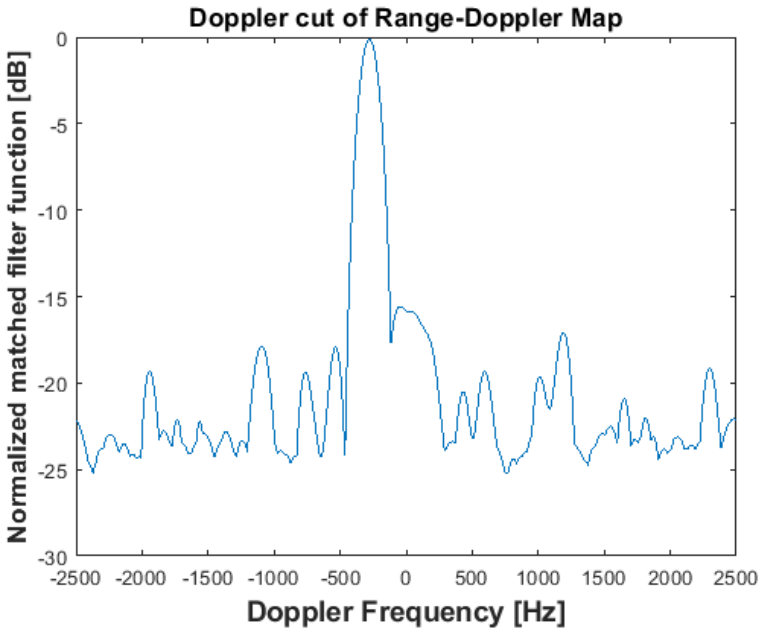

(a) Doppler-cut for the target moving away from the radar after windowing

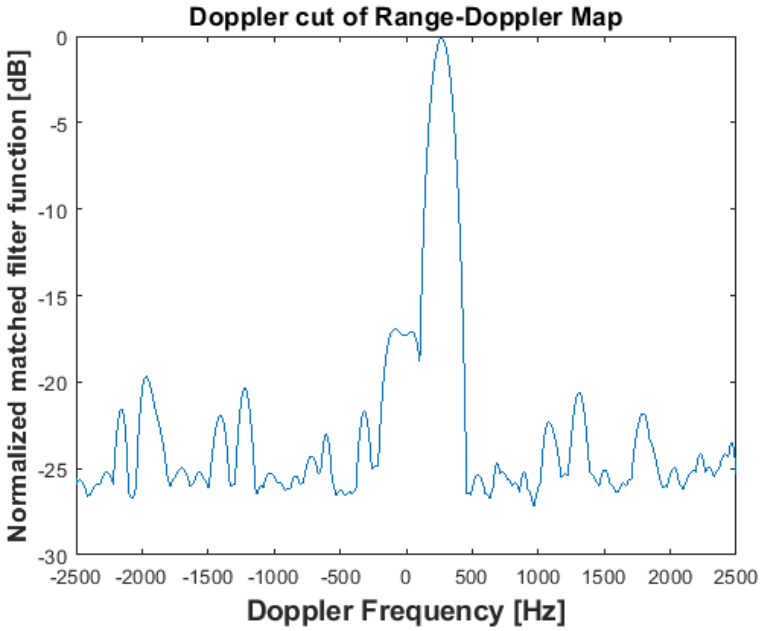

(b) Doppler-cut for the target moving towards the radar after windowing

Figure 5.9: Doppler-cuts for monostatic configuration after windowing

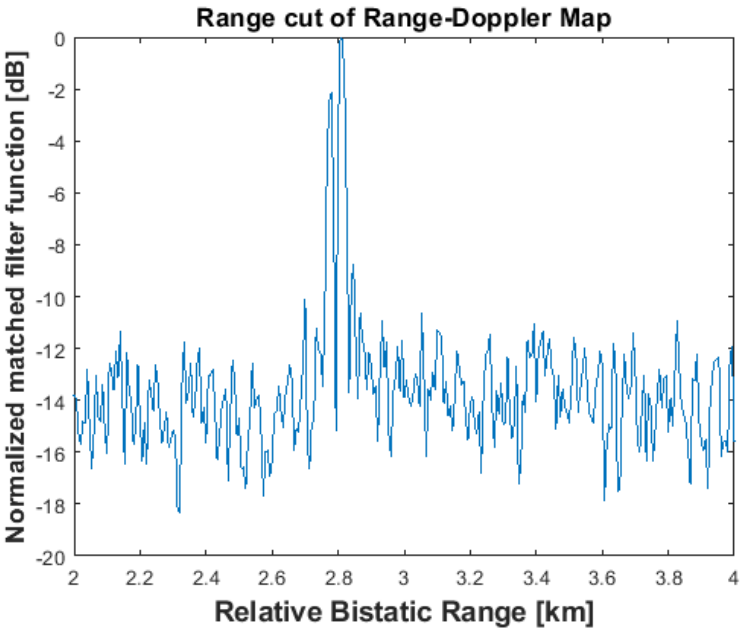

(a) Range-cut for the target moving away from the radar after windowing

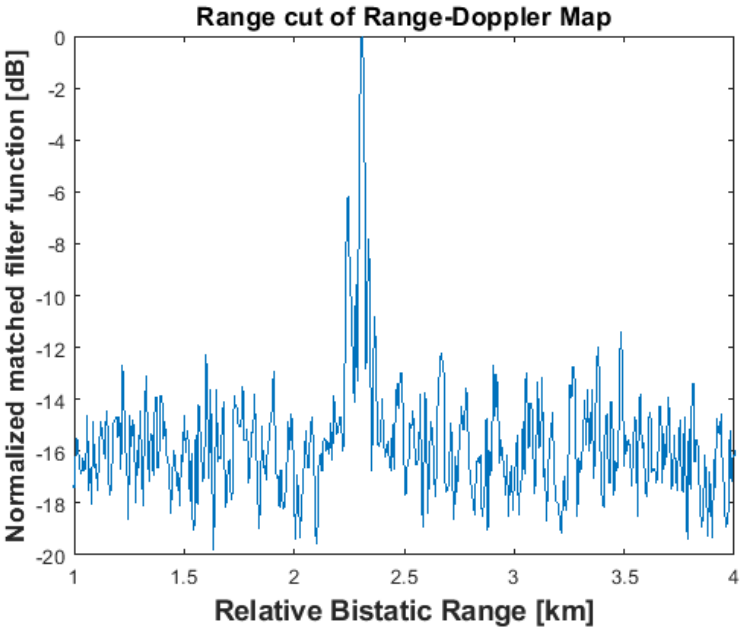

(b) Range-cut for the target moving towards the radar after windowing

Figure 5.10: Range-cuts for monostatic configuration after windowing

5.3.2 Bistatic Configuration

In the bistatic experiment, the parameters were the same used in the monostatic experiment and given in Table 5.1. A car with velocity at 11.5 m/s (24.6 mph) was used as the moving target. The experiment was conducted with target moving in two directions with respect to the transmitter and the receiver. The passive receiver worked independently with the transmitter. Again, a mostly empty car park was used in order to reduce the clutter.

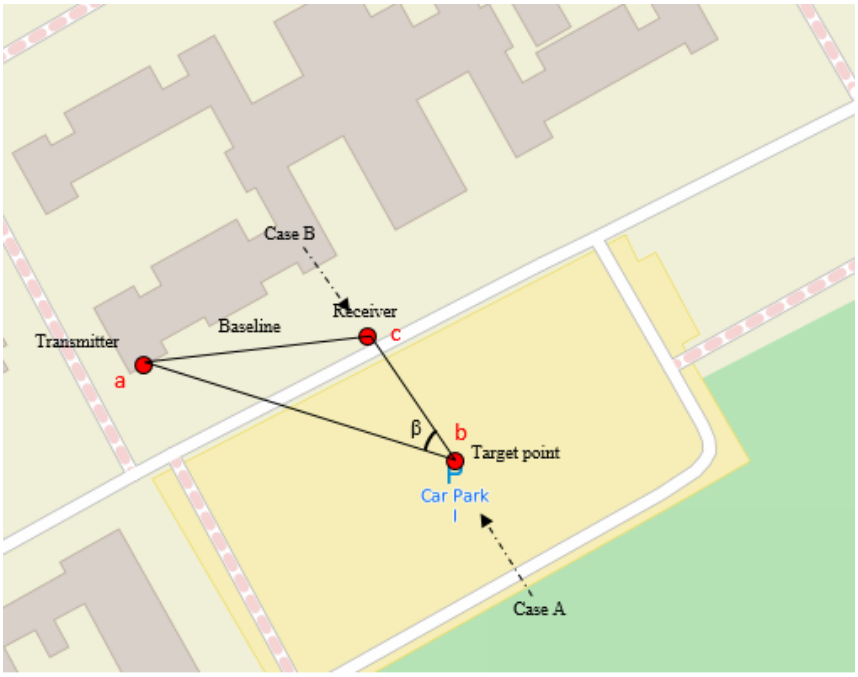

Figure 5.11: Bistatic configuration that shows directions of the target

The geometry of the bistatic experiment is shown in Figure 5.11. In this experiment, two USRPs were used, one located at the transmitter and one at the receiver. The receiver and the transmitter were independently deployed as two different platforms to allow passive bistatic measurements. The figure shows the location of the transmitter (a), the receiver (c), and the target point (b). The distance between

the transmitter and the receiver (baseline distance) remained constant at 44.8 m. The measurement was manually triggered when the target reached the maximum velocity at the target point (b). The transmit signal was a series of Linear Frequency Modulated (LFM) pulses with constant amplitude, bandwidth B and pulse width τ as described in Equation 5.2. Due to the removal of a reference channel, there will be no range information about the detected target. There is no absolute range in the results due to no synchronisation from the reference channel. However, with the pulse compression applied in the processing, it is possible to retrieve the range resolution and resolve target in range.

The formula used to obtain the bistatic angle was presented in Equation 4.3 in Chapter 4 and that to obtain the bistatic Doppler shift in Equation 3.42 in Chapter 3. Based on the geometry in Figure 5.11, the bistatic angle found at the target point (b) was 32.18°. This was used as a reference point to calculate the expected Doppler shifts for the target. The relative velocity angle δ, which depends on the direction of the target, was calculated using Equation 3.42. In case A, the target was moving towards the transmitter and the receiver with δ equal to 32.18° and inducing a positive Doppler shift. For case B, the target moving away from the transmitter and the receiver with δ equal to -212.18° inducing a negative Doppler shift. The expected Doppler shifts were calculated as in Equation 3.42. For the target moving away from the radar it was -298.2 Hz and for the target moving towards the radar it was 298.2 Hz.

The experiments started with the measurement of a stationary target to ensure the passive radar receiver was working correctly. The results are shown in Figure 5.12. In the figure, there is a Doppler displacement which should not be there because there is no velocity induced from the stationary target. Even with zero

Doppler removal, the point is still there and when the measurement was repeated, it had moved to a different range. This Doppler displacement is random and it will have moved again for the measurement of the moving target. This Doppler displacement occurred due to the frequency offset caused by non-ideal properties of the independent transmitter and receiver designs and in particular an independent LOs. With this Doppler displacement having been noted, the experiment was continued with the moving target. The results for these two cases is shown in Figure 5.13.

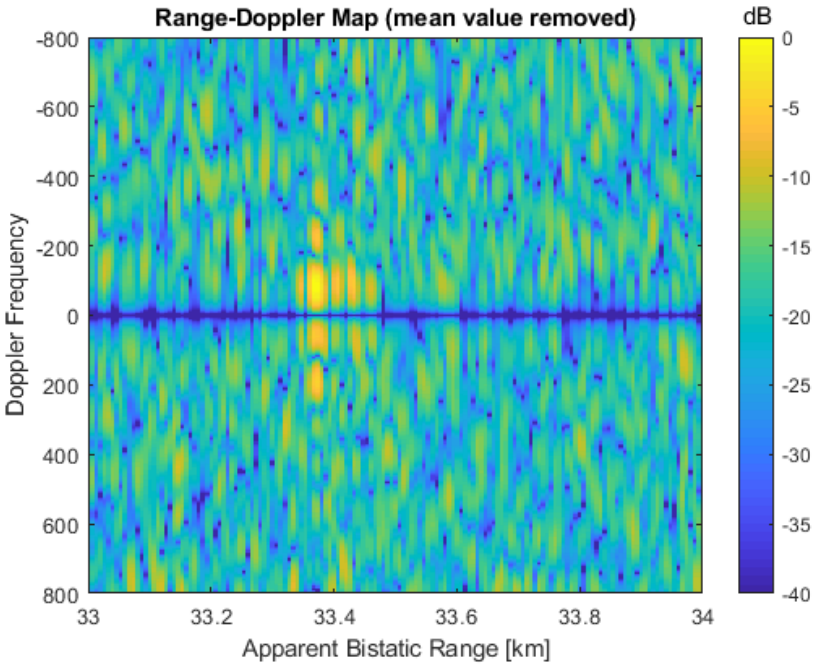

Figure 5.12: Bistatic Configuration: Stationary target

Figure 5.13a, shows the result relative to the target moving towards the radar, with two non-zero-Doppler detections at 219.7 Hz and -92.8 Hz. Similarly, Figure 5.13b shows the results for the target moving away from the radar and two detections are again in the range-Doppler map at -405.3 Hz and -112.1 Hz. In these results, the mean value was removed from the data. The Doppler-cut was plotted to show all detections that appeared in the range-Doppler map.

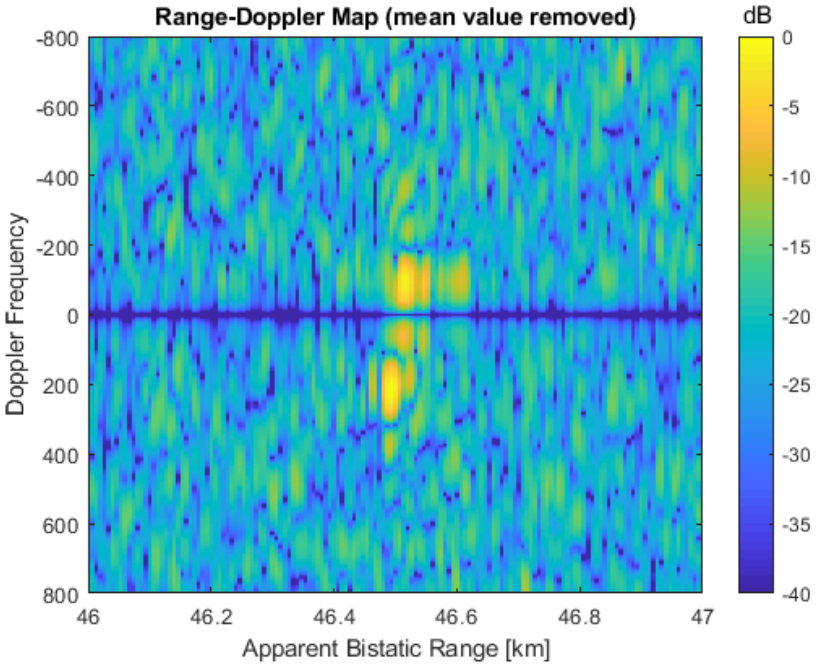

(a) Case A: Target moving towards the receiver

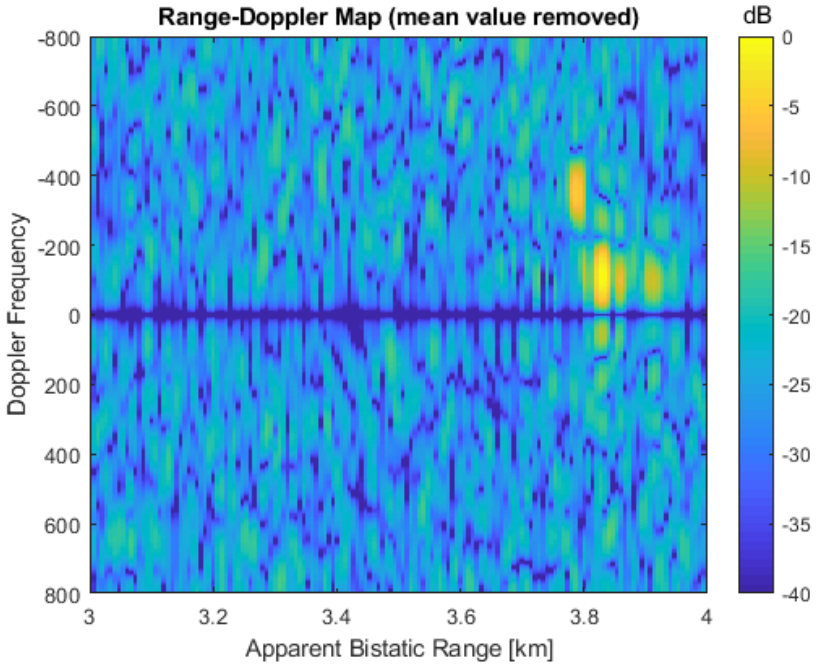

(b) Case B: Target moving away from the receiver

Figure 5.13: Results for bistatic configuration for the target moving towards the receiver and target moving away from the receiver

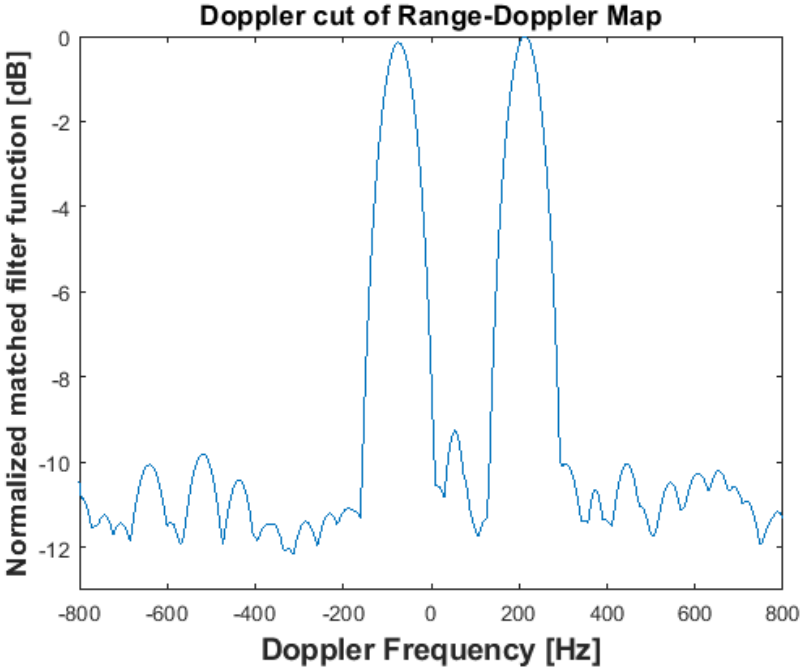

(a) Doppler-cut for target moving towards the receiver

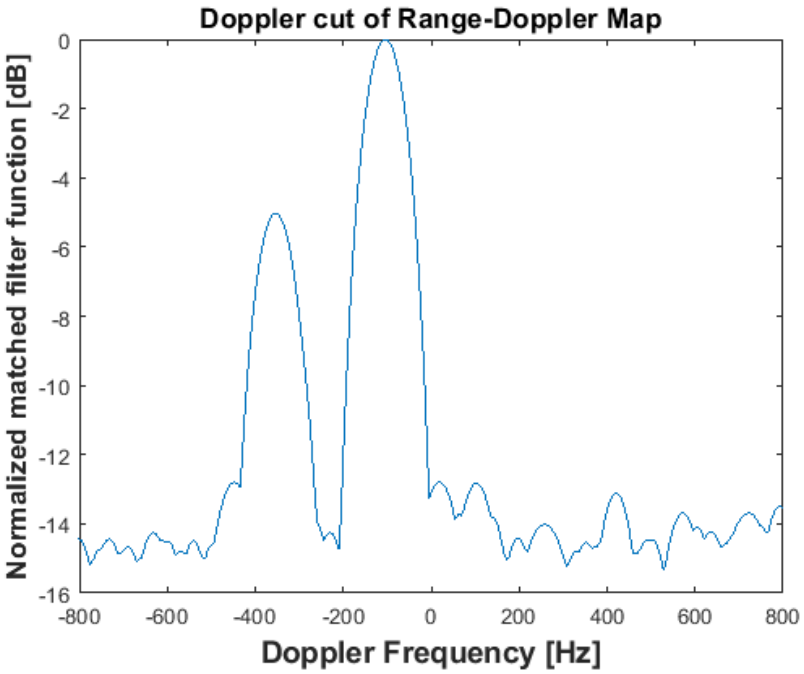

(b) Doppler-cut for target moving away from the receiver

Figure 5.14: Doppler-cuts for the target moving towards and away from the receiver

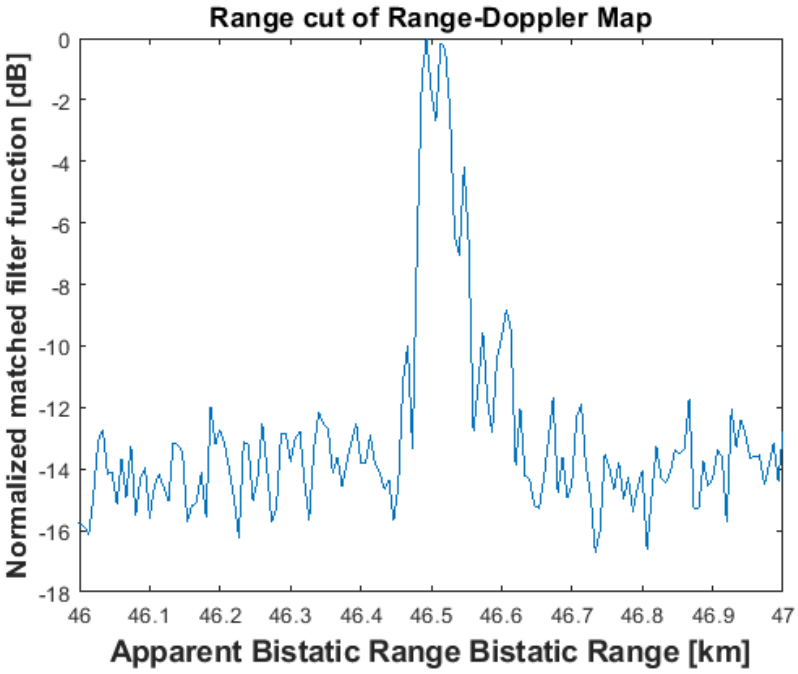

(a) Range-cut for target moving towards the receiver

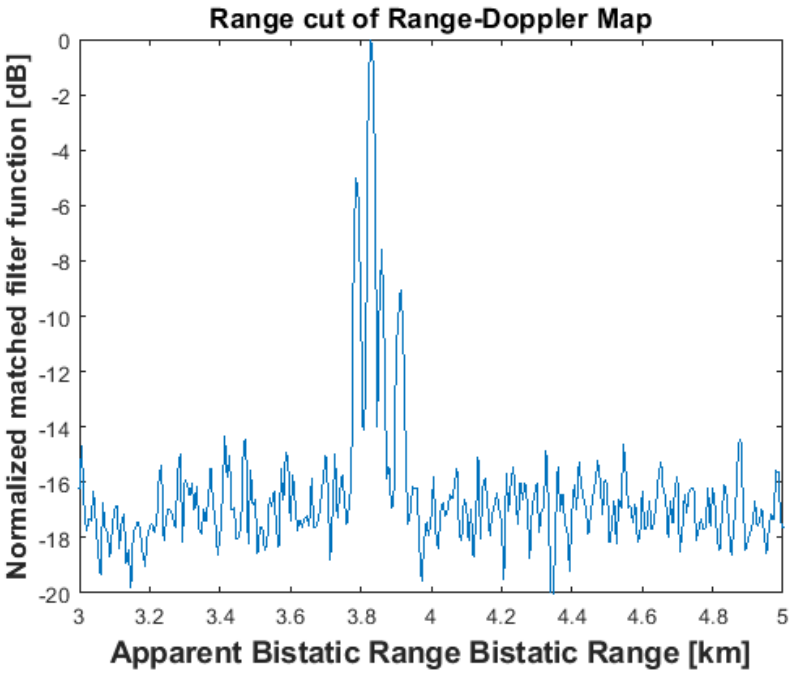

(b) Range-cut for target moving away from the receiver

Figure 5.15: Range-cuts for the target moving towards and away from the receiver

In both cases, there are two non-zero-Doppler detections despite only one target was moving during the recordings, as shown in Figure 5.14. One detection is relative to the moving target's Doppler frequency and the other is a phantom target (offset) resulting from the system. This is due to a non-coherency between the local oscillator (LO) at the transmitter and that at the receiver and, in this thesis, will be referred to as the Carrier Frequency Offset (CFO). The frequency offset does not appear in conventional passive radar employing a reference channel, because the reference signal is used to down-convert the surveillance signal, but it is unavoidable in single-channel passive radar technology where the transmitter and the receiver are inherently independent.

In addition, the range-cut was plotted shown in Figure 5.15. Both cases shows that the mainlobe was suffered with the clutter. Figure 5.15a shows that there is two peaks whilst Figure 5.15b shows that the there were sidelobes appeared around -5 dB.

Various measurement were carried out to map the offset behaviour with stationary targets, such as that shown in Figure 5.12, and it was found that the frequency Doppler offset varied between each acquisition. The frequency offset shifts the real value of the target Doppler frequency and needs to be taken into account and subtracted from the results to acquire the real target Doppler frequency. So, the Doppler frequency of the target moving towards the radar is 312.47 Hz (as expected a positive Doppler) whereas for the target moving away from the radar it is -293.2 Hz. Due to the removal of the reference channel, the bistatic range cannot be measured and the bistatic range shown in the results are noted as apparent bistatic range. A summary of the results is shown in Table 5.2.

Table 5.2: Results of the experiments

Direction of the target	Doppler detected (A)	CFO (B)	Final Doppler Value (A-B)
Towards the radar	219.7 Hz	-92.8 Hz	312.5 Hz
Away from the radar	-405.3 Hz	-112.1 Hz	-293.2 Hz

Based on the result from Table 5.2, the experimental Doppler frequency detected for the car moving towards the radar (case A) is 312.5 Hz and for the car moving away from the radar (case B) it is -293.2 Hz. The theoretical Doppler frequency calculated for both cases is 298.2 Hz for case A and -298.2 for the case B. The percentage error calculated for case A is 4.8% and for the case B is 1.7%. This result shows very close agreement with the expected theoretical values.

5.4 Carrier Frequency Offset

The Carrier Frequency Offset (CFO) is caused by non-ideal properties of the independent transmitter and receiver designs. These include sampling clock offset, power amplifier noise, phase noise and non-linearities linearity. This phenomenon is due to a frequency mismatch between the transmitter and the receiver local oscillators (LO) which are independent in single channel passive radar solutions that exploit radar signals of opportunity. The USRP used in this study experienced CFO because the LO used for down-conversion in the receiver was not synchronized with the carrier signal of the transmitter to emulate a single-channel passive radar scenario. The frequency offset inevitably upsets the Doppler measurements and leads to mismatch between the experimental and theoretical values of the target's Doppler.

Figure 5.16 shows the block diagram of a single-channel passive radar. As signals

are transmitted over the transmission path, they will experience an attenuation due to path loss and will arrive at the receiver after a propagation delay. Therefore, the received signal is the delayed version of the transmitted signal $S_T(t)$ and can be expressed as $S_R(t)$. In the receiver, the received signal is down-converted in the mixer using the LO, to recover the information of the signal. In the case of a monostatic or passive radar with reference channel, the recovered version of the received signal would be down-converted with respect to one reference LO only. In Figure 5.16, the term $e^{-j2\pi\theta_o(t)}$ and $e^{-j2\pi\theta_1(t)}$ represent the non-ideality of the system which results in the frequency offset.

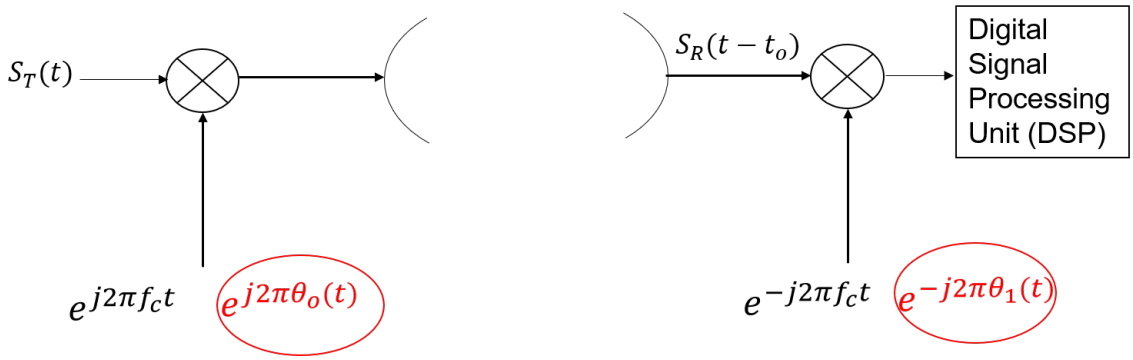

Figure 5.16: Block Diagram of a mixer at a transmitter and a receiver

The phase difference between the LO around the nominal carrier frequency creates the frequency offset in the USRP which leads to the frequency shift in the received signal. The transmitted signal can be expressed as:

$$S_T(t) = a(t)e^{j2\pi f_c t}e^{j2\pi\theta_o(t)} \tag{5.4}$$

where $a(t)$ is the complex envelope of the pulsed signal with an amplitude of 1. In equation 5.4, the term $\theta_o(t)$ is a non-ideal phase contribution that depends on the

time t which can be approximated by a first order Taylor expansion expressed as

$$\theta_o(t) = \theta_o + \theta_o^{'} t + \frac{\theta_o^{''}}{2} t^2 \tag{5.5}$$

By rearranging the equation, the final transmitted signal will be

$$S_T(t) = a(t) e^{-j2\pi(f_c + \theta_o^{'})t} e^{-j2\pi\theta_o} e^{-j\pi\theta_o^{''} t^2} \tag{5.6}$$

From equation 5.6, the carrier frequency is added with the offset $\theta_o^{'}$ from the LO and this term shifts the measured Doppler frequency. The term $e^{j\pi\theta_o^{''} t^2}$ will be neglected in this calculations.

At the receiver side, the received signal with the delay before the mixer is expressed as below

$$S_R(t - t_0) = a(t - t_0) e^{j2\pi(f_c + \theta_o^{'})(t - t_0)} e^{-j2\pi\theta_o} \tag{5.7}$$

Because,as shown in Figure 5.16, the system uses a separate LO at the receiver, the LO for the mixer is given as

$$LO_{signal} = e^{-j2\pi f_c(t)} e^{-j2\pi\theta_1(t)} \tag{5.8}$$

and applying Taylor expansion at the term $\theta_1(t)$ yields to

$$\theta_1(t) = \theta_1 + \theta_1^{'} t + \frac{\theta_1^{''}}{2} t^2 \tag{5.9}$$

Multiplying this term and the carrier frequency with the delayed signal in the mixer

leads to the equation below

$$S_R(t-t_0) = a(t-t_0)e^{j2\pi f_c t_o}e^{j2\pi\theta_o^{'}(t-t_o)}e^{j2\pi\theta_o}e^{-j2\pi\theta_1}e^{-j2\pi\theta_1^{'}t} \tag{5.10}$$

Simplifying this equation, gives

$$S_R(t-t_0) = a(t-t_0)e^{j2\pi f_c t_o}e^{j2\pi(\theta_o-\theta_1)}e^{j2\pi(\theta_o^{'}-\theta_1^{'})t}e^{-j2\pi\theta_o t_o}e^{-j2\pi\theta_1 t_o} \tag{5.11}$$

From equation 5.11 the frequency offset can be estimated from the term $e^{j2\pi(\theta_o^{'}-\theta_1^{'})t}$ as

$$f(t) = \frac{1}{2\pi}\frac{d\phi(t)}{dt} \tag{5.12}$$

where $\phi(t) = 2\pi(\theta_o^{'}-\theta_1^{'})t$ and this leads to the frequency offset expression as below

$$CFO = \theta_o^{'}-\theta_1^{'} \tag{5.13}$$

The frequency offset occurred randomly over time t and hence changed every time the data was taken. Based on the algorithm proposed above, the results from the experiment can be corrected by applying an additional down-conversion, here referred to as DC conversion, following the estimation of the CFO. The CFO can be used by using stationary scatterers in the scene or a leakage of the direct signal from the transmitter through the receiving antenna sidelobes.

Figure 5.17 shows the results after DC conversion. Note that there are two responses with respect to Figures 5.17a and 5.17b. It can be seen one of the response is now at zero-Doppler. This response is the frequency offset which results from DC conversion. This offset was removed as follows. Firstly, the frequency corresponding to the highest peak in the range-Doppler map (assuming the contribution of the

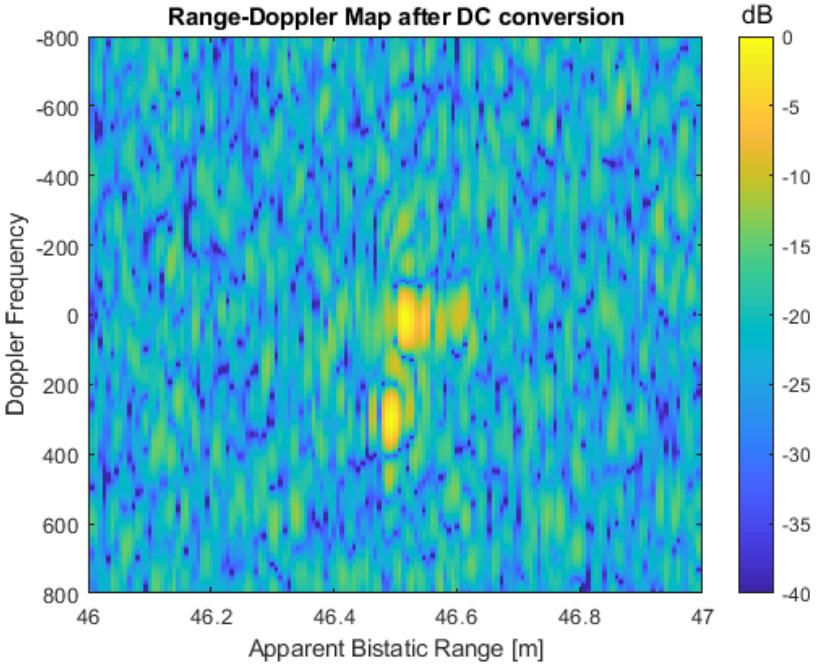

(a) Target moving towards the radar after DC conversion

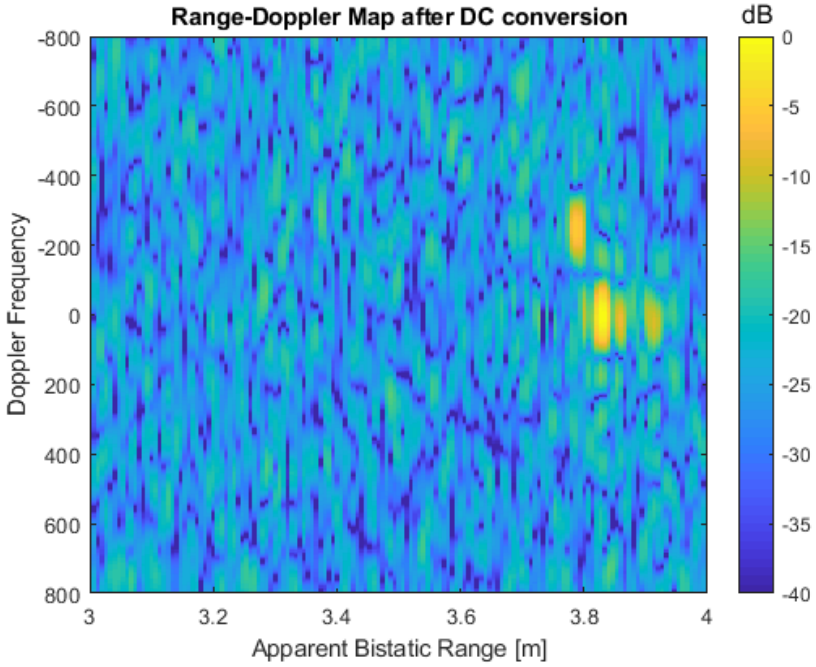

(b) Target moving away from the radar after DC conversion

Figure 5.17: Results for bistatic configuration after DC conversion

direct signal or stationary clutter is stronger than the target) in the first result of target detection was found. Then, the DC conversion was done by down-converting the first result in the time domain using this frequency. After the DC conversion, the mean value was removed so that only Doppler from the target echo remains.

Figure 5.18 shows the results after DC conversion after mean value was removed. Results shows the frequency offset was successfully removed and only the point indicating the target detection was left in the figures. It was also shown in the Doppler-cut plots shown in Figure 5.19. The final Doppler detected for the target moving towards the radar is 302.7 Hz and for the target moving away from the radar is -244.1 Hz. This result was closed to the final experimental results shown in Table 5.2. This results validates the DC conversion to remove CFO appeared in moving target detection. The range-cuts was also shown in Figure 5.20. As mentioned before, the bistatic range found in the target detection is an apparent bistatic range. This is due to the removal of a reference channel.

Target detection performance was evaluated by calculating the signal-to-noise-ratio (SNR). This was calculated from the range-Doppler data as the ratio between the power level of the target and the mean power of the noise. The SNR found for case A, is 22.01 dB and for case B is 25.02 dB.

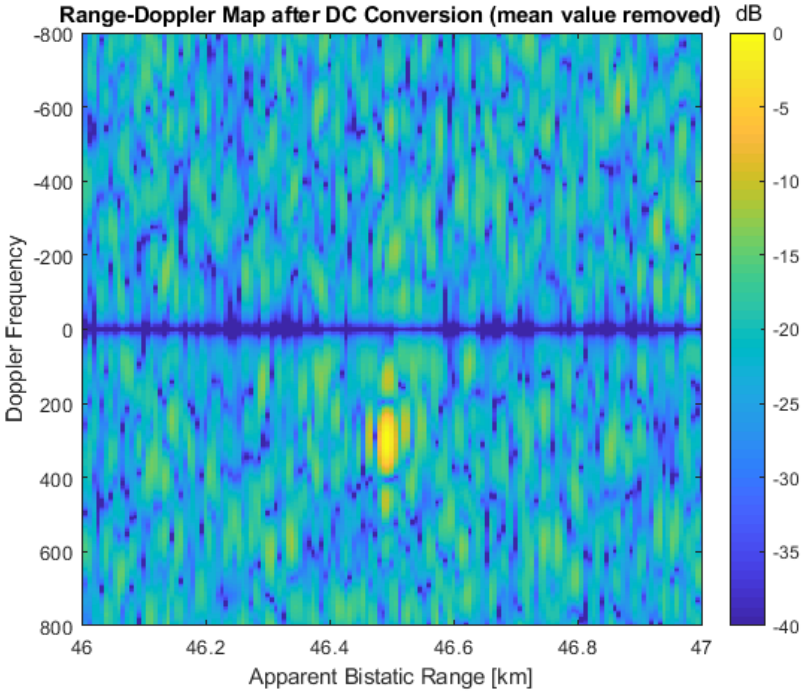

(a) Target moving towards the radar after DC conversion with mean value removal

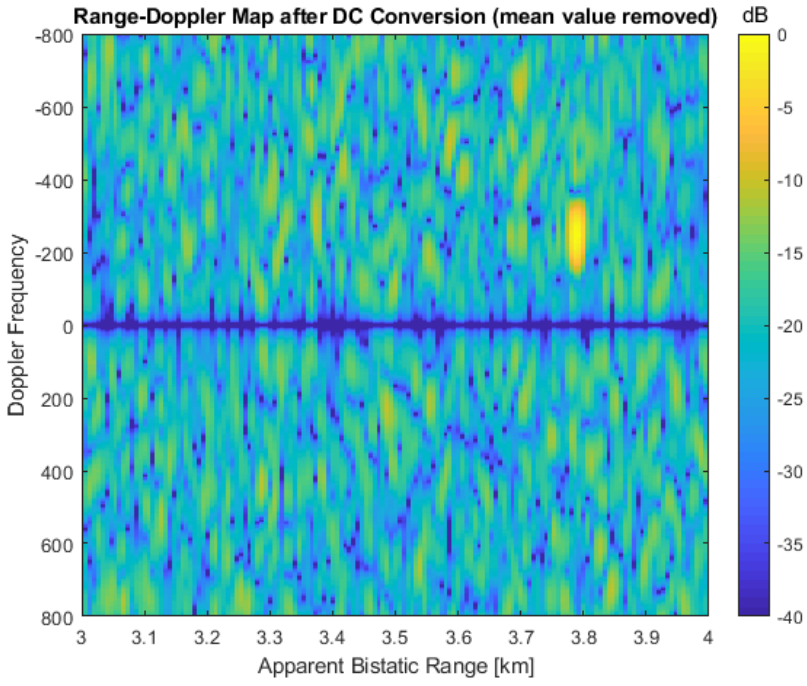

(b) Target moving away from the radar after DC conversion with mean value removal

Figure 5.18: Results for bistatic configuration after DC conversion with mean value removal

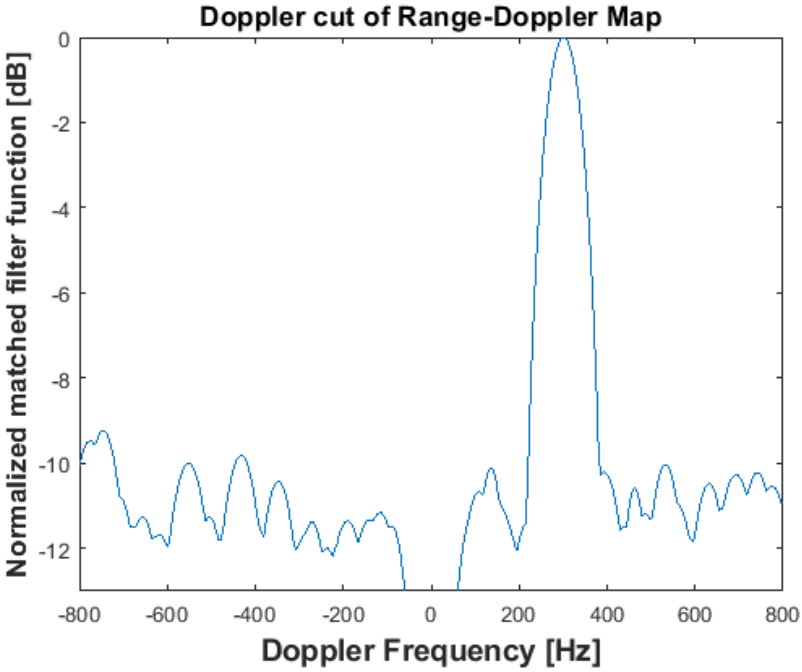

(a) Doppler-cut for target moving towards the radar after DC conversion

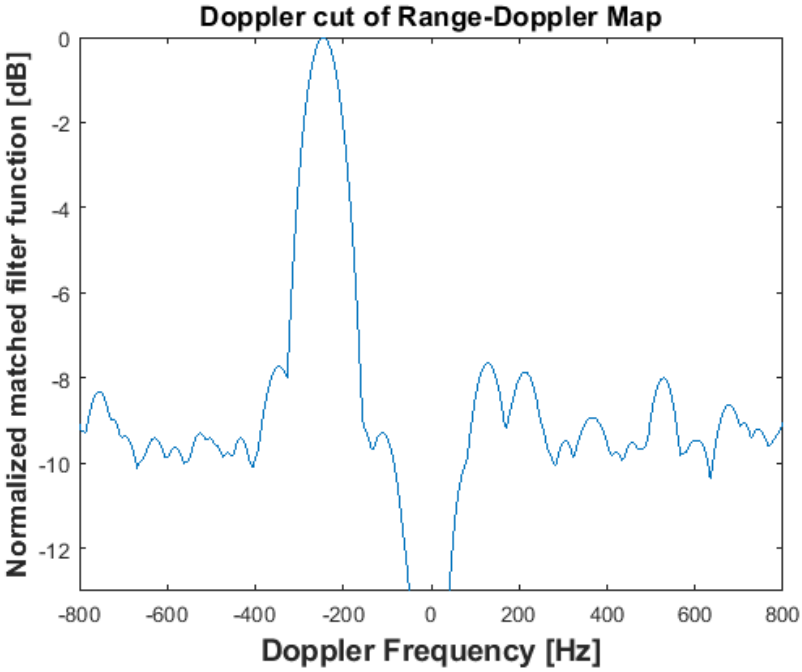

(b) Doppler-cut for target moving away from the radar after DC conversion

Figure 5.19: Doppler-cuts for the target moving towards and away from the radar after DC conversion

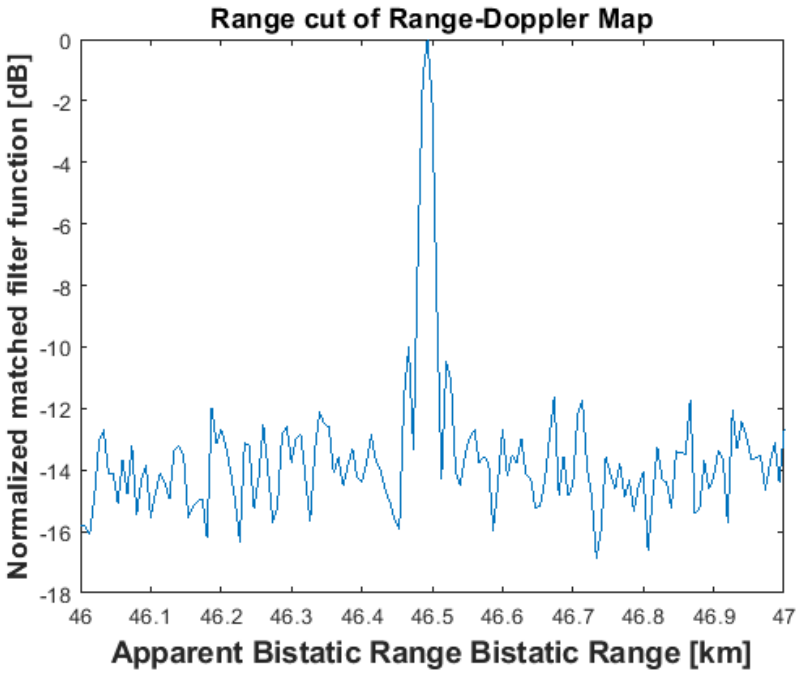

(a) Range-cut for target moving towards the radar after DC conversion

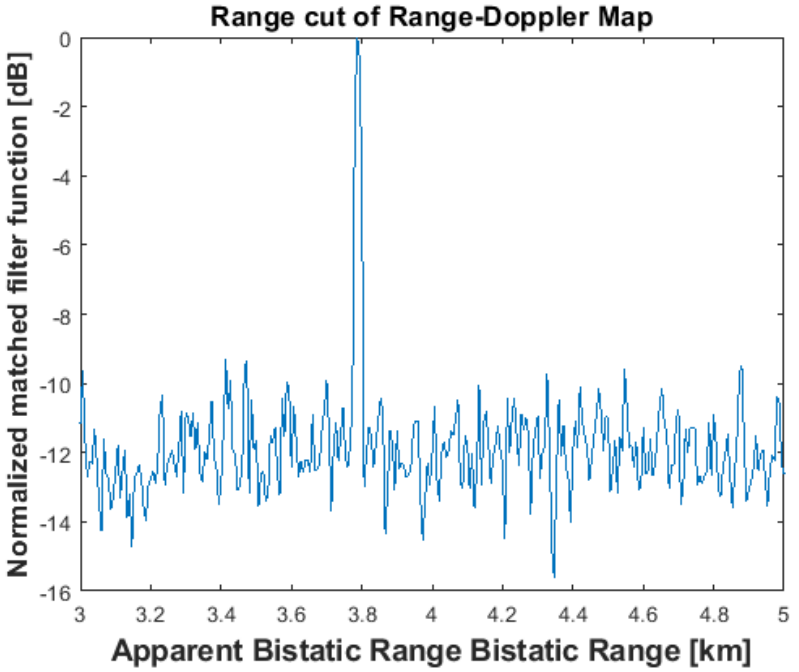

(b) Range-cut for target moving away from the radar after DC conversion

Figure 5.20: Range-cuts for the target moving towards and away from the radar after DC conversion

5.5 Offset Assessment

It was shown in the previous section that the CFO was induced by independent LOs in the single-channel passive radar system. The performance of the radar is directly proportional to the performance of its oscillator [93] because the oscillator must provide precisely controlled sources for frequency conversion. From the results that were presented in the previous section, it was clearly shown that the instability in timing and frequency is due to the oscillator performance. This will have direct effects for a radar detecting and measuring the Doppler shift of the target.

The effect of CFO was assessed in a closed-loop experiment that involved a single USRP and two independent USRPs (i.e. as in the single-channel passive radar) in order to understand how to mitigate this effect. With the single USRP, a Tx and Rx port was connected directly while with two USRPs a Tx port from first USRP was connected to the Rx port on the second USRP. This experiment was carried out to investigate differences in frequency offset with respect to the number of USRPs used and to ensure that the CFO was resulting from the equipment itself.

In this assessment, a continuous transmit signal consisting of 44 LFM pulses was transmitted with a PRI of 0.2 ms, resulting in a 8.8 ms integration time. In the first stage of the experiment, a closed-loop experiment with a single USRP was used in order to observe whether this offset can be found with only one USRP. In the second stage, the experiment was continued with two USRPs in a closed loop connection as previously described. The received signal pulse compression and pulse integration was plotted to show direct relationship between these two.

Figure 5.21 shows the result of the matched-filtering of a single USRP in closed-

loop connection and also the integration of pulses. Note that the integration gain is 43.87 which is very close to the expected gain of 44 (the number of pulses transmitted). This shows that as expected there are no frequency offset effects when only one USRP is used. Figure 5.22 shows the result of the matched-filtering of two USRP in closed-loop connection and the integration of the pulses captured in that setup. This result shows that the system suffered a 10 dB power loss. The difference in the two results is due to the frequency offset and timing accuracy from two different free running oscillators in two different USRPs.

Continuing with further measurement, the effect of CFO can be reduced by providing a reference signals to the REF IN port in both USRPs. This can be done by applying an external 10 MHz reference signal that works by phase locking the two USRPs which makes the reference clock frequency equal to the LO. The REF IN used in both USRPs were supplied from the same source. Figure 5.23 shows the result of applying external reference signal to a single USRP in closed loop configuration. This does not change the power loss from the USRP seen in Figure 5.21. Figure 5.24 shows the result of applying the 10 MHz external input to the two USRPS, and the CFO effect was reduced to a loss of 1 dB. Note that in PBR, due to the separation of the receiver and the transmitter, sharing the same LO is not possible, but these experiments were the key to identifying the causes of the CFO in the experimental data and also show a way to possibly reduce it in future experiments.

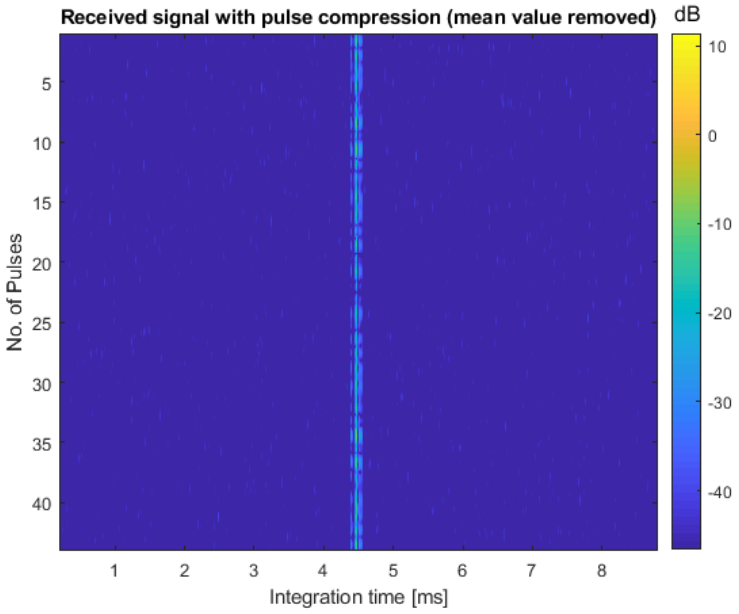

(a) The result of matched filtering of a single USRP in a closed loop connection

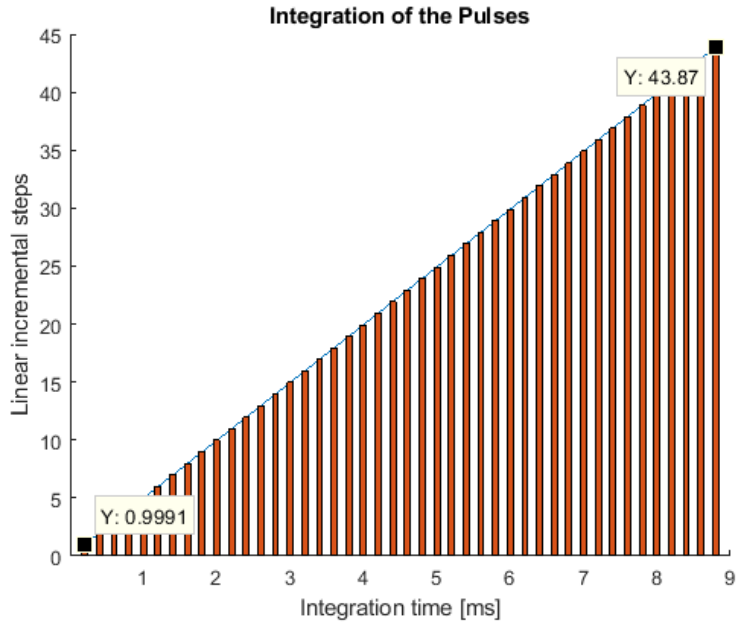

(b) Integration of the pulses captured with a USRP

Figure 5.21: Results for the closed loop experiment using a single USRP

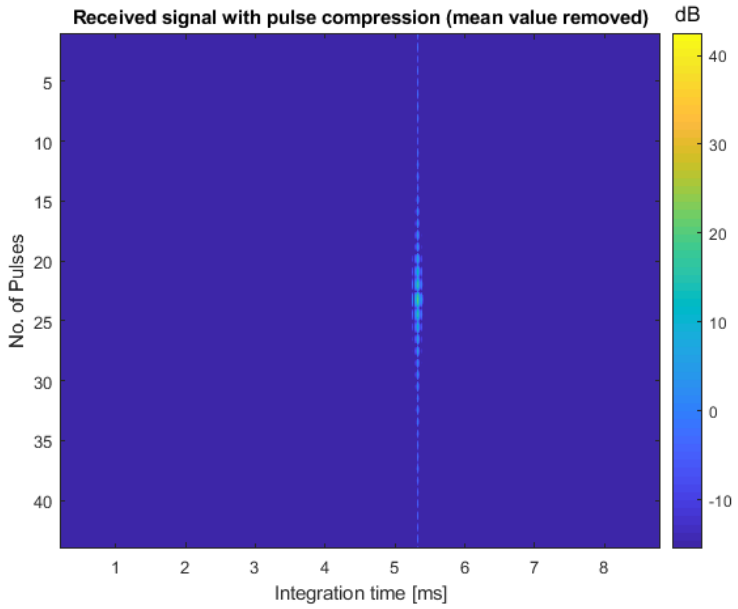

(a) The result of matched filtering of two USRPs in a closed loop connection

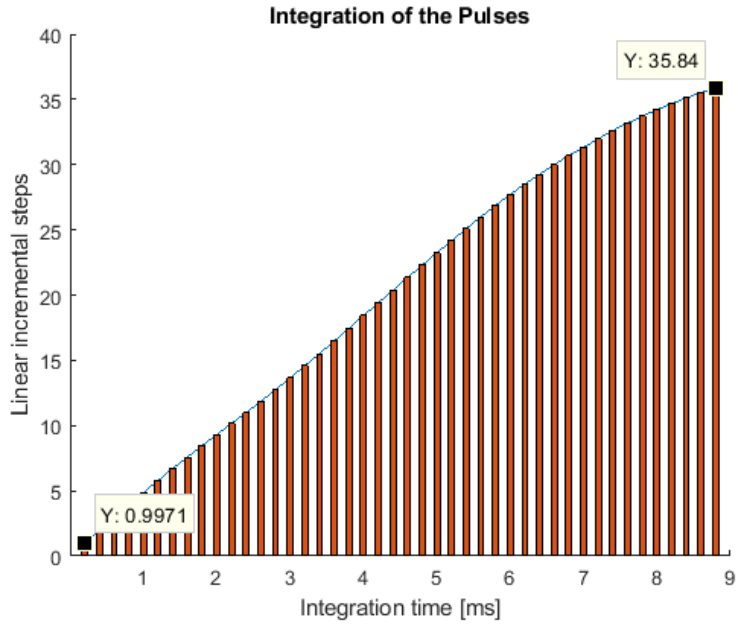

(b) Integration of the pulses captured with two USRPs in a closed loop connection

Figure 5.22: Results for the closed loop experiment with two USRPs

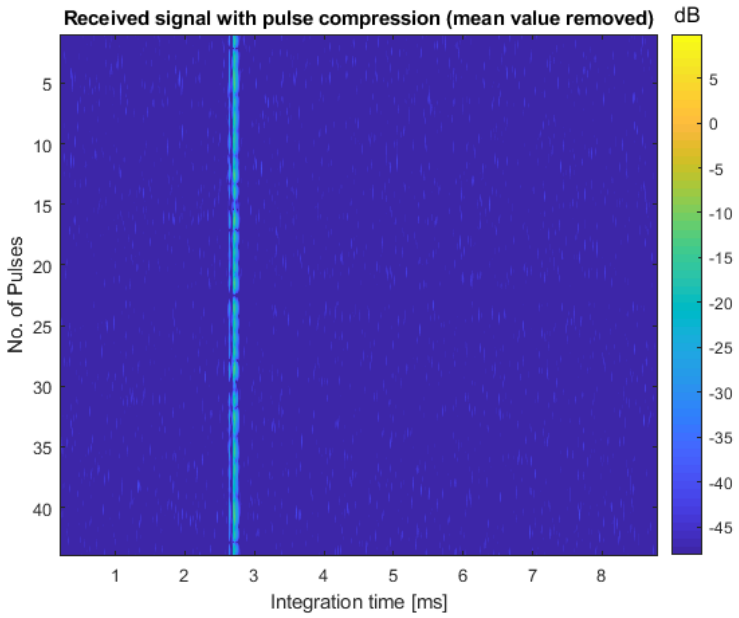

(a) The result of matched filtering of a single USRP in closed loop connection supplied with an external 10 MHz input (mean value removed)

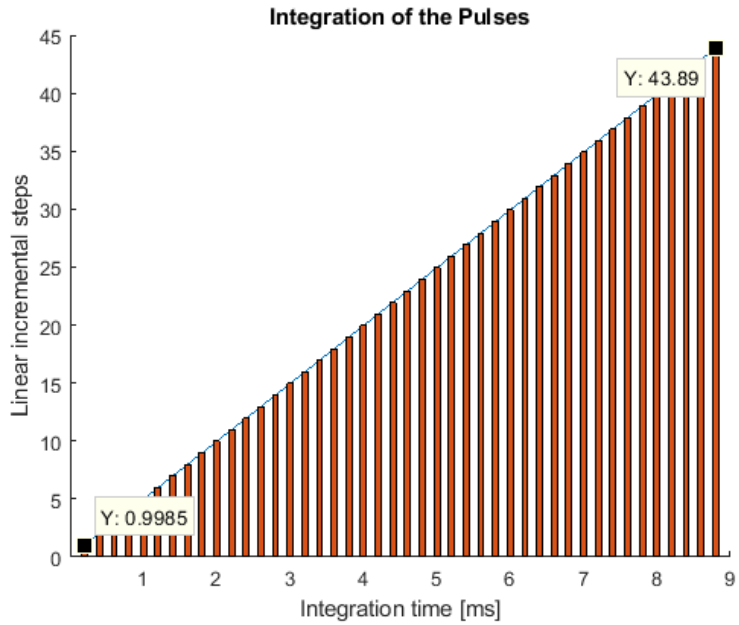

(b) Integration of the pulses captured with a USRP with an external 10 MHz input

Figure 5.23: Results for the closed loop experiment with a single USRP with an external 10 MHz input

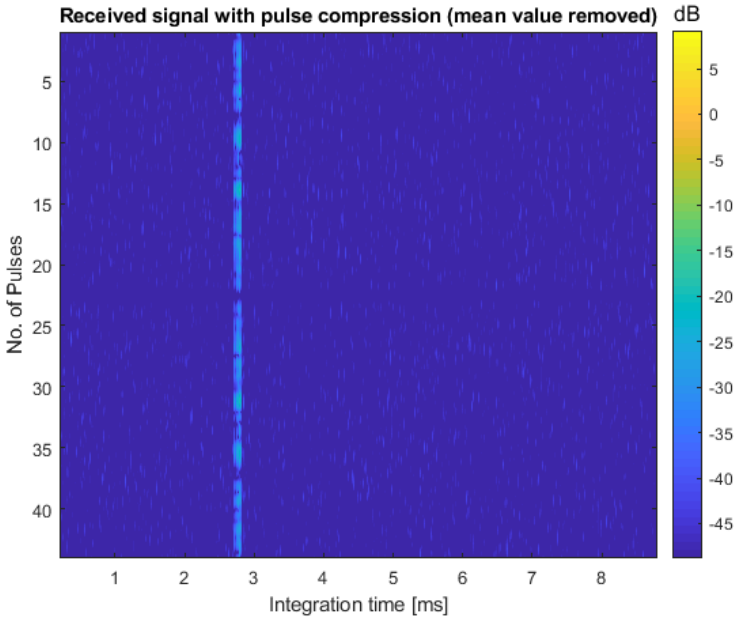

(a) The result of matched filtering of two USRPs in closed loop connection supplied with an external 10 MHz input (mean value removed)

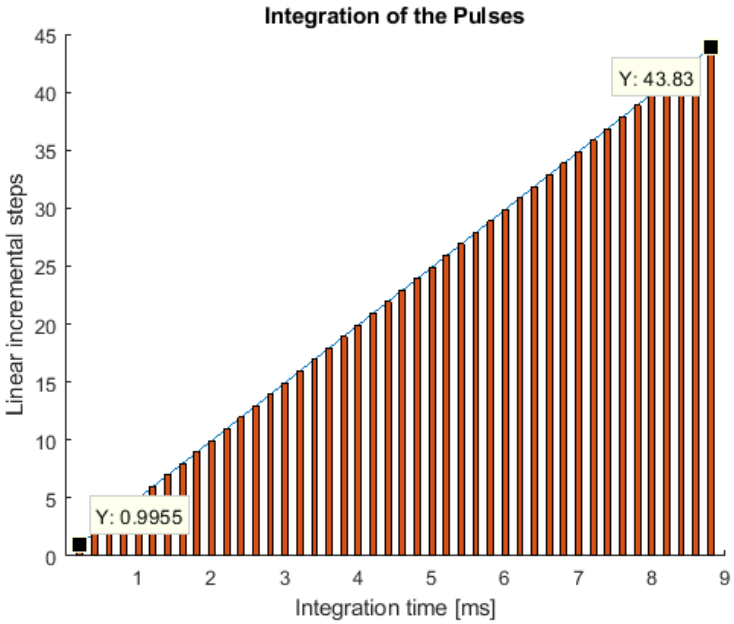

(b) Integration of the pulses captured with two USRPs with an external 10 MHz input

Figure 5.24: Results for the closed loop experiment with two USRPs with an external 10 MHz input

5.6 Summary

This chapter presents the exploitation of deterministic signals for PBR target detection. The low cost passive receiver consisting of a USRP, an antenna and an off-the-shelf host computer was introduced in the experimental campaign. A target was successfully detected when it was moving away from and towards the radar. However, without a reference channel there is no exact range information and may require a priori knowledge of the environment or target, but targets were successfully resolved from the Doppler frequency. Thus, the aim of the experiment to detect a moving target without the use of a reference channel was successfully shown.

From the results, it was found that the system experienced CFO which shifted the measured value of the target's Doppler shift. The CFO is caused by non-coherencies and an unstable independent LOs, which are expected with typical of low-cost SDR in a passive single channel configuration. However, this can be mitigated by applying DC conversion on the results gathered. It was also found that the use of an external 10 MHz reference signal reduced the CFO and thus improved the properties of the received signal. This assessment is important for future experiments where the passive receiver will be supplied with this external 10 MHz reference signal.

Chapter 6

Exploitation of Staring Radar for PBR

In the previous chapter, an experimental study that demonstrated passive bistatic radar (PBR) without the use of a reference channel was presented, and a moving target was successfully detected. In this chapter, the staring Thales-Aveillant Gamekeeper radar is introduced which will be the non-cooperative illuminator of opportunity (IO) at the centre of this thesis. A performance analysis of staring radar together with the results of an experimental campaign will be presented. In the experiments, there are three types of target that will be detected. A person running, a moving car and a flying drone.

6.1 Staring Radar

Conventional radar operates by scanning the field of view with a rotating antenna and concentrating radio beams on a target. An example is the classic Air Traffic Control (ATC) radar system. Due to this operation, a key drawback is that the radar cannot provide continuous target illumination which makes it poorly suited to detecting targets with low RCS and low speed such as drones.

Unlike conventional radar, staring radar looks continuously at a whole volume of space. Depending upon the characteristics of the target returns, the staring radar can characterise, identify and intelligently decide what to do with the echo it receives whilst maintaining constant monitoring of the area. Using a transmitting antenna with a wide beam, the Thales-Aveillant Gamekeeper radar is a staring array radar that provides constant illumination over the entire volume under surveillance [94][95].

The radar operates in L-band with the carrier frequency at 1.25 GHz, a bandwidth of 1 MHz and a PRI of 136 μs. This bandwidth gives a maximum range resolution of 150 m. The staring radar transmits a continuous train of pulses with a low-gain and wide-beam antenna. It constantly provides coverage of a 90° azimuth sector centred around the antenna boresight to an elevation of 30° from the horizontal.

On receive, the multiple digital beams are generated from the data acquired with a digital receiving array. The radar illuminates targets continuously with long integration times up to 1 s and hence can achieve a high Doppler resolution (up to 1 Hz). This enables it to detect small airborne targets with RCS values of 0.01 m^2 up

to range of 5 km with an update rate interval from 0.25 sec to 1 sec [96]. The signal transmitted from the staring radar contains inter-pulse coding to mitigate range ambiguities [97] and to allow target ranging at further ranges [98]. The radar is particularly well suited for exploitation by passive radar system because it provides constant coverage and no need for pulse-chasing.

6.2 Simulated Signal

As mentioned in the previous section, the staring radar transmits pulses with inter-pulse coding. This code needs to be considered when simulating the signal and assess its properties. This is important so that the deterministic properties of the signal are understood to enable target detection without the use of a reference channel. The simulations also shows the influence of a code in AF.

A train of rectangular pulses was firstly analysed in the simulations. For start, the periodic impulse train, $s(t)$ can be written as [99]

$$s(t) = \sum_{m=-\infty}^{\infty} x(t - mPRI) \tag{6.1}$$

where the Fourier transform is

$$S(f) = \sum_{m=-\infty}^{\infty} X(f) e^{-j2\pi f m\mathrm{PRI}} \tag{6.2}$$

The term $X(f)$ does not depend on the summation and thus

$$S(f) = X(f) \sum_{m=-\infty}^{\infty} e^{-j2\pi f m\mathrm{PRI}} \tag{6.3}$$

After applying the equality

$$\sum_{m=-\infty}^{\infty} e^{-j2\pi f m\mathrm{PRI}} = \frac{1}{PRI}\sum_{m=-\infty}^{\infty}\delta\left(f-\frac{m}{PRI}\right) \tag{6.4}$$

Equation 6.3 can be written as

$$S(f) = X(f)\frac{1}{PRI}\sum_{m=-\infty}^{\infty}\delta\left(f-\frac{m}{PRI}\right) \tag{6.5}$$

where $X(f)$ represents the Fourier transform of the Rect pulse of duration τ. Thus, Equation 6.5 can be written as

$$S(f) = \frac{1}{PRI}\sum_{m=-\infty}^{\infty} X\left(\frac{m}{PRI}\right)\delta\left(f-\frac{m}{PRI}\right) \tag{6.6}$$

To obtain a finite duration signal, $s(t)$ is multiplied by a rectangular window of duration T_{int} as shown in Equation 6.7. In the frequency domain, this corresponds to the convolution with a sinc function as in Equation 6.8

$$s(t) = \sum_{m=-\infty}^{\infty} x(t-mPRI)A\,Rect\left(\frac{t}{T_{int}}\right) \tag{6.7}$$

$$S(f) = \frac{1}{PRI}\sum_{m=-\infty}^{\infty} X\left(\frac{m}{PRI}\right)\delta\left(f-\frac{m}{PRI}\right)\bigotimes AT_{int}\,sinc(fT_{int}) \tag{6.8}$$

where A is the amplitude and T_{int} is the integration time of the signal. After applying the convolution to Equation 6.8, the final result for a limited rectangular pulse train in the frequency domain can be written as

$$S(f) = \frac{AT_{int}}{PRI}\sum_{m=-\infty}^{\infty}\tau\,sinc\left(\frac{m\tau}{PRI}\right)sinc\left(T_{int}\left(f-\frac{m}{PRI}\right)\right) \tag{6.9}$$

The relationship in Equation 6.9 shows that the Fourier transform of a limited train

of pulses consists of sinc function occurred every integer multiple of PRF modulated by a wider sinc function that depends on the duration of a single pulse τ.

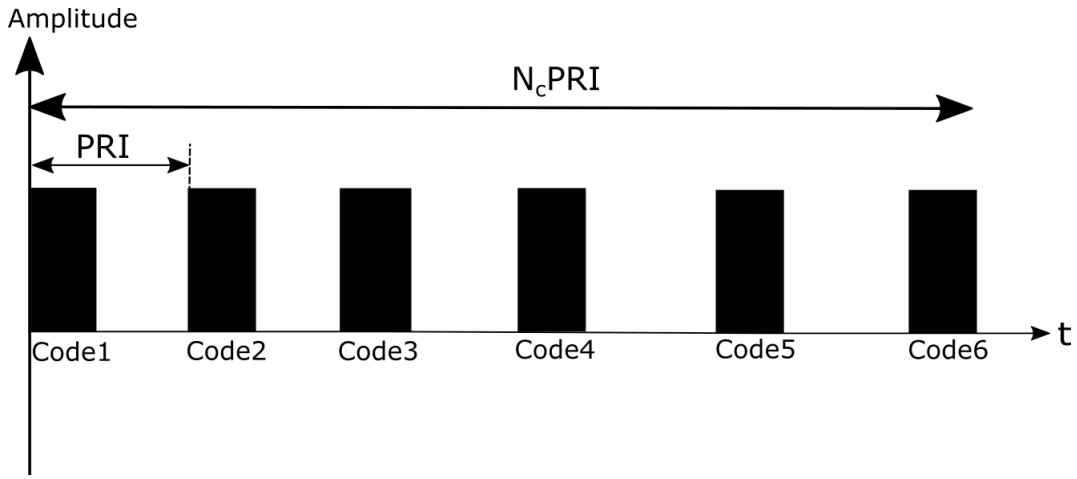

Figure 6.1: The transmit pulse consisting of the inter-pulse coding

The transmit pulse consists of the inter-pulse coding is shown in Figure 6.1. In the simulation, an N_c digit long coded period was generated. The PRF of the radar is known to be 7352.94 Hz, however, because the code repeats itself every N_cPRI the resulting signal periodicity is N_cPRI and the frequency spectrum is the result of interfering lines separated at PRF/N_c. The spectrum of one period of the signal was generated by applying an FFT.

Figure 6.2 shows the Fourier transform of the pulses forming one of two code sections with PRF/N_c. Figure 6.3 shows the spectrum of a full period of the signals. With the two signals summed together, all the lines at integer PRF are cancelled due to destructive interference between the two signal components. This yield to separation between each line at PRF/2.

For the ambiguity function (AF) of this signal, due to the different codes in the signal, care should be taken to ensure cross-correlation of the first pulse with the

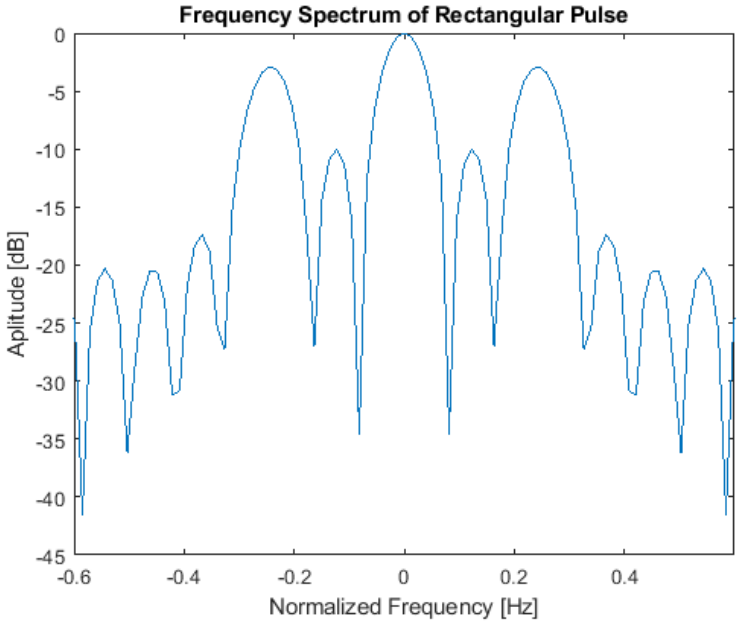

(a) Frequency Spectrum with the first part of code

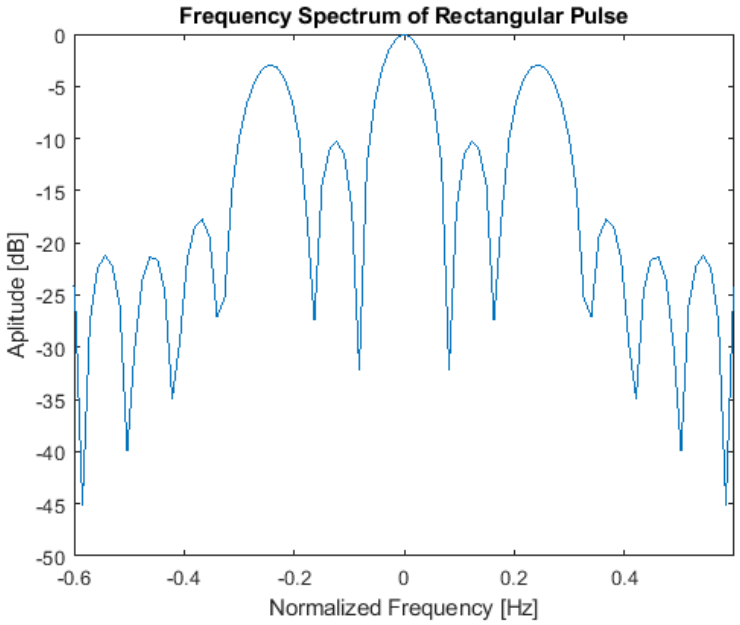

(b) Frequency Spectrum with the second part of the code

Figure 6.2: Frequency Spectrum for first and second part of the rectangular pulse train

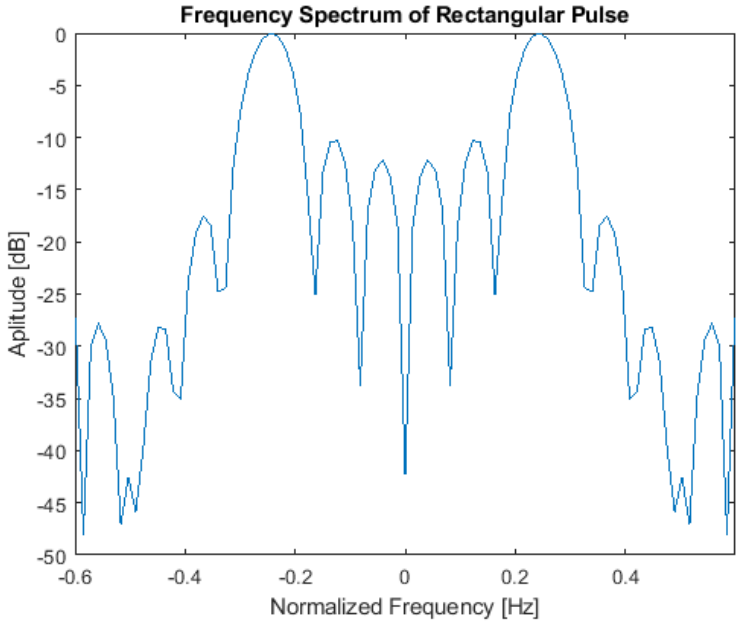

Figure 6.3: The resulting spectrum with peak separation of PRF/2

same codes of signal. A train of coded signal can be describe mathematically as

$$s(t) = \sum_{i=0}^{N-1} C_i \, x(t - i\text{PRI}) \tag{6.10}$$

where PRI is the pulse repetition interval, and N is the number of pulses in the train. Meanwhile, the output of AF is given as

$$\chi(\tau_d, f_D) = \int_{-\infty}^{\infty} s(t) s^*(t + \tau_d) e^{j2\pi f_D t} dt \tag{6.11}$$

where $\chi(\tau_d, f_D)$ is the AF of the signal at delay τ_d and Doppler f_D. Substituting Equation 6.10 into Equation 6.11 and interchange the summation gives

$$\chi(\tau_d, f_D) = \sum_{i=0}^{N-1} \sum_{j=0}^{N-1} C_i \, C_j \int_{-\infty}^{\infty} x(t - i\text{PRI}) x^*(t - j\text{PRI} - \tau_d) e^{j2\pi f_D t} dt \tag{6.12}$$

From Equation 6.12, by marking the change of variable $t_1 = t - i\text{PRI}$ yield to

$$\chi(\tau_d, f_D) = \sum_{i=0}^{N-1} C_i \, e^{j2\pi f_D i\text{PRI}} \sum_{j=0}^{N-1} C_j \int_{-\infty}^{\infty} x(t_1) x^*(t_1 - [\tau_d - (i-j)]PRI) e^{j2\pi f_D t_1} dt_1 \tag{6.13}$$

The integral inside in Equation 6.13 shows that the output of the AF for a single pulse and is referred as χ_1 which can be written as

$$\chi(\tau_d, f_D) = \sum_{i=0}^{N-1} C_i \, e^{j2\pi f_D i\text{PRI}} \sum_{j=0}^{N-1} C_j \, \chi_1[\tau_d - (i-j)\text{PRI}, f_D] \tag{6.14}$$

It was shown in Equation 6.14, the AF for for a pulse train is the superposition of the single AF. The AF of the simulated signal was found and plotted in Figure 6.4.

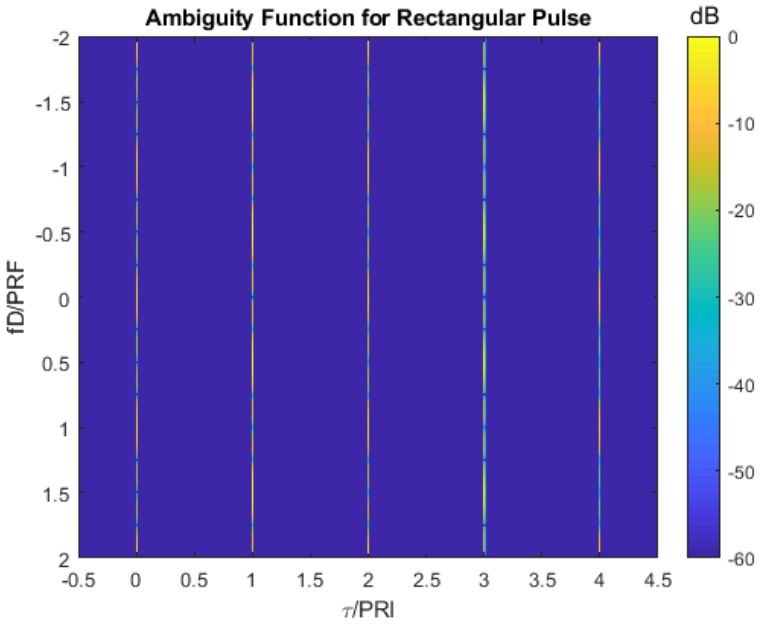

Figure 6.4: Ambiguity Function for a Burst of Rectangular Pulse

The range cut was obtained by setting $f_D = 0$ and from $|\chi(\tau_d, 0)|$ shown in Figure 6.5. It can be seen in the figure that the repetition peaks in range appear every 2PRI. Therefore, the maximum unambiguous range is doubled compared to

the uncoded case. The output is the same as that obtained after the matched-filter for a stationary target.

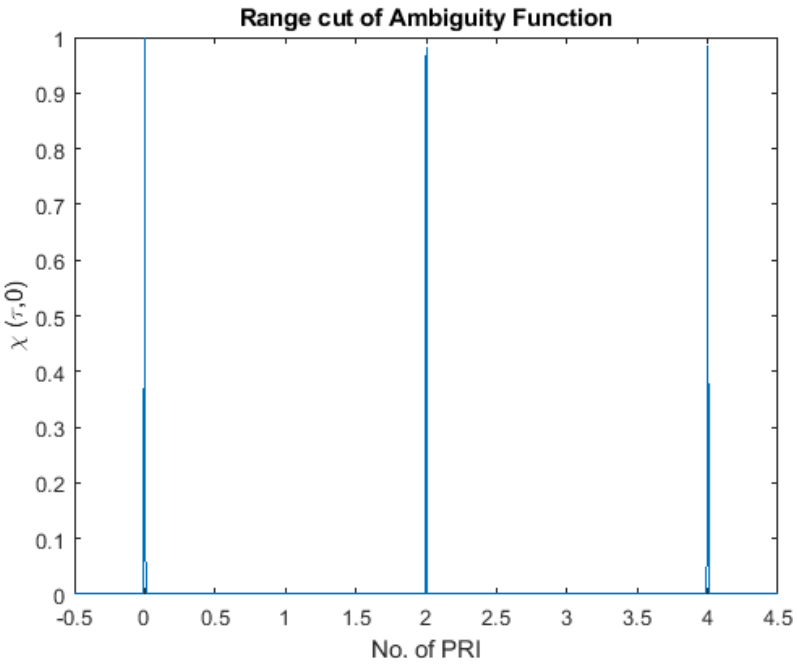

Figure 6.5: Range cut of AF at $\chi(\tau_D, 0)$

It can be seen in Figure 6.4 there is a straight line at PRI and 3PRI which do not appear in the range cut graph. However, by zooming-in on Figure 6.4 in each straight line, at the point where zero-Doppler occurred, it can be seen that the power is 0 as shown in Figure 6.6. This means that no signal will be detected in every odd-number PRI for stationary targets. Applying coding in the signals increases the the effective periodicity from the actual PRI to the much longer PRI sequence.

Meanwhile, the zero-Delay cut or Doppler cut was found by setting $\tau_d = 0$ as shown in Figure 6.7. The result of this equation is the sinc function with the first zero crossing occurring at $f_D = 1/\text{PRI}$ and repeated every 1/PRI as shown in Figure 6.7. It can be seen in the Doppler-cut figure the peak occurred at every PRF, which

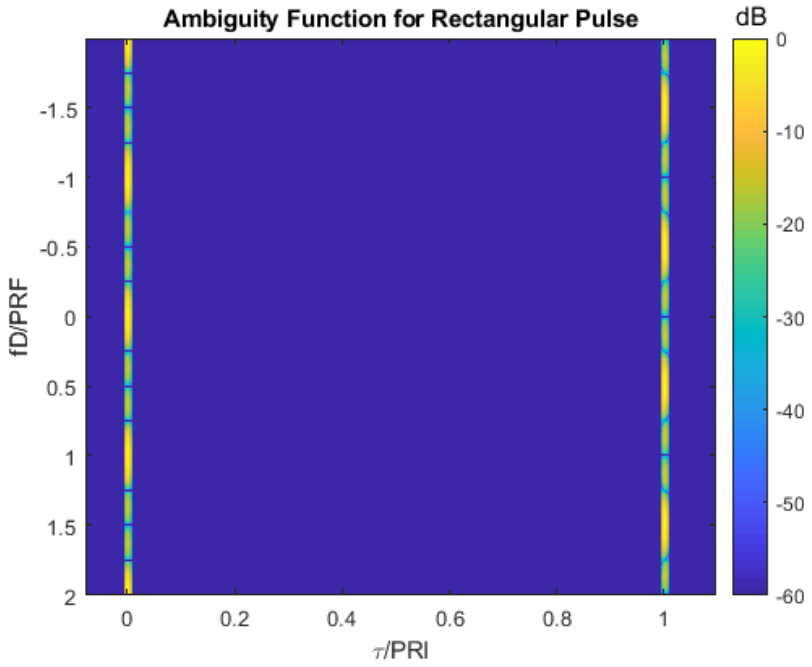

Figure 6.6: The zoom-in of AF

is not the same with the Fourier transform of the coded signal. This is because the output of the Doppler-cut plotted is the FFT of the amplitude square of the coded signal.

It was shown in all the AF plots how the coded pulse determines the resolution and ambiguities in the range and Doppler. It can be said from the AF plots that the length of pulse gives the desired range resolution, whilst the PRI and the code set the ambiguity in both Doppler and delay and finally the number of pulses determines the Doppler resolution from $(1/(N\text{PRI}))$ Hz (where N is the number of pulse transmitted).

From the simulated signal shown, the transmit signal from the staring radar was known from the priori knowledge. In future world deployment, a preliminary covert measurement of the transmitter signal would be possible enabling real time

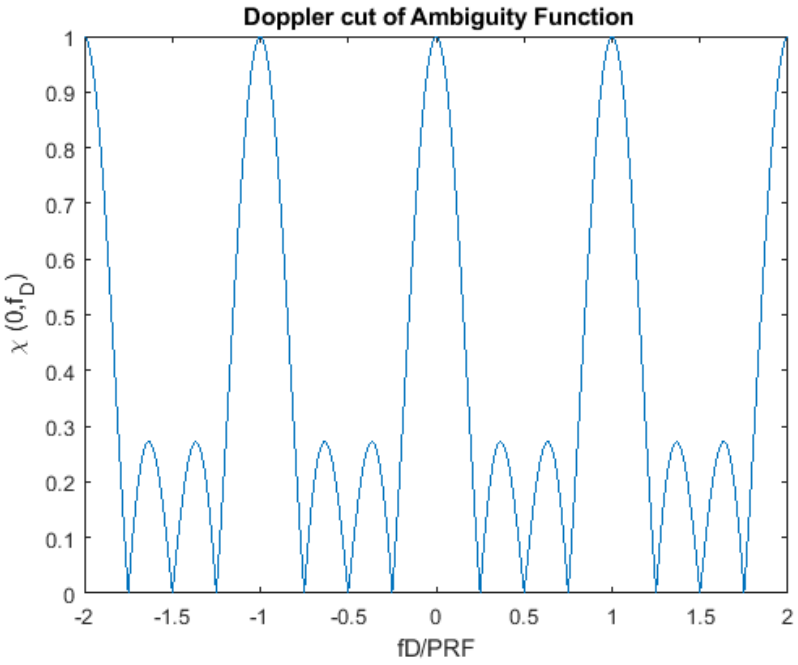

Figure 6.7: Doppler cut of AF at $\chi(0, f_D)$

the reference signal construction. Thus, this would make the system a true PBR exploiting non-cooperative illuminator of opportunity.

6.3 Experimental Design

In this section, the experimental setup for target detection using PBR is presented. The developed passive receiver prototype was employed in conjunction with the staring radar and experiments were initially run when both the reference and surveillance signals were acquired.

The external reference signal of 10 MHz was fed to both channels of the receiver to provide them with a more accurate reference clock. RX1 was connected to the reference channel and RX2 to the surveillance channel. The receiving antenna for

the reference channel was a double ridge horn antenna with a 10 dB gain and 33.1° vertical and 55.9° horizontal beamwidths. The surveillance antenna was a standard horn antenna with 15.2 dB gain and 34.4° vertical and 25.1° horizontal beamwidths.

The experiment was conducted at Deenethorpe Airfield, a former Royal Air Force station located about 3 km east of Corby in England. During the experiment the area surrounding the radar was clear of unwanted targets. A series of measurements were taken with the receiver in proximity with the Aveillant 3D radar for three different targets; a running person, a car and a flying drone.

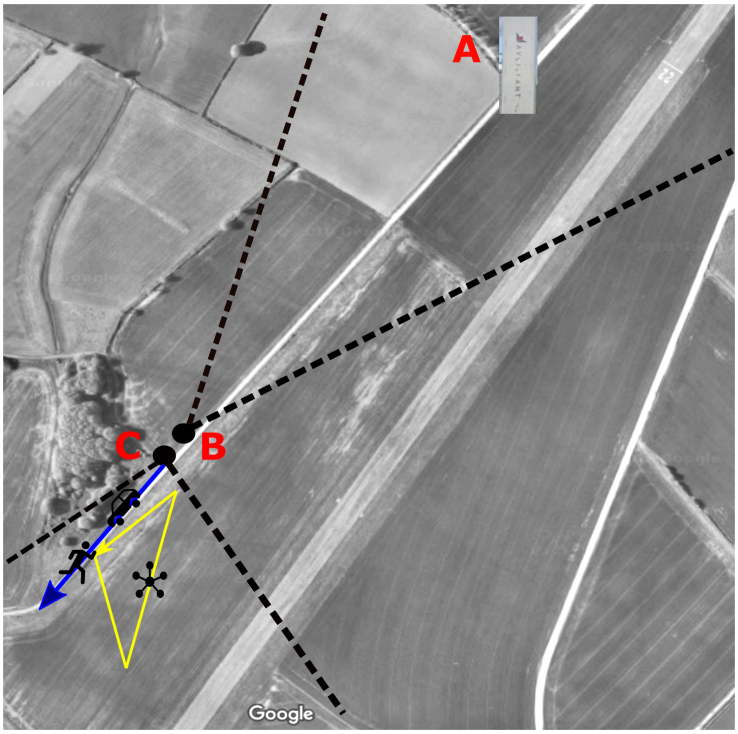

Figure 6.8: Bistatic geometry of the target detection experiments. The 3D Staring radar is in a fixed position labelled as (A), the reference antenna is labelled as (B) and the surveillance antenna is labelled as (C). The yellow line represents the trajectory of the drone and the blue line represents the trajectory of the car and a person

Figure 6.8 shows the experimental configuration. The staring radar location is

shown at (A), the reference signal antenna at (B) and the surveillance signal antenna at (C). The path of the person running and the moving car is shown in blue and the path for the drone is shown in yellow while the beam of the reference antenna and surveillance antenna are indicated by the black dotted lines. Note that the running human target and the car moved along the same path along the line-of-sight between the transmitter and the receiver. The surveillance antenna pointed away from the transmitter (denoted as transmitter at angle 180°). The reference antenna was pointed direct to the transmitter to collect a clean copy of the transmitted signal. During the experiment, the trajectories of the car and the drone were recorded with a GPS receiver to provide ground truth information for the targets. The distance between the transmitter and the receiver (baseline distance) remained constant at approximately 635 m.

Processing Techniques

In the reference channel, it was found that the pulse width (τ) for the signal is 1μs and the PRI is 136 μs. The spectrum of the signal is shown in the next section. In Matlab, the resulting I/Q signals from each channel were matched-filtered to form a slow-time fast-time map and the FFT was carried out to produce range-Doppler maps. Each pulse in the reference channel was cross-correlated with each pulse in the surveillance channel.

During signal processing, the reference and surveillance channel were treated separately and referred as $SR0$ for the reference signal and $SR1$ for the surveillance signal. The I/Q signals from both signals where then stored in a slow-time fast-time

matrix (slow-time rows and fast-time in columns). The signal was received in the long blocks of data in a vector form. Based on the number of pulses received, each of the pulse was filtered with the single pulse matched filter where the outputs then was combined. The slow-time refers to the pulse (this increments each PRI) and the fast-time refers to the range bin number where the sampling interval T_s was used to determine the spacing Δx between consecutive samples. This can be written as

$$\Delta x = \frac{cT_s}{2} \tag{6.15}$$

with $F_s = 1/T_s$ is the sampling frequency at 14.704 MHz. After the signals were stored in the slow-time and fast-time, the signals need to be shifted back to zero frequency. This is because the signal received is demodulated away from DC as shown in Figure 6.11 to allow digital suppression of the USRP unwanted quantization noise around DC.

The reference and surveillance signal were down-converted to 1.253 GHz for filtering, however, this filtered signal needs to be down-converted again to the transmitter carrier frequency as they were demodulated away from DC. This was done by shifting the signal back to zero frequency. In the frequency domain, the maximum frequency of one pulse from the reference signal was found and this frequency was used to shift both reference and surveillance signals to zero frequency. In this case, because the matched-filter was applied between the surveillance and reference signal any offsets will be cancelled. However, this step is important for windowing implementation. The windowing was applied to the signal after zero frequency down-conversion.

In the processing, Hamming window was chosen due to its performance in can-

celling the sidelobe. Hamming window does not reach zero at both ends and has a slight discontinuity in the signal. The windowing was done in the reference signal before the matched-filter. Figure 6.9 shows the plot of the Hamming window and

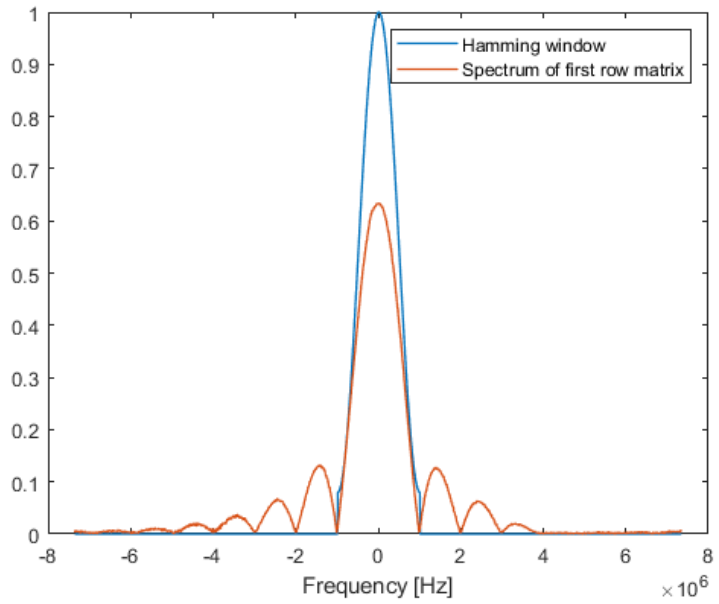

Figure 6.9: The plot of a Hamming window and the spectrum of the pulse in the first row of the surveillance channel matrix after zero-frequency conversion

the spectrum of the first pulse extracted from the reference signal after the zero-frequency conversion. The Hamming window was applied to all rows of the data matrix of the reference signal (that is for each PRI). The next step for the processing is the matched-filter which was done by cross-correlating each PRI of the reference signal with the corresponding PRI of the surveillance signal. This will produce a range-map.

The matched-filtering operation gives the range profile of the scene, indicating the bistatic range to the target. It was done in one dimension in fast-time matrix. However, the target response will not be visible if the target is swamped by clutter caused by unwanted reflections from the environment. To solve this, the

stationary target was removed by removing the mean value of the signals. This is also called zero-Doppler suppression and eliminates stationary targets leaving only moving targets.

Next, windowing in slow time was applied by multiplying a Hamming window with each columns of the data matrix. Windowing in data suppressed the spurious sidelobes in the received signal. Finally, the range-Doppler map was formed by applying an FFT to the final output of the matched-filter (after windowing). Overall, the data matrix in slow time was converted to Doppler and fast time was converted to range. The range-Doppler map enables discrimination between stationary and moving returns, which separate the moving target from the stationary clutter.

6.4 Ground Truth Data Convention

As previously mentioned, two of the targets (car and drone) used during this experiment had GPS receivers fitted, which enabled their position and velocity to be recorded. GPS data uses the World Geodetic System (WGS 84) for reference coordinates with the centre of the mass of the earth as the coordinate origin. A conversion between the WGS 84 coordinate to Cartesian (x,y,z) coordinate was required to compare the experimental results with the GPS ground truth.

An assumption was made for that ellipsoidal based datum of the WGS 84 which was modelled as a sphere and this gives constant radius of Earth as shown in Figure 6.10. With this assumption, the ratio of the arc length and circumference is equal to the ratio of α and 2π:

$$\frac{L}{C} = \frac{a}{2\pi} \tag{6.16}$$

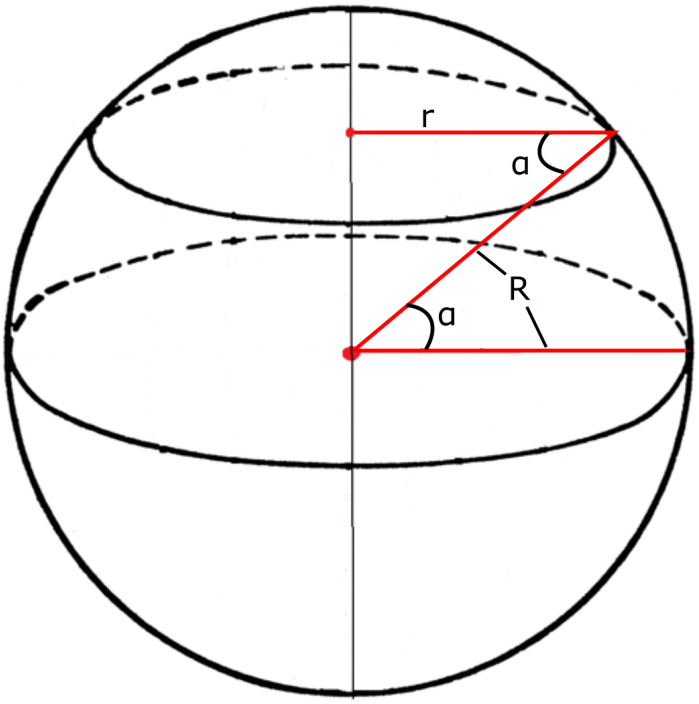

Figure 6.10: Arc Length at Equator

where L is the arc length, C is the circumference of the sphere, α is the latitude of the location, R is the radius of the earth and therefore $r = Rcos(\alpha)$. For simplicity, the value of α is chosen to be 1° (in radian is $\pi/180$). Rearranging this equation, it was found that the arc length at the equator is

$$L = \frac{R * \pi}{180} \tag{6.17}$$

The value obtained from this formula represents the distance on the Earth's surface between one degree of longitude at the equator. For the WGS 84 coordinates, a datum needs to be established from which each point on the Earth will be referenced. In this conversion, the datum is the minimum observed longitude, latitude

and elevation. By selecting this datum, all the converted data will be positively referenced from the datum. Equation 6.18 and 6.19 can be used to find the Cartesian coordinates of the GPS data.

$$x = (Observed\ longitude - Minimum\ longitude) * l \tag{6.18}$$

$$y = (Observed\ latitude - Minimum\ latitude) * L \tag{6.19}$$

where l=r*π/180. For the z-position (height), the elevation corresponds to the altitude of the target compared to sea level. To do this, the elevation of the target's trajectory was subtracted from the raw GPS data.

With the Cartesian coordinates for the targets found, the velocity profile of the target can be constructed. This was done by estimating the velocity using the formula shown in Equation 6.20

$$V = \frac{\sqrt{(x_{(m-1)} - x_m)^2 + (y_{(m-1)} - y_m)^2 + (z_{(m-1)} - z_m)^2}}{(t_{(m-1)} - t_m)} \tag{6.20}$$

where V is the velocity of the target in m/s, and m is integer ($m = 2, 3, 4..$).

In this experiment, the transmitter and receiver locations were fixed and this enabled the coordinates of both to be easily found in Cartesian form. With the coordinates of the transmitter (Tx) and receiver (Rx) known, the range between the two can be found by subtracting the location of the transmitter and the receiver. Using Equations 6.21 and 6.22:

$$R_{Tx} = \sqrt{(Tx_x - x_m)^2 + (Tx_y - y_m)^2 + (Tx_z - z_m)^2} \tag{6.21}$$

$$R_{Rx} = \sqrt{(x_m - Rx_x)^2 + (y_m - Rx_y)^2 + (z_m - Rx_z)^2} \tag{6.22}$$

where m is integer ($m = 1, 2, 3..$), Tx is in Cartesian form of [x,y,z], Rx is in Cartesian form of [x,y,z], R_{Tx} is the range of the transmitter and R_{Rx} is the range of the receiver.

The radial components of the velocity with respect to the Rx and Tx can also be found from the GPS coordinates. With the calculated ranges, the Doppler frequency can be found. This is done by finding the derivatives of the range with respect to time as shown in Equations 6.23 and 6.24

$$\frac{dR_{Tx}}{dt} = \frac{R_{Tx}(t+\Delta t) - R_{Tx}(t)}{\Delta t} \tag{6.23}$$

$$\frac{dR_{Rx}}{dt} = \frac{R_{Rx}(t+\Delta t) - R_{Rx}(t)}{\Delta t} \tag{6.24}$$

where dR_{Tx}/dt is the derivative of the range relative to the transmitter with respect to time and dR_{Rx}/dt is the range relative to the receiver with respect to time. Using the results of Equations 6.23 and 6.24, the Doppler frequency can be calculated by the formula shown in Equation 6.25

$$f_D = -\frac{f_0}{c}\left[\frac{dR_{Tx}}{dt} + \frac{dR_{Rx}}{dt}\right] \tag{6.25}$$

6.5 Experimental Results

This section presents the results of the experiments. The integration time used was 0.05 s for the person running and the moving car and 0.1 s for the drone. For a person running and a moving car, this integration time covers 366 pulses whilst for the flying drone 735 pulses were received and integrated. The received signals were down-converted and sampled at 14.704 MHz sampling rate by the USRP receiving

prototype.

The received signal was tested with the surveillance antenna pointed directly at the transmitter for a brief check and to confirm reception. From the received signal, it was found that a modulation by the USRP occurred at zero frequency. This undesired modulation can be seen in the frequency domain of the received signal and must be removed. This unwanted signal can be removed by filtering the received signal. Normally, the received signal was down-converted at the carrier frequency of the transmit signal which, for the Aveillant Radar is 1.25 GHz. In order to isolate the unwanted modulation from the USRP, the LO frequency supplied to the mixer in the USRP was changed to 1.253 GHz. The reference and surveillance channel were down-converted of 1.253 GHz and the unwanted contribution was filtered out.

Figure 6.11 shows the spectrum of the received signals before and after filtering. Note that before filtering, there is a straight line around 0 Hz. The top figure shows the unwanted modulation introduced by the USRP, that is independent of the radar signal, which occurs in both the reference channel and the surveillance channel. It was found that the exact modulation occurred at frequency of 5 kHz. After filtering, the modulation was removed in both channels. Data was taken continuously with the length of the integration time and the two channels were stored in two different files.

Figure 6.12 shows the range-Doppler maps produced as described in the previous section for a person running away from and towards the receiver after zero-Doppler suppression. Figure 6.12a shows the range-Doppler map for a person running away from the passive receiver and it can be seen that the target appears with a negative Doppler shift as expected. In the series of data, the target was detected in frame 6

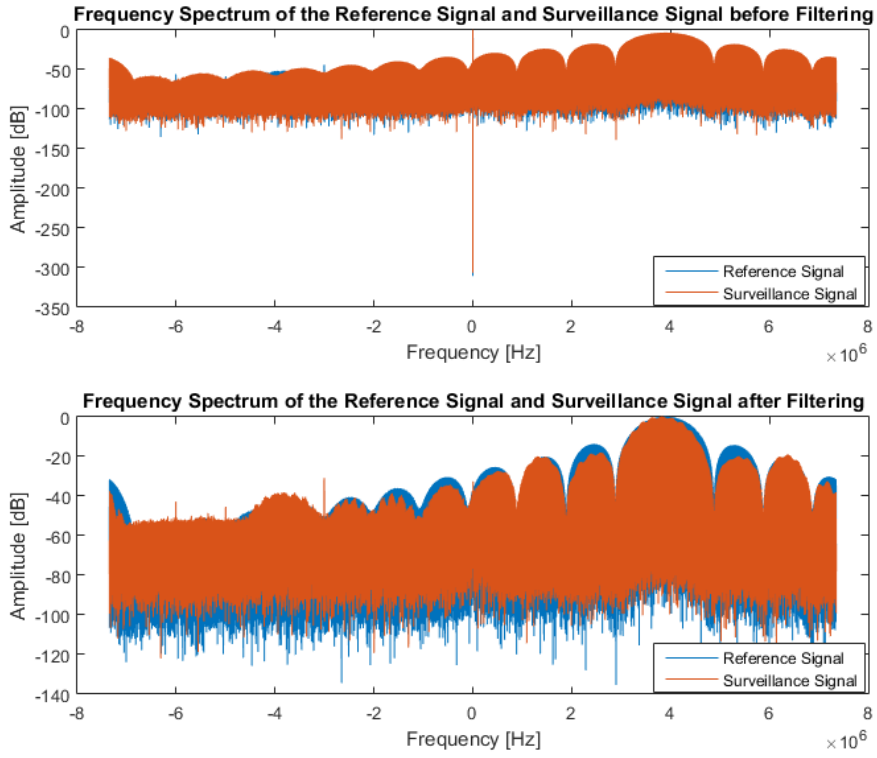

Figure 6.11: The frequency spectrum for the signals before the filtering and after filtering

with a Doppler shift of -36.8 Hz by integrating 366 pulses. Figure 6.12b shows the range-Doppler map for a person running towards the receiver where the response appears at a positive Doppler shift as expected. The target was detected in frame 6 with a Doppler shift of 36.8 Hz.

The measured Doppler shifts for the runner indicate a speed of 4.4 m/s (9.8 mph) and this is in agreement with a typical speed for the runner. It was shown that the algorithm can accurately resolve speed. The speed of the runner was consistent between running away from the receiver and towards the receiver but the Doppler shift changed sign as expected. In the range-Doppler maps, the relative bistatic ranges shown are the difference between the transmitter to target distance plus

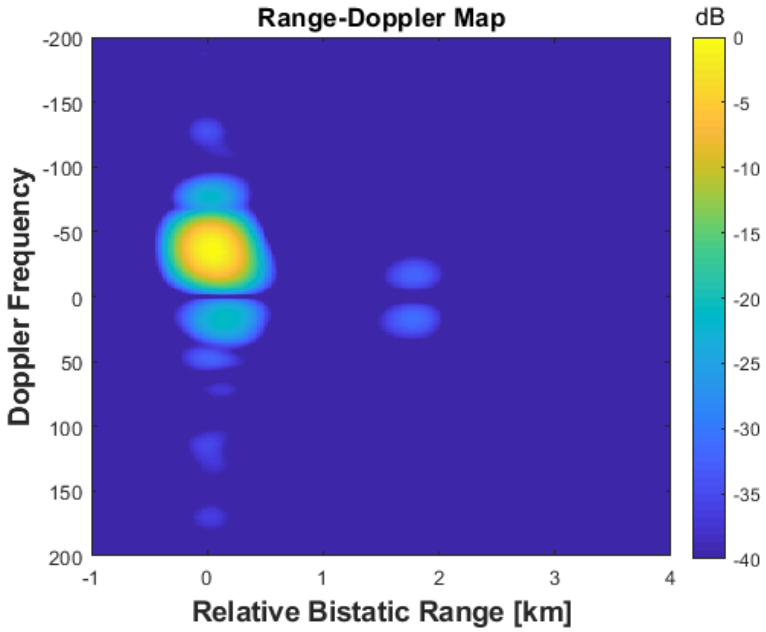

(a) Range-Doppler map for a person running away from the receiver. 50 ms integration time used

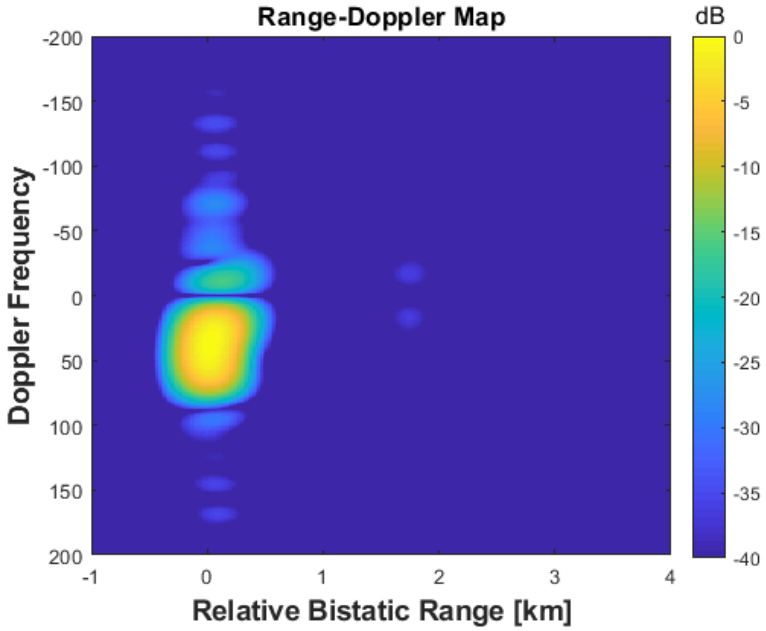

(b) Range-Doppler map for a person running towards the receiver. 50 ms integration time used

Figure 6.12: Range-Doppler maps after zero-Doppler suppression for a person running away from the receiver and towards the receiver

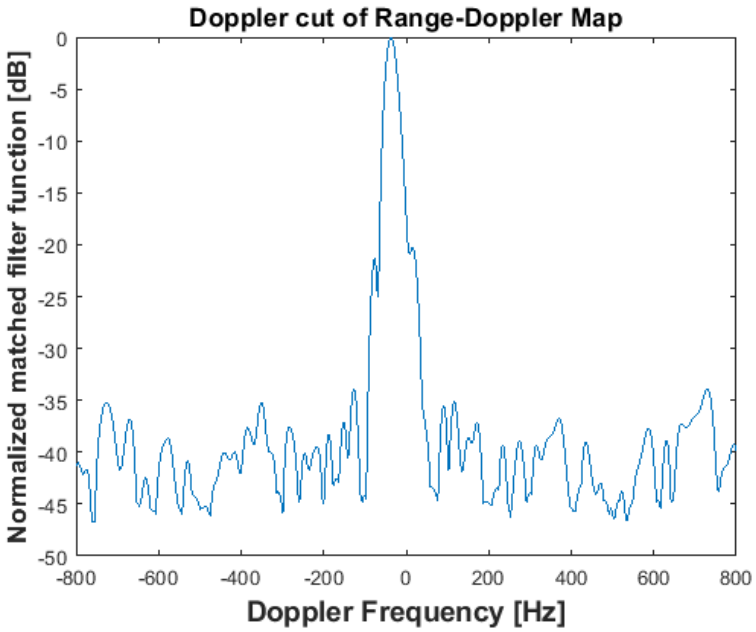

(a) Doppler-cut for a person running away from the receiver. 50 ms integration time used

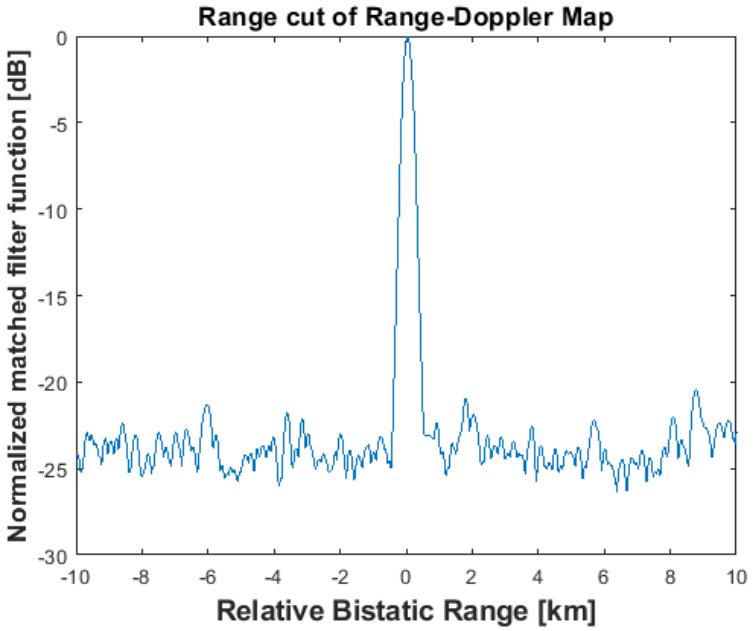

(b) Range-cut for a person running away from the receiver. 50 ms integration time used

Figure 6.13: Doppler and range cuts after zero-Doppler suppression for a person running away from the receiver

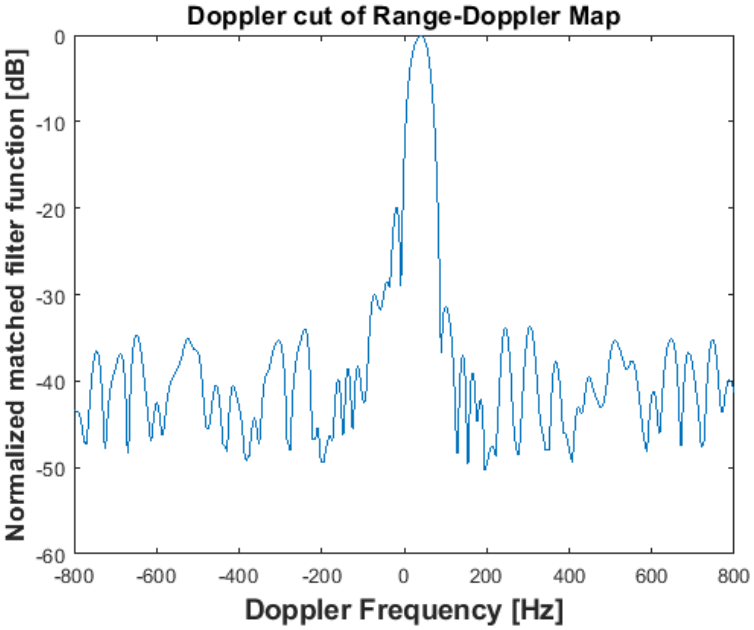

(a) Doppler-cut for a person running towards the receiver. 50 ms integration time used

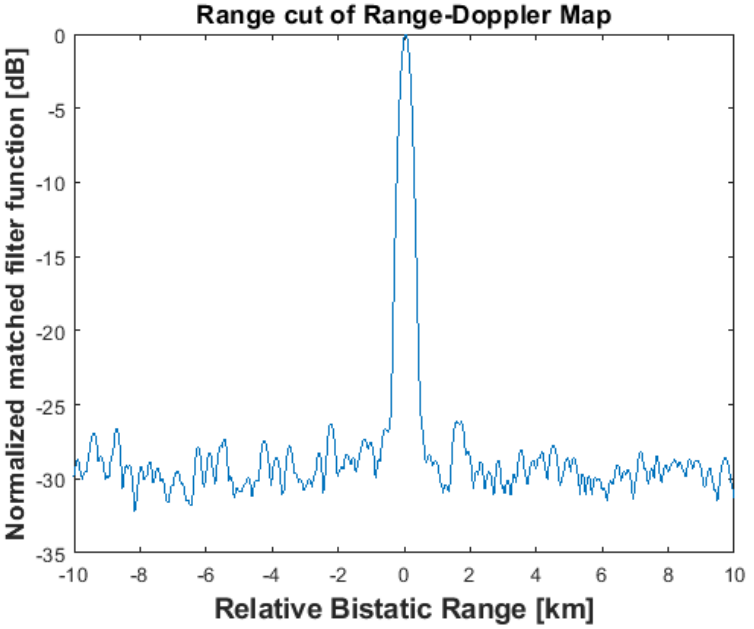

(b) Range-cut for a person running towards the receiver. 50 ms integration time used

Figure 6.14: Doppler and range cuts after zero-Doppler suppression for a person running towards the receiver

target to passive receiver distance and the baseline distance between the transmitter and the passive receiver.

In addition to the range-Doppler maps shown, the Doppler and range profiles for the targets were also plotted. The Doppler profile was obtained from the Doppler-cut along the Doppler frequency axis containing the target and for the range profiles from the range-cut along the range axis containing the target. Both cuts were obtained straightly from the range-Doppler map.

Figures 6.13 and 6.14 shows the Doppler and range cuts for a person running away and towards the passive receiver. The high peak values in the Doppler-cuts correspond to the Doppler frequency obtained in the range-Doppler map. It can be seen in the range-cuts that the sidelobes from the output of the matched filter for both cases fall below the receiver noise floor. For a person running away from receiver, the SNR is approximately -25 dB shown in Figure 6.13b whereas for a person running towards the receiver, the SNR is approximately -30 dB shown in Figure 6.14b.

Figure 6.15 shows the range-Doppler maps for the moving car. The car that was used for this experiment was a Skoda Octavia estate. The car moved in the vicinity of the passive receiver. Figure 6.15a shows the range-Doppler map for the car moving away from the passive receiver produced using the same integration time as the runner. Results show a peak response with a Doppler shift of -90.07 Hz which was detected in frame 5. Figure 6.15b shows the range-Doppler map for the car moving towards the passive receiver. The peak response was seen at a positive Doppler shift at 68.9 Hz detected in frame 14.

The difference in the absolute value of Doppler shift when the car was moving

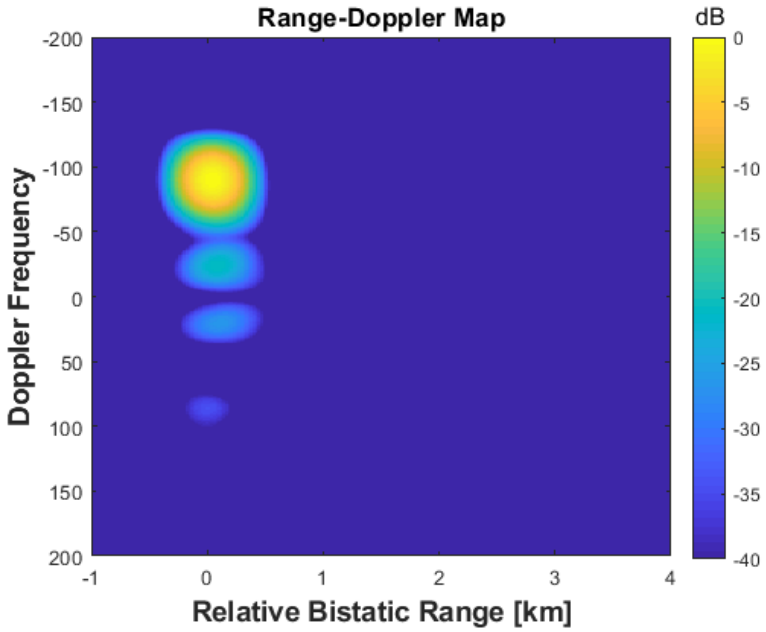

(a) Range-Doppler map for a car moving away from the receiver with 50 ms integration time

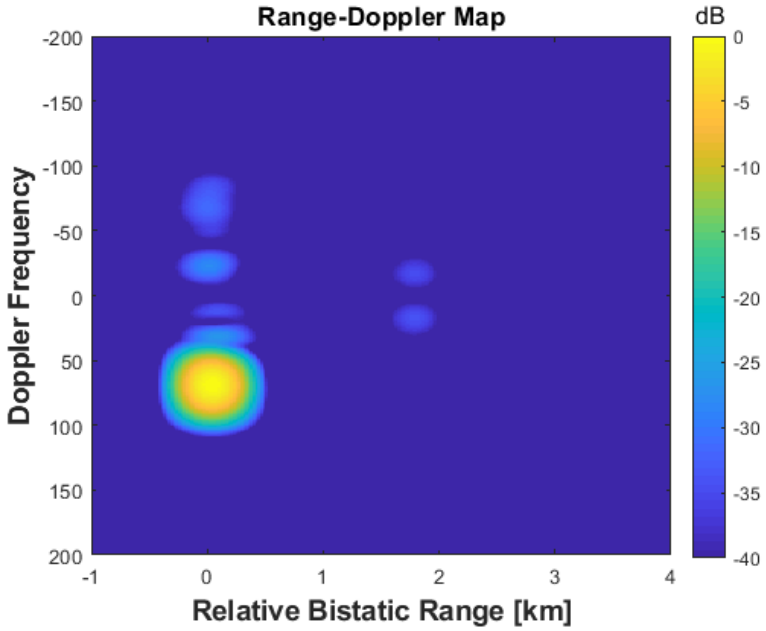

(b) Range-Doppler map for a car moving towards the receiver with 50 ms integration time

Figure 6.15: Range-Doppler maps after zero-Doppler suppression for a car moving away from the receiver and towards the receiver

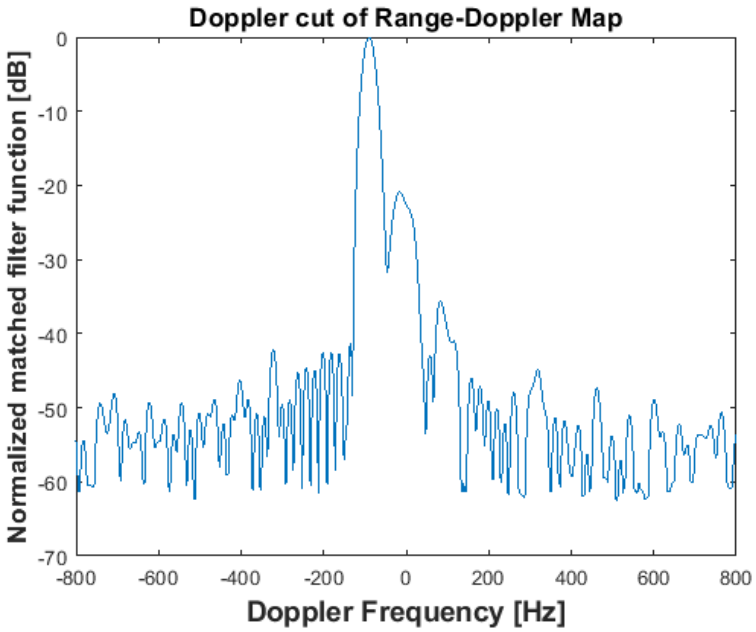

(a) Doppler-cut for a car moving away from the receiver with 50 ms integration time

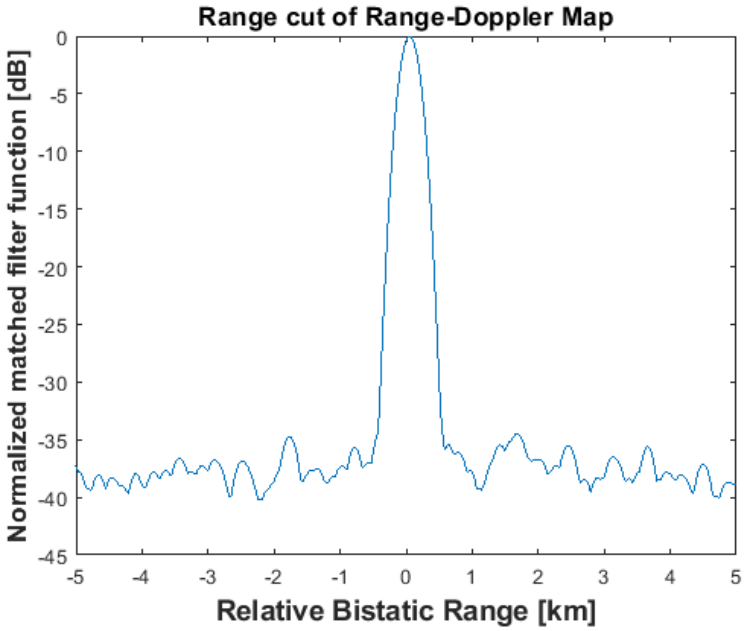

(b) Range-cut for a car moving away from the receiver with 50 ms integration time

Figure 6.16: Doppler and range cuts after zero-Doppler suppression for a car moving away from the receiver

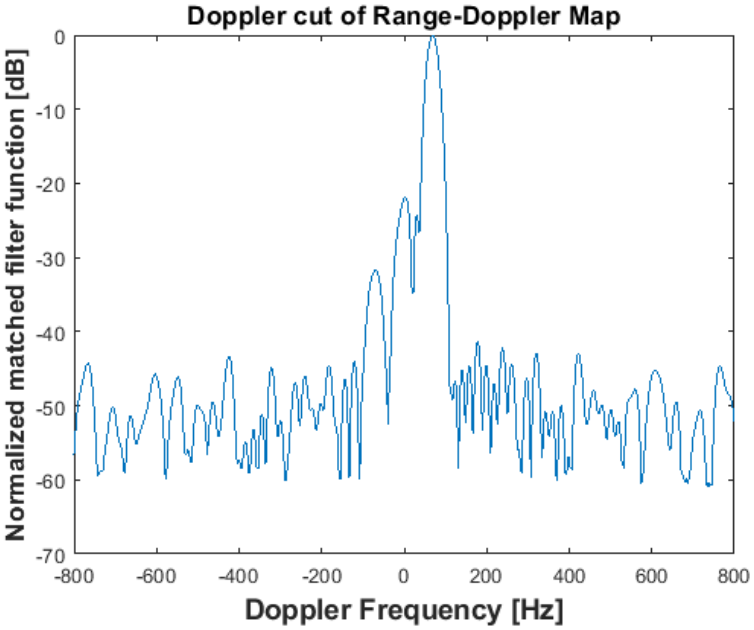

(a) Doppler-cut for a car moving towards the receiver with 50 ms integration time

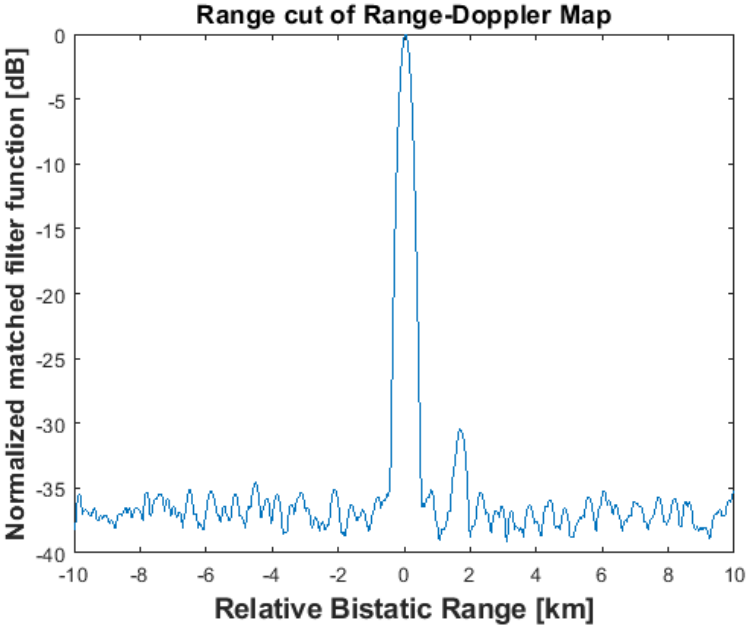

(b) Range-cut for a car moving towards the receiver with 50 ms integration time

Figure 6.17: Doppler and range cuts after zero-Doppler suppression for a car moving towards the receiver

towards the receiver was due to the different speeds the car reached in each direction. When the car was driven towards the receiver, it picked up speed from a stationary position and reached only a modest speed. However, when the car was driven away from the receiver, it was driven along the runway and reached a higher speed. The measured Doppler shifts (-90.07 Hz and 68.9 Hz) gives the speed of 10.8 m/s (24.2 mph) when the car was moving away from the receiver and 8.2 m/s (18.3 mph) when it was moving towards the receiver.

Figures 6.16 and 6.17 shows Doppler and range cuts for the moving car. From the Doppler-cuts obtained in both directions, the peak value was consistent to the Doppler frequency obtained in the range-Doppler map. The SNR for the car moving away and towards the passive receiver is approximately -37 dB as shown in Figures 6.16b and 6.17b. The result shows that the SNR for the car in both directions agree with each other.

With a running person and a car successfully detected, the last target used was a drone. The drone used in this experiment was a DJI Inspire drone which has a diameter of 0.5 m and weighs 3 kg. Due to the lower RCS and speed of the drone, the integration time needed to be longer. This is to improve the detection ability of the receiver and to increase Doppler resolution. This was achieved by increasing the number of samples in the receiver channel. The integration time was increased to 0.1 s, equivalent to integrating 734 pulses. The drone was flown at a height of 10 m during the measurements. Continuous measurements were taken and several passes of the drone were recorded. The drone was successfully detected within the beamwidth of the surveillance antenna when the drone flew away and towards the receiver.

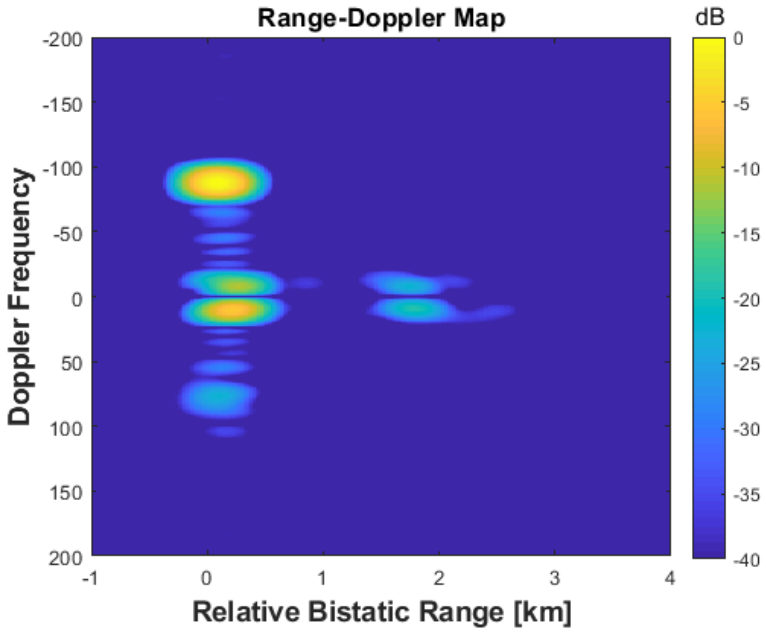

(a) Range-Doppler map for a drone flying away from the receiver with 0.1 s integration time

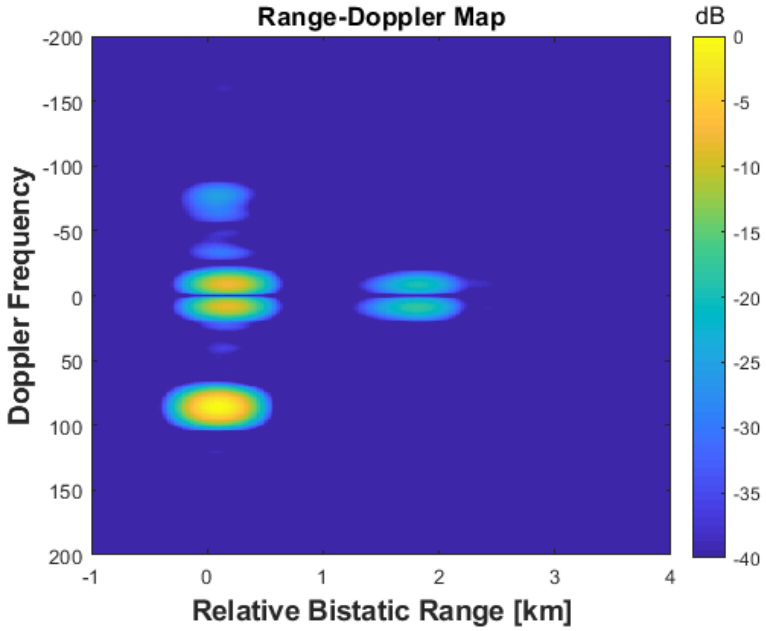

(b) Range-Doppler map for a drone flying towards the receiver with 0.1 s integration time

Figure 6.18: Range-Doppler maps after zero-Doppler suppression for a drone flying away from the receiver and towards the receiver by integrating 734 pulses

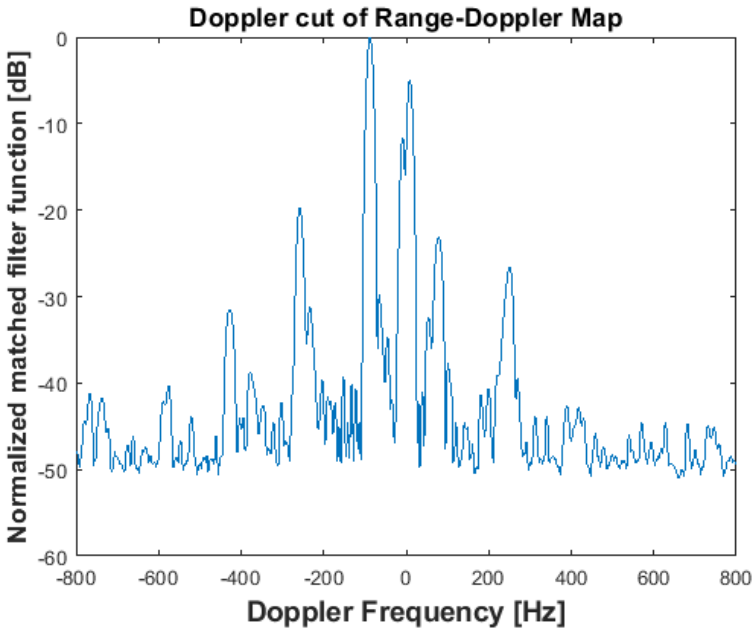

(a) Doppler-cut for a drone flying away from the receiver with 0.1 s integration time

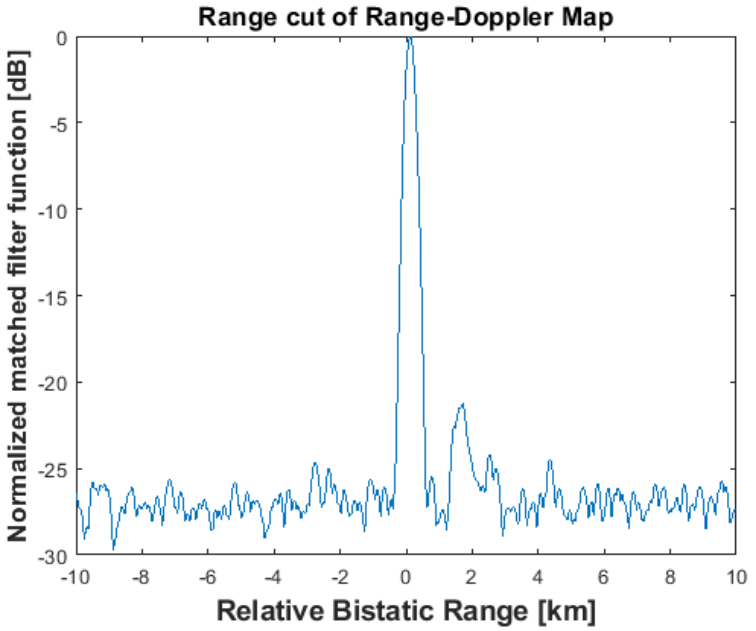

(b) Range-cut for a drone flying away from the receiver with 0.1 s integration time

Figure 6.19: Doppler and range cuts after zero-Doppler suppression for a drone flying away from the receiver

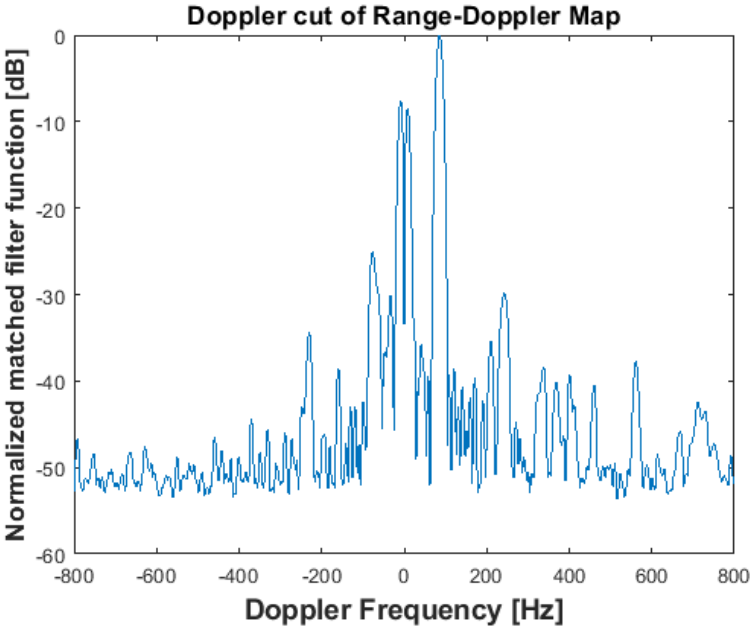

(a) Doppler-cut for a drone flying towards the receiver with 0.1 s integration time

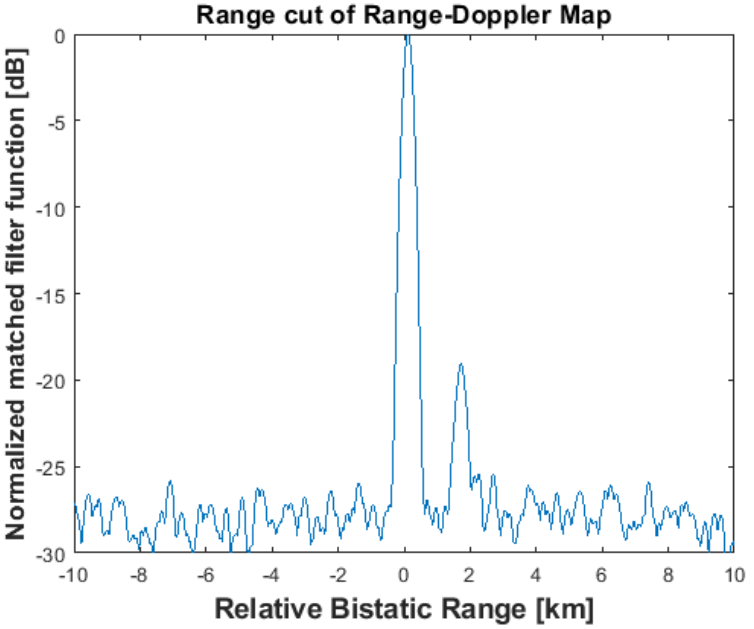

(b) Range-cut for a drone flying towards the receiver with 0.1 s integration time

Figure 6.20: Doppler and range cuts after zero-Doppler suppression for a drone flying towards the receiver

Figure 6.18 show the range-Doppler maps for the drone flying away from the receiver and towards the receiver. Figure 6.18a shows the range-Doppler map for the drone flying away from the receiver and shows, the peak response with a negative Doppler shift of -85.48 Hz. This was detected at frame 8. Figure 6.18b shows the range-Doppler map for the drone flying towards the receiver. The peak response can be seen with Doppler shift of 85.48 Hz, detected at frame 12. The drone was also detected in other frames from the few passes it made within the proximity of the passive receiver. The drone was also detected in frames 22 and 27. In these two frames similar Doppler shifts were measured.

It can be seen in the Figure 6.18 that there is also a weak response at -10 dB around zero-Doppler. This could be coming from the relatively stronger clutter returns in a different geometric arrangement and to a drop in clutter suppression gain due to the use of a longer integration time. The effects of the clutter can be seen clearly from the Doppler and range cuts as shown in Figures 6.19 and 6.20. In the Doppler-cut figures for both directions, the difference between the peak value and clutter is -8.3 dB and this is quite high.

Because more pulses were integrated, the resulting longer integration clutter made it more difficult to remove the clutter with a standard low-pass filter (i.e. clutter coherency was partially lost during the dwell time) and due to the non-stationary target. The effect of longer integration time also yields to lower quality of the image detected in the range-Doppler map. Moreover, the processing load and time also increase with the data getting bigger. Hence, the integration time should not be too long as it will effect the detected results and the processing. This return does not influence the response from the target and one way to remove it is to reduce the number of pulses integrated. To verify this, the number of pulse integrated was

reduced to 366, that is same as for the previous experiment with a person and a car.

Figure 6.21 shows the range-Doppler map produced when the number of pulses were reduced to 366 to reduce the clutter. It can be seen in the two figures that this has been very effective at removing the clutter. This refinement can also be seen in the Doppler and range cuts taken through the peak response, shown in Figures 6.22 and 6.23.

The Doppler profiles in Figures 6.22a and 6.23a show peaks corresponding to the range bin of the drone. The peak values were -85.48 Hz for the drone flying away from the receiver and 85.48 Hz for the drone flying towards the receiver which corresponds to a velocity of 10.3 m/s (23.0 mph). It can be seen in the figures that the Doppler resolution is approximately at 25 Hz (after windowing) at -3 dB bandwidth. However there is 5 Hz difference with the value calculated using the inverse of the dwell time. This is due to the windowing applied in both range and Doppler domain widen the mainlobe of the signal. The windowing and decreased coherent integration time applied during processing yields to an improved signal to clutter ratio. The Doppler sidelobes have been suppressed and cleaner Doppler spectrum was produced. Results from the Doppler profiles also shows that the clutter was reduced by integrating less pulse.

Figure 6.22b and 6.23b shows the range profile taken from the Doppler bin containing the drone. It can be seen that the sidelobes from the output of the matched filter fall below the receiver noise floor. The SNR for the drone flying away from the receiver is approximately -25 dB and this is the same for the drone flying towards the receiver.

From the results presented above, it was shown that there is a weak response

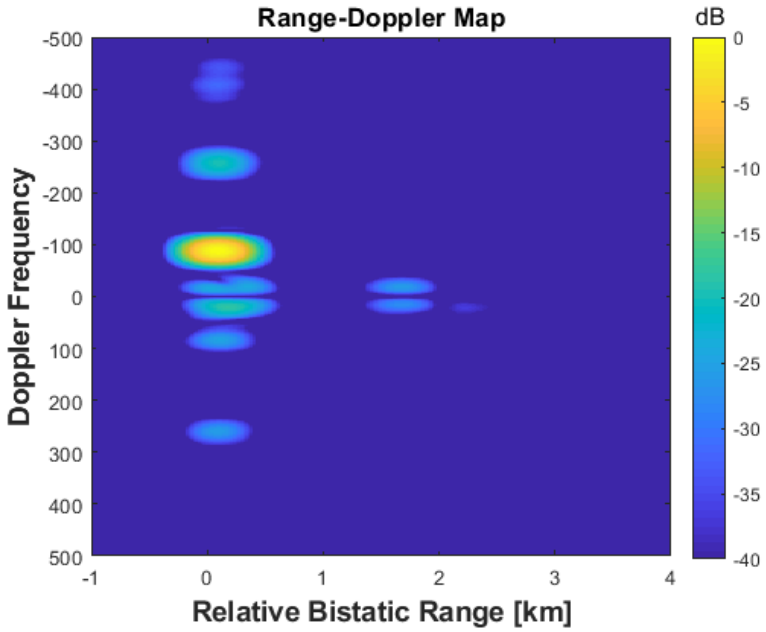

(a) Range-Doppler map for a drone flying away from the receiver with 50 ms integration time

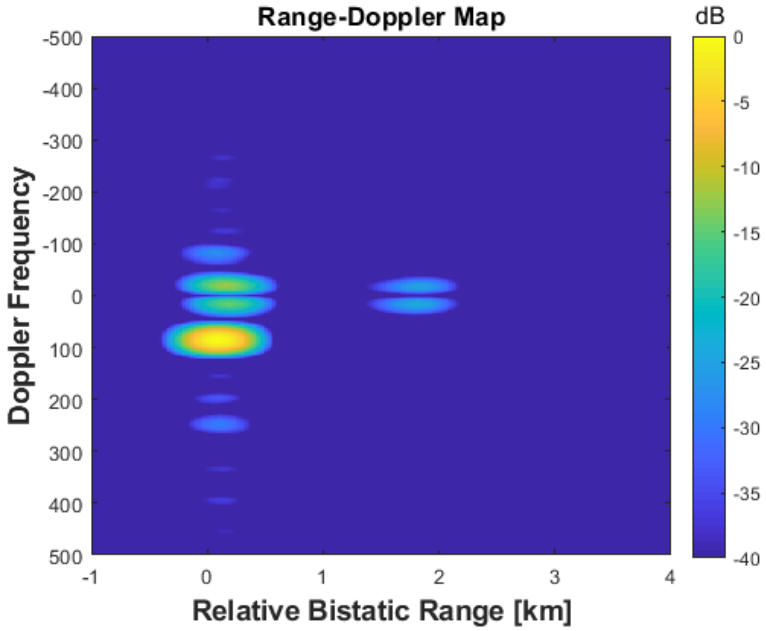

(b) Range-Doppler map for a drone flying towards the receiver with 50 ms integration time

Figure 6.21: Range-Doppler maps after zero-Doppler suppression for a drone flying away from the receiver and towards the receiver by integrating 366 pulses

around zero-Doppler from the drone detection. This response could be the effect of multipath from the trees around the airfield. The movement from the trees due to wind flow introduce Doppler shift that was captured by the receiving antenna. In addition, this response could be from passive receiver due to the vibration that yield to system noise in the USRP which resulted in frequency shift of Doppler frequency.

The experimental results presented in this section give an insight to the capability of using staring radar to detect targets passively. It confirmed the concept of using staring radar as illuminator of opportunity in detecting three different targets. The successful outcome is shown from the results obtained from a person running, a moving car and a flying drone. In the next section, using the GPS data that was recorded during the experiment, the velocity profile of the moving car and flying drone will be extracted. This will also give the information of the targets' trajectory and also validate the Doppler frequency obtained from the range-Doppler maps.

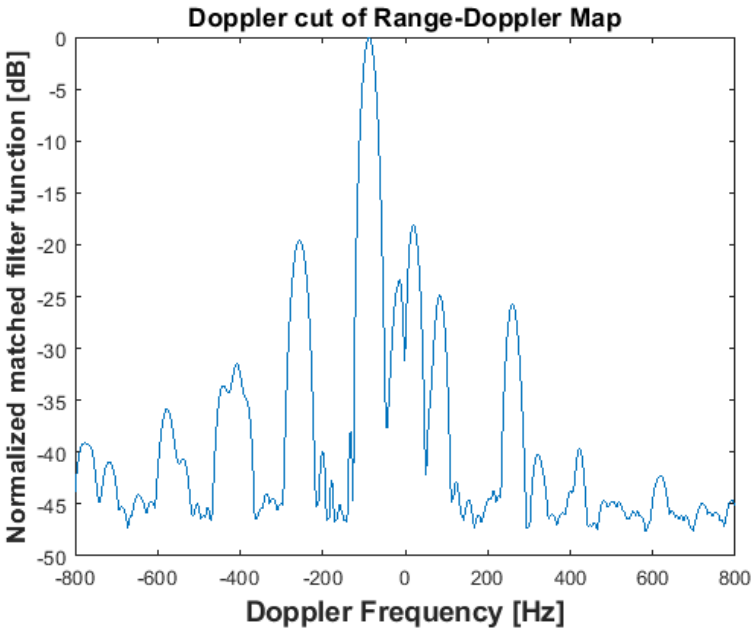

(a) Doppler-cut for a drone flying away from the receiver

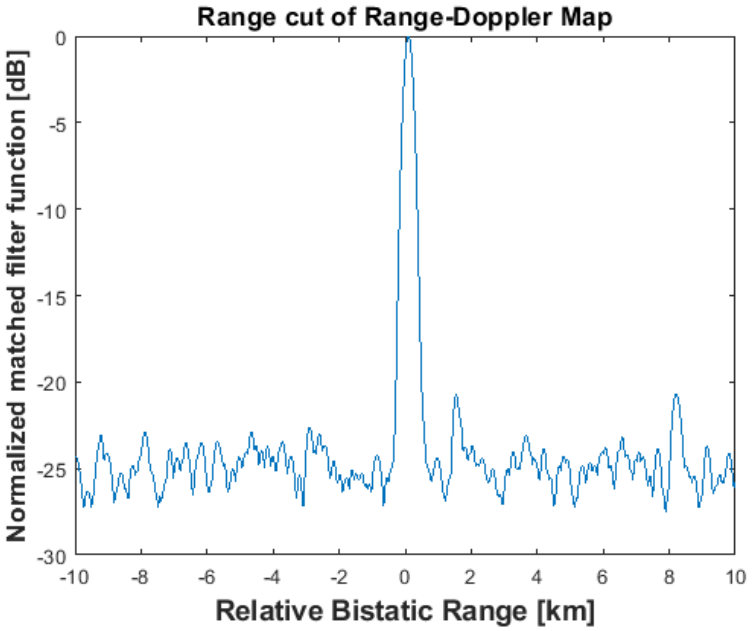

(b) Range-cut for a drone flying away from the receiver

Figure 6.22: Doppler-cut and range-cut for a drone flying away from the receiver after zero-Doppler suppression. 366 pulses integration used

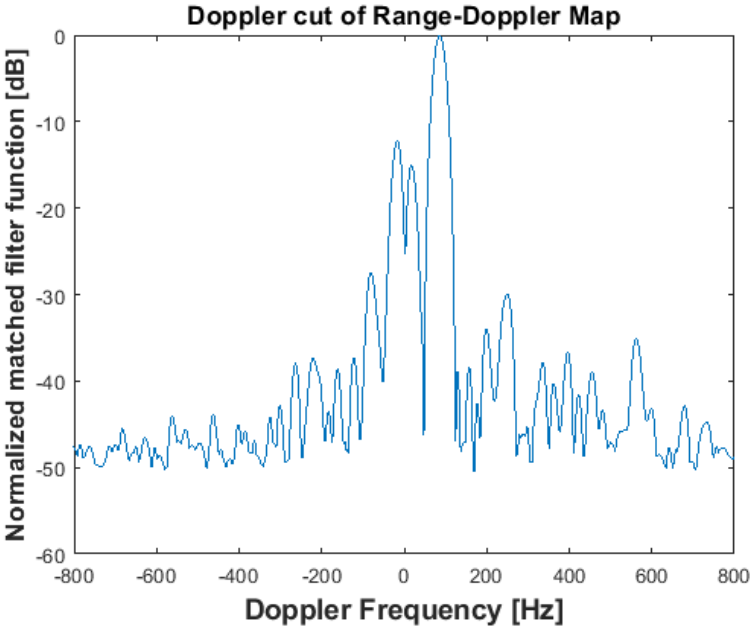

(a) Doppler-cut for a drone flying towards the receiver

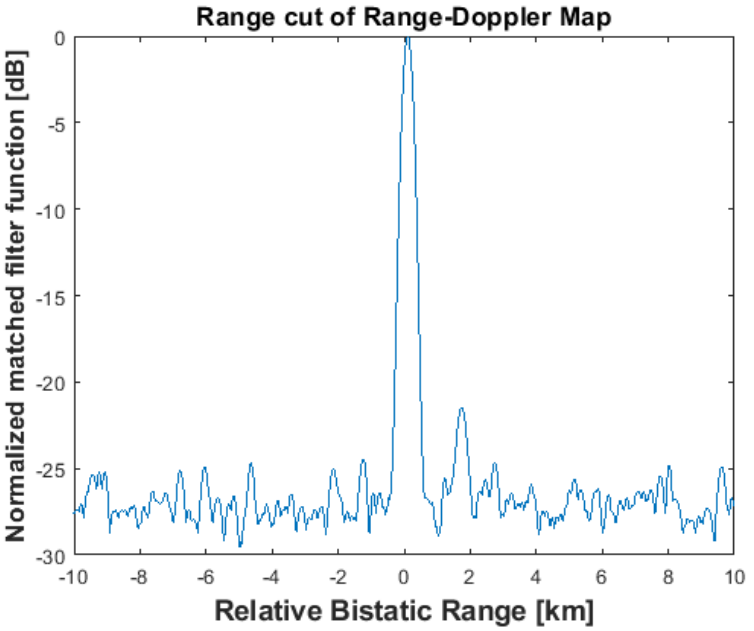

(b) Range-cut for a drone flying towards the receiver

Figure 6.23: Doppler-cut and range-cut for a drone flying towards the after zero-Doppler suppression by integrating 366 pulses

6.6 Velocity Profile

By applying the equations shown in Section 6.4 from Equations 6.16 to 6.25 to the experimental data, the Doppler frequency calculated from the GPS information can be found and is shown in Figure 6.24 to 6.26.

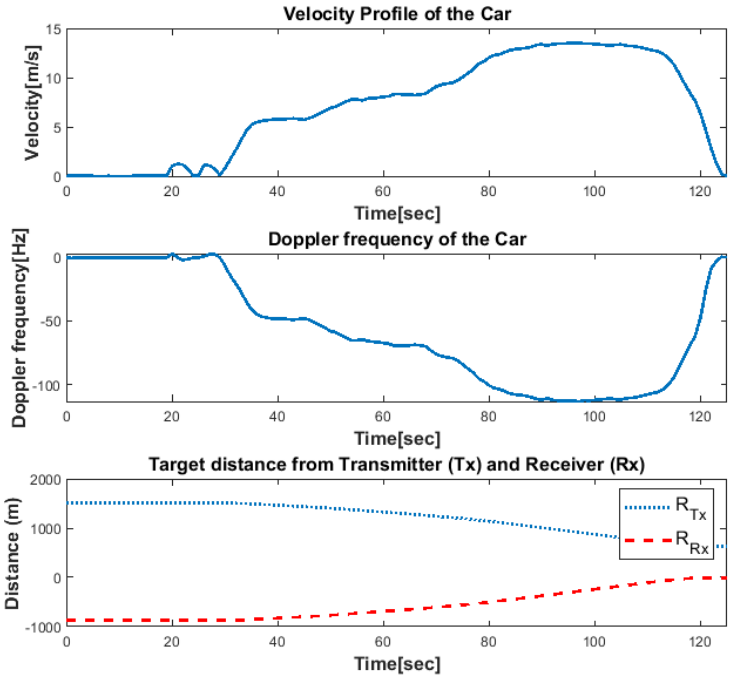

Figure 6.24: Result for a car moving away from the receiver

The velocity and Doppler frequency calculated from the GPS data is shown in Figure 6.24 for the car moving away from the receiver and in Figure 6.25 moving towards the receiver. The ground-truth velocity profile of the car is shown in the first plot in both figures. The middle plot in both figures shows the Doppler frequency profile for the car extracted from the GPS data. Finally, the bottom plot shows the range profile of the car. For the car moving away from the receiver, data was taken from 12:40:15 PM to 12:42:19 PM. The GPS derived velocity for the car

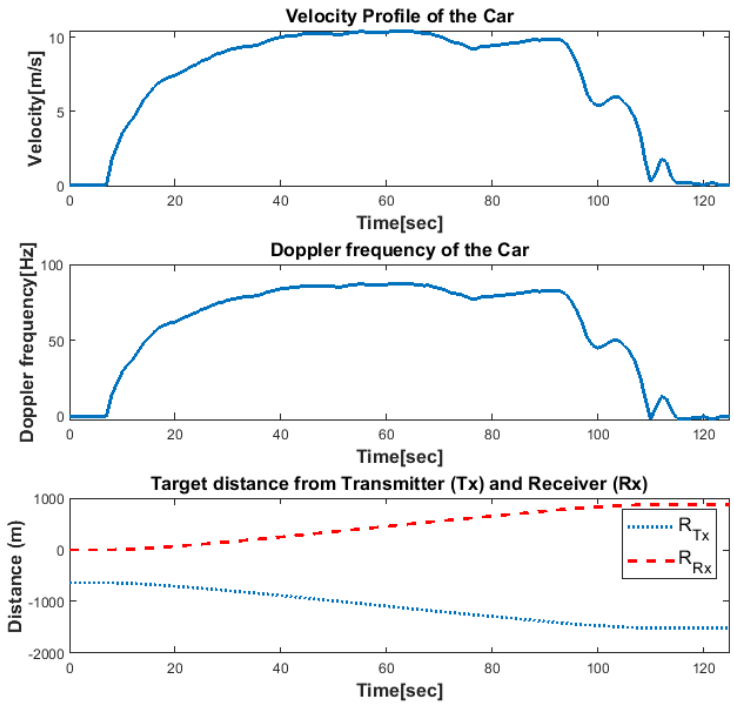

Figure 6.25: Result for a car moving towards the receiver

moving away from the receiver is 10.85 m/s (24.3 mph) at Doppler frequency -90.88 Hz. This agrees well with the velocity derived from the Doppler shift obtained in the range-Doppler map. For car moving towards the receiver data was taken from 1:06:15 PM to 1:08:12 PM. The velocity obtained from the GPS data is 8.2 m/s (18.3 mph) at Doppler frequency 68.4 Hz. This value also agrees well with the velocity derived from the Doppler shift in the range-Doppler map.

Figure 6.26 shows the GPS derived velocity profile and the measured Doppler frequency profile of the drone taken from 2:17:20 PM to 2:20:36 PM. Note that as previously described, the GPS plot is absolute velocity. From the results, it can be seen that the drone flew eight passes in close proximity of the surveillance antenna. Comparing the result with the range-Doppler map of the drone shown in

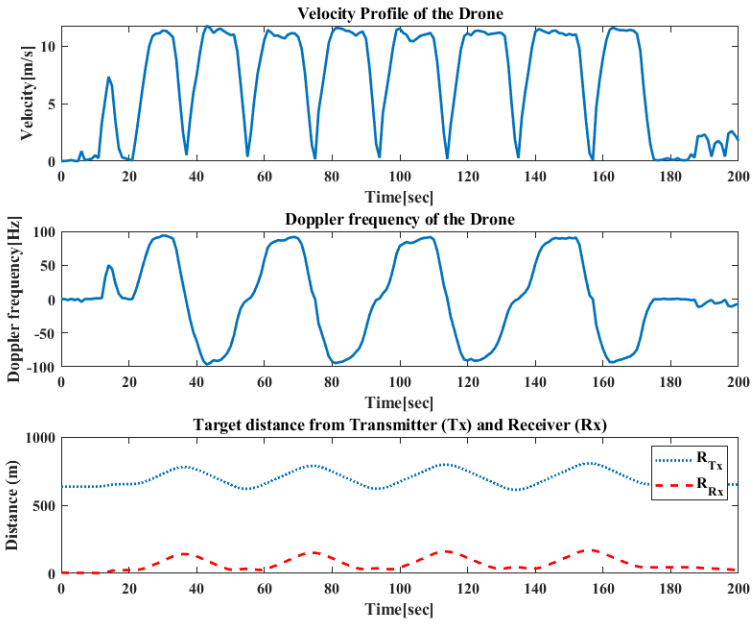

Figure 6.26: Result for a drone flew around with the proximity of receiver

Figure 6.18, it was found that there is good agreement between the profile and the instantaneous measurement. From the figure, at 48 seconds, the Doppler frequency is -86.2 Hz with the velocity of 11.3 m/s (25.3 mph) (the drone flying away from the surveillance antenna) and at 63 seconds (the drone flying towards the surveillance antenna), the Doppler frequency is 85.3 Hz with the velocity of 10.9 m/s (24.4 mph). These results show that there is good agreement between the range-Doppler maps and the ground-truth data. Furthermore, Figure 6.26 shows that the Doppler derived velocity and the GPS measured velocity are continuously in good agreement at all speeds.

These results clearly show that the targets were successfully detected using the Aveillant 3D staring radar as an illuminator of opportunity. Data from the experiments and GPS shows very good agreement between each other and thus proved

success of target detection. The summary of the result between these two data is presented in Table 6.1.

Table 6.1: Summary of the Doppler frequency detected from range-Doppler map and GPS data

	Range-Doppler map	GPS data
Car moving away	-90.07 Hz	-90.88 Hz
Car moving towards	68.9 Hz	68.4 Hz
Drone flying away	-85.5 Hz	-86.2 Hz
Drone flying away	85.5 Hz	85.3 Hz

6.7 Summary

This chapter demonstrated the exploitation of staring radar as an illuminator of opportunity in PBR application. This validates one of the basic concepts to detect target with the use of a reference channel. Because this type of illuminator is deterministic, a simulation of the signal was performed in order to understand the signal's characteristic. It was plotted and shown in Section 6.2. Next, an experiment was done in a passive bistatic configuration using three different targets. A person running, a moving car and a drone. This was carried out using a real deployment of the radars compared to previous chapter where experiments were done in a more controlled environments.

These targets were all successfully detected. Accurate measurements of Doppler shift and relative bistatic range were obtained. The most significant result was the accurate detection of the flying drone which was known to have a small radar cross-section (RCS) and was operating at a low altitude. These results show the ability of staring radar as an illuminator of opportunity in PBR due to its capability to

continuously provide illumination on targets over the entire 3D search volume. This shows that using PBR and staring radars to detect airborne (as opposed to ground) targets is feasible.

It was found in the processing that the direct signal interference was reduced by applying sidelobe reduction techniques to the reference signal. From the GPS data that was collected, the velocity profile and the total distance of the target were extracted. Comparison of this information to that obtained by the radar showed that the radar measurements were very accurate.

It was also shown that the frequency offset contributed by the receiver can be reduced with the use of the reference channel. However, there is still a modulation given by the receiver and this needed to be considered when processing the signal. In the next chapter, PBR target detection without the use of a reference channel will be presented.

Chapter 7

PBR Without Reference Channel

This chapter presents the experimental results of passive target detection using the Aveillant radar without a reference channel. The aim of this chapter is to study PBR without the use of a reference channel using the same data that was collected in Chapter 6. This enable comparison to be made between the system with and without a reference channel. A simulation of PBR using parameters from the staring radar is presented. This simulation is important to understand the effects of eliminating the reference channel and to better understand the experimental results. The geometry of the transmitter, the receiver and trajectories of the target is simulated, as well as the transmitted and received signals.

Scenarios that affect target detection are also simulated including direct signal interference. Due to the removal of the reference channel, matched-filtering is achieved by cross-correlating the signal with a digital copy of the transmitted pulse. Finally, experimental results of target detection without the reference channel, resulting from the same trial as described in Chapter 6, are presented.

7.1 Target Simulation

The simulation included three points in a 2D Cartesian coordinate system, denoted as the transmitter, the receiver and the target. The location of the transmitter was defined as (0,0) and the receiver was located at (0,-150). The receiver coordinate was chosen to simulate the experimental arrangement of Chapter 6. The target velocity was 10 m/s, comprising of both x and y components, and the position of the target with respect to time was

$$\begin{aligned} P_x &= X_0 + vt \\ P_y &= Y_0 + vt \end{aligned} \tag{7.1}$$

where X_0 is the initial x-position of the target, Y_0 is the initial y-position of the target, v is the velocity component in x and y of the target and t is the time.

Under this geometry, $R1$ is the range from the transmitter to the target, $R2$ is the range from the target to the receiver and $R3$ is the direct distance from the transmitter to the receiver. Due to the movement of the target, $R1$ and $R2$ are a function of time whilst because the transmitter and receiver are stationary, $R3$ is constant. This is called the baseline distance. These three ranges were calculated from the equations below as

$$\begin{aligned} R1 &= \sqrt{(Tx_x - P_x)^2 + (Tx_y - P_y)^2} \\ R2 &= \sqrt{(P_x - Rx_x)^2 + (P_y - Rx_y)^2} \\ R3 &= \sqrt{(Tx_x - Rx_x)^2 + (Tx_y - Rx_y)^2} \end{aligned} \tag{7.2}$$

where Tx_x is the x-position of the transmitter, Tx_y is the y-position of the transmitter, Rx_x is the x-position of the receiver and Rx_y is the y-position of the receiver.

Figure 7.1 graphically shows the geometry used during the simulation.

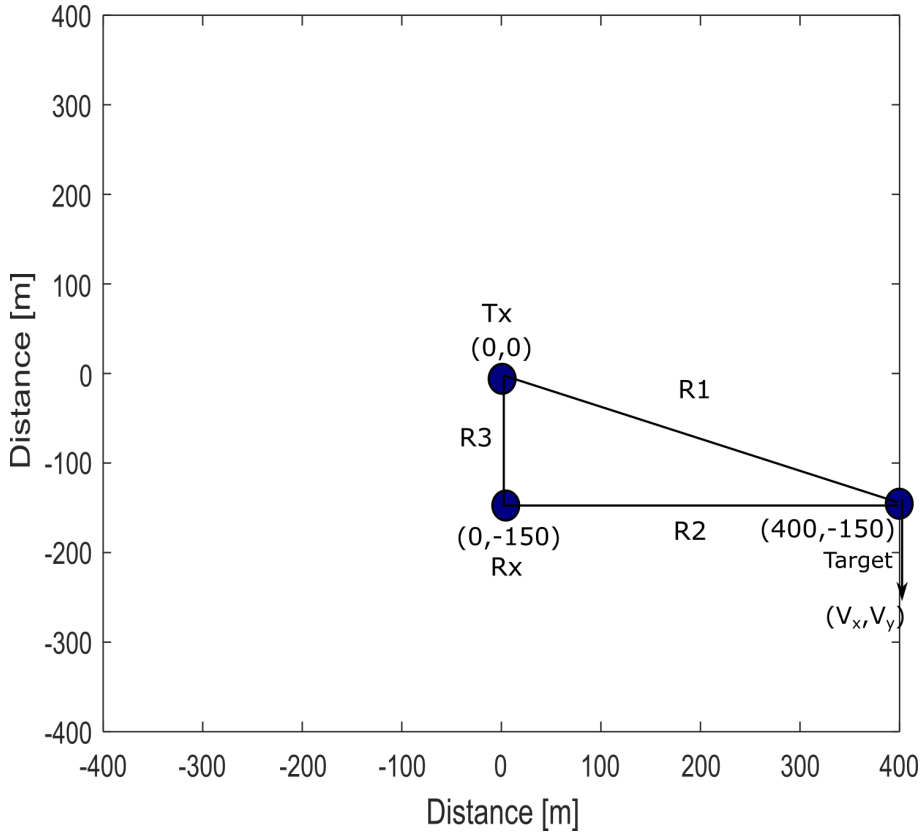

Figure 7.1: Plot showing the location of the transmitter at (0,0), the location of the receiver at (0,-150) and the starting position of the target at (400,-150). The target was moved with the velocity trajectory in xy direction which is expressed as (V_x, V_y)

The transmitted signal used in the model is a train of coded rectangular pulse. At the receiver side (Rx), the signal received from the target can be written as

$$\hat{s1}(t-t_0) = \sum_{j=0}^{\infty} x(t-t_0-j\text{PRI})e^{-j2\pi f_{tx}(t-t_0)} \tag{7.3}$$

where $s1(t-t_0)$ is the received signal with a time delay of t_0 given by $(R1+R2)/c$ and f_{tx} is the frequency of the transmitter (also called carrier frequency).

In a real scenario, there will be noise and interference coming from the environ-

ment and the instrument itself and the signal would be attenuated to propagation effects and the characteristics of the target. Because the radar transmitter and the receiver are non-cooperative, the LOs at the transmitter and the receiver are also independent, and therefore the received signal after down-conversion can be expressed as

$$\hat{s1}(t-t_0) = \sum_{j=0}^{\infty} x(t-t_0-j\text{PRI})e^{-j2\pi f_{tx}(t-t_0)}e^{j2\pi f_{LO}t}\sigma_n \tag{7.4}$$

where f_{LO} is the frequency of the receiver LO and σ_n is the propagation noise. Equation 7.4 can be simplified as

$$\hat{s1}(t-t_0) = \sum_{j=0}^{\infty} x(t-t_0-j\text{PRI})e^{-j2\pi (f_{tx}-f_{LO})t}e^{-j2\pi f_{tx}t_0}\sigma_n \tag{7.5}$$

where the frequency shift was shown in $f_{tx} - f_{LO}$ term. The direct signal from transmitter to the receiver after down-conversion can be written as

$$\hat{s2}(t-t_1) = \sum_{j=0}^{\infty} x(t-t_1-j\text{PRI})e^{-j2\pi f_{tx}(t-t_1)}e^{j2\pi f_{LO}t} \tag{7.6}$$

which is simplified to

$$\hat{s2}(t-t_1) = \sum_{j=0}^{\infty} x(t-t_1-j\text{PRI})e^{-j2\pi (f_{tx}-f_{LO})t}e^{-j2\pi f_{tx}t_1} \tag{7.7}$$

where $\hat{s2}(t-t_1)$ is the direct signal from transmitter to the receiver which does not depend on the trajectory of the target and t_1 is given by $R3/c$. This signal also contains the frequency offset term f_{fLO}.

In the simulation, 140 pulses were transmitted corresponding to a 20 ms integration time. The coded transmit signal was constructed with the frequency offset included in the signals based on Equations 7.5 and 7.7. The effect of the coded and

modulated frequency offset signal is shown in Figure 7.2.

The total echo signal for the signal at the receiver is $\hat{s1}(t-t_0)+\hat{s2}(t-t_1)$, this is the signal from the transmitter-target-receiver and the direct signal from the transmitter to the receiver. The total echo signal in the time domain then was split into slow-time and fast-time and placed in a matrix for matched-filter processing. This was done by reshaping the total echo signal to the length of F_s/PRF in every row of PRI (under the assumption of a known PRF).

The matched-filter is a cross-correlation of the received signal and a software copy of a transmitted pulse, that is a rectangular pulse with the same pulse width as the transmitted signal. The reference signal was cross-correlated with each row of the received signal matrix.

Finally, to decode the signal from the staring radar, the signals were multiplied with all possible combination of the transmitted code. By multiplying these signals with the code, the phase of each pulse was corrected and this is an important step because if the matched-filter is not multiplied with the correct code, the Doppler frequency obtained will be ambiguous.

The output of the matched-filter gives the range profile map. This output contains only the apparent range information of the target. The Doppler frequency of the target was found by applying an FFT to the output of the matched-filter results. The end result from the FFT is the range-Doppler map of the target. The process of producing the simulated signal is shown in Figure 7.2 where each step of the processing is also shown.

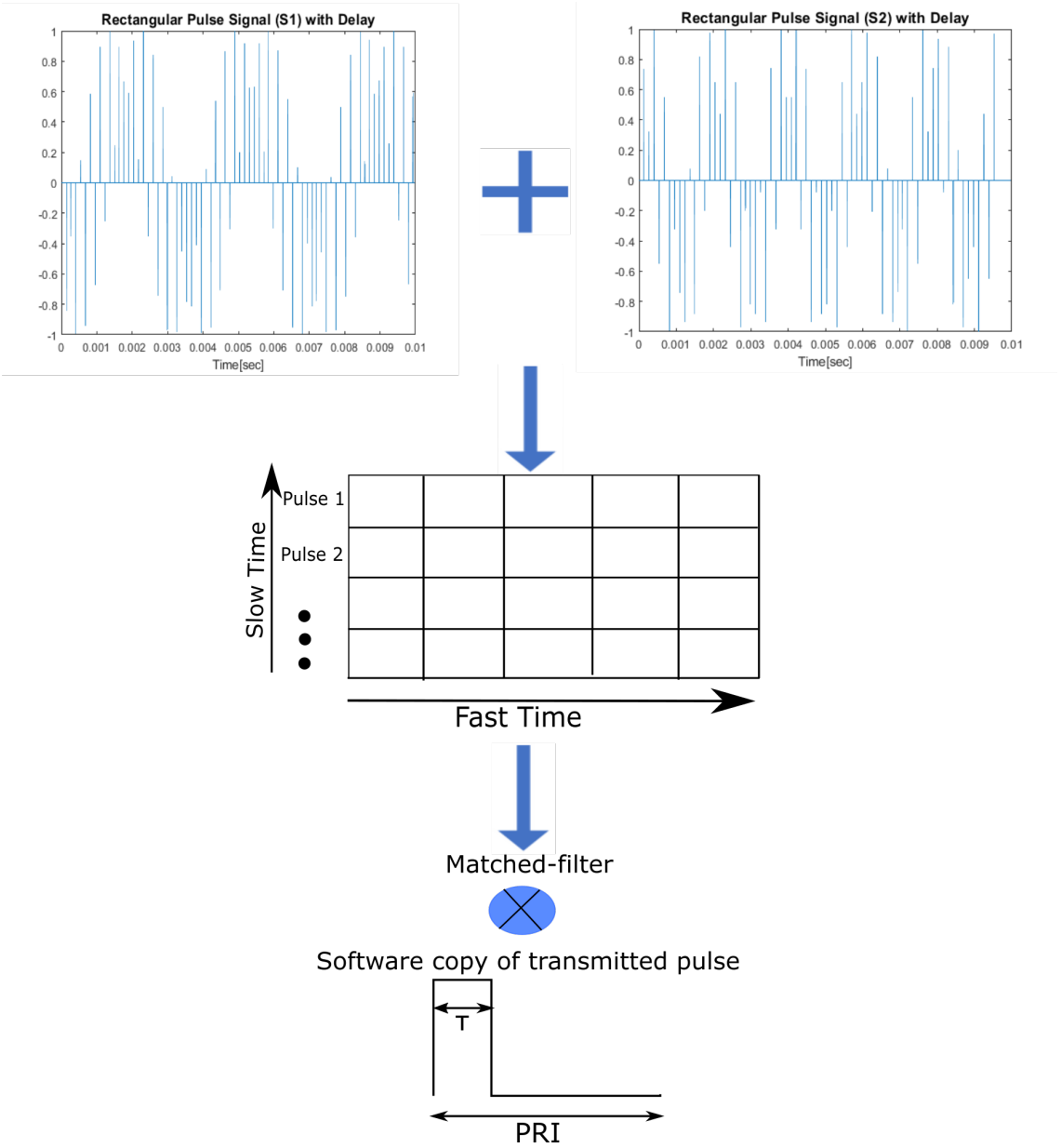

Figure 7.2: Figure on the steps of simulating signal for target detection without the reference channel. At the first stage, two signals were added together which this is the signal from transmitter-target-receiver and transmitter-receiver path. This signal then was break into slow time and fast time where the first row is the pulse 1 and so on. After that, each pulse from each row was matched-filtered (MF) with a software copy of a transmitted pulse at PRI

7.2 Simulation Results

In this section, results obtained from the simulation described in the previous section are shown. In the previous section, the radial component and the range of the target was formulated and this can be used to calculate the theoretical value for the Doppler frequency induced by the target.

Firstly, the range of the target was calculated using Equation 7.2, which results in $R1$=427.4 m, $R2$=400.2 m and $R3$=150 m. Based on these values, the bistatic angle for the target was determined by applying Equation 4.3. The bistatic angle β for the trajectory of the target is 20.54° and δ was estimated at 169.73°. Based on the β and δ value found, the Doppler frequency for the simulated target(calculated using Equation 3.42) was expected to be -81.32 Hz. The frequency offset is 500 Hz.

The calculated Doppler value, is negative which shows that the target is moving away from the transmitter and the receiver. It was expected that there will be two returns; one from the direct signal and the other from the target echo signal. The integration time for the simulation is 20 ms, which gives a frequency resolution of 50 Hz (obtained from $1/T_{int}$). However, to get better frequency resolution which is important when there is more than one target present, the dwell time can be increased. By increasing the dwell time, more pulses are sent and recorded which results in a narrower target response in Doppler.

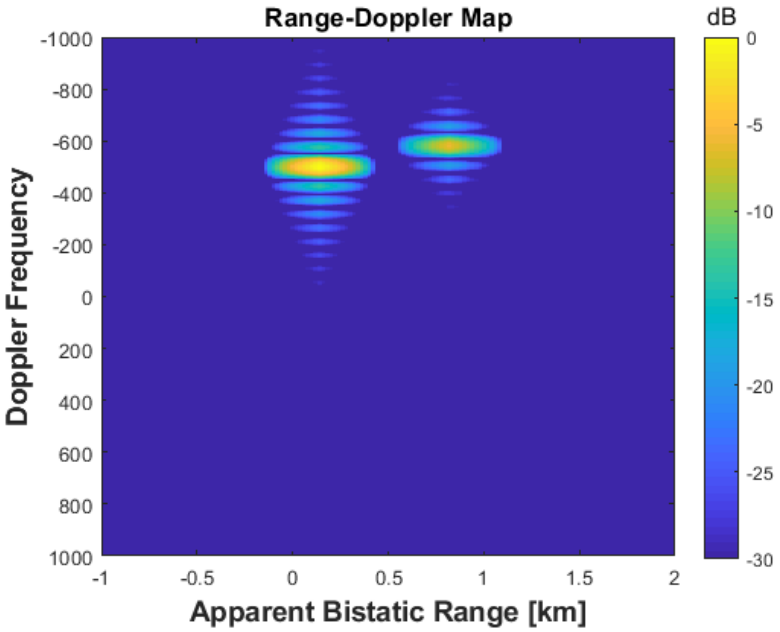

(a) Range-Doppler map for the received signal with the frequency offset at the receiver using combination code 1

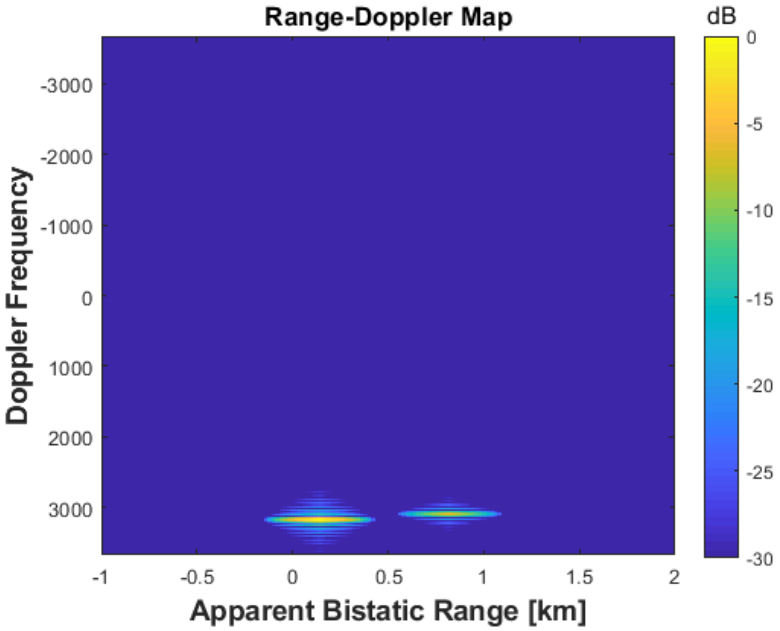

(b) Range-Doppler map for the received signal with the frequency offset at the receiver using combination code 2

Figure 7.3: Range-Doppler maps for the received signal with the frequency offset using two different code combinations

Figure 7.3a shows a range-Doppler map for the signal received at the receiver produced by the simulation using combination code 1. From the figure, it can be seen that there are two responses present. These responses are the two received signals, $\hat{s1}$ which contains the information of the target's velocity and trajectory and $\hat{s2}$ which is the direct signal from the transmitter to the receiver. The direct signal needs to be removed from the result as only the received signal $S1$ is of interest.

The shift in the figure is due to the frequency offset between the receiver and transmitter LOs which moves the direct signal from the transmitter away from zero-Doppler. The shift is applied to both the signals at the receiver and shifts the Doppler frequency from the accurate reading. This shift also makes the results look like there are two moving targets even though the direct signal has no Doppler shift. The direct signal is characterised by the frequency obtained from the two responses. Note that one of the responses has a frequency Doppler at 500 Hz which is the frequency offset of the receiver LO (f_{LO}). The direct signal was resolved from the highest response in the figure. Because of the received signal contains noise, the response was lower compared to the direct signal. It was shown in the figures that the direct signal have strong return while the return from the received signal around -5 dB lower.

The other combination of the code is shown to observe if wrong code was used as shown in Figure 7.3b. It can be seen in the figure the two responses were moved. The responses have a positive Doppler shift whereas a negative Doppler shift was expected based on the motion of the target. Note the response is now moved to PRF/2 minus the frequency f_{LO}. This is because all wrong code pushes to all PRF. The calculated value is 3176.5 Hz while the value obtained from the range-Doppler

map is 3177 Hz. It can be seen in Figures 7.3a and 7.3b different code combination yield to different direct signal frequency response. At this stage, the correct code combination is significant.

Figure 7.4 shows a range-Doppler map for the signal received at the receiver after the DC conversion using two different code combination. Comparing this figure with Figure 7.3, the two responses are moved to different positions due to the DC conversion. This process was applied to the received signals in the time-domain, where the frequency of the maximum response being found first.

The DC conversion was achieved by mixing to the frequency of the peak response (f_{max}). The frequency f_{max}, used in the carrier frequency term ($e^{-j2\pi f_{max}t}$), was multiplied with the data matrix containing the received signal. This process achieved the down-conversion of the received signal to the carrier frequency of the transmit signal. After this process, the Doppler shift is at the correct frequency where the response is -82.58 Hz.

It can be seen in Figure 7.4 after DC conversion, using different code combination did not effect the results. Both result shows the same response where direct signal was moved to zero-Doppler frequency. At this stage it can be concluded that after DC conversion, using different code combination did not give significant effects on the results. In addition, the Doppler resolution in the simulation is limited by the number of pulse transmitted. Result shows that the DC conversion was successful. It can also be seen in the figure that the direct signal was moved to zero Doppler frequency as expected.

The results presented in previous figure show that there is a frequency offset present in the receiver system. A question that may arise is for the system that

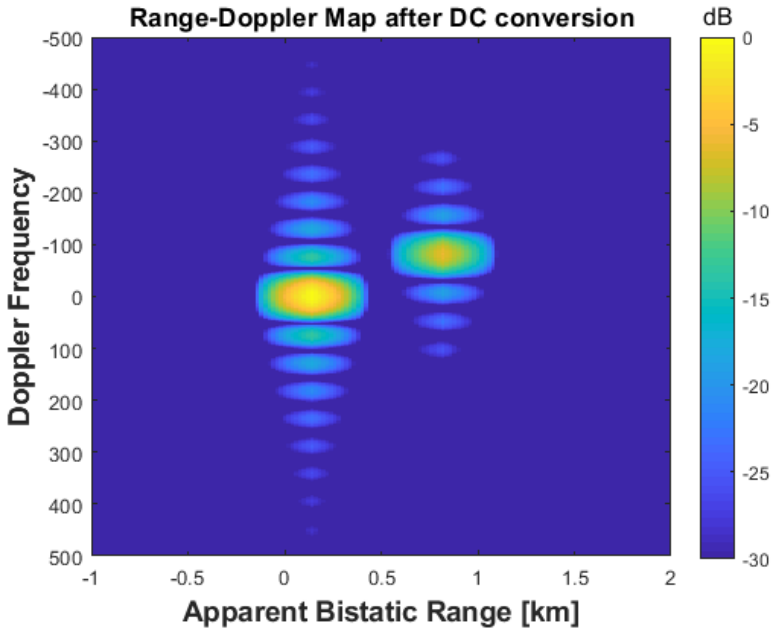

(a) Range-Doppler map for the received signal after DC conversion using combination code 1

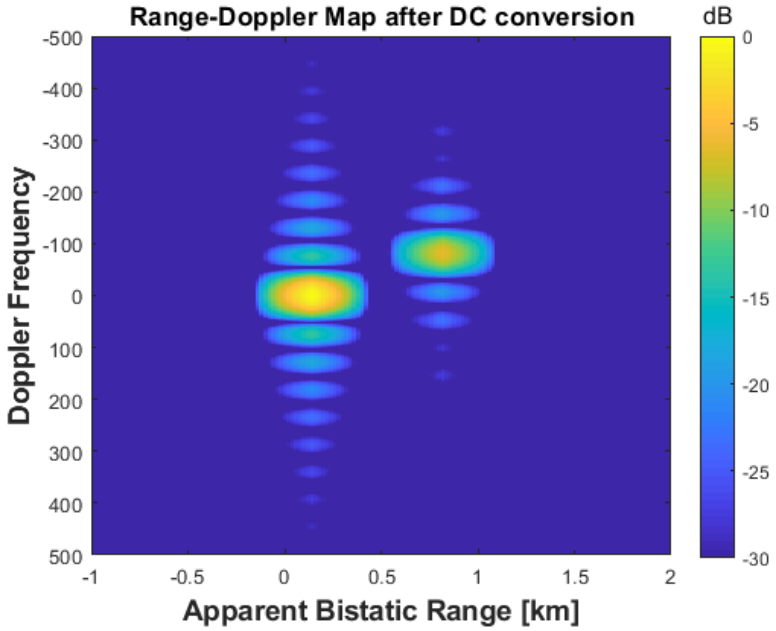

(b) Range-Doppler map for the received signal after DC conversion using combination code 2

Figure 7.4: Range-Doppler maps for the received signal after DC conversion using two different code combinations

does not have frequency offset. Can the same processing be applied? Does the code remain insignificant after DC conversion?. To answer these questions, simulations were repeated without the frequency offset.

Figure 7.5 shows the range-Doppler maps for the received signal without the frequency offset at the receiver. It can be seen in Figure 7.5a, the coded signal without the frequency offset was shifted to PRF/2. There is also two sets of responses at positive and negative Doppler. The Doppler frequency from the direct signal is found at 3676 Hz which this is also the frequency obtained from PRF/2. The target response however is found to be more obvious at positive Doppler with Doppler frequency around 3595 Hz and no response at negative Doppler. This result shows that the direct signal and target response was broken at PRF/2. Because the target response have Doppler shifts, it is more obvious in one region than the other.

After the DC conversion, both responses was moved. Figure 7.5b shows that the response from the direct signal is moved to zero-Doppler and the target response moved to correct Doppler frequency. From these results, it can be conclude that the same processing can be applied even without frequency offset. It was also proved that coded signal does not effect the processing once DC conversion was applied.

Figure 7.6 shows a range-Doppler map for the signal received after DC conversion and zero-Doppler removal. The purpose of zero-Doppler removal is to remove stationary targets. This was done by finding the mean or average value of the data (after DC conversion) and subtracting that mean value from the data. Note that the direct signal has been removed and only the target response remains. The Doppler shift in this figure is the same as the Doppler shift seen in the DC converted result (-82.58 Hz) showing that mean value removal is not altering the result. There is 1

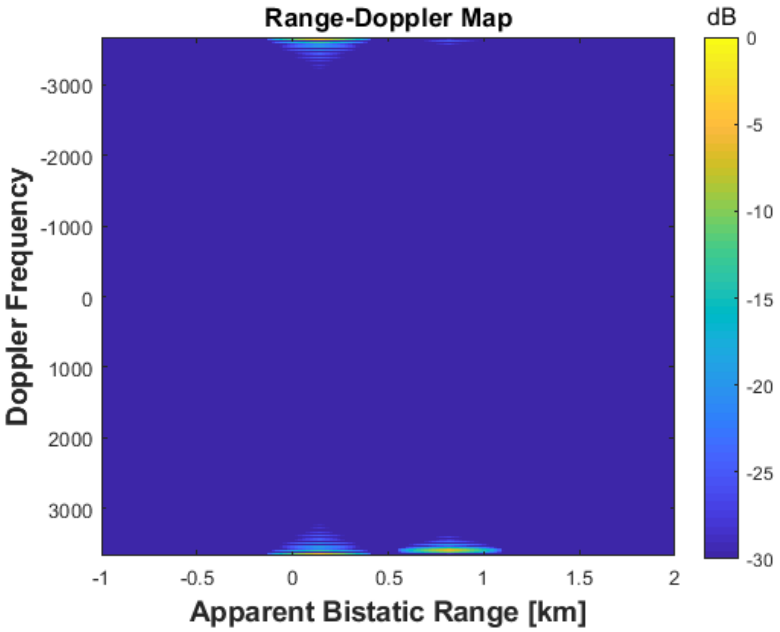

(a) Range-Doppler map for the received signal without the frequency offset

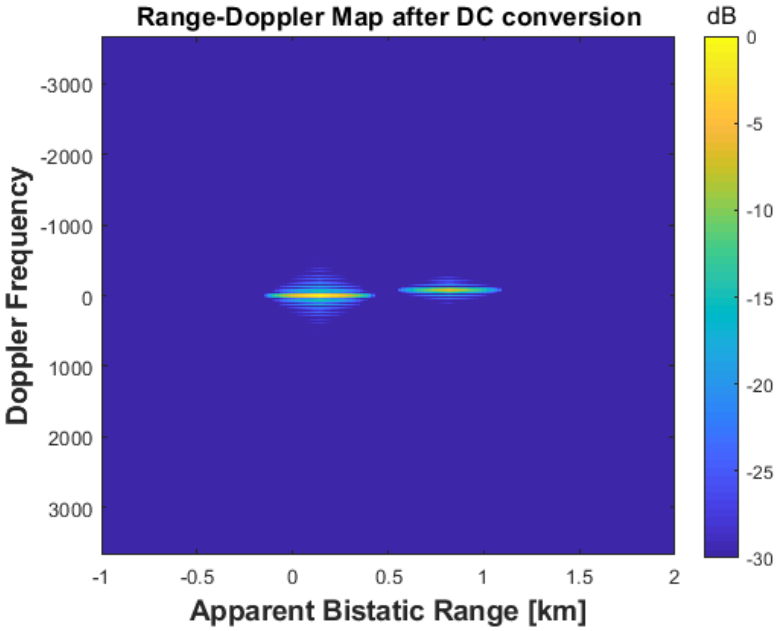

(b) Range-Doppler map for the received signal after DC conversion without the frequency offset

Figure 7.5: Range-Doppler maps for the received signal without the frequency offset at the receiver

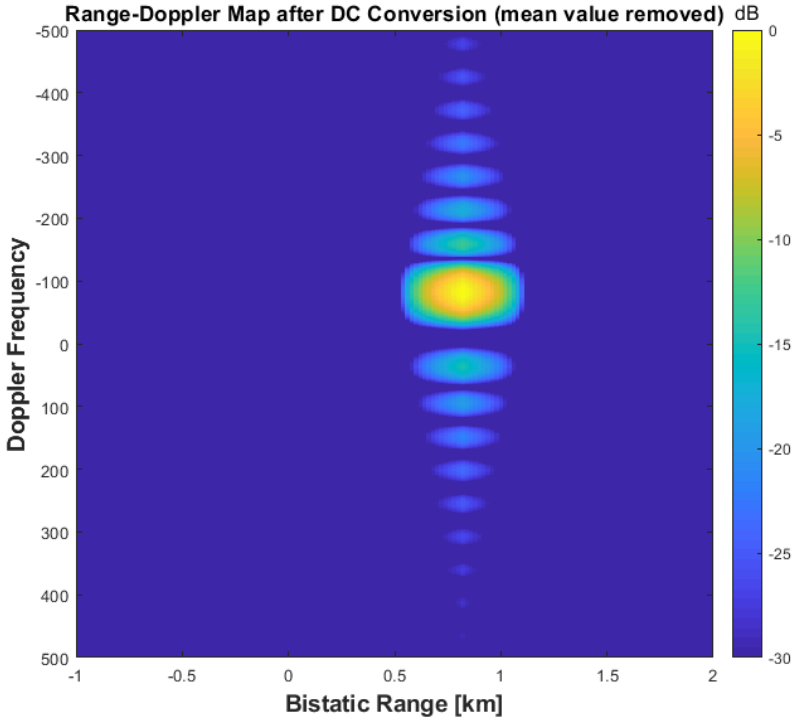

Figure 7.6: Range-Doppler map for the received signal after DC conversion with mean value removal

Hz difference from the calculated value. This difference is acceptable because the Doppler resolution in the simulation is 50 Hz as previously mentioned.

The PBR simulation has successfully shown that a target can be detected without the use of a reference channel and that DC conversion and mean value removal can work correctly once the frequency offset has been estimated. It was also shown in the simulation coded signal did not give any significant effect in processing the signal after DC conversion was applied, provided knowledge of a strong stationary reflector or direct signal. The same processing can also be applied if there is no frequency offset presents in the system. Even though the receiver system experienced carrier frequency offset and the direct signal interference, it was possible to successfully extract the Doppler frequency shift of a moving target. In the next section, Doppler

results with real data without a reference channel will be presented.

7.3 Reference Channel Removal

Based on the processing used in the simulations, it was shown that the target could be detected without the use of a reference channel. The detection was improved by identifying the Doppler bin containing a stationary target for the direct signal from the transmitter to estimate the frequency offset and implement a DC conversion and clutter removal.

In a bistatic radar, the reference channel is key to estimate the target bistatic range. By removing the reference channel, target range information is no longer available but tracking is still possible. In a typical PBR, target range is found by cross-correlating the signal from the reference channel with the surveillance channel. Nonetheless, in this thesis, by exploiting deterministic signals the passive receiver becomes less computationally expensive, smaller and even lower cost at the expense of the measurement of the bistatic range.

In this thesis, we assume the prior knowledge of the radar signal. With knowledge of the type of signal transmitted, a rectangular pulse with pulse width $\tau = 1\mu s$ was constructed. This rectangular pulse signal was used in place of the reference signal and cross-correlated with the surveillance signal. Because of time synchronisation with the radar is random, the range obtained from the cross-correlation is not the relative bistatic range, but an apparent range.

The demonstration of target detection without the reference channel used the

same targets and the same data set as in Chapter 6. This enables comparisons to be made between the two studies. There were several challenges faced when extracting targets without the use of a reference channel. The first challenge is coming from the hardware. As shown in Chapter 5, there is a carrier frequency offset introduced by the system due to the two LOs used. It was found that applying an external 10 MHz reference signal to both of the hardware reduced the effect of the frequency offset. However, in this experiment, because the radar and the receiver is non-cooperative and have independent LOs, the system also introduces different LO frequencies. As shown in the previous section, it is possible to remove it using DC conversion and thus, extract only Doppler frequency.

The second challenge is in the cross-correlation stage. Because F_s/PRF is not an integer, this introduces shift in slow-time (in every pulse in the data matrix). To demonstrate this effect, results from the surveillance signal without target are first shown and discussed. The surveillance stationary signal was captured when the surveillance antenna was operating in vertical polarisation with an integration time of 50 ms. Figure 7.7 shows the effect on the range-profile map caused by the inconsistency in the data matrix.

It can be seen in Figure 7.7 that the yellow line of maximum response is tilted. This is the result of the cross-correlation between surveillance signal and one pulse of rectangular signal. This incoherency must be fixed because it will give an undesired range migration. In the range-profile above, when forming the data matrix, the vector signal was reshaped to the length of F_s/PRF. This is only accurate for the first pulse that was received and if the signal is constantly received within the exact window. Because the received signal length is not integer of PRI when it was reshaped to F_s/PRF, errors occurred. If this errors is not addressed, it will be

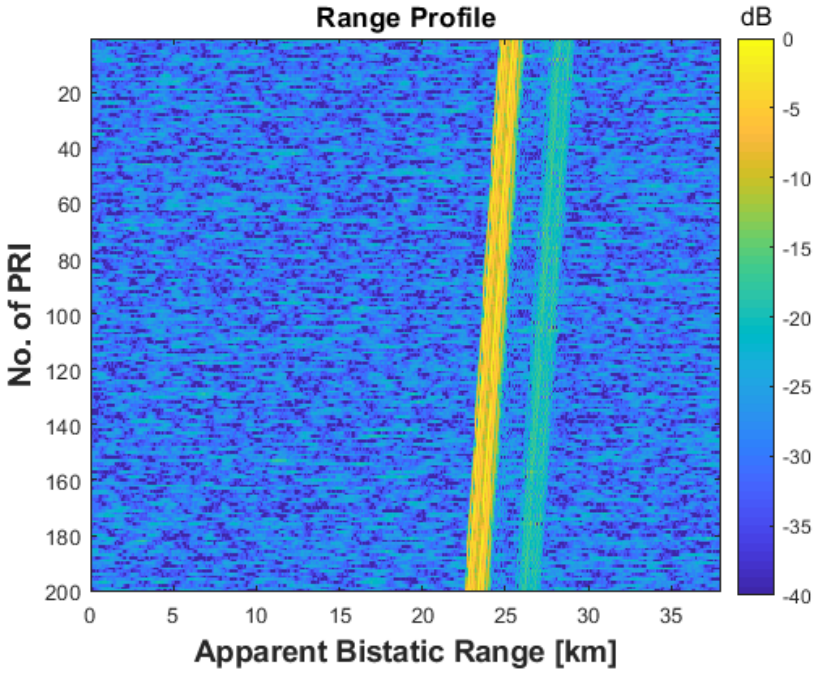

Figure 7.7: Range-Profile after cross-correlation of surveillance stationary signal and a pulse of rectangular signal

accumulated with slow time. This was fixed by finding the correct index to split the signal. The index was found from the first point from $t > m * \text{PRI}$ where m is the number of received pulse and t is the signal length. Then, this index was used to define the length of the each row of the matrix. The result of applying this improvement is shown in Figure 7.8

Figure 7.8 shows the range-profile map after cross-correlation when the signal was split using the correct indices. It can be seen that the yellow line is now vertical. The line has also moved slightly because the new index only select the signal within its length and ignored the remaining signal. Figure 7.7 shows that there is background noise and Figure 7.8 shows that the background noise is removed. This is because in Figure 7.8 only the part that contained target is selected.

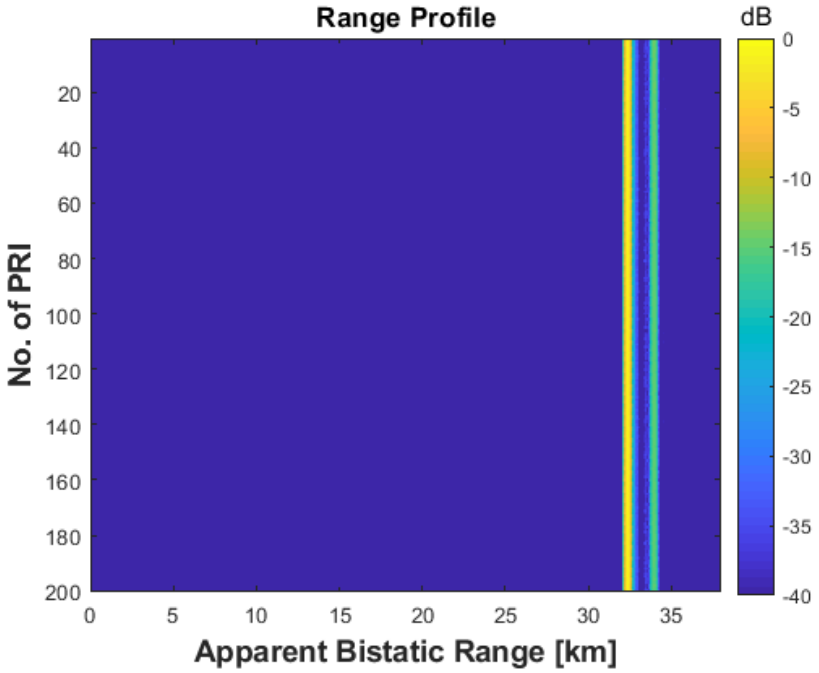

Figure 7.8: Range-Profile after cross-correlation of surveillance stationary signal and a pulse of rectangular signal after index's improvement

As mentioned in Chapter 6, the surveillance signal was down-converted to a frequency of 1.253 GHz due to the undesired modulation which occurred at zero frequency. In this chapter, the down-conversion processing is the same as that in the previous chapter. By converting the signal to zero frequency, after a low-pass filter to remove the system non-idealities, windowing could be applied in the frequency domain before cross-correlation. For this work, a Hamming window was chosen as this was found to work well.

The Hamming window was applied to the frequency spectrum of the surveillance signal. This windowing widens the mainlobe of the Doppler spectrum. After windowing in the frequency domain the signal must be converted back to time-domain for cross-correlation. The signal was converted back to the time-domain by performing an IFFT, in order to cross-correlate the surveillance signal with the constructed

reference signal.

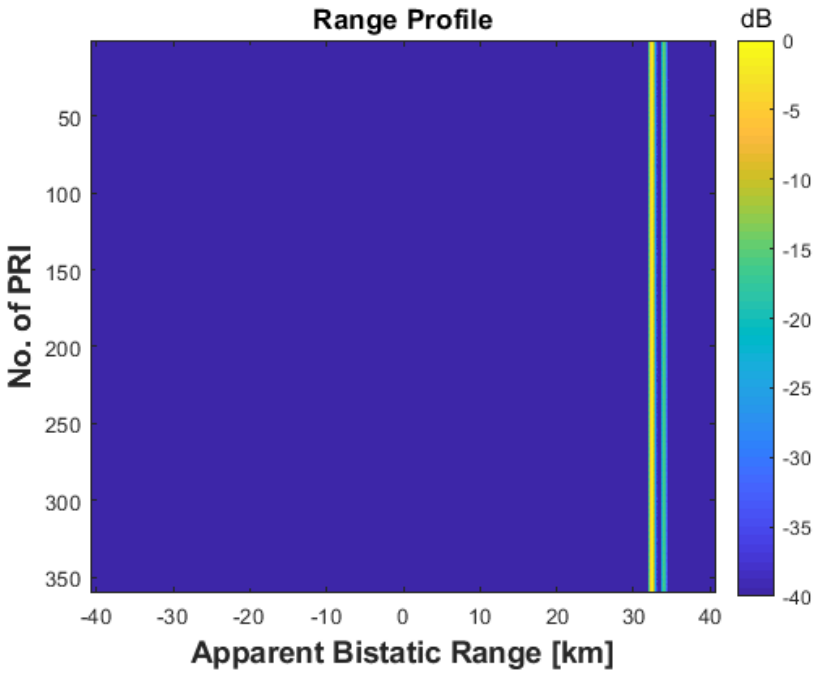

Figure 7.9: Range-Profile after cross-correlation of surveillance stationary signal and a pulse of rectangular signal after windowing

Figure 7.9 shows the result after windowing was applied to the surveillance signal before the cross-correlation. Windowing results in lower sidelobe. As mentioned before, the cross-correlation still gives the range information, however, this is an apparent range. The apparent range is the result of cross-correlating the surveillance signal with a digital rectangular pulse in every row matrix.

The processing was continued in order to extract a range-Doppler map from the signal. The range-Doppler map was created by applying an FFT to the output of the matched-filtering operation. However, because the signal from the staring radar was coded, the signal needed to be multiplied with the code in each row of the matrix. To do this, a new matrix with the same size as the surveillance signal's matrix was formed, containing the code. Then, this coded matrix was multiplied element by

element with the surveillance signal's matrix. Finally, the range-Doppler map was produced by applying FFT to the coded surveillance signal. As mentioned in the simulation section, before the DC conversion, any code combination is significant. So, random code combination was used because after the DC conversion, the code does not give any effects on the target response.

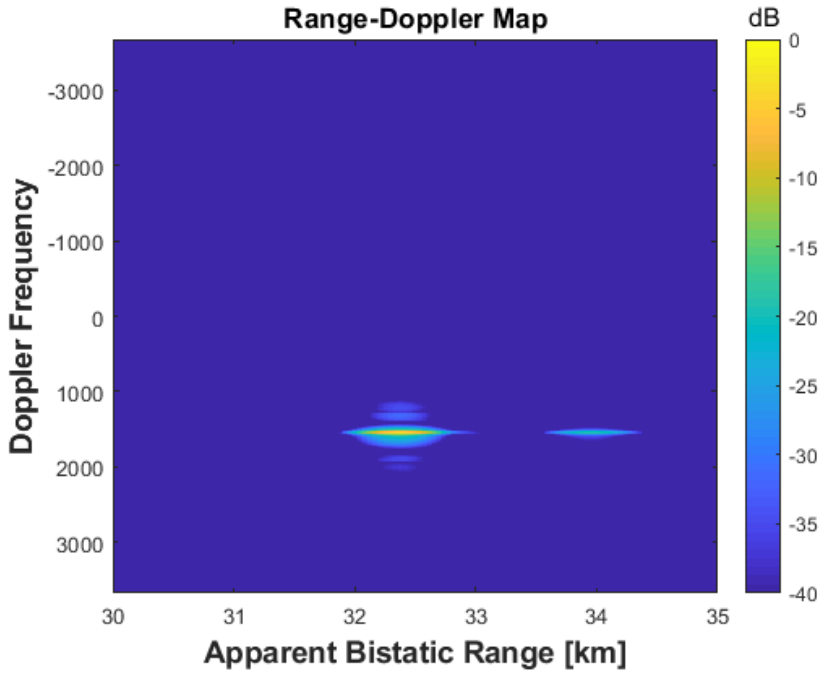

Figure 7.10: Range-Doppler map for the stationary signal

Figure 7.10 shows the result of range-Doppler map of the surveillance stationary signal. This shows that the signal gives false Doppler values for the stationary signal, the response (shown in yellow) should be at zero Doppler. This result suggests that there is a frequency offset present in the surveillance signal. As shown in the previous section, the frequency offset was removed using the DC conversion process.

To recap, the DC conversion was done by finding the Doppler bin containing the stationary clutter. This was estimated as the bin containing the maximum value in the range-Doppler map before the DC conversion, and extracting the frequency of

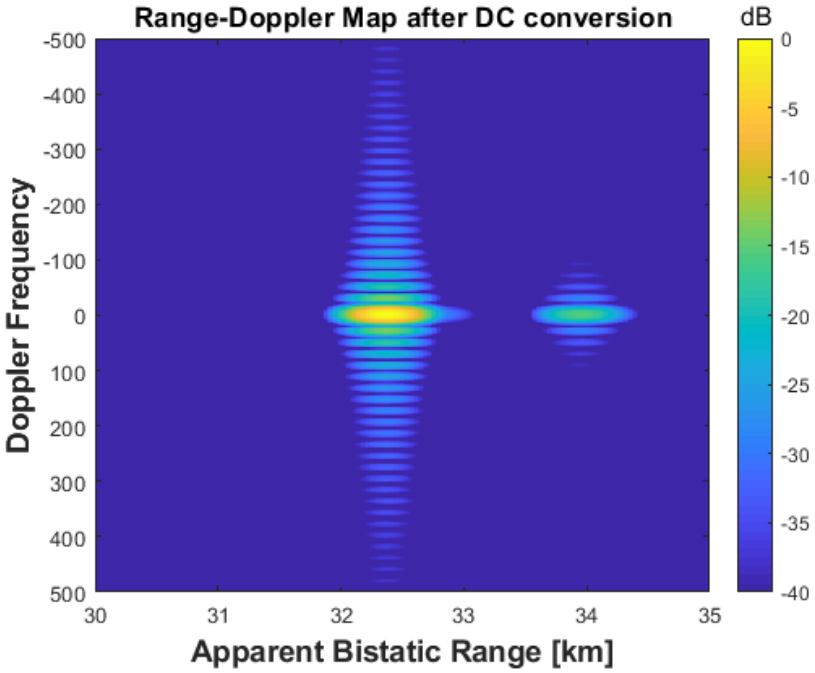

Figure 7.11: Range-Doppler map for the stationary signal after DC conversion

that maximum value. Then, this frequency was used in the carrier frequency term ($e^{-j2\pi f_{max}t}$) and multiplied with the coded surveillance signal in order to remove the frequency offset.

Figure 7.11 shows the resulting range-Doppler map after DC conversion. In the figure, it can be seen that the stationary response has now moved to zero Doppler frequency. Mean value removal was then applied in order to remove the stationary response. At this point, windowing can be applied again. The windowing was performed in the time-domain, hence the signal was improved in Doppler dimension by lowering the sidelobes. The final result is shown in Figure 7.12.

Figure 7.12 shows a range-Doppler map for the surveillance signal with reference channel removal. It can be seen in the figure that windowing in the range dimension reduced the sidelobe but widened the mainlobe when compared to Figure 7.11. The

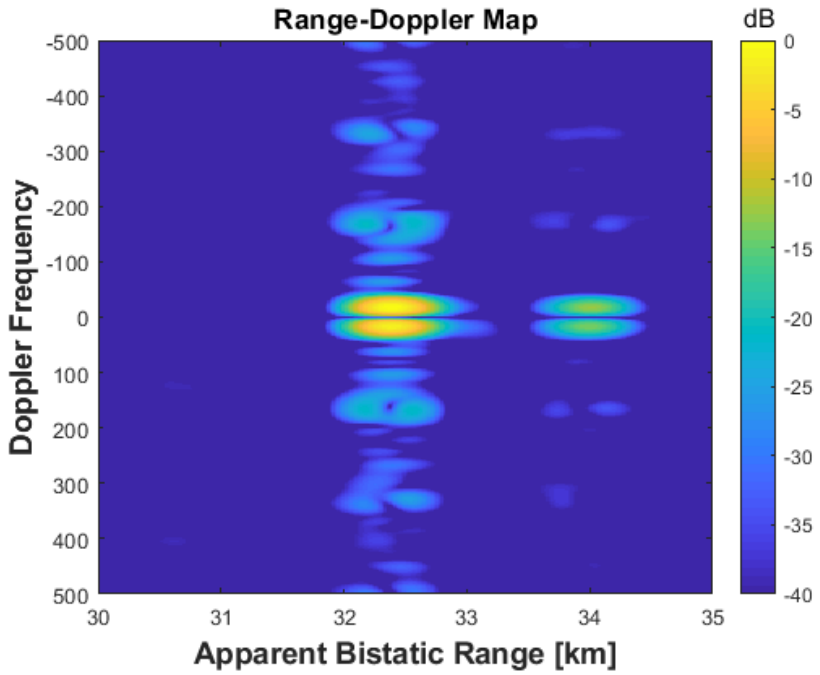

Figure 7.12: Range-Doppler map for the stationary signal. Result shows the range-Doppler map after mean value removal and windowing was applied

effect of windowing in the results was very significant because it was applied in both Doppler and range dimensions. It was shown in the result the sidelobes were reduced and the mainlobe is widened.

Figure 7.12 also shows the clutter spectrum around the zero Doppler region. These maybe caused by the clutter from the ground reflections or from the receiver system. Because the received antenna was pointing towards the target which is on the ground, it also illuminated the ground.

This effect can be seen clearly in the Doppler-cut shown in Figure 7.13. This Doppler-cut was taken from Figure 7.12. It can be seen in the Doppler-cut that the clutter responses had a Doppler bandwidths. The Doppler detected from the two peaks were -17.46 Hz and 17.46 Hz corresponding to the speed of 2.1 m/s (4.7 mph).

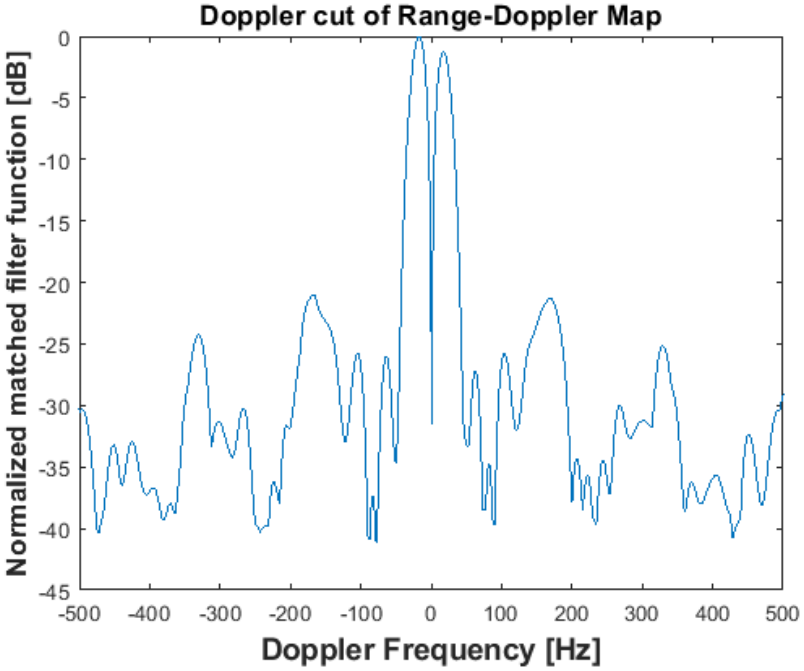

Figure 7.13: Doppler-cut for the stationary signal. Result shows the clutter response happened at negative and positive Doppler

There is two peaks detected in the Doppler because it was taken from Figure 7.12 where the DC component is zero. This clutter might be a moving object that was captured in the antenna sidelobe such as trees moving back and forth in the wind or from the vibrations in the passive receiver system.

This section outlined the processing of real data containing a stationary target. Processing without the use of a reference channel was explained. Methods for improving target detection in the presence of an offset in the receiver were also shown. The final result shows that there is clutter with a Doppler shift in the range-Doppler map. This clutter Doppler spreads needs to be noted when processing the data that contain moving targets.

7.4 Target Detection Without Reference Channel

The data used here are the same as in Chapter 6 for a person running, a moving car and a flying drone. The reference channel was ignored and data was processed using the algorithm presented in Section 7.3. Results obtained in this experiment will be compared with the results in Chapter 6, so, it is important to use the same processing parameters used in Chapter 6. One of them is the number of FFT points. This is important because it will determine the sampling of the Doppler frequency spectrum obtained from the experiment without the reference channel. The remaining parameters such as sampling frequency and integration time were also the same as those used in the target detection with the reference channel.

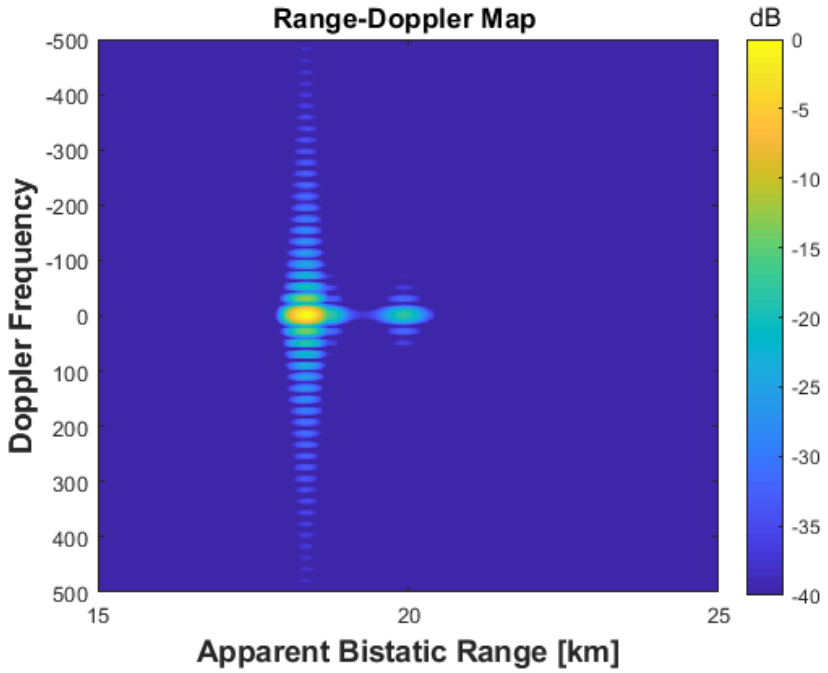

Figure 7.14: Range-Doppler map for a person running away from the receiver before mean value removal

The first result without the use of a reference channel is shown in Figure 7.14

for a person running away from the receiver. The number of pulses received and the integration time for the processing are the same as in Chapter 6. This result shows that there is a strong response around zero Doppler. This response is the clutter which concealed the target. The zero Doppler clutter can be removed by applying mean value removal which will remove any stationary clutter.

Figure 7.15a shows the range-Doppler map obtained after mean value removal. It can be seen in the figure that the clutter spread is wide and the target response cannot be seen clearly. However, the Doppler cut can be used to observe the presence of the target. Figure 7.15b shows the Doppler-cut for a person running away from the receiver. It can be seen in the results a high peak that suggests a response from the target.

From the highest peak response in the Doppler-cut result, the Doppler frequency obtained is -39.52 Hz corresponding to radial velocity of 4.7 m/s (10.5 mph). In this result, it was also found that the positive clutter Doppler spread is the same obtained in Section 7.3. The positive clutter was found to be at 17.46 Hz while for the negative clutter, it cannot be seen directly from the figure. However, note that there is a small peak that has merged with the peak response. This response was found at -17.46 Hz which is the same value obtained from the negative clutter Doppler spread.

Figure 7.16 shows the range-Doppler map obtained for a person running towards the receiver. The result shows similar response as the one obtained from a person running away from the receiver. There is a strong response at zero Doppler which swamped the target. The clutter at zero Doppler is removed by mean value removal.

The results for a person running towards the receiver after mean value removal

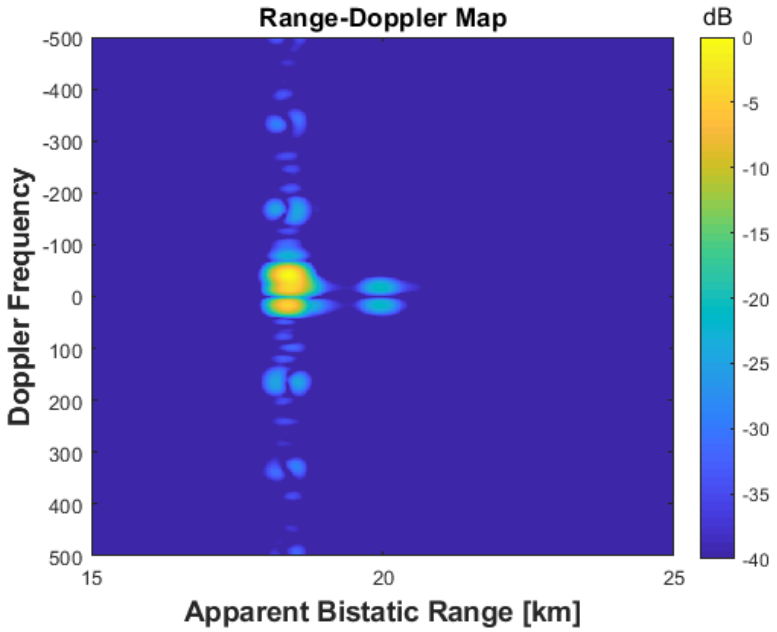

(a) Range-Doppler map for a person running away from the receiver

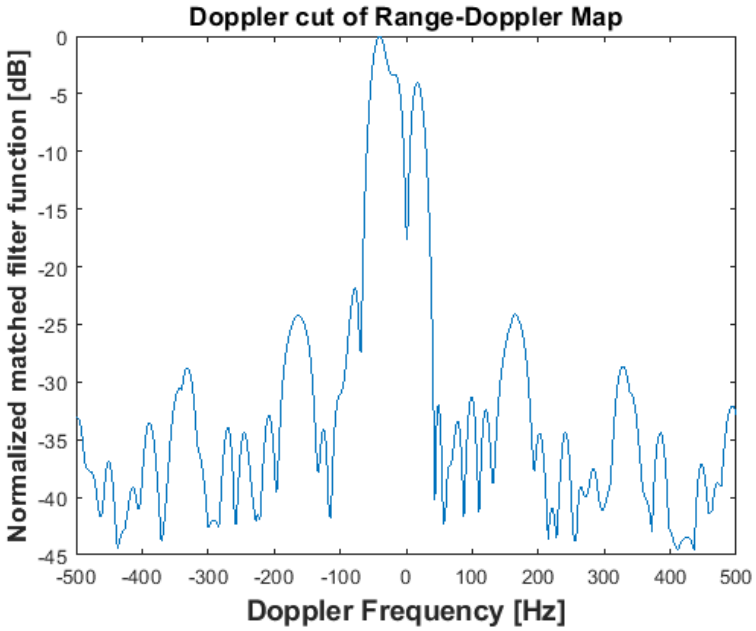

(b) Doppler-cut for a person running away from the receiver

Figure 7.15: Results for a person running away from the receiver after mean value removal and windowing with the top figure is the range-Doppler map and the bottom figure is the Doppler-cut

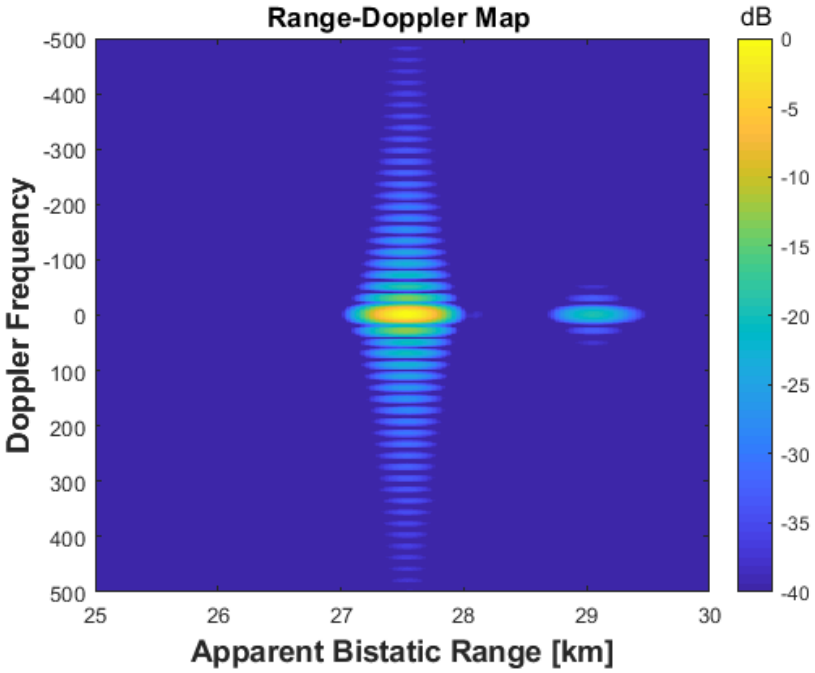

Figure 7.16: Range-Doppler map for a person running towards the receiver before mean value removal

are shown in Figure 7.17. In the range-Doppler map shown in Figure 7.17a, the response from the target was merged with clutter. This is the same as seen when the person was running away from the receiver. The peak response that was obtained from the range-Doppler map is at 22.98 Hz corresponding to 2.8 m/s (6.2 mph) and this value agrees with the Doppler-cut. As can be seen in the Doppler-cut, the Doppler frequency from the target has merged with the clutter.

Result from a person running shows different target response. For a person running away from the receiver, the Doppler frequency obtained is -39.52 Hz while for a person running towards the receiver, the Doppler frequency obtained is 22.98 Hz. This difference maybe from the effect of the clutter where the reflected echo from a person running towards the receiver is weaker and therefore it is more difficult to separate it with the clutter. It can be seen in both of the results that the clutter

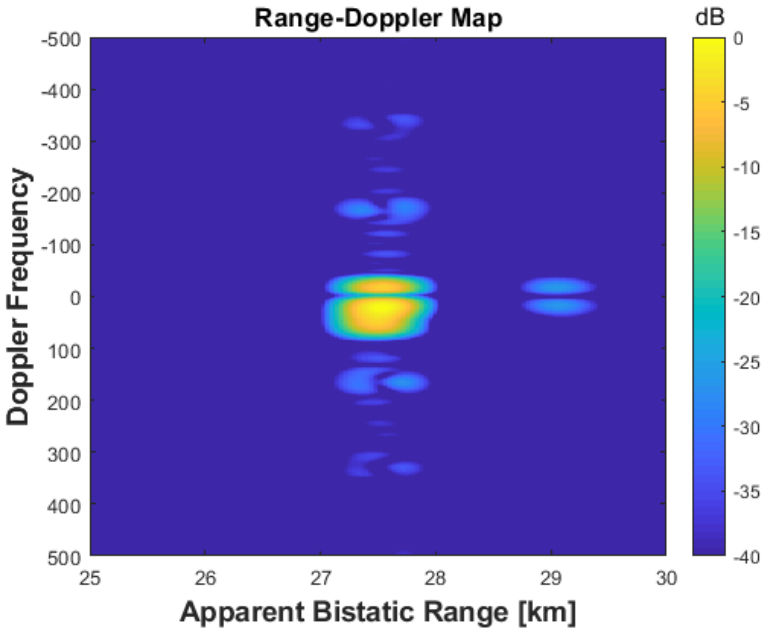

(a) Range-Doppler map for a person running towards the receiver

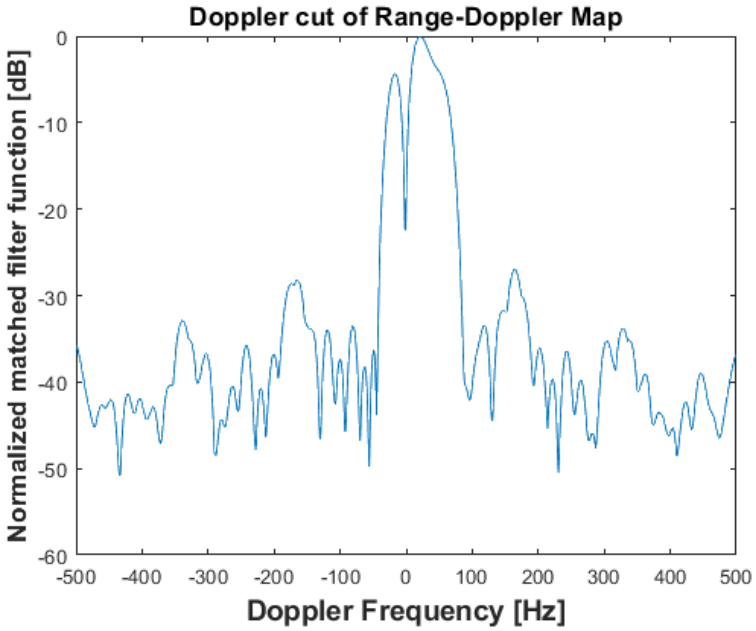

(b) Doppler-cut for a person running towards the receiver

Figure 7.17: Results for a person running towards the receiver after mean value removal and windowing with the top figure is the range-Doppler map and the bottom figure is the Doppler-cut

Doppler spread swamped the target and masked the detection. It was also seen that the mean value removal applied to the results only remove stationary clutter.

Target detection depends on the Radar Cross Section (RCS) of the object. Because the integration time is not too long (50 ms), the energy that was reflected to the target is very small and with the small RCS of a person running (with typical value is 1 m^2 [84]), the person is difficult to detect. This also influences the ability of the receiver to detect and distinguish the target from the clutter. In addition, because it was the same person running, there might be different speed during the two runs (away from and towards the receiver) caused by the tiredness of the person. It was concluded that for the person running, Doppler estimation is corrupted by clutter Doppler spread.

Figures 7.18 and 7.19 shows the results for a car moving away and towards the receiver before the mean value removal. A strong response around zero-Doppler can be seen in both figures. There is also a weak response at negative Doppler for a car moving away from the receiver and at positive response for a car moving towards the receiver. To remove the clutter around zero Doppler the mean value removal was applied in both results so only the detected Doppler frequency remains.

Figure 7.20 shows the result for a car moving away from the receiver. A range-Doppler map in Figure 7.20a indicates that the Doppler frequency response is at -90.07 Hz. This can be validated by the Doppler-cut of the target which shows the highest peak response occurred at -90.07 Hz, as shown in Figure 7.20b. For a car moving towards the receiver, a range-Doppler map is shown in Figure 7.21a where the peak response is detected at 68.01 Hz. This was also shown in the Doppler-cut result shown in Figure 7.21b where the peak response has the same value.

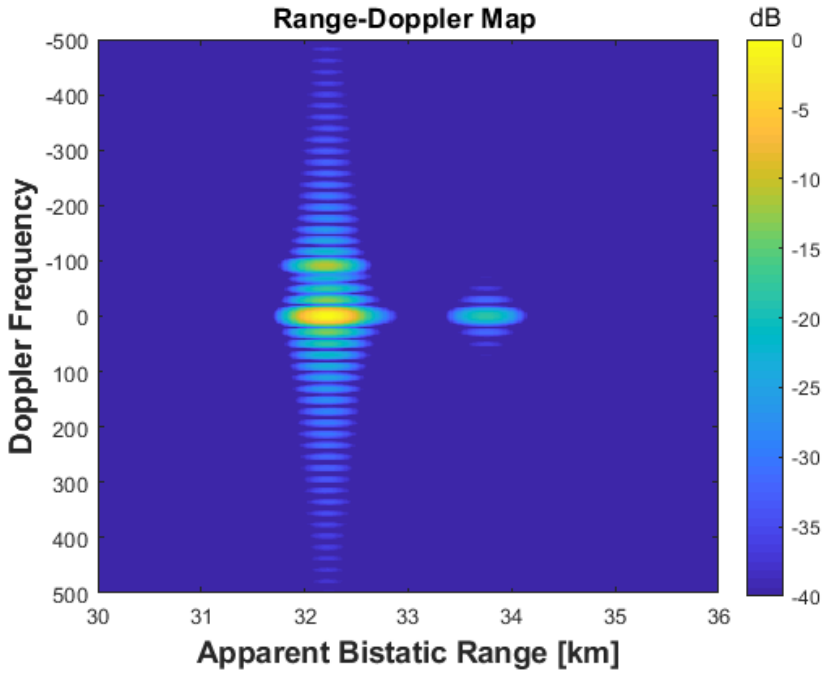

Figure 7.18: Range-Doppler map for a car moving away from the receiver before mean value removal

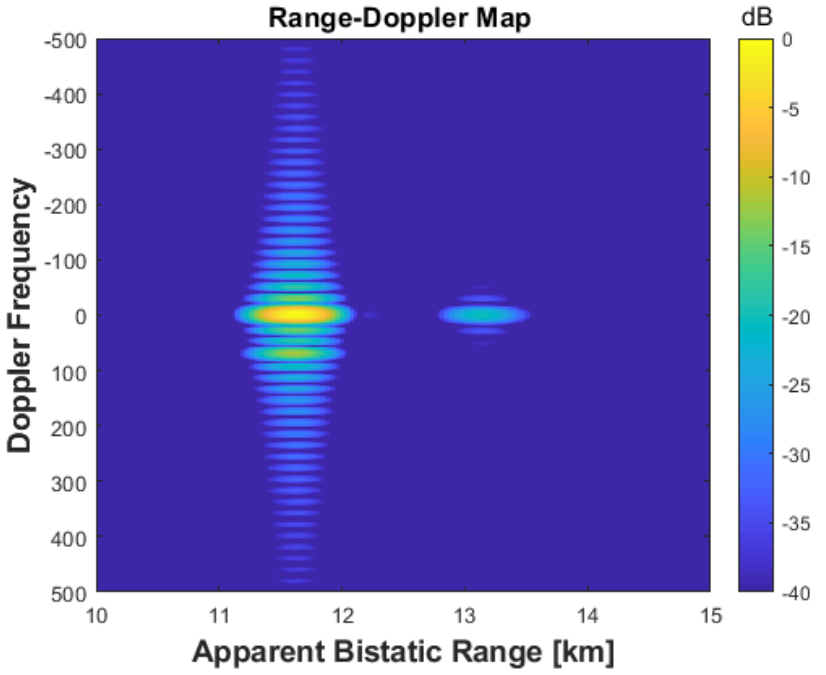

Figure 7.19: Range-Doppler map for a car moving towards the receiver before mean value removal

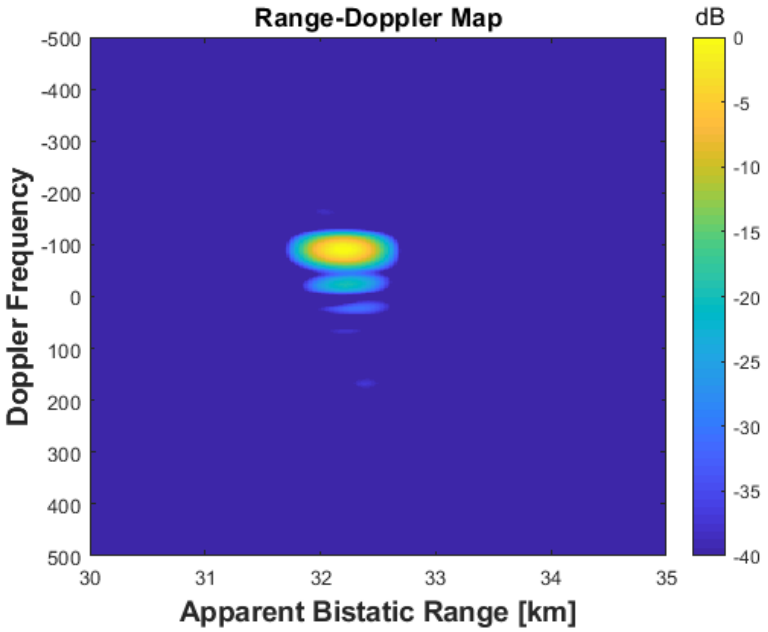

(a) Range-Doppler map for a car moving away from the receiver

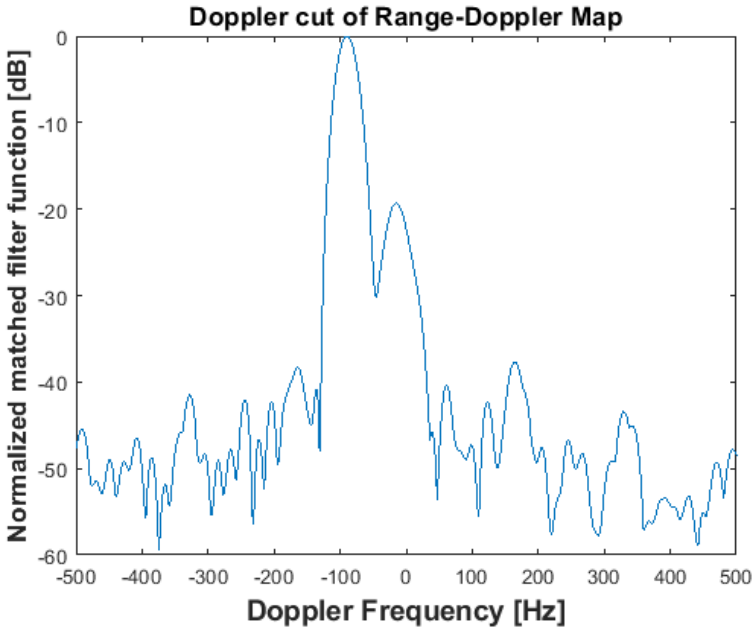

(b) Doppler-cut for a car moving away from the receiver

Figure 7.20: Results for a car moving away from the receiver after mean value removal and windowing with the top figure is the range-Doppler map and the bottom figure is the Doppler-cut

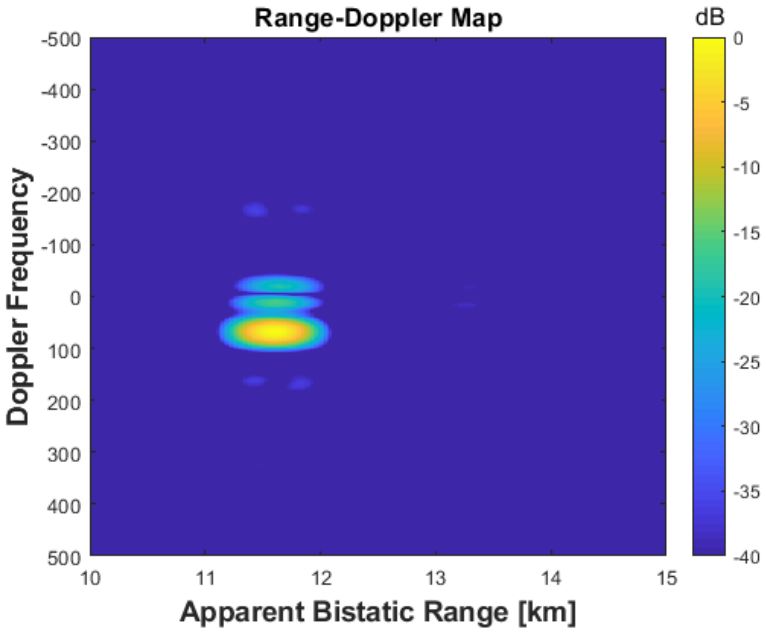

(a) Range-Doppler map for a car moving towards the receiver

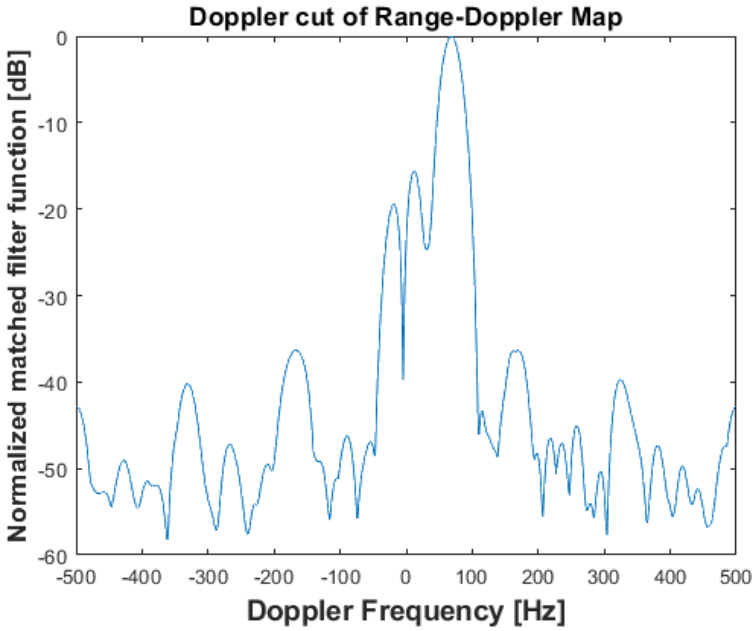

(b) Doppler-cut for a car moving towards the receiver

Figure 7.21: Results for a car moving towards the receiver after mean value removal and windowing with the top figure is the range-Doppler map and the bottom figure is the Doppler-cut

Figure 7.20b shows that the clutter response is reduced with clutter to signal ratio approximately at -20 dB. Target was successfully separated from the clutter spread and the Doppler frequency was extracted. For the case of a car moving towards the receiver, the clutter response is also lower with clutter to signal ratio approximately at -18 dB.

It can be seen in these results that that target was very well detected in both trajectories. With the same integration time as used for the person running (50 ms), the car was nicely detected due to the speed of the car which enabled it to be separated from the clutter. This is also due to the car being bigger than a person and also the material of the car which is more reflective than human body. This is indicated by the RCS of a car which has a typical value of 100 m^2 [84].

Based on the Doppler frequency shift gathered from the clutter response from a person running and the moving car, it was useful to determine the speed of the wind. It was found that the maximum clutter frequency in both cases happened at $\pm$17.46 Hz is equal to a speed of 2.09 m/s (4.67 mph). This is the typical speed of a light breeze according to [100]. With the speed of the wind found, it was verified that the clutter response having the Doppler frequency shift is due to the wind and the moving tree.

Figures 7.22 and 7.23 shows the range-Doppler map for a drone flying away and towards the receiver. Both figures show that there is a strong response around zero Doppler. This response is similar as the response found in previous results which was the clutter. Figure 7.22 shows that there is a weak response at negative Doppler which could be the target. A similar result was found in Figure 7.23 which shows that there is a weak response at positive Doppler. This could be resolved by applying

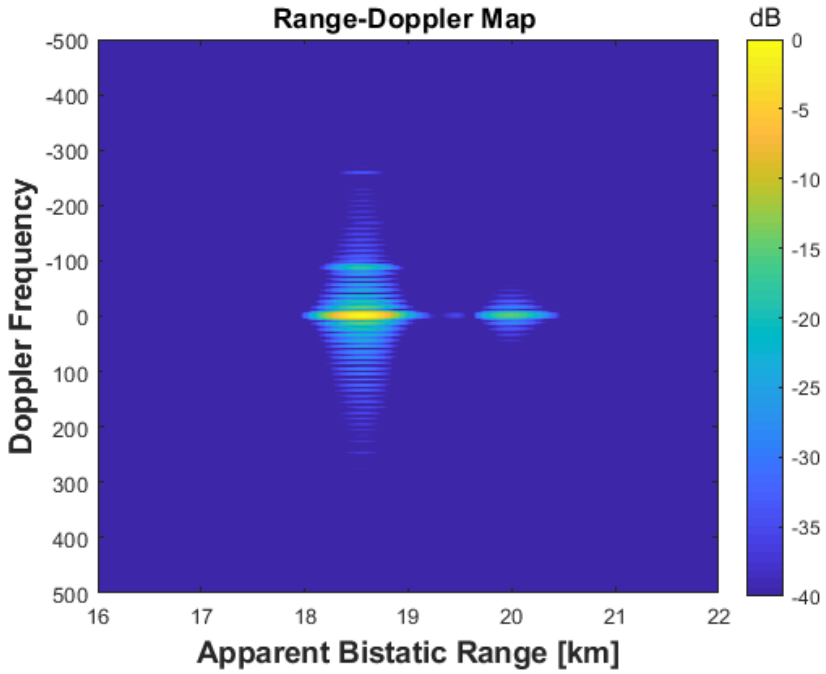

Figure 7.22: Range-Doppler map for a drone flying away from the receiver before mean value removal

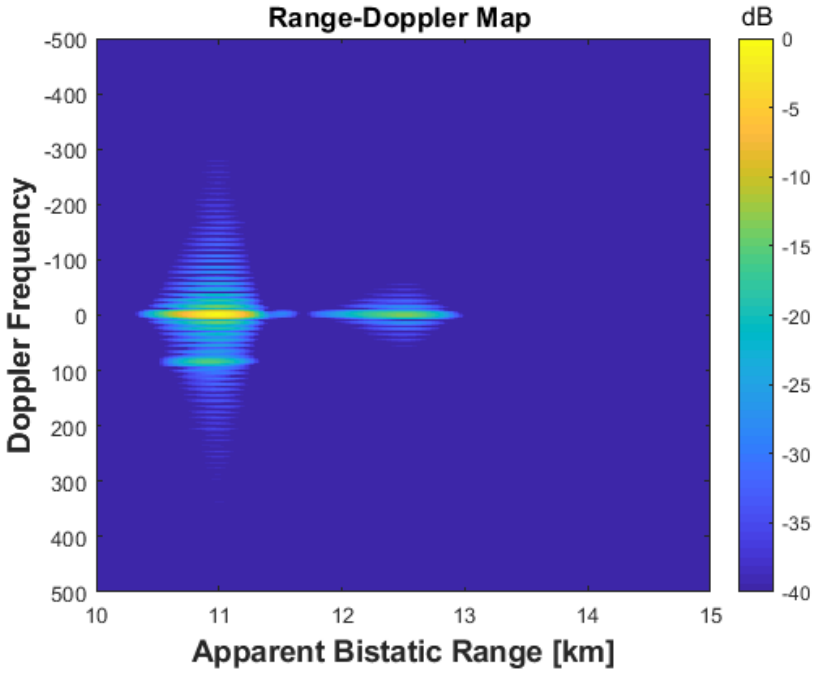

Figure 7.23: Range-Doppler map for a drone flying towards the receiver before mean value removal

mean value removal to both results.

Figure 7.24 shows the result for a drone flying away from the receiver. The range-Doppler map in Figure 7.24a shows the peak response at -88.24 Hz corresponding to 10.6 m/s (23.7 mph). This is also shown in the Doppler-cut in Figure 7.24b where the highest peak response also occurred at -88.24 Hz. It can be seen in the Doppler-cut figure that the clutter response is high, the difference between the highest peak and the clutter response is only 0.3 dB. However, from the range-Doppler map, it can be clearly seen that the target was separated in frequency from the clutter.

Figure 7.25 shows the result for a drone flying towards the receiver. The range-Doppler map is shown in Figure 7.24a where the peak Doppler response is at 84.56 Hz corresponding to 10.1 m/s (22.6 mph). This is also shown in the Doppler-cut result shown in Figure 7.24b where the similar Doppler frequency value is obtained. It can be seen in the range-Doppler map that the clutter response is weak and this is also seen in the Doppler-cut. The difference between the highest peak response and the clutter response is 8 dB. This probably due to the light wind that was blowing during the measurement.

It can be seen that in both of the cases that the clutter to signal ratio is slightly different. There is -7.7 dB difference in clutter amplitude when the drone flying towards the receiver and when it is flying away from the receiver. The measurement was taken continuously whilst the drone passed the receiver a few times (with 0.1 s integration time). The variation in clutter might be from the sudden gust of wind that affected the measurement when the drone was flying away from the receiver. Because the antenna was pointed towards the sky, this wind was caught by the radar receiver. It was also shown in these results that by increasing the integration time,

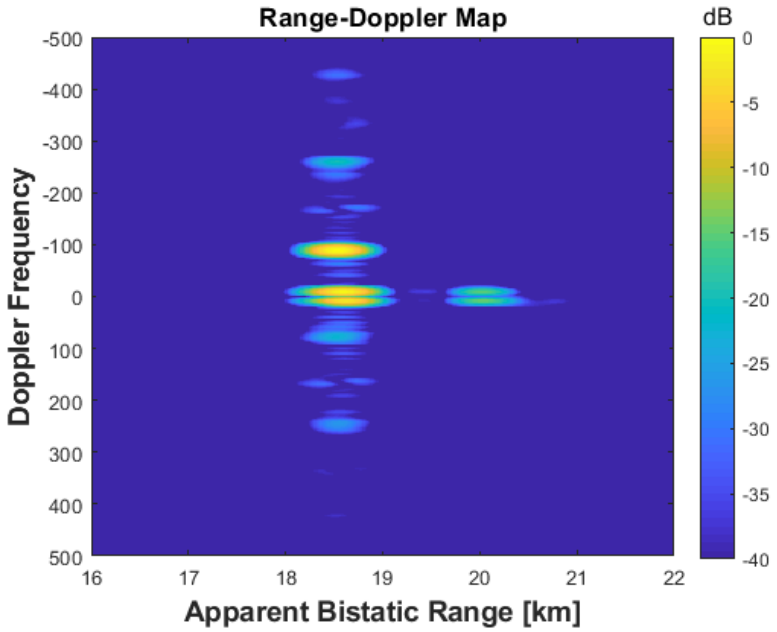

(a) Range-Doppler map for a drone flying away from the receiver

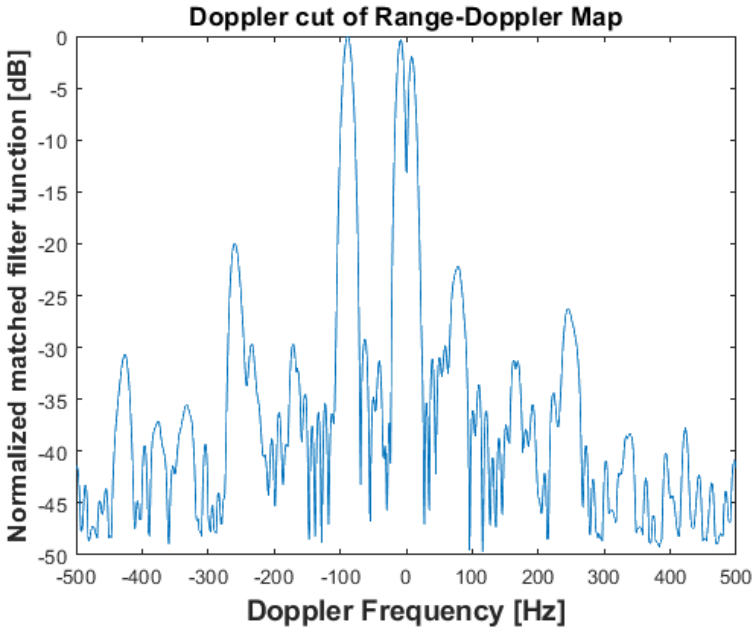

(b) Doppler-cut for a drone flying away from the receiver

Figure 7.24: Results for a drone flying away from the receiver after mean value removal and windowing with the top figure is the range-Doppler map and the bottom figure is the Doppler-cut

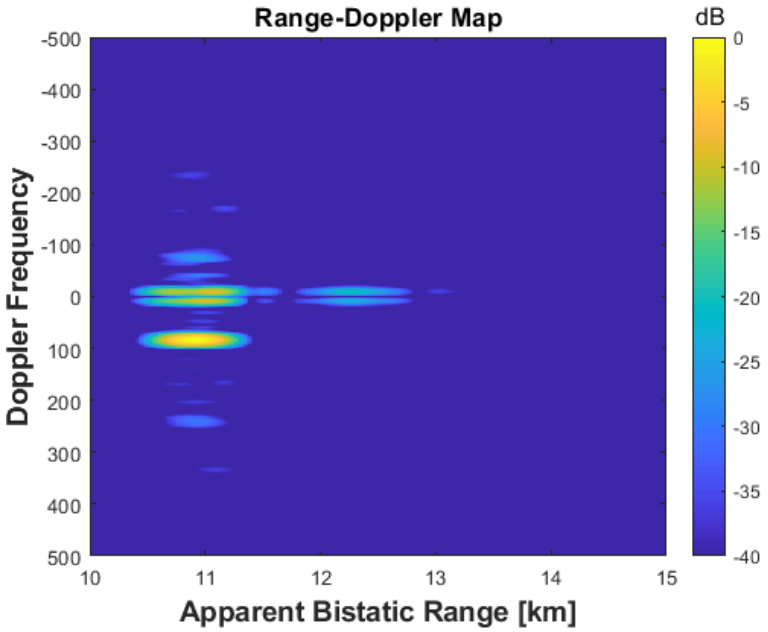

(a) Range-Doppler map for a drone flying towards the receiver

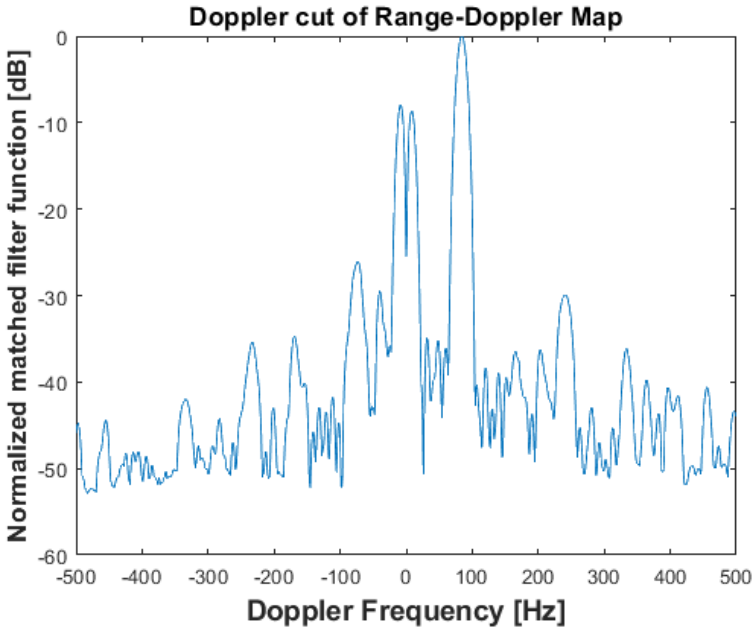

(b) Doppler-cut for a drone flying towards the receiver

Figure 7.25: Results for a drone flying towards the receiver after mean value removal and windowing with the top figure is the range-Doppler map and the bottom figure is the Doppler-cut

target can be detected even when the target has a small RCS. This is because the staring sensor from the staring radar gives a high update rate where the radar is able to maintain high detection capability.

It can be seen in Figures 7.24a and 7.25a that the gust of wind introduced a strong response but, with low clutter Doppler at ±8.2 Hz. The drone was flying in the air and so had less clutter from the ground and any moving tree. Moreover, because the receiver continuously received the data over the long period of integration time (0.1 s), there were times when the gust of wind became slow and only gave a weak clutter response as shown in Figure 7.25a.

This section has shown the result of target detection without the use of a reference channel. Apart from a person running (where it was concealed with the clutter), result shows that a car and a drone were successfully detected. It was also shown that there is a clutter that had introduced Doppler shifts in all the results. The clutter was consistent in all results which suggests it was introduced by the ground clutter such as trees moving in the wind. In the next section, the clutter response will be further explored and the corresponding radial velocity of the target will be presented.

7.5 Result Comparisons

Based on the results obtained from Chapter 6 and Chapter 7, the comparison between the two experiments will be presented. To make the comparisons easier, Doppler frequencies obtained from the two experiments were given in Table 7.1.

Table 7.1: Results for moving target detection with the reference channel and without the reference channel

Target	Trajectory	Ref. Channel	No Ref. Channel	% Difference
A person	Away from the receiver	-36.8 Hz	-39.52 Hz	7.39 %
	Towards the receiver	36.8 Hz	22.98 Hz	37.5 %
A car	Away from the receiver	-90.07 Hz	-90.07 Hz	0 %
	Towards the receiver	68.93 Hz	68.01 Hz	1.33 %
A drone	Away from the receiver	-85.48 Hz	-88.24 Hz	3.22 %
	Towards the receiver	85.48 Hz	84.56 Hz	1.07 %

Table 7.1 shows target detection results both with and without the use of reference channel. The percentage was calculated by taking the result without the use of reference channel as the experimental value and with the reference channel as the theoretical value. This is because results with the use of a reference channel have very close agreement with the GPS data thus make it reliable to be used as theoretical value in percentage difference calculation. Based on the results shown, the only high percentage difference is with a person running towards the receiver. To make the comparison easier, the two related range-Doppler maps and Doppler-cuts are shown in Figures 7.26 and 7.27.

Figure 7.26a shows the range-Doppler map for a person running towards the receiver with the use of the reference channel. It can be seen in the figure that the yellow response (corresponding to the person) is rather broad. This suggest that the person was successfully detected from the peak response in the Doppler-cut. In Figure 7.26b, a similar response from the person was seen, with the response being spread quite substantially. The clutter can also be seen in the figure. From the range-Doppler map, the target merged with the clutter due to there being no separation between the target and the clutter.

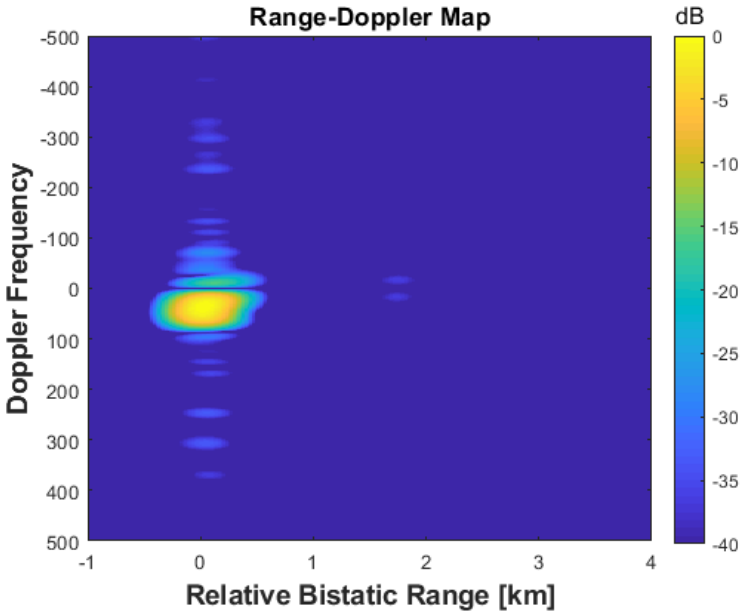

(a) Range-Doppler map for a person running towards the receiver with the use of a reference channel

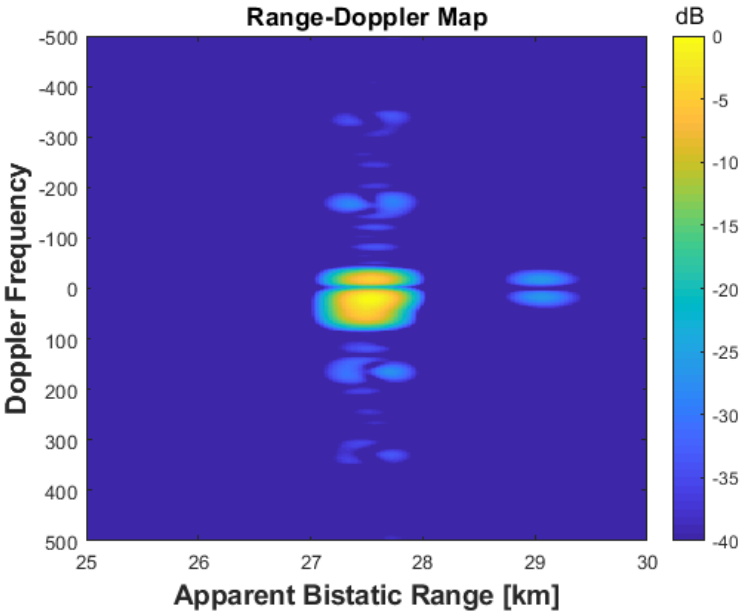

(b) Range-Doppler map for a person running towards the receiver without the use of a reference channel

Figure 7.26: Range-Doppler map for a person running towards the receiver. Top figure shows the result with use of a reference channel. Bottom figure shows the result without the use of a reference channel

Doppler-cuts for a person running towards the receiver with the use of a reference channel show a clear peak response. This target response was compared with the response obtained from reference channel removal which show the opposite result. The Doppler-cut shown in Figure 7.27b suggests that the target was swamped in the clutter. Considering the peak response is the detected target, the target can still be extracted from the peak response.

Figures 7.26a and 7.26b inferred that the Doppler clutter spread is strong and might have swamped the target. However, in the case with a reference channel, the target may be seen due to the reference signal compensating the surveillance signal in the matched-filter. In the case without a reference channel, the surveillance signal was matched-filtered with only a digital copy of the transmitted signal. This exposed the clutter received in the surveillance channel.

From the table of results, it can be seen that the car was successfully detected with the percentage error being very low in both cases. The best result is for the car moving away from the receiver, where the result was identical to the result obtained with the use of the reference channel. With the low percentage error obtained, this experiment confirmed the ability of the PBR system to detect a moving car without the use of the reference channel. It was also shown that with the integration time of 50 ms, the detection of the car was a success. Even though there is clutter present, this is low with a SNR of -20 dB. The car was detected and was able to be separated from merging with the clutter. This was shown in the Doppler frequency shift obtained from the experiments.

For the drone detection, it was shown in Table 7.1 that the percentage error between two cases was also less than 5 %. The results show that the drone was

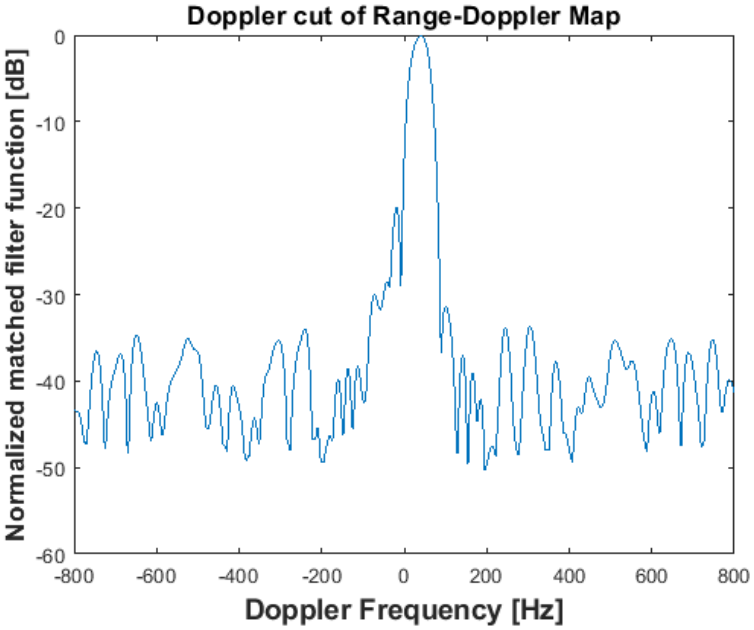

(a) Doppler-cut for a person running towards the receiver with the use of a reference channel

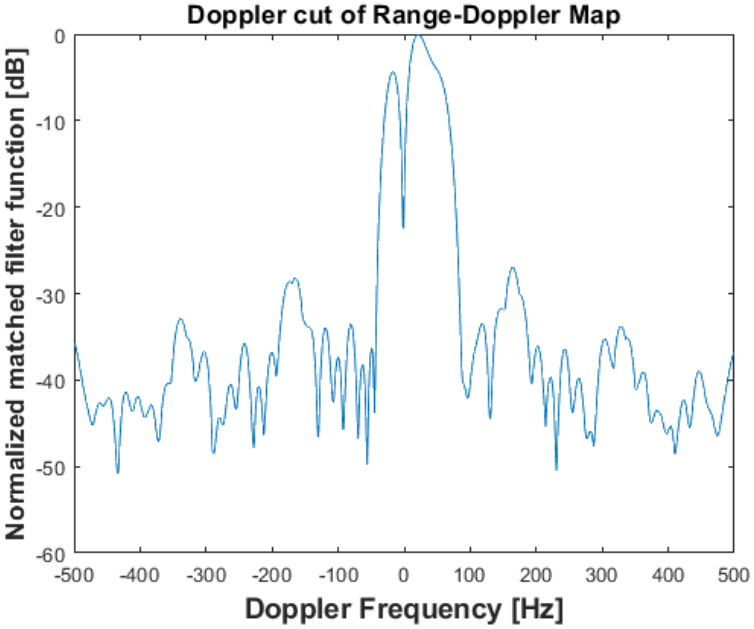

(b) Doppler-cut for a person running towards the receiver without the use of a reference channel

Figure 7.27: Doppler and range cuts after zero-Doppler suppression for a person running towards the receiver

successfully detected within the clutter presence. Even with the small RCS of the drone, it was successfully detected because the integration time was increased. The integration time for the drone detection is 0.1 s which allows the passive receiver to dwell on the drone for a longer time. This is different to a person running. The integration time for a person running was 50 ms that might be enough for detection, but, with the clutter Doppler spread, the detection experienced strong clutter which swamped the target.

It was also shown that the clutter was noticeable without the use of a reference channel. This is because when the reference channel was employed, the matched filter was done perfectly using both the surveillance and the reference signals. So, any irregularities in the surveillance signal were compensated for, which reduced the clutter. However, without the use of a reference channel, any irregularities in the surveillance signal were picked up and contributed to the high levels of clutter.

From these results, it is suggested that the clutter was contributed from the environment and may also be from the passive receiver. This is because the data was processed in the same way for every target. The experiment also used the same configuration and setup for each target. Removing the reference channel did not affect the ability of the passive receiver to detect the target, provided the processing was able to separate the target from the clutter.

Real-time Operational Issues

In this study, it was shown that target detection without the use of a reference channel is feasible provided the knowledge of the signal transmit is known a-priori

or had been estimated. Data was gathered and recorded where the processing was not done in real time. However, this system is not only limited into non-real-time application and can be expanded by real-time application. With real-time application, there might be some operational issues that need to be considered.

For real-time application, the hardware need to be ready to receive long stream of data. With the USRP, this can be done by changing the code in LabView to receive continuous stream of data. However, with longer integration time, there will be limitation in term of memory used. This could be solved by programming FPGA inside the USRP. In this study, the default FPGA configurations was used with custom signal processing. But, programming FPGA is challenging and require more time and understanding because it involve hardware and software configuration.

In addition, in real-time application, the continuous data stream might require big storage for the host computer which will increase computational load. Thus, having small storage in host computer might effect the processing in real time especially if it was done in Matlab. The data might need longer time to process and to produce results. This issue might be critical if longer integration was applied. Therefore, the system need to be ready to receive and process big data for real-time application.

7.6 Summary

In this chapter, the results for target detection without the reference channel were shown. The target was simulated to examine the characteristics of the signals (surveillance and the direct signals) and to find the Doppler frequency shift. The

carrier frequency offset that was known to exist when using the passive receiver with reference channel removal was included in the simulation. The simulation results show that target was successfully detected even with a carrier frequency offset that shifted the target's Doppler frequency from the correct value. It was also shown that the direct signal was removed and only the surveillance signal that contains target information remained.

In the analysis of the reference channel removal using real data, the same data as Chapter 6 was used. It was shown in the results that targets were successfully detected and extracted.

The comparisons between target detection with the reference channel and without the reference channel was made. Results was shown in the table to observe the performance between these two setup. It can be concluded that, target detection without the use of a reference channel is a success even care must be taken when the clutter was presence.

In the next chapter, the overall conclusions and suggestions for future work will be presented.

Chapter 8

Conclusion and Future Works

This chapter summarises the experiments that have been done through out this research and also includes the conclusions. The significance of the results will be presented along with suggestions for future work.

8.1 Summary of Results

The main objective of this thesis is to study the feasibility of PBR without the use of a reference channel by exploiting deterministic signal as illuminator of opportunity. A number of experiments have been done to prove the concept of target detection when the reference channel was removed. An experiment using staring radar as an illuminator of opportunity was used to make this comparison. Two sets of results were obtained from the signal processing exploiting staring radar, one with a reference channel and one without.

The preliminary experiment which used a signal generator, signal analyzer and

horn antennas was carried out in Chapter 4. The initial results showed that a moving target could be detected from the Doppler frequency shift of its response. The bistatic angle was calculated based on the distance of the transmitter, the receiver and the target point. The δ value was estimated from the trajectory of the targets. It was also shown that this system introduced jitter due to the system noise introduced by the instruments. Finally, this experiment used a simple processing scheme, where the direct FFT was applied to extract the Doppler frequencies.

In Chapter 5, the prototype PBR system was introduced. This prototype used a USRP-2943R that provided a fast solution in target detection. Furthermore, it is small which makes it easy to transport to field experiments. This prototype was used through out the rest of the experiments. The prototype was tested in monostatic configuration and successfully detected a moving target. The results showed that the prototype was successful in detecting a moving target. Then, a bistatic experiment was done with the same prototype. The results showed a moving target was successfully detected from the Doppler frequency shifts. The Doppler frequency shifts induced by the target were extracted from the range-Doppler map. The results also showed that the USRP introduced a frequency offset that shifts the Doppler frequency from the correct reading. The offset assessment was presented where it was concluded that by applying an external 10 MHz reference signal the frequency offset was reduced.

In Chapter 6, results for the PBR exploiting staring radar with the reference channel were presented. Three targets were successfully detected in two trajectories, moving away from the radar and towards the radar. The staring radar signals were simulated and the ambiguity function (AF) was shown. It was shown in the AF, the signals the peak response occurred every PRF/2. The signal processing to form

range-Doppler map was also outlined and also the ground truth data convention to extract GPS data. Results showed very close agreement between experimental and GPS data. To the best of our knowledge, this is the first experiment exploiting staring radar as illuminator of opportunity.

In Chapter 7, using the same radar and data from Chapter 6, results for PBR without the use of reference channel were presented. These two results were compiled and were shown in Table 7.1. It was found in the analysis that there is a clutter Doppler spread that concealed the target during detection. This effect was obvious in a person running where the clutter swamped and concealed the target. However, positive results were gathered for a car and a drone. These two targets were successfully separated from the clutter spread. This is due to the size and speed of the car and longer integration time for the drone.

PBR without the use of a reference channel provides a simple and cheap solution for target detection. Without the need to setup the reference channel, moving targets were successfully detected. Using a deterministic signal (namely staring radar), and based on the findings of this experimental work, this system can be applied in short range applications. With the increasing number of drones these days, the work in this thesis can be used as a basis for Unmanned Aerial Vehicle (UAV) monitoring in high-risk areas such as airports and other high security area.

8.2 Suggestions for Future Work

This study has made significant novel contributions to the field of PBR and has proved the concept of removing the reference channel in PBR. With the series of ex-

periments presented in the thesis it has been shown that by exploiting deterministic signals as illuminators of opportunity, targets were successfully detected.

However, there are several points that can be explored to further demonstrate the ability of target detection without the use of a reference channel. The prototype can be improved by employing real-time measurement and processing. This will provide fast and real-time results.

Furthermore, a precise synchronization method for PBR can be employed. With the precise synchronisation, multistatic PBR can be employed. This can be done by having a single transmitter of opportunity with multiple receivers. Thus, it can improve coverage of the PBR systems.

It was shown in Chapter 4, the value of the angle of the projected velocity vector δ was estimated from the target's trajectories. The estimated value may introduce inaccuracy in the calculation of the Doppler frequency. So, it is possible to use GPS in moving target detection to give accurate ground truth results. This was shown in the experiment with staring radar where the use of GPS data provided accurate ground truth data that was compared with experimental results. In addition, target tracking can also be implemented. This can be done from the Doppler shift and direction of arrival (DOA) induced by the target to acquire the target's track [19].

The study of clutter echoes is one of the key areas that require further study in PBR signal processing. The effect of this clutter is substantial especially to a target moving at slower speed where it can be masked by the clutter. Thus, this will reduce the efficiency of target detection. It is suggested that future work studies this clutter and multipath echoes. This can be done by applying clutter cancellation in the surveillance signal. There are a few techniques that can be applied to cancel

clutter such as the Extensive Cancellation Algorithm (ECA) [101] and ECA-sliding (ECA-S) approaches [102].

Additional experimental aspects are also suggested. This includes detecting different targets at longer ranges. Due to the advantages of staring radar presented in previous chapters, it is possible for staring radar to detect targets at longer ranges. Staring radar can also be exploited to detect traffic movement in high clutter environments. The integration time of PBR can be varied. With longer integration times, it is possible to detect more than one target in one measurement.

An experimental scenario with multiple targets could be explored. This would enable PBR without the reference channel to demonstrate the simultaneous detection and localisation of multiple targets. This would be analogous to a real world deployment.

This study can be implemented into a PBR exploiting non-cooperative illuminator of opportunity as shown in Chapter 6. The characteristics of transmit signal can be estimated instead of having priori knowledge of the signal. This can be done by estimating the reference signal. PRI could be estimated from the time difference between estimated Time of Arrival (TOA). Meanwhile, TOA of received pulse can be estimated by threshold processing after pulse compression as presented in [64].

8.3 Novel Aspects of Work

The main original contributions from this work can be summarised as follows:

- A feasibility study on PBR target detection without the use of a reference

channel was performed. A deterministic rectangular pulse signal was exploited for this purpose (Chapter 4). The initial prototype showed that there were few improvements that can be done to make this system more feasible in terms of signal processing and hardware used. Target was successfully detected from the bistatic geometry from the Doppler frequency obtained.

- A prototype that provides a fast, reliable and feasible solution was developed. The prototype was first used in a monostatic configuration to evaluate system performance (Chapter 5). Then, it was used in a bistatic configuration and throughout the rest of the experiments. The value of this prototype can be added in the future with real-time application. This will enable fast and reliable system in PBR target detection.

- The presence of a frequency offset inherent to this application was identified and investigated (Chapter 5). The results from the experiment were published in [103]. The effect of frequency offset was mitigated by applying external 10 MHz reference signal. This finding is significant where in future experiment, there is no shift in Doppler frequency detected.

- The exploitation of a staring radar for PBR target detection was demonstrated experimentally (Chapter 6). Targets were detected with the presence of a reference channel. To the best of my knowledge, this was the first experiment that exploits staring radar as an illuminator of opportunity in PBR.

- Successful PBR target detection without the use of a reference channel exploiting staring radar. The experimental results show that target detection without the use of a reference channel is feasible (Chapter 7). Targets were detected passively where the priori knowledge of the transmit signal is known.

This is a novel and significant result. In future, a preliminary covert measurement of the transmitter can be done to enable real-time reference signal reconstruction.

8.4 Summary

This thesis successfully achieved the overall objective that was presented in Chapter 1 which was target detection without the use of a reference channel by exploiting deterministic signals. The specific objectives were also achieved which are:

- the feasibility study into target detection without the use of a reference channel was successfully shown in Chapter 4
- the prototype that provides reliable and fast target detection was successfully built and shown in Chapter 5
- the evaluation of the prototype build was shown from the experimental work where targets were successfully detected
- target detection exploiting staring radar as an illuminator of opportunity was shown through the detection of a human, a car and a drone
- target detection without the use of a reference channel was successfully performed and this was shown in the results obtained

Bibliography

[1] N. J. Willis and H. D. Griffiths, *Advances in Bistatic Radar*. Raleigh: SciTech Publishing, Inc, 2007.

[2] S. Bayat, M. M. Nayebi, and Y. Norouzi, "Target detection by passive coherent FM based bistatic radar," in *Proceedings of the 2008 International Conference on Radar, Radar 2008*, pp. 412–415, IEEE, September 2008.

[3] P. Howland, "Editorial: Passive radar systems," *IEE Proceedings - Radar, Sonar and Navigation*, vol. 152, no. 3, p. 105, 2005.

[4] F. Alfonso and H. Kuschel, "Guest editorial special issue on passive radar (Part I)," *Aerospace and Electronic Systems Magazine, IEEE*, vol. 27, p. 5, October 2012.

[5] S. Searle, L. Davis, and J. Palmer, "Signal processing considerations for passive radar with a single receiver," in *2015 IEEE International Conference on Acoustics, Speech and Signal Processing (ICASSP)*, pp. 5560–5564, IEEE, April 2015.

[6] G. Fang, J. Yi, X. Wan, Y. Liu, and H. Ke, "Experimental Research of Multistatic Passive Radar With a Single Antenna for Drone Detection," *IEEE Access*, vol. 6, pp. 33542–33551, 2018.

[7] W. Katy, "Venezuela President Maduro survives 'drone assassination attempt' - BBC News," August 2018.

[8] C. Baker and H. Griffiths, "BISTATIC AND MULTISTATIC RADAR SENSORS FOR HOMELAND SECURITY," in *Advances in Sensing with Security Applications*, pp. 1–22, Dordrecht: Kluwer Academic Publishers, 2006.

[9] C. J. B. Paul E. Howland, Hugh D. Griffiths, "Passive Bistatic Radar Systems," in *Bistatic Radar: Emerging Technology* (M. Cherniakov, ed.), ch. 7, pp. 283–285, West Sussex: John Wiley & Sons, Ltd, 1st ed., 2008.

[10] N. J. Willis, *Bistatic Radar*. Norwood: Artech House, Inc, 1st ed., 1991.

[11] G. W. Arend, "Radar Versus Stealth: Passive Radar and the Future of U.S. Military Power," *JOINT FORCE QUARTERLY (JFQ)*, vol. 4th Quarte, no. 55, pp. 136–143, 2009.

[12] I. Suberviola, I. Mayordomo, and J. Mendizabal, "Experimental Results of Air Target Detection With a GPS Forward-Scattering Radar," *IEEE Geoscience and Remote Sensing Letters*, vol. 9, pp. 47–51, Jan 2012.

[13] M. Gashinova, L. Daniel, E. Hoare, V. Sizov, K. Kabakchiev, and M. Cherniakov, "Signal characterisation and processing in the forward scatter mode of bistatic passive coherent location systems," *EURASIP Journal on Advances in Signal Processing*, vol. 2013, p. 36, December 2013.

[14] P. Krysik, K. Kulpa, and P. Samczyński, "GSM based passive receiver using forward scatter radar geometry," in *2013 14th International Radar Symposium (IRS)*, (Dresden), pp. 637–642, IEEE, 2013.

[15] T. Martelli, F. Colone, and P. Lombardo, "First experimental results for a WiFi-based passive forward scatter radar," in *2016 IEEE Radar Conference (RadarConf)*, pp. 1–6, IEEE, May 2016.

[16] M. Mandlik and Z. Nemec, "An accuracy synchronization method for passive radar system," in *2014 24th International Conference Radioelektronika*, pp. 1–4, IEEE, April 2014.

[17] H. D. Griffiths and N. R. W. Long, "Television-based bistatic radar," *IEE Proceedings F - Communications, Radar and Signal Processing*, vol. 133, no. 7, pp. 649–657, 1986.

[18] M. A. Ringer, G. J. Frazer, and S. J. Anderson, "Waveform Analysis of Transmitters of Opportunity for Passive Radar," tech. rep., Defence Science and Technology Organisation.

[19] P. Howland, "Target tracking using television-based bistatic radar," *Radar, Sonar and Navigation, IEE Proceedings*, vol. 146, pp. 166–174, June 1999.

[20] J. D. Sahr and F. D. Lind, "The Manastash Ridge radar: A passive bistatic radar for upper atmospheric radio science," *Radio Science*, vol. 32, pp. 2345–2358, November 1997.

[21] H. D. Griffiths and C. J. Baker, "Measurement and analysis of ambiguity functions of passive radar transmissions," in *IEEE International Radar Conference, 2005*, (Arlington, VA), pp. 321–325, IEEE, 2005.

[22] H. Griffiths and C. Baker, "Passive coherent location radar systems. Part 1: Performance prediction," *IEE Proceedings - Radar, Sonar and Navigation*, vol. 152, no. 3, p. 153, 2005.

[23] Z. Jiabing, T. Liang, and H. Yi, "A direct path interference cancellation approach to passive radar based on FM radio transmitter," in *2006 IEEE International Conference on Electro/Information Technology*, (East Lansing, MI), pp. 55–59, IEEE, 2006.

[24] P. Howland, D. Maksimiuk, and G. Reitsma, "FM radio based bistatic radar," *IEE Proceedings - Radar, Sonar and Navigation*, vol. 152, no. 3, p. 107, 2005.

[25] O. Bialer and S. Kolpinizki, "Multi-Doppler Resolution Automotive Radar," in *25th European Signal Processing Conference(EUSIPCO)*, (Kos), pp. 1937–1941, 2017.

[26] A. S. Tasdelen and H. Koymen, "Range Resolution Improvement in Passive Coherent Location Radar Systems Using Multiple FM Radio Channels," in *The Institution of Engineering and Technology Forum on Waveform Diversity and Design in Communications, Radar and Sonar*, (London, UK), pp. 23–31, Institution of Engineering and Technology, 2006.

[27] C. Bongioanni, F. Colone, and P. Lombardo, "Performance analysis of a multi-frequency FM based passive bistatic radar," in *2008 IEEE Radar Conference*, (Rome), pp. 1–6, IEEE, 2008.

[28] K. E. Olsen and K. Woodbridge, "FM based passive bistatic radar range resolution improvement," in *2011 12th International Radar Symposium (IRS)*, (Leipzig), pp. 327–332, IEEE, 2011.

[29] M. Edrich, F. Meyer, and A. Schroeder, "Design and performance evaluation of a mature FM/DAB/DVB-T multi-illuminator passive radar system," *IET Radar, Sonar & Navigation*, vol. 8, no. October 2013, pp. 114–122, 2014.

[30] H. Kuschel, M. Ummenhofer, P. Lombardo, F. Colone, and C. Bongioanni, "Passive Radar Components of ARGUS 3D," *Aerospace and Electronic Systems Magazine, IEEE*, vol. 29, no. March, pp. 15–25, 2014.

[31] L. Wan, X. Wang, and G. Bi, "A range-Doppler-angle estimation method for passive bistatic radar," in *2018 International Conference on Signals and Systems (ICSigSys)*, pp. 213–218, 2018.

[32] D. Tan, H. Sun, Y. Lu, M. Lesturgie, and H. Chan, "Passive radar using Global System for Mobile communication signal: theory, implementation and measurements," *IEE Proceedings - Radar, Sonar and Navigation*, vol. 152, no. 3, p. 116, 2005.

[33] M. Kubica, V. Kubica, X. Neyt, J. Raout, S. Roques, and M. Acheroy, "Optimum Target Detection using Illuminators of Opportunity," in *2006 IEEE Conference on Radar*, (Verona, NY), pp. 417–424, IEEE, 2006.

[34] K. Chetty, Q. Chen, and K. Woodbridge, "Train Monitoring using GSM-R Based Passive Radar," in *2016 IEEE Radar Conference (RadarConf)*, (Philadelphia, PA), pp. 1 – 4, IEEE, 2016.

[35] R. S. A. Raja Abdullah, F. H. Hashim, A. A. Salah, N. E. Abdul Rashid, A. Ismail, and N. H. Abdul Aziz, "Experimental investigation on target detection and tracking in passive radar using long-term evolution signal," *IET Radar, Sonar & Navigation*, vol. 10, pp. 577–585, mar 2016.

[36] A. A. Salah, R. R. Abdullah, A. Ismail, F. Hashim, and N. A. Aziz, "Experimental study of LTE signals as illuminators of opportunity for passive bistatic radar applications," *Electronics Letters*, vol. 50, no. 7, pp. 545–547, 2014.

[37] R. S. A. Raja Abdullah, A. A. Salah, A. Ismail, F. Hashim, N. E. Abdul Rashid, and N. H. Abdul Aziz, "LTE-Based Passive Bistatic Radar System for Detection of Ground-Moving Targets," *ETRI Journal*, vol. 38, pp. 302–313, April 2016.

[38] C. Klock, V. Winkler, and M. Edrich, "LTE-signal processing for passive radar air traffic surveillance," in *2017 18th International Radar Symposium (IRS)*, pp. 1–9, IEEE, June 2017.

[39] R. S. Thomä, C. Andrich, G. D. Galdo, M. Döbereiner, M. A. Hein, M. Käske, G. Schäfer, S. Schieler, C. Schneider, A. Schwind, and P. Wendland, "Cooperative Passive Coherent Location: A Promising Service for Future Mobile Radio Networks," *IEEE Communications Magazine*, 2018.

[40] D. Gould, R. Pollard, C. Sarno, and P. Tittensor, "A multiband passive radar demonstrator," in *2006 International Radar Symposium*, (Krakow), pp. 1–4, IEEE, 2006.

[41] D. Gould, R. Pollard, C. Sarno, and P. Tittensor, "Developments to a multiband passive radar demonstrator system," in *2007 IET International Conference on Radar Systems*, (Edinburgh, UK), pp. 1–5, IET, 2007.

[42] J. Palmer, D. Merret, S. Palumbo, J. Piyaratna, S. Capon, and H. Hansen, "Illuminator of Opportunity Bistatic Radar Research at DSTO," (Adelaide, SA), pp. 701 – 705, IEEE, September 2008.

[43] D. Langellotti, F. Colone, P. Lombardo, E. Tilli, M. Sedehi, and A. Farina, "Over the horizon maritime surveillance capability of DVB-T based passive radar," in *European Microwave Week 2014: "Connecting the Future", EuMW 2014 - Conference Proceedings; EuRAD 2014: 11th European Radar Conference*, (Rome, Italy), pp. 509–512, IEEE, 2014.

[44] Z. Gao, R. Tao, Y. Ma, and T. Shao, "DVB-T signal cross-ambiguity functions improvement for passive radar," in *2006 CIE International Conference on Radar*, (Shanghai), pp. 1–4, IEEE, 2006.

[45] J. L. Barcena-Humanes, J. Martin-de Nicolas, C. Solis-Carpintero, M. P. Jarabo-Amores, M. Rosa-Zurera, and D. Mata-Moya, "DVB-T ambiguity peaks reduction in passive radar applications based on signal reconstruction," in *2014 44th European Microwave Conference*, pp. 1900–1903, IEEE, 2014.

[46] F. Colone, D. Langellotti, and P. Lombardo, "DVB-T Signal Ambiguity Function Control for Passive Radars," *IEEE Transactions on Aerospace and Electronic Systems*, vol. 50, pp. 329–347, Jan 2014.

[47] H. Guo, K. Woodbridge, and C. J. Baker, "Evaluation of WiFi beacon transmissions for wireless based passive radar," in *2008 IEEE Radar Conference, RADAR 2008*, no. 1, (Rome), pp. 1–6, 2008.

[48] K. Chetty, G. E. Smith, and K. Woodbridge, "Through-the-wall sensing of personnel using passive bistatic wifi radar at standoff distances," *IEEE Transactions on Geoscience and Remote Sensing*, vol. 50, no. 4, pp. 1218–1226, 2012.

[49] P. Falcone, F. Colone, and P. Lombardo, "Potentialities and challenges of WiFi-based passive radar," *IEEE Aerospace and Electronic Systems Magazine*, vol. 27, pp. 15–26, 2012.

[50] Q. Chen, K. Chetty, K. Woodbridge, and B. Tan, "Signs of life detection using wireless passive radar," in *2016 IEEE Radar Conference (RadarConf)*, pp. 1–5, IEEE, May 2016.

[51] H. Griffiths and A. Garnett, "Bistatic Radar using satellite-borne illuminators of opportunity," in *92 International Conference on Radar*, vol. 6, pp. 276–279, 1992.

[52] J. B. Tsui and R. L. Shaw, *Passive ranging through global positioning system.* Google Patents, Feb 1993.

[53] V. Koch and R. Westphal, "New approach to a multistatic passive radar sensor for air/space defense," *Aerospace and Electronic Systems Magazine, IEEE*, vol. 10, no. 11, pp. 24–32, 1995.

[54] M. Antoniou and M. Cherniakov, "Passive GNSS-Based SAR Resolution Improvement Using Joint Galileo E5 Signals," *IEEE Geoscience and Remote Sensing Letters*, vol. 12, pp. 1640–1644, August 2015.

[55] E. P. Glennon, A. G. Dempster, C. Rizos, and Others, "Feasibility of air target detection using GPS as a bistatic radar," *Journal of Global Positioning Systems*, vol. 5, no. 1-2, pp. 119–126, 2006.

[56] Iridium, "Iridium Satellite Communications."

[57] M. Cherniakov, D. Nezlin, and K. Kubik, "Air target detection via bistatic radar based on LEOS communication signals," *IEE Proceedings-Radar, Sonar and Navigation*, vol. 149, no. 1, pp. 33–38, 2002.

[58] H. Griffiths, C. Baker, and J. Baubert, "Bistatic radar using satellite-borne illuminators," in *RADAR 2002*, (Edinburgh, UK), pp. 1–5, IET, 2002.

[59] R. K. Raney, "Synthetic aperture imaging radar and moving targets," *Aerospace and Electronic Systems, IEEE Transactions on*, no. 3, pp. 499–505, 1971.

[60] A. P. Whitewood, B. R. Muller, H. D. Griffiths, and C. J. Baker, "Bistatic synthetic aperture radar with application to moving target detection," in *2003 Proceedings of the International Conference on Radar (IEEE Cat. No.03EX695)*, (Adelaide), pp. 529–534, IEEE, 2003.

[61] A. P. Whitewood, C. J. Baker, and H. D. Griffiths, "Bistatic radar using a spaceborne illuminator," in *2007 IET International Conference on Radar Systems*, (Edinburgh, UK), pp. 1–5, 2007.

[62] E. S. A. (ESA), "ESA declares end of mission for Envisat / Envisat / Observing the Earth / Our Activities / ESA," 2012.

[63] P. Samczyński, M. Wilkowski, and K. Kulpa, "Trial Results on Bistatic Passive Radar Using Non-Cooperative Pulse Radar as Illuminator of Opportunity," *International Journal of Electronics and Telecommunications*, vol. 58, no. 3, pp. 291–294, 2012.

[64] T. Ito, R. Takahashi, S. Morita, and K. Hirata, "Experimental result of passive bistatic radar with unknown transmitting radar pulse," in *2013 European Radar Conference*, (Nuremberg), pp. 455–458, IEEE, 2013.

[65] J. Thomas, C. Baker, and H. Griffiths, "DRM signals for HF passive bistatic radar," in *IET International Conference on Radar Systems 2007*, pp. 166–166, IEE, 2007.

[66] Wan Xianrong, Zhao Zhixin, Zhang Delei, and Shao Qihong, "HF passive bistatic radar based on DRM illuminators," in *Proceedings of 2011 IEEE CIE International Conference on Radar*, pp. 157–160, IEEE, October 2011.

[67] Z. Zhao, X. Wan, D. Zhang, and F. Cheng, "An Experimental Study of HF Passive Bistatic Radar Via Hybrid Sky-Surface Wave Mode," *IEEE Transactions on Antennas and Propagation*, vol. 61, pp. 415–424, Jan 2013.

[68] M. Ritchie, F. Fioranelli, H. Griffiths, and B. Torvik, "Monostatic and bistatic radar measurements of birds and micro-drone," in *2016 IEEE Radar Conference (RadarConf)*, pp. 1–5, IEEE, May 2016.

[69] A. Aldowesh, M. Shoaib, K. Jamil, S. Alhumaidi, and M. Alam, "A passive bistatic radar experiment for very low radar cross-section target detection," in *2015 IEEE Radar Conference*, pp. 406–410, IEEE, October 2015.

[70] T. Martelli, F. Murgia, F. Colone, C. Bongioanni, and P. Lombardo, "Detection and 3D localization of ultralight aircrafts and drones with a WiFi-based Passive Radar," in *International Conference on Radar Systems (Radar 2017)*, (Belfast), pp. 1–6, Institution of Engineering and Technology, 2017.

[71] A. Chadwick, "Micro-Drone Detection using Software-Defined 3G Passive Radar," in *International Conference on Radar Systems (Radar 2017)*, (Belfast), pp. 1–6, Institution of Engineering and Technology, 2017.

[72] Y. Liu, X. Wan, H. Tang, J. Yi, Y. Cheng, and X. Zhang, "Digital television based passive bistatic radar system for drone detection," in *2017 IEEE Radar Conference (RadarConf)*, pp. 1493–1497, IEEE, May 2017.

[73] A. Evers and J. A. Jackson, "Cross-ambiguity characterization of communication waveform features for passive radar," *IEEE Transactions on Aerospace and Electronic Systems*, vol. 51, pp. 3440–3445, October 2015.

[74] W. C. Barott and J. Engle, "Single-antenna ATSC passive radar observations with remodulation and keystone formatting," in *2014 IEEE Radar Conference*, pp. 0159–0163, IEEE, May 2014.

[75] Y. Zhang, Y. Li, W. Li, and Y. Wei, "Target detection with single surveillance channel for PBR," in *2016 IEEE International Geoscience and Remote Sensing Symposium (IGARSS)*, pp. 6409–6412, IEEE, July 2016.

[76] M. N. Cohen, "Pulse Compression in Radar Systems," in *Principles of Modern Radar*, pp. 465–501, Boston, MA: Springer, 1987.

[77] B. R. Mahafza, *Radar Systems Analysis and Design Using Matlab*. Alabama: CRC Press, 3rd ed., 2013.

[78] N. Levanon and E. Mozeson, *Radar Signals*. New Jersey: John Wiley & Sons Inc., 1st ed., 2004.

[79] IEEE Aerospace and Electronic Systems Society. Radar Systems Panel., Institute of Electrical and Electronics Engineers., and IEEE-SA Standards Board.,

IEEE standard for letter designations for radar-frequency bands. Institute of Electrical and Electronics Engineers, 2003.

[80] B.J. Reits and A. Groenenboom, "FMCW signal processing for a pulse radar," in *92 International Conference on Radar*, (Brighton), p. 544, IET, 1992.

[81] G. L. Charvat, *Small and Short-Range Radar Systems*. Florida: CRC Press, 1 ed., 2014.

[82] J. R. Klauder, A. C. Price, S. Darlington, and W. J. Albersheim, "The Theory and Design of Chirp Radars," *Bell System Technical Journal*, vol. 39, pp. 745–808, July 1960.

[83] K. Georgiev, A. Balleri, A. Stove, and M. W. Holderied, "Bio-inspired processing of radar target echoes," *IET Radar, Sonar & Navigation*, July 2018.

[84] M. I. Skolnik, *Introduction to Radar Systems*. McGraw-Hill, 3rd ed., 2001.

[85] G. W. Stimson, H. D. Griffiths, C. J. Baker, and D. Adamy, *Introduction to Airborne Radar*. SciTech Publishing, 3rd ed., May 2014.

[86] P. M. Woodward, *Probability and Information Theory with Applications to Radar*. New York: Mc Graw-Hill, 1953.

[87] M. A. Richards, *Fundamentals of Radar Signal Processing*. McGraw-Hill Education, 2nd ed., 2014.

[88] MathWorks United Kingdom, "Generalized Cosine Windows."

[89] Europian Union, "Regulation No 39 of the Economic Commission for Europe of the United Nations (UN/ECE) — Uniform provisions concerning the

approval of vehicles with regard to the speedometer equipment including its installation," *Official Journal of the European Union*, vol. 53, pp. 40–48, 2010.

[90] National Instruments, "USRP-2943 - National Instruments."

[91] B. Brannon, "Software Defined Radio," tech. rep.

[92] N. Pandeya and N. Temple, "About USRP Bandwidths and Sampling Rates - Ettus Knowledge Base," 2016.

[93] D. M. Pozar, *Microwave and RF Design of Wireless Systems*. John Wiley & Sons, Ltd, 1st ed., 2000.

[94] G. K. A. Oswald, "Holographic surveillance radar," in *Proceedings SPIE 7308, Radar Sensor Technology XIII, 73080* (K. I. Ranney and A. W. Doerry, eds.), vol. 7308, (Florida), p. 73080D, International Society for Optics and Photonics, May 2009.

[95] M. Jahangir and C. Baker, "Robust Detection of Micro-UAS Drones with L-Band 3-D Holographic Radar," in *2016 Sensor Signal Processing for Defence (SSPD)*, (Edinburgh), pp. 1–5, IEEE, September 2016.

[96] M. Jahangir and C. J. Baker, "Extended dwell Doppler characteristics of birds and micro-UAS at L-band," in *Proceedings International Radar Symposium*, (Prague), 2017.

[97] N. Levanon, "Inter-pulse coding for ideal range response," in *2008 IEEE Radar Conference*, pp. 1–6, IEEE, May 2008.

[98] N. Levanon, "Mitigating Range Ambiguity in High PRF Radar using Inter-Pulse Binary Coding," *IEEE Transactions on Aerospace and Electronic Systems*, vol. 45, pp. 687–697, April 2009.

[99] S. Haykins, *Communication Systems*. John Wiley & Sons Inc., 3rd ed., 1994.

[100] National Meteorological Library, "National Meteorological Library Archive Fact sheet 6 - The Beaufort Scale," tech. rep., National Meteorological Library, 2010.

[101] F. Colone, D. W. O'Hagan, P. Lombardo, and C. J. Baker, "A Multistage Processing Algorithm for Disturbance Removal and Target Detection in Passive Bistatic Radar," *IEEE Transactions on Aerospace and Electronic Systems*, vol. 45, pp. 698–722, April 2009.

[102] F. Colone, C. Palmarini, T. Martelli, and E. Tilli, "Sliding extensive cancellation algorithm for disturbance removal in passive radar," *IEEE Transactions on Aerospace and Electronic Systems*, vol. 52, pp. 1309–1326, June 2016.

[103] N. Ghazalli, A. Balleri, and F. Colone, "Exploitation of Deterministic Signals for Passive Single-Channel Detection," in *2017 Sensor Signal Processing for Defence Conference (SSPD)*, pp. 1–5, IEEE, December 2017.